

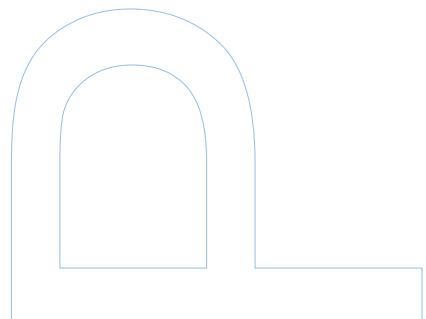
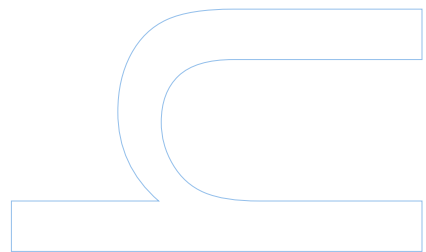
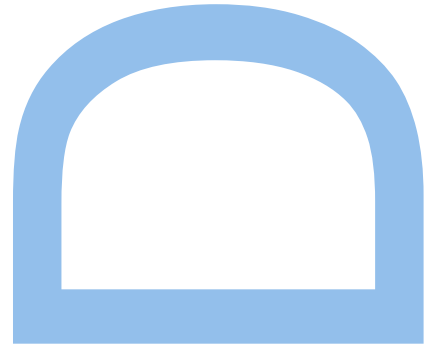
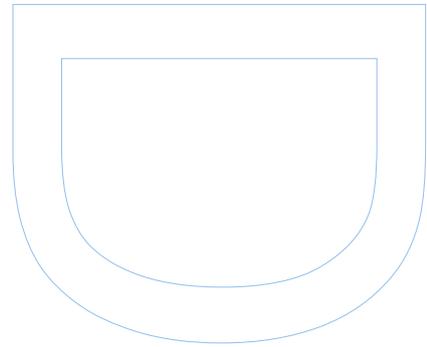
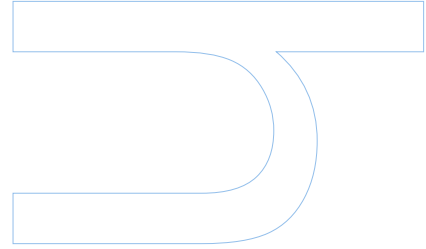
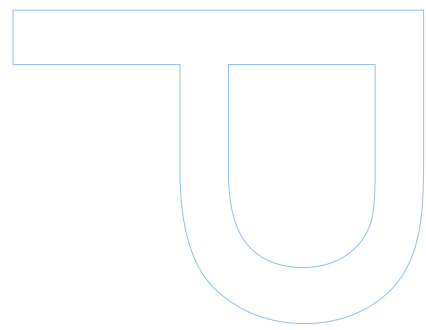
# Spectral Methods in Quantum Transport

Simão Meneses João

Doutoramento em Física  
Departamento de Física e Astronomia  
2022

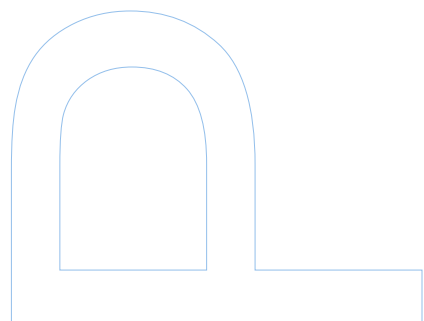
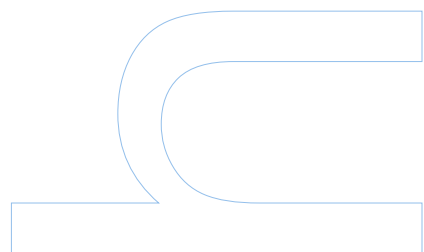
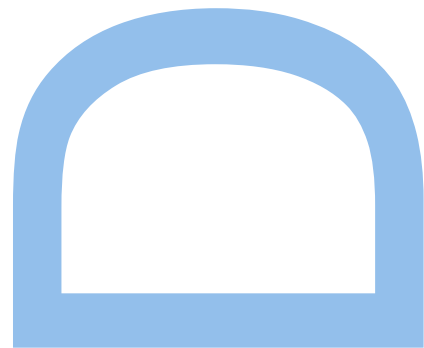
**Orientador**

João Manuel Viana Parente Lopes  
Professor Auxiliar Convidado  
Faculdade de Ciências da Universidade do Porto





Universidade do Minho



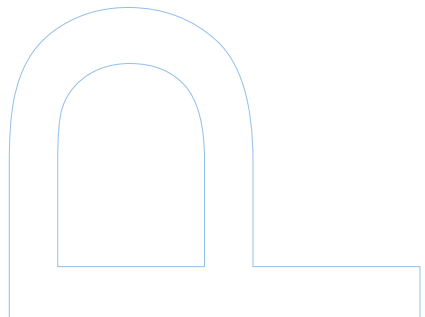
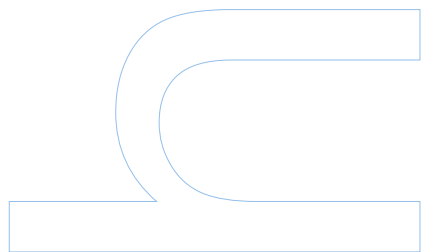
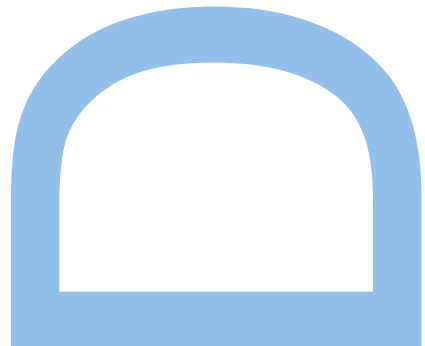
Todas as correcções determinadas pelo júri, e só essas, foram efetuadas.

O Orientador,



Porto,

2, 10, 2022



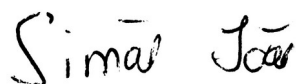
# Declaração de Honra

Eu, Simão Meneses João, inscrito no Programa Doutoral em Física da Faculdade de Ciências da Universidade do Porto declaro, nos termos do disposto na alínea a) do artigo 14. do Código Ético de Conduta Académica da U.Porto, que o conteúdo da presente tese reflete as perspetivas, o trabalho de investigação e as minhas interpretações no momento da sua entrega.

Ao entregar esta tese, declaro, ainda, que a mesma é resultado do meu próprio trabalho de investigação e contém contributos que não foram utilizados previamente noutros trabalhos apresentados a esta ou outra instituição.

Mais declaro que todas as referências a outros autores respeitam escrupulosamente as regras da atribuição, encontrando-se devidamente citadas no corpo do texto e identificadas na secção de referências bibliográficas. Não são divulgados na presente tese quaisquer conteúdos cuja reprodução esteja vedada por direitos de autor.

Tenho consciência de que a prática de plágio e auto-plágio constitui um ilícito académico.

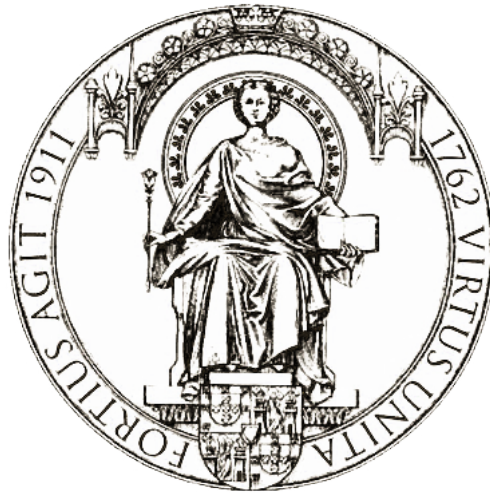


Simão Meneses João

30 de Setembro de 2022, Porto

Faculdade de Ciências da Universidade do Porto

# Spectral Methods in Quantum Transport



**Simão Meneses João**

May 16, 2022

Dissertation submitted to the Faculty of Sciences of the University of Porto for the  
degree of Ph.D in Physics

## Acknowledgements

This thesis is not just the product of four intense years of learning and research. It is the culmination of 10 years of Physics education and insertion in a scientific community. Even though it has been written from the comfort of my house, I will be telling my grandchildren that this thesis was written under a deadly pandemic and during the course of the largest military conflict in Europe since the second world war. These events marked my PhD, but also showed me that people are capable of doing incredible things when the situation requires them to do so.

I would like to begin by expressing my utmost gratitude to my supervisor Dr. *João Viana Lopes*, whom I will always remember as the professor who kept an open door for anyone (literally and figuratively) and whose main teaching purpose is to be an elevator: to lift his students above himself. He was always invariably available to help and discuss, and the rigor and numerical expertise which he has imprinted unto me will remain with me for the rest of my life. The KITE project would not be possible without him, and I owe a lot of my academic achievements to this project. I must extend my gratitude to Dr. *Aires Ferreira* for the constant support and enthusiasm throughout my whole PhD. I have had the opportunity of working with his group in the beautiful city of York in the UK for several months, and from these visits one of the defining ideas of this thesis was Born - the exact calculation of the self-energy - as well as other ideas which didn't make it into this thesis. I would also like to thank Dr. *Branislav Nikolic* for hosting me during my visit to his group in the University of Delaware USA, where I had the opportunity of learning a great deal about spintronics and Green's functions methods. A special thanks is also due to Prof. *Lopes dos Santos* for his valuable insights and enlightening discussions.

In an unprecedented move for the physics department, in part due to the need for a larger teaching body because of COVID, PhD students were hired for the first time to teach undergraduate students. I was lucky enough to be part of the original set of people chosen for this task and I have kept that task for four semesters, teaching Statistical Physics and Computational Physics. This has been a tremendous experience for myself. The students, of course, also benefited by having someone closer to their age explain things to them, someone who has had the same education, with the same teachers. So I would like to dedicate this paragraph to my students who have taught me so much.

My friends were responsible for keeping me sane during the mentally demanding periods of lockdown in Madeira, be it through informal zoom meetings, Discord sessions or our crazy trips around the island. In this and many other aspects, I am indebted to *André* and *Filipe Moura*, *Luísa* and *Margarida Mendonça*, *Christopher Freitas*, *Carolina Freitas* and *Carolina Vieira*. This gratitude is extended to my friends in my *de facto* second home, Porto: *Nelson Eiró*, *José Dias*, *João Guerra*, *Carlos Fernandes*, *Guilherme Guedes*, *Maria Ramos*, *Maurício Quintela*, *Beatriz Gamboa*, *Daniel Santos*, *Gonçalo Roboredo*, *António Antunes* and *José Matos*. I would also like to thank *João Pinho* and *Henrique Veiga* directly for their close collaboration with me. A special thanks goes to *João Pires*, with

whom I shared a PhD and a supervisor, and whose encyclopedic knowledge of Physics never stops to amaze me. I would also like to thank *Luísa Pinto Pereira* for hosting me during most of my time in Porto.

Finally, and most importantly, I have to dedicate my sincerest thanks to my family: my father *José Simão*, my mother *Esmeralda* and my sister *Carolina*. We are greatly defined by our education, and I was lucky enough to have a loving and supporting family who was always able to provide me with the best education and support me financially during this academic adventure.

Even more finally, I would like to gratefully acknowledge financing by Fundação para a Ciência e Tecnologia (FCT) under the grant no. PD/BD/142798/2018, financial support from the FCT, COMPETE 2020 programme in FEDER component (European Union), through projects POCI-01-0145-FEDER028887 and UID/FIS/04650/2013 and further acknowledge financial support from FCT through national funds, co-financed by COMPETE-FEDER (grant no. M-ERANET2/0002/2016 – Ultra-Graf ) under the Partnership Agreement PT2020. The numerical simulations were performed in the Viking HPC facilities of the University of York and the GRID computing cluster at the Faculty of Engineering of the University of Porto.



## Resumo

Os métodos espectrais estão entre os candidatos modernos mais promissores no que toca à implementação de algoritmos de escalamento linear  $\mathcal{O}(N)$  para a simulação de transporte quântico e propriedades electrónicas. O objectivo desta tese é estender o seu alcance e a aplicabilidade em várias áreas do transporte quântico.

Nos primeiros dois capítulos, começo por abordar o estado da arte e por analisar com detalhe alguns aspectos importantes dos métodos espectrais que vão ser relevantes para o resto da tese, tal como a decomposição de Chebyshev e a avaliação estocástica do traço.

O capítulo seguinte é dedicado a uma das principais ideias originais desta tese: o primeiro cálculo exacto do operador auto-energia devido a desordem, com recurso a uma avaliação extremamente precisa da função de Green desordenada média. Graças a isto, conseguimos ver fenómenos não perturbativos de baixa energia no operador de auto-energia que podem estar relacionados com a robustez dos modos de energia nula no grafeno.

O quarto capítulo foca-se no cálculo da resposta óptica não linear com métodos espectrais. Usando o formalismo de Keldysh, desenvolvo um esquema diagramático perturbativo que pode ser usado directamente por métodos espectrais, estendendo a abordagem de Weisse à condutividade AC. Este método é usado para estudar o efeito de vários tipos de desordem no grafeno e no h-BN.

No capítulo 5, aplico uma avaliação estocástica do traço para calcular a corrente fora-de-equilíbrio entre dois reservatórios através de uma amostra. Isto torna linear a complexidade do cálculo da corrente de Landauer.

No capítulo final, apresento uma variação do formalismo de Chebyshev-Bogoliubov-de Gennes que usa vectores aleatórios para calcular o parâmetro de ordem em supercondutores. Isto é aplicável a impurezas dilutas e remove uma grande porção da complexidade numérica deste tipo de cálculos.

Todos estes métodos foram implementados por mim no projecto open-source KITE, num pacote a ser lançado numa versão futura.

## Summary

Spectral methods are among the most promising modern candidates to implement large scale linear scaling  $\mathcal{O}(N)$  algorithms for quantum transport and electronic properties simulations. The goal of this thesis is to extend their scope and applicability in several areas of quantum transport.

In the first two chapters, I begin by addressing the state of the art and by analyzing in detail some important aspects about spectral methods which are going to be relevant for the remainder of the thesis, such as the Chebyshev decomposition and the stochastic trace evaluation.

The next chapter is devoted to one of the main original ideas of this thesis: the first exact calculation of the disorder self-energy operator in graphene, with resort to an extremely finely resolved disorder-averaged Green's function. This reveals previously unseen low-energy nonperturbative momentum dependency of the self-energy operator which could be related to the robustness of zero-energy modes in graphene.

The fourth chapter is centered around the calculation of the nonlinear optical response with spectral methods. Using the Keldysh formalism, I develop a diagrammatic perturbation scheme directly usable by spectral methods, to extend Weisse's approach to linear AC conductivity. This is used to study the effect of different kinds of disorder in graphene and h-BN.

Chapter 5 sees the application of a stochastic trace evaluation to calculate the out-of-equilibrium current through two leads across a sample. This turns the complexity of the calculation of the Landauer current into a linear scaling one.

In the final chapter, I present a variation of the Chebyshev-Bogoliubov-de Gennes formalism which uses random vectors to compute the order parameter in superconductors. This is applicable to dilute impurities and removes a large portion of the numerical complexity of this kind of calculation.

All of these methods have been implemented by myself in the KITE open-source software, in a package that will be released in a future version.



# Publications by the Author

## Peer-Reviewed Papers:

- [1] S. Meneses, J. Penedones, S. Rychkov, J. M. Viana Parente Lopes, and P. Yvernay, “A structural test for the conformal invariance of the critical 3d ising model”, *Journal of High Energy Physics* 2019, 115 (2019)
- [2] S. M. João and J. M. V. P. Lopes, “Basis-independent spectral methods for non-linear optical response in arbitrary tight-binding models”, *Journal of Physics: Condensed Matter* 32, 125901 (2019)
- [3] S. M. João, M. Anđelković, L. Covaci, T. G. Rappoport, J. M. V. P. Lopes, and A. Ferreira, “KITE: high-performance accurate modelling of electronic structure and response functions of large molecules, disordered crystals and heterostructures”, *Royal Society Open Science* 7, 191809 (2020)
- [4] S. Meneses João, J. P. Santos Pires, and J. M. Viana Parente Lopes, “A new microscopic look into pressure fields and local buoyancy”, *American Journal of Physics* 90, 179–186 (2022)
- [5] S. M. João, J. M. V. P. Lopes, and A. Ferreira, “High-resolution real-space evaluation of the self-energy operator of disordered lattices: gade singularity, spin-orbit effects and p-wave superconductivity”, arXiv:2110.00574 [cond-mat] (2021)
- [6] J. P. S. Pires, S. M. João, A. Ferreira, B. Amorim, and J. M. V. P. Lopes, “Nodal vacancy bound states and resonances in T-symmetric weyl semimetals: spectral and bulk transport properties”, (2022)
- [7] J. P. Santos Pires, S. M. João, B. Amorim, A Ferreira, and J. M. Viana Parente Lopes, “Anomalous charge transport in T-symmetric weyl semimetals with point defects”, (2022)

## Peer-Reviewed Conference Proceedings:

- [8] M. F. C. M. Quintela, J. C. C. Guerra, and S. M. João, “Electronic properties of twisted bilayer graphene in the presence of a magnetic field”, *EPJ Web of Conferences* 233, Publisher: EDP Sciences, 03004 (2020)

- [9] S. M. João and J. M. V. P. Lopes, “Non-linear optical response in disordered 2d materials”, EPJ Web of Conferences 233, Publisher: EDP Sciences, 03002 (2020)

## **Keywords**

Quantum Transport, KPM, Spectral Methods, Superconductivity, Self-energy, Disorder, Nonlinear optics



# Contents

<b>1</b>	<b>Introduction</b>	<b>1</b>
<b>2</b>	<b>Introduction to spectral methods</b>	<b>13</b>
2.1	General overview . . . . .	13
2.2	Chebyshev polynomials of the first kind . . . . .	15
2.3	Convergence . . . . .	17
2.3.1	Comparison with Taylor series . . . . .	18
2.4	Chebyshev expansion for operators . . . . .	19
2.5	Chebyshev expansion for known functions . . . . .	21
2.5.1	Dirac delta . . . . .	21
2.5.2	Complex exponential . . . . .	21
2.5.3	Green's function . . . . .	22
2.5.4	Fermi-Dirac distribution . . . . .	25
2.6	Stochastic trace evaluation . . . . .	28
2.6.1	Variance of Chebyshev moments . . . . .	30
2.7	Applications to quantum transport . . . . .	31
2.7.1	Reducing the price of a double expansion . . . . .	32
2.7.2	Avoiding a double expansion . . . . .	34
2.8	Further applications . . . . .	35
<b>3</b>	<b>Diagrammatics in disordered systems</b>	<b>37</b>
3.1	Intuitive introduction to the disorder self-energy . . . . .	37
3.2	Self-energy and the disorder averaged Green's function . . . . .	39
3.3	Diagrammatics . . . . .	40
3.3.1	Correlators with Anderson disorder . . . . .	41
3.3.2	Correlators with impurity disorder . . . . .	43
3.3.3	Diagrammatic representation . . . . .	47
3.3.4	Fourth order diagrams . . . . .	49
3.4	Diagrammatics with spectral methods . . . . .	50
3.5	Self-energy and approximation techniques . . . . .	50
3.5.1	Born approximation . . . . .	52
3.5.2	Self-consistent Born approximation . . . . .	52
3.5.3	T-matrix . . . . .	53
3.5.4	T-matrix in graphene with vacancies . . . . .	54
3.5.5	A different T-matrix for graphene . . . . .	56

## Contents

3.6	Exact calculation of the self-energy operator . . . . .	56
3.6.1	Numerical procedure . . . . .	57
3.6.2	Considerations on convergence . . . . .	58
3.7	Self-energy in SRO . . . . .	59
3.7.1	Tight-binding Hamiltonian and band structure . . . . .	60
3.7.2	Anderson disorder . . . . .	61
3.7.3	Vacancies . . . . .	64
3.8	Self-energy in graphene with vacancies . . . . .	65
3.8.1	Self-energy . . . . .	67
3.8.2	Convergence study . . . . .	69
<b>4</b>	<b>Nonlinear optical conductivity</b>	<b>71</b>
4.1	Keldysh Formalism . . . . .	71
4.1.1	Definitions . . . . .	71
4.1.2	Non-interacting electronic systems . . . . .	73
4.2	Tight-binding Hamiltonian with external electric field . . . . .	75
4.2.1	Series expansion . . . . .	75
4.2.2	Perturbative expansion of the conductivity . . . . .	77
4.3	Spectral methods . . . . .	79
4.3.1	Expansion in Chebyshev polynomials . . . . .	79
4.3.2	Considerations on the numerical storage of $\Gamma$ . . . . .	80
4.4	Numerical results . . . . .	81
4.4.1	Linear optical response in graphene . . . . .	81
4.4.2	Gapped graphene . . . . .	82
4.4.3	Sublattice displacement . . . . .	83
4.4.4	Photogalvanic effect in gapped graphene with Anderson disorder . . . . .	85
4.4.5	Second-harmonic generation of gapped graphene with vacancies . . . . .	86
4.4.6	Considerations on convergence and accuracy . . . . .	86
4.4.7	Considerations on efficiency . . . . .	90
<b>5</b>	<b>Stochastic conductance</b>	<b>91</b>
5.1	Setup . . . . .	91
5.1.1	Partition-free . . . . .	92
5.1.2	Partitioned . . . . .	93
5.2	Nonlinear local current . . . . .	95
5.3	Linear local current . . . . .	96
5.4	Comparison with other formalisms . . . . .	97
5.4.1	Landauer formula . . . . .	98
5.4.2	Bulk Kubo's formula . . . . .	99
5.5	Time-dependent current across a tight-binding chain . . . . .	100
5.5.1	The role of the leads . . . . .	103

5.6	Generalization to cross sections . . . . .	104
5.6.1	Consideration on scaling . . . . .	105
5.7	Stochastic current . . . . .	106
5.7.1	Average over cross-sections . . . . .	107
5.7.2	Choice of random vectors . . . . .	109
5.7.3	Operator order . . . . .	110
5.8	Stochastic vs exact . . . . .	112
5.9	Further optimizations and limitations . . . . .	113
5.10	Further applications . . . . .	115
<b>6</b>	<b>Spectral methods in superconductors with dilute impurities</b>	<b>117</b>
6.1	Interacting Hamiltonian . . . . .	117
6.1.1	The Bogoliubov-de Gennes Hamiltonian . . . . .	119
6.1.2	Spin, symmetry and types of superconductors . . . . .	121
6.1.3	Nonmagnetic materials . . . . .	123
6.1.4	Consideration on numerical efficiency . . . . .	125
6.2	Dealing with inhomogeneities . . . . .	125
6.2.1	Considerations on the choice of $z$ . . . . .	129
6.2.2	Higher dimensions and further generalization . . . . .	129
6.3	Superconducting graphene . . . . .	130
<b>7</b>	<b>Conclusion</b>	<b>135</b>
<b>8</b>	<b>Appendix</b>	<b>147</b>
8.1	Self averaging property . . . . .	147
8.1.1	Weak disorder . . . . .	147
8.1.2	Localized states . . . . .	149



# List of Figures

1.1	Structure of a generic unit cell. . . . .	9
1.2	Structure of a generic lattice constructed with the previous unit cell. This particular 2D lattice has periodic boundary conditions along the 1 direction, but open boundary conditions along the 2 direction. . . . .	10
2.1	First few Chebyshev polynomials. . . . .	16
2.2	Comparison between a Taylor expansion and a Chebyshev expansion using $N = 100$ polynomials for each. . . . .	19
2.3	Comparison between a Taylor expansion and a Chebyshev expansion in the complex plane for different numbers of polynomials. . . . .	20
2.4	Convergence properties of the Chebyshev expansion of the Green's function, as a function of the number of polynomials used to expand it. Each curve represents a different value of the broadening parameter $\eta$ . . . . .	25
2.5	Convergence properties of the Fermi function of chemical potential $\mu = 0.2$ at zero temperature. . . . .	27
3.1	Spectral function of the 1D TB model of hopping $t$ and lattice constant $a$ , for several Anderson disorder strengths. The yellow dashed line represents the dispersion relation for the clean model. . . . .	38
3.2	Diagrammatic representation of the disordered Green's function, before averaging over disorder configurations. . . . .	40
3.3	Example of different Anderson disorder configurations for a square lattice. The color represents the value of the local potential. . . . .	41
3.4	Different configurations of mutually exclusive impurities (top row) and non-mutually exclusive impurities (bottom row) in a square lattice. Sites in yellow (red) have local energy $\varepsilon$ ( $2\varepsilon$ ). The remaining sites have local energy zero. . . . .	43
3.5	Diagrammatic representation of the process of disorder averaging with one disorder insertion (left) and two disorder insertions (right). . . . .	48
3.6	Diagrams appearing in fourth order when the odd moments are zero. . . . .	49
3.7	Self-energy operator (a) as a sum of one-particle irreducible diagrams, and the disorder-averaged Green's function as a sum over self-energy operators (b). Note that these diagrams do not have the external propagators. . . . .	51

List of Figures

3.8	a) Born approximation (BA), b) Self-consistent Born approximation (SCBA), c) T-matrix approximation (TMA) and d) self-consistent T-matrix approximation (SCTMA). The thin lines with arrows represent the clean Green's function $g$ and the thick lines with arrows the disorder-averaged complete Green's function $\bar{G}$ . . . . .	52
3.9	SrRuO <sub>3</sub> embedded in a SrTiO <sub>3</sub> matrix. . . . .	59
3.10	Band structure (left) and density of states (right) of SRO. . . . .	61
3.11	Independent matrix elements of the self-energy operator for weak correlated Anderson disorder of strength $W = 0.1\text{eV}$ in SRO. Each matrix element is color coded. The complete matrix is displayed on the right. Matrix elements with the same color are related to each other by a factor of $1, -1, i$ or $-i$ . . . . .	62
3.12	Three selected matrix elements of the self-energy operator for stronger correlated Anderson disorder of strength $W = 0.5\text{ eV}$ in SRO. The other matrix elements have been omitted for clarity, and the self-energy matrix still follows the same structure as in Fig. 3.11. . . . .	63
3.13	Independent matrix elements of the self-energy operator for uncorrelated Anderson disorder $W = 0.2\text{ eV}$ in SRO. . . . .	63
3.14	Independent matrix elements of the self-energy operator at $\mathbf{k} = \mathbf{M}$ for a 0.1% concentration of vacancies in SRO. . . . .	64
3.15	Comparison between the T-matrix approximation (normalized to the concentration of vacancies) and the exact self-energy operator for two concentrations of vacancies (0.1% and 6%) in SRO. . . . .	64
3.16	$d_{yz\uparrow}d_{yz\uparrow}$ component of the self-energy as a function of concentration for several values of the energy in SRO (dotted lines in Fig. 3.15). . . . .	65
3.17	Graphene lattice with vacancies. . . . .	67
3.18	Components of the imaginary part of the self-energy operator as a function of energy for a vacancy concentration of 0.3% (top) and 1% (bottom) in graphene. Each color represents a different point in the Brillouin zone (bottom right hexagon). The T-matrix and the self-consistent T-matrix approximations are represented by black curves. . . . .	68
3.19	AA component of the imaginary part of the self-energy operator at the Dirac point for several concentrations in graphene. The right panel shows the collapsed self-energy matrix using the ansatz $\Sigma(\varepsilon) = c^\alpha f(\varepsilon c^\alpha)$ with $\alpha \approx 0.56$ . . . . .	69
3.20	Convergence study for the imaginary part of the AA component of the disorder self-energy operator in graphene. . . . .	70
4.1	Diagrammatic representation of the expected value of the current operator in Fourier space. The horizontal straight line ending in a circle is the lesser Green's function and the wavy line beginning in a circle represents the current operator. . . . .	72

4.2	Diagrammatic representation of the lesser Green's function. . . . .	74
4.3	Diagrammatic representation of the external perturbation. . . . .	76
4.4	Diagrammatic representation of the current operator. The single small circle is to be understood as a Dirac delta. . . . .	77
4.5	Expansion of the expected value of the conductivity in (a) first and (b) second order. . . . .	77
4.6	Honeycomb lattice and choice of primitive vectors. . . . .	82
4.7	First-order longitudinal $yy$ conductivity for graphene in units of $\sigma_0 = e^2/\hbar$ . Hopping parameter: $t = 2.33\text{eV}$ , temperature: $T = 2.33\text{mK}$ , chemical potential: $\mu = 0.466\text{eV}$ , broadening parameter: $\eta = 38.8\text{meV}$ , number of Chebyshev moments used: $M = 2048$ , lattice size: $L = 4096 \times 4096$ . The solid curves represent the optical conductivity obtained by KITE (real part in green, imaginary in blue). The superimposed dashed lines are obtained in [64]. . . . .	83
4.8	Second-order $yyy$ photogalvanic effect for gapped graphene. Hopping parameter: $t = 2.33\text{eV}$ , temperature: $T = 0\text{K}$ , chemical potential: $\mu = 0\text{eV}$ , gap $\Delta = 7.80\text{eV}$ broadening parameter: $\eta = 39\text{meV}$ , number of Chebyshev moments used: $M = 2048$ , lattice size: $L = 4096 \times 4096$ . The imaginary part disappears after the result is properly symmetrized. . . . .	84
4.9	Displaced honeycomb lattice and choice of primitive vectors. . . . .	85
4.10	Second-order $xyy$ photogalvanic effect for displaced gapped graphene. Hopping parameter: $t = 2.33\text{eV}$ , temperature: $T = 0\text{K}$ , chemical potential: $\mu = 0\text{eV}$ , gap $\Delta = 7.8\text{eV}$ broadening parameter: $\eta = 39\text{meV}$ , number of Chebyshev moments used: $M = 512$ , lattice size: $L = 1024 \times 1024$ . . . . .	86
4.11	Photogalvanic effect for gapped graphene in the presence of Anderson disorder of varying strength $W$ and a broadening parameter of $\eta = 23\text{meV}$ . The parameters are the same as for Fig. 4.4.2 except for the number of polynomials, which is $M = 512$ . The dashed lines represent the imaginary part of the conductivity. . . . .	87
4.12	Second-harmonic generation in gapped graphene for a varying concentration of vacancies and $\eta = 2.3\text{meV}$ . The blue (red) curves represent the real (imaginary) part of the conductivity. The darker curves have a higher concentration of vacancies. System size: $L = 2048$ , number of polynomials: $M = 512$ . All the other parameters are the same as in Fig. 4.11. . . . .	88

List of Figures

4.13	First-order optical $yy$ conductivity per spin of graphene for $M = 16384$ and $L = 2048$ now as a function of the broadening parameter $\eta$ . The remaining parameters remain the same as for Fig. 4.7. The solid (dashed) curves represent the real (imaginary) part of the conductivity. The legend shows the values for the broadening parameter. The lower inset shows the evolution of the value of the conductivity for each $\eta$ as the number of polynomials is increased for $\hbar\omega = 2.33\text{eV}$ . The upper inset shows the same thing but for several very close frequencies around $\hbar\omega = 4.66\text{eV}$ . The darker curves correspond to higher frequencies. . . . .	89
5.1	Partition-free setup. . . . .	92
5.2	Partitioned setup. The chemical potential is not specified inside the sample because it is not needed. In effect, the sample can be considered to be deprived of particles initially. . . . .	94
5.3	Current as a function of time for a 1D TB model with different values of the potential drop. The (red) black dashed lines represent the (linear) nonlinear Landauer current. . . . .	101
5.4	Charge across different parts of the system as a function of time, for several values of the potential drop across the leads. The region between the red dashed lines represents the sample. The chemical potential is $\mu = 0.3t$ . The points within the two red lines have a higher resolution than the ones outside. . . . .	102
5.5	Current as a function of time for several Fermi energies, small leads and a sufficiently large time observation window to be able to see the reflected current arrive at the center of the sample. . . . .	103
5.6	Close-up of the current at the plateau. On the left, the drop in potential is fixed to $\Delta V = 0.02t$ and the lead size is varied. On the right, the lead size is fixed to 960 and the drop in potential is varied. In both cases, the current has been rescaled by $\Delta V$ . . . . .	104
5.7	Two different cross sections across an armchair graphene nanoribbon. The first cross section only crosses horizontal bonds, but the second cross section crosses more generic bonds. $i$ and $j$ denote a site to the left and to the right of one of the cross sections, respectively. . . . .	105
5.8	Current across an armchair graphene nanoribbon of width 4 (metallic, top) and width 5 (non-metallic, bottom). The cross-section over which the current is being calculated is shown in Fig. 5.7. The graphs on the left show the current across each individual bond, and the graphs on the right represent the total current. . . . .	106
5.9	Current across a very small armchair graphene nanoribbon calculated using random vectors with different distributions. . . . .	110

5.10	Statistical analysis of the current calculated with 2000 random vectors and different random vector distributions (blue - complex exponential minus initial current, orange - cosine distribution, green - uniform distribution). Panel a) shows the average current as a function of time for each distribution and panel b) shows the standard deviation of the stochastic current for each method. . . . .	111
5.11	Histogram of the stochastic current normalized by the potential drop $\Delta V$ with and without the rotated trace. . . . .	112
5.12	Current across a sample estimated through random vectors for different cross-section widths $W$ . Each sample is a square of dimensions $W \times W$ . The 2D TB lattice has length $L_x = 16384$ (which includes both leads and sample length). . . . .	112
5.13	The effect of modulated hoppings in the stationary current plateau (left) and modulation profile (inset). The region between the vertical dashed lines in the inset represents the sample. . . . .	114
6.1	Representation of the order parameter around several impurities. . . . .	127
6.2	Graphene lattice with symmetric bond impurities. The red lines represent the bonds that have been modified from $t$ to $t'$ . The green circles have radius $z$ and correspond to the area where the order parameters are allowed to vary.	133
6.3	Change to the bulk superconducting order parameters $\Delta_0^*$ and $\Delta_1^*$ . . . . .	133
8.1	Feynman diagrams that contribute to the variance of $\text{Im } G_{\mathbf{k}}$ up to second order in $\hat{V}_{\text{dis}}$ . . . . .	148



# Nomenclature

BA	Born Approximation
BdG	Bogoliubov - de Gennes
CBdG	Chebyshev - Bogoliubov - de Gennes
CPA	Coherent potential approximation
CPGF	Chebyshev polynomial Green's function
h-BN	Hexagonal-Boron Nitride
KPM	Kernel polynomial method
MVM	Matrix-vector multiplication
NEGF	Non-equilibrium Green's function
NLO	Nonlinear optics
PBC	Periodic boundary conditions
RGF	Recursive Green function
SCBA	Self-consistent Born approximation
SCTMA	Self-consistent T-matrix approximation
SRO	SrRuO <sub>3</sub> (Strontium Ruthenate)
STE	Stochastic trace evaluation
TMA	T-matrix approximation
ZEM	Zero-energy modes



# 1 Introduction

Quantum transport is a very complex subject. While the macroscopic classical concept of current flowing through a wire is simple to understand intuitively, the microscopic quantum reality of electron transport is much more complicated. Electrons are subject to a plethora of classical and quantum effects, which makes a realistic description of quantum transport a massive undertaking.

Based on our understanding of the macroscopic world, several concepts have been introduced to help break down the several effects that are going on and to characterize the transport regime. Classically, the **ballistic** regime is the simplest one - electrons behave like bullets subject only to Newton's laws and largely unimpeded by scattering events. However, a purely classical description of ballistic transport leads to infinite conductivities. Instead, the electrons were assumed to be in a **diffusive** regime, bouncing around scatterers but otherwise behaving like gas particles in a container. This led naturally to the use of the Boltzmann transport equation to describe them. Scattering due to defects and impurities was treated as a phenomenological term for this equation.

In the 50s, the quantum revolution was well under way, and it was becoming clear that disorder had a more fundamental role in quantum transport than to just mediate diffusion. In 1957, Anderson showed that if disorder is sufficiently strong, no transport at all can take place [10], in stark contrast to what's expected from a diffusive behavior. This new behavior marked a **localized** regime, where the wavefunctions of the system were confined to finite regions in space and charge propagation was only possible through quantum tunneling.

## Diagrammatic formulation of disorder

The formulation of a diagrammatic treatment of disorder in quantum mechanics marked an important step in our modern understanding of electronic structure and quantum transport. Kohn's work in 1957 [11] marked one of the first uses of configurational disorder averaging to put disorder on the same quantum mechanical ground as the rest of the system. At that time, the Boltzmann equation was the main tool to study quantum transport and this work put the collision term on a rigorous ground under a controlled perturbative approximation. In the following year, Edwards showed how the same rationale used in Feynman's diagrams could also be used to study disordered one-point and two-point correlation functions [12], paving the road for our modern approach to diagrammatics in disordered systems. From this point on, all the powerful tools from quantum field theory could also be used to study disordered systems.

This opened up the door for the treatment of disorder in a fully quantum mechanical

## 1 Introduction

fashion. This method also brings other benefits: it allows us to build up our intuition on the nature of scattering events by realizing which are the most relevant diagrams for the processes at hand. In its simplest form, this procedure is subject to the limitations of perturbation theory and its rather common zero radius of convergence. This is why several nonperturbative techniques exist, such as the T-matrix, self-consistent T-matrix approximation (SCTMA), self-consistent Born approximation (SCBA). Even these advanced techniques capture just a subset of diagrams, so they might be missing something out. Notorious elements missing from all these techniques are the crossing diagrams, which represent quantum interference processes. In the semiclassical limit of high energies and momenta, these should be negligible [13]. However, under some circumstances, they can play a dominant role, such as the case of zero-energy modes existing in graphene with vacancies. This shortcoming was evaded by using field-theoretical tools [14–16], which correctly predicted the divergence of the DoS, but its correct scaling law is still being debated.

The disorder self-energy  $\Sigma$  is the mathematical object which is able to encapsulate the complete statistical properties of disorder in quantum systems at the level of two-point correlation functions. It appears naturally within the context of diagrammatics as the set of one-particle irreducible diagrams, and explains the broadening of spectral lines as complex shifts of the poles of the correlators. While precise, this mathematical definition hides its relation to the mean free path of electron transport. This connection appears when considering the dominant subset of terms contributing to diffusive transport, and matches the collision term appearing in Boltzmann’s equation. This is why the disorder self-energy can be used to estimate the mean free path  $\ell$  of electrons as  $\Sigma \sim iv_F/\ell$  where  $v_F$  is the Fermi energy.

## Steady state transport

The Kubo formula [17–19] marked the first fully quantum-mechanical formula for quantum transport, in the sense that it could include disorder in the Hamiltonian. Despite being exact to linear order, it was difficult to use for practical calculations, and in its early years it merely served as a validation for Boltzmann’s equation. Before it was of mainstream use, it required several simplifying iterations. In the next year, Greenwood applied it to independent electrons, in what is now called the Kubo-Greenwood formula [20], and by 1965 Kubo had developed his formula into a fully fledged formalism [21] to study galvanomagnetic effects at very strong fields. Also in the same topic, Bastin [22] and Streda [23] formulated it in terms of Green’s functions, which is the form best known today. Further improvements were made by separating the Kubo formula into several distinct contributions, in the Kubo-Streda formula [24] and still to this day new decompositions are being developed [25].

At around the same time as Kubo’s formula was published, Landauer proposed that conduction could be interpreted as a transmission problem [26] and described through a

transmission probability  $T(E)$ . This brings the physically intuitive picture of two probes (or leads) connected to a sample which scatters electrons travelling from one lead to the other. Later, Büttiker [27] generalized this setup to a multiprobe scenario. The very same problem was approached from a different point of view by Caroli [28]. Motivated by recent experimental results on tunneling currents through two metals separated by a thin oxide layer [29, 30] and Bardeen’s initial theoretical work on that aspect [31], Caroli used the machinery of the recently developed non-equilibrium Keldysh formalism [32] to develop a formula for the current across two contacts in terms of Green’s functions. This was made possible thanks to Keldysh’s seminal work, because a current flowing across two leads cannot be described in terms of just equilibrium Green’s functions.

Caroli’s formula required knowledge of the surface Green’s functions of the leads and the full Green’s function of the device. In the 80s, a very efficient means of calculating each of these objects was developed. Sancho utilized an extremely efficient decimation method to compute the surface Green’s functions [33], while MacKinnon [34] utilized the Recursive Green’s Function method (RGF) to recursively construct the device’s Green’s function out from one lead to the other. Originally, this method was used as a means to obtain the localization length, but later it made its way into the Caroli formula, having further been generalized to more complicated lattices [35].

As years progressed, and as devices became ever smaller, it became important to understand exactly what was going on with the current inside the device, not just across it. Interest started shifting towards the local current profile. In the late 90s, Nonoyama [36] used Keldysh’s formalism to study the local current profile inside a constricted sample for the first time. A few years later, Cresti [37] applied it to a disordered sample inside a magnetic field, providing some beautiful numerical evidence for the random path followed by the current and solidifying the formalism. This work was part of a generalized renewed interest in the field motivated by experimental results using a scanning probe microscope to map the spatial profile of the current in a 2D electron gas. Later works by Nikolic and Zârbo extended this mapping procedure to spin currents [38] and to Dirac materials when graphene was discovered [39].

At around the same time, interest was also growing in obtaining not just the steady state current but also the full current in time, a field pioneered by Jauho and Wingreen [40] using the Keldysh nonequilibrium Green’s function in the 90s. Several numerical schemes were invented to deal with the resulting equations, among which Croy’s [41–43] which sets up an equation of motion for the current matrices in terms of the self-energies and is among the most efficient ones. This has been used to study the emergence of Bloch oscillations [44, 45] in a two-probe system.

In all of these situations, infinite leads were a requirement. The continuous spectrum of the leads is responsible for the steady state of the current for long times. It is also this requirement that is responsible for the kinds of methods used to calculate the current across a sample. If the leads were finite, one could simply perform a unitary time evolution of the system and read off the current when it reaches the steady state, opening up a plethora

## 1 Introduction

of different methods. Therefore, this begs the question: just how large do the leads need to be? This question was approached for the first time in 2004 [46–49] in the context of time-dependent Density-Matrix Renormalization Group (DMRG). Later, this method was applied to quantum transport along 1D chains and analyzed in detail by Pires [50]. Due to the finite nature of the leads, the steady state cannot last forever and is instead understood as a quasi-steady state.

### Optical transport

Frequency-resolved measurements such as the optical conductivity provide yet another probe into the materials' electronic and transport properties. The advent of the laser in 1960 marked the beginning of intense investigation in both the linear and the nonlinear optical response of materials. The intense electric fields provided by the laser took the optical response away from the linear regime and into the realm of nonlinear optics. From this point on, the flood gates were open. In 1961, P. Franken [51] was able to experimentally demonstrate second harmonic generation (SHG), in 1962 Bass [52] demonstrated optical rectification, and even higher order phenomena were demonstrated in 1967 by New and Ward [53]. A systematic theoretical study of the field ensued, and it was quickly realized that the higher-order terms in the susceptibility tensor calculated perturbatively were plagued by zero-frequency divergences. This is to be expected in a metal treated without scattering mechanisms, but semiconductors were suffering from the same fate. It was later realized that these kinds of divergences were unphysical and could be eliminated through a clever manipulation of the formulas in some particular cases [54]. The unphysical nature of these divergences was identified as coming from the interband contribution of filled bands to the optical conductivity, and this was the motivating reason for the development of a formalism which separated both contributions from the start [55]. This work was motivated by the first numerical full-band studies of the nonlinear optical conductivities of ZnSe, ZnTe and CdTe crystals, which started appearing in the 90s [56].

Graphene brought upon this field a surge of renewed interest because of its very strong nonlinear response and potential optical applications such as frequency multiplication [57–59]. The first numeric studies utilized the Dirac approximation [60, 61] but the strong nonlinearities and discrepancy with experiments demanded a better approach, which included band effects. Conflicting analytical results between the length and velocity gauges in the literature motivated the first time-resolved full-band simulations [62], free from any spurious perturbative artifacts. Subsequently, in a series of papers by Ventura and Passos [63, 64], it was made clear how to make both gauges compatible to any order.

The characterization of disorder in optical conductivity is much less developed than its clean counterpart. The first studies in disordered systems were done using scaling arguments [65, 66], but the first numerical AC signatures of the Anderson transition began in the 90s with direct diagonalization [67] and later using the forced oscillator method of solving the Schrödinger equation [68]. The behavior close to  $\omega = 0$  was notoriously difficult

to study because it requires it requires optical transitions between energy levels which are very close. Computational limitations at the time, as well as level repulsion made this a difficult task, limited to very small systems ( $\approx 30^3$ ). In 2004, Weisse developed a linear scaling basis-independent algorithm for the computation of the linear optical conductivity [69, 70] which, coupled with the relentless increase in computational efficiency at the time, enabled the unprecedented simulation of lattices of size  $100^3$ . Since then, optical conductivity applications were largely based on Weisse’s work for the real part of the optical conductivity [71, 72]. The next methodological leap came by João in 2019 [2], which set up the framework to extend Weisse’s work to the complex optical conductivity and to higher orders in the perturbation extension. Most recently, this method has been used to investigate the relevant parameters to nonlinear optical responses [73].

## Superconductivity

The history of superconductivity starts in the Netherlands in H. K. Onnes’ lab when, for the first time in history, liquid Helium was produced on 10th of July of 1908 at a temperature of just  $4K$ . Being able to produce and store liquid Helium at these temperatures opened up the possibility to test physical theories on materials at their extreme limits. In the years that followed this breakthrough, many experiments were performed to obtain data at this new range of temperatures. One of the most noticeable of these was the discovery in 1911 (also by Onnes) of superconductivity [74]. The liquefaction of liquid Helium and its consequences earned Onnes the 1913 Nobel prize.

Superconductivity is arguably one of the most striking and important effects in Condensed Matter Physics. Since 1911, a tremendous amount of effort has been put into its explanation, among which the highly successful phenomenological Ginsburg-Landau theory and the microscopic BCS theory [75] (1957) (Nobel 1972). The advance in theoretical understanding of the superconductivity phenomenon since its discovery was shaped by several key experiments which provided some clues into what’s going on in a microscopic level.

1. The exponential decay of the specific heat at low temperatures was one of the very first indications that the new state had a gap in the energy spectrum
2. In 1933, Meissner discovered that the superconductor repelled magnetic flux below the critical temperature, the so-called Meissner effect, making it a perfect diamagnet. This couldn’t be explained by perfect conductivity alone, so perfect conductivity couldn’t be the fundamental mechanism driving the microscopic phenomena.
3. Another key observation was the isotope effect in 1950. Experiments carried out on various isotopes of mercury showed a very characteristic dependence of the critical temperature on the isotope mass,  $T_c \sim M^{-1/2}$ . In a stationary lattice, the mass of the ions shouldn’t affect the electronic and transport properties of the material, so

## 1 Introduction

this was an indication that lattice vibrations - phonons - were playing a critical role in the formation of the superconducting state [76–78].

In the same year, H. Fröhlich put forward a theory explaining how an effective attraction between electrons may arise from their interaction with the underlying lattice [79]. Now we know that the main mechanism is an attractive interaction between electrons mediated by phonons: as electrons move through the medium, they attract the atoms in the material, which causes an effective positively charged electric field around the electron and which attracts other electrons. This causes pairing between time-reversed electrons (the Cooper pairs) and opens an energy gap, which explains the robustness.

The superconducting state is very sensitive to thermal agitation. Once the thermal excitations exceed a certain threshold, the Cooper pairs are broken up and the material loses its superconductivity, so superconductivity typically happens at extremely low temperatures near absolute zero. For a while, it was thought that there was a theoretical maximum critical temperature of 40K for superconductivity within the BCS picture [80], attainable by alloys. In 1986, research by Bednorz and Müller [81] (Nobel 1987) into copper oxides revealed unconventional superconducting phases with critical temperature above 35K. In the next year, the BCS prediction had already been shattered. Nowadays, superconductors with  $T_c$  above 250K exist, albeit under very high pressures (170 GPa). These materials are dubbed unconventional superconductors because they cannot be explained by the BCS theory alone. The latest surprise came in 2018 when it was found that twisted bilayer graphene could display superconductivity [82].

Understanding high temperature superconductivity is still one of the major challenges of modern Condensed Matter Physics. Several other mechanisms have been proposed as being responsible for superconductivity, such as plasmon-mediated superconductivity [83] and the Resonating Valence Bond theory put forward by Anderson [84], but this is still a topic of huge debate. A lot of work is also being developed in the study of disordered superconductors, as it is hoped that understanding the mechanisms that destroy superconductivity may shine some light on the physics behind it. One of the most important experimental techniques for this is scanning tunneling microscopy (STM), which allows probing of the local density of states (LDoS) in a material. In the late 90s and early 2000s, STM studies [85] carried out around impurities in superconductors brought the theoretical necessity to describe the LDoS of inhomogeneous superconductors in an efficient manner.

From the theoretical side, several approaches have been developed to tackle inhomogeneous superconductors. In [86] the authors use the Coherent Potential Approximation (CPA) to obtain the disordered self-energy as a stepping stone for the calculation of other quantities. They use an alloy disorder - a local energy  $\varepsilon_A$  with a certain concentration  $c$  or  $\varepsilon_B$  with concentration  $1 - c$ . The innovation in this paper comes from using an order parameter that may be different in a  $A$  site or  $B$  site and imposing self-consistency conditions on both. This method is unable to capture interference between impurities as it relies on the CPA, and the self-consistency is only satisfied on average. The authors improve

on this method by considering a cluster approach in another paper [87] and are able to adequately obtain a resonance near  $E = 0$  in the DoS, just like in Pan's STM studies [85]. In this paper, they allow the self-energy to vary in discrete steps in the first Brillouin zone (FBZ). In fact, a lot of the work developed at this time relied on very elaborate schemes to perform the self-consistent calculation of the Bogoliubov-de Gennes (BdG) equations in the presence of disorder, obtain the self-energy and then the DoS and LDoS.

More recently, spectral methods have begun to be used instead in the numerical investigations [71, 72, 88–91], allowing not only the computation of the DoS immediately, but also (and very importantly) the LDoS and the attention of research has converged in this direction. This is the recurring theme of this thesis: because spectral methods avoid the need for an exact diagonalization by sacrificing the fine details of the spectrum, a large computational improvement is achieved. Superconductors benefit from this greatly, because the order parameters no longer need to be calculated with exact diagonalization. Self-consistency still has to be enforced for the order parameter at every point in space, and that remains one of the main sources of computational complexity in these problems.

## The need for larger simulations

A common thread here is the growing trend towards equations amenable to numerical computations - not analytical ones, which was made possible thanks to the exponential increase in computational resources in the last decades. In the late 1800s, scientists would work in their labs, experiments in tandem with theory. Nowadays, computers have become the numerical laboratory for theoreticians, where their theories can be tested and simulated in unprecedented scales, before even making it into the real experimental laboratory. The search is two-fold, as it becomes increasingly important to look not just for useful theories, but also efficient algorithms with which to test them.

For this reason, the numerical scaling of the methods is critical. For example, the numerical complexity of the RGF method for the conductance scales as  $LW^3$ , where  $L$  is the length of the sample and  $W$  is its cross section area (or width in the 2D case), enabling very efficient computations for long systems but not so much so for wide ones. While Sancho's [33] and MacKinnon's [34] contributions from the 80s were instrumental to increase the performance of the method, they are still bounded by this scaling. Under some specific circumstances, it is possible to reduce the scaling to  $LW^2$ , but in exchange for a very large RAM consumption [92, 93]. Ideally, one would like a  $LW$  scaling, making it a linear scaling algorithm (order  $\mathcal{O}(N)$ ) in line with those used with Kubo's formula and its derivatives as done by Weisse [3, 5, 69, 94, 95]. Recent steps towards this goal have already been taken. With regards to the lead-sample-lead setup, if the number of transport channels of the leads is small comparatively to the number of sites in the sample, a continued fraction of the sample's Green's function can be performed for each matrix element between the leads [96]. Each of these matrix elements is an order  $\mathcal{O}(N)$  computation. Alternatively, the Green's function can be evaluated with the Chebyshev Polynomial Green's Function

(CPGF) method [5, 94] for the same effect.

### KPM and Spectral methods

In this thesis, I want to specifically focus on one kind of numerical applications to not only quantum transport but also some electronic properties - spectral methods. In one way or another, the investigations described in the previous paragraphs converged to the usage of spectral methods, and this has revealed to be one of the most promising numeric fields at the current time for large-scale quantum transport simulations.

This field was effectively started in 1984 by Tal-Ezer and Kosloff [97] as an efficient way to evolve the quantum states in time, an alternative to Euler's method or second-order Taylor approximations of the time-evolution operator. The Chebyshev expansion of the time-evolution operator led to a massive increase in stability and efficiency. They have devoted a lot of work into numerical methods to evolve both time-independent and time-dependent Hamiltonians [98]. In 1994, Silver [99], seemingly unaware of Tal-Ezer's work, also applied the idea of Chebyshev expansion to the Dirac delta operator in the density of states  $\text{Tr}[\delta(\varepsilon - H)]$ , convolving the pathological operator with a kernel to regularize it. By itself, this already represents a fundamental shift in ideology. Instead of requiring perfect knowledge of the position of every single eigenvalue, the usage of a regularized kernel smoothens the Dirac delta, introducing an effective resolution. This also allows the usage of the full Hamiltonian, including disorder.

The efficient tradeoff between numerical resolution and numerical efficiency is one of the ingredients that makes the Kernel Polynomial Method (KPM) so powerful. The trace itself was calculated with a novel method at the time - the Stochastic Evaluation of the Trace (STE), which was being used to compute moments of operators. The innovation here was using Chebyshev polynomials, with much greater convergence properties. Instead of calculating all the matrix elements for the trace, random vectors were used. In average, the result is the same, and the efficiency gain from using random vectors is immense, despite their stochastic nature. Both these ingredients represent a shift in numerical simulations nowadays: Chebyshev expansion of operators and STE.

Weisse's work [69] for the optical conductivity marked another leap for KPM, as the optical conductivity required a double Chebyshev expansion, one for each of the Dirac deltas in the formula, and it was the first application to response functions. In the mean time, Chebyshev expansions, STE and KPM (henceforth collectively called Spectral Methods) have found applications in many places [100], ranging from nonperturbative disorder phenomena [16, 94], topological materials [6, 101, 102], superconductivity [71, 72, 89] and many more.

### Goal of the thesis

In this thesis, I am going to bring spectral methods into several new areas and extend them in others. I'm going to begin with an introduction to spectral methods in Chap-

ter 2. In Chapter 3, I develop one of the main original ideas of this thesis: the first complete calculation of the disorder self-energy operator in graphene, with resort to an extremely finely resolved disorder-averaged Green’s function. This reveals previously unseen low-energy nonperturbative momentum dependency of the self-energy operator which could be related to the robustness of zero-energy modes in graphene. Chapter 4 is devoted to the development of a diagrammatic formalism based on the Keldysh formalism to obtain higher-order optical conductivity tensors **compatible with spectral methods**. In Chapter 5, I followed Pires [50] and generalized the computation of the nonlinear Landauer conductance with finite leads for arbitrary lattices and dimensions, introducing STE to compute the current and Chebyshev expansions to compute the Fermi and time-evolution operators, turning it into an order  $\mathcal{O}(N)$  process to calculate the conductance in real space. In the final Chapter 6, motivated by Moradian’s paper and the imposition of self-consistency on average, the main goal of this chapter is to develop a new method of average self-consistency that takes into account a lot more detail about the order parameters around the impurities. I developed a new way to treat disorder in superconductors, by isolating the regions of highest variation of the order parameters and establishing a self-consistent equation for the average between them. All of these have been implemented by myself in the KITE open-source software [3], in a package that will be released in a future version.

## Preliminaries

All of the systems explored in the course of this thesis are described in the tight-binding framework and assume a uniform underlying regular lattice (finite, with or without periodic boundary conditions). This structure is used to specify the Hamiltonian, which is then used to calculate Green’s functions, time evolution operators, etc. To calculate all of these operators, the most essential and common operation required is the successive product of the Hamiltonian matrix by a certain vector within the Hilbert space, that is, a matrix vector multiplication (MVM). Naturally, it is of critical importance to make this operation as efficient as possible. Since we are only interested in sparse Hamiltonians of relatively regular lattices, we decided to implement a rigid lattice structure upon which disorder is added which does not interfere with the lattice structure, such as vacancies, local disorder and bond disorder. This predictability removes all the redundancy of storing the Hamiltonian in memory and simplifies the par-

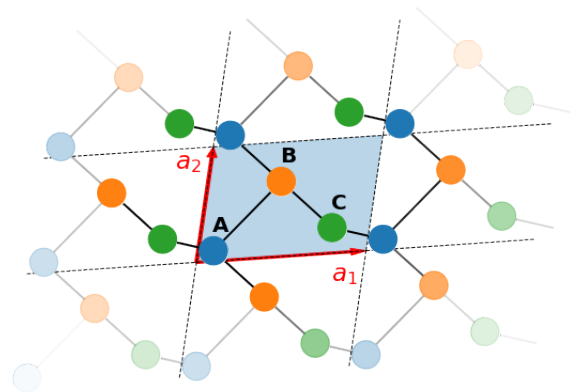


Figure 1.1: Structure of a generic unit cell.

## 1 Introduction

allelization process as well. This section intends to unify and clarify the description of all the systems explored in this thesis.

The smallest building block is the unit cell (see Fig. 1.1), which is codified by specifying the primitive vectors and can contain several sites inside. For the remainder of this thesis, we shall refer to the degrees of freedom inside the unit cells as “orbitals”. This denomination encompasses sites at different positions, spin and orbital (in the proper atomic sense) degrees of freedom. The unit cell is repeated along every direction a certain number of times. Let  $n$  be the number of orbitals per unit cell, and  $N_i$  be the number of times the unit cell is repeated in each direction  $\mathbf{a}_i$ , for a total of  $N = \prod_i N_i$  unit cells. Periodic boundary conditions may be utilized in any set of directions.

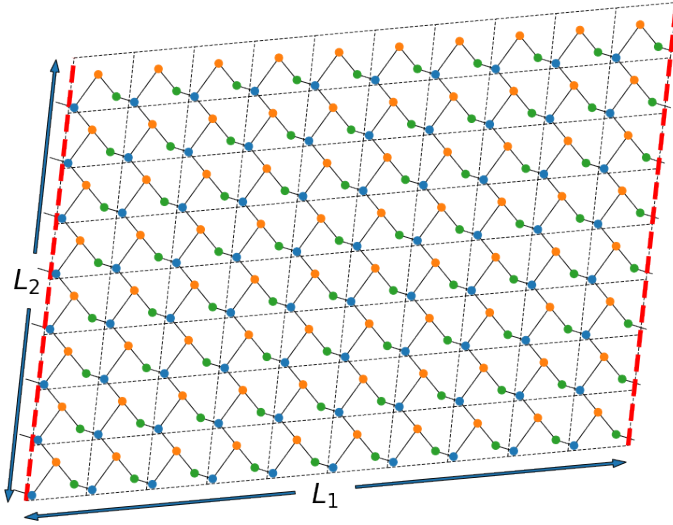


Figure 1.2: Structure of a generic lattice constructed with the previous unit cell. This particular 2D lattice has periodic boundary conditions along the 1 direction, but open boundary conditions along the 2 direction.

The many-body Hamiltonian is defined with this lattice structure in mind:

$$\mathcal{H} = \begin{pmatrix} \mathbf{c}_1^\dagger \\ \mathbf{c}_2^\dagger \\ \vdots \\ \mathbf{c}_n^\dagger \end{pmatrix}^T \begin{pmatrix} \mathbf{H}_{11} & \mathbf{H}_{12} & \cdots & \mathbf{H}_{1n} \\ \mathbf{H}_{21} & \mathbf{H}_{22} & \cdots & \mathbf{H}_{2n} \\ \vdots & \vdots & \ddots & \vdots \\ \mathbf{H}_{n1} & \mathbf{H}_{n2} & \cdots & \mathbf{H}_{nn} \end{pmatrix} \begin{pmatrix} \mathbf{c}_1 \\ \mathbf{c}_2 \\ \vdots \\ \mathbf{c}_n \end{pmatrix} = \sum_{ij} \mathbf{c}_i^\dagger \mathbf{H}_{ij} \mathbf{c}_j$$

where each  $\mathbf{H}_{ij}$  is a sparse  $N \times N$  matrix and  $\mathbf{c}_i^\dagger$  ( $\mathbf{c}_i$ ) is a vector of creation (annihilation) operators in orbital  $i$ , also of dimension  $N$ . The Hamiltonian can be written out explicitly as

$$\mathcal{H} = \sum_{ij} \sum_{\mathbf{R}\mathbf{R}'} H_{ij}^{\mathbf{R}\mathbf{R}'} c_{\mathbf{R},i}^\dagger c_{\mathbf{R}',j}$$

where  $\mathbf{R}$  and  $\mathbf{R}'$  index the unit cells and  $i$  and  $j$  index the orbitals of those cells, respectively. Here,  $c_{\mathbf{R},i}^\dagger$  ( $c_{\mathbf{R},i}$ ) creates (annihilates) an electron in orbital  $i$  at unit cell  $\mathbf{R}$ .

Disorder is described with this structure in mind. For the purposes of this thesis, only disorder which preserves this structure is considered. This includes vacancies (which simply remove some sites, but otherwise leaves the lattice intact), local (Anderson) disorder and bond disorder. Coincidentally, these are precisely the kinds of disorder implemented in KITE. The strict regularity of this description allows for some impressive numerical performance gains and for more straightforward parallelization schemes. For example, the predictability of the Hamiltonian allows it to be stored in memory by simply specifying how each unit cell connects to the next. Vacancies are stored as individual positions (a small number compared to the size of the Hilbert space). The only thing that has to be stored explicitly is the local disorder.



## 2 Introduction to spectral methods

There is a recurring theme in this thesis: the usage of random vectors to calculate transport quantities usually incurs in impressive performance gains because it allows the quantities to be calculated with simple matrix vector multiplications (MVM). This is formalized under the name “Spectral Methods”, and the point of this chapter is to provide a broad overview of their usage while particularizing for the cases that are going to be studied in the remainder of the thesis.

### 2.1 General overview

To get a better grasp of the usefulness of spectral methods, let’s begin by analyzing a simple example. Suppose we want to calculate the density of states (DoS) of a 3D tight-binding cubic lattice, associated with a single-particle Hamiltonian  $H$ . For concreteness, let’s assume periodic boundary conditions and a lattice of dimensions  $N_x \times N_y \times N_z$  for a total Hilbert space of dimension  $N$ . The DoS is normalized to one and is calculated as such:

$$\rho(\varepsilon) = \frac{1}{N} \sum_n \delta(\varepsilon - \varepsilon_n),$$

where  $\varepsilon_n$  is the eigenenergy associated with the eigenvector  $|n\rangle$  of  $H$ . We have several options to compute the DoS. The most straightforward way is to diagonalize the Hamiltonian and to build the histogram of the eigenvalues. It is also the most inefficient, because the numerical complexity of this process is  $\mathcal{O}(N^3)$  using standard diagonalization algorithms. For translation-invariant systems, the Hamiltonian is easily diagonalizable, and the DoS can be expressed as an integral over the First Brillouin Zone (FBZ):

$$\rho(\varepsilon) = V_c \int_{\text{FBZ}} \frac{d^3\mathbf{k}}{(2\pi)^3} \delta(\varepsilon - \varepsilon(\mathbf{k}))$$

where  $\varepsilon(\mathbf{k})$  is the dispersion relation and  $V_c$  denotes the volume of the 3-dimensional unit cell. For these kinds of purposes, the Dirac delta is resolved as the imaginary part of a Green’s function, and this integral has to be repeated for every energy. What if we have a large system without translation invariance? Under these circumstances, one of the most efficient ways to compute the DoS is through a stochastic evaluation of the trace in real space.

## 2 Introduction to spectral methods

Let's begin by expressing the DoS as a trace:

$$\rho(\varepsilon) = \frac{1}{N} \text{Tr} [\delta(\varepsilon - H)]$$

or, choosing a basis of positions  $\mathbf{R}$  in real space,

$$\rho(\varepsilon) = \frac{1}{N} \sum_{\mathbf{R}} \langle \mathbf{R} | \delta(\varepsilon - H) | \mathbf{R} \rangle.$$

The first problem that we have to solve is how to calculate these matrix elements. A direct evaluation of the Dirac delta matrix is out of the question because it requires going into the eigenbasis of  $H$ , so an alternative is required. Thus, the Dirac delta is expanded as a polynomial series of the Hamiltonian that composes it <sup>1</sup>:

$$\delta(\varepsilon - H) = \sum_{n=0}^{\infty} \Delta_n(\varepsilon) T_n(H).$$

where  $\Delta_n(\varepsilon)$  is a coefficient and  $T_n(H)$  is the  $n$ -th order Chebyshev polynomial. Any set of orthogonal polynomials can be used, but Chebyshev polynomials are especially useful because of their convergence properties. In practice, the sum is carried out to finite order  $M$  once the desired accuracy has been achieved. Since these are polynomials, their action on  $|\mathbf{R}\rangle$  is easy to calculate, unlike  $\delta(\varepsilon - H)$ . Therefore, the problem now comes down to evaluating  $\langle \mathbf{R} | T_n(H) | \mathbf{R} \rangle$  for all  $\mathbf{R}$  and  $n$ .

This sum over  $\mathbf{R}$  can be avoided by resorting to random vectors. Let  $|\xi\rangle$  be a vector defined in the whole Hilbert space with random independent entries  $\xi_{\mathbf{R}}$ , as

$$|\xi\rangle = \frac{1}{\sqrt{N}} \sum_{\mathbf{R}} \xi_{\mathbf{R}} |\mathbf{R}\rangle,$$

where each  $\xi_{\mathbf{R}}$  is taken from a distribution of average zero and variance 1. Then,  $\rho$  can be obtained as an average:

$$\rho(\varepsilon) = \sum_{n=0}^M \Delta_n(\varepsilon) \overline{\langle \xi | T_n(H) | \xi \rangle}$$

where the line above denotes average over random vectors and  $\overline{\langle \xi | T_n(H) | \xi \rangle}$  is defined as the  $n$ -th order Chebyshev moment  $\mu_n$ . Later, we will see that the number  $N_R$  of random vectors required to have a statistically significant DoS is very small; in some cases only one is needed.

We are now in conditions to understand why KPM is so powerful. First, let's look at the product  $T_n(H) |\xi\rangle$  more carefully. Chebyshev polynomials satisfy a recurrence relation. Let  $|\xi_n\rangle = T_n(H) |\xi\rangle$  be the result of the  $n$ -th Chebyshev operator acting on the random vector. Then, thanks to the recurrence relation of these polynomials, we can also establish

---

<sup>1</sup>Later we will see why this is justified, but for now one can imagine the Dirac delta being approximated by a Lorentzian, which can then be expanded.

a two-step recurrence relation between all the  $|n\rangle$ :

$$\begin{aligned} |\xi_1\rangle &= H |\xi\rangle \\ |\xi_{n+1}\rangle &= 2H |\xi_n\rangle - |\xi_{n-1}\rangle. \end{aligned}$$

This means that to get to  $|\xi_M\rangle$ , we only need to operate with the Hamiltonian  $M$  times. If the Hamiltonian is sparse, then this is an operation of complexity  $\mathcal{O}(N)$ . Overall, the numerical effort to compute all the required Chebyshev momenta is an operation of complexity  $\mathcal{O}(NN_RM)$ . The final step is to sum the momenta for all the energies

$$\rho(\varepsilon) = \sum_{n=0}^M \Delta_n(\varepsilon) \mu_n,$$

which is an operation of complexity  $\mathcal{O}(N_E M)$ , where  $N_E$  is the number of energy points. Using the fact that typically  $N_R \approx 1$  and that the final step of resumming the DoS is very quick and model-independent, we arrive at the final complexity of  $\mathcal{O}(NM)$ . This is valid for sparse but otherwise arbitrary Hamiltonians, even in the presence of disorder. Part of the extraordinary efficiency of this method is due to the Chebyshev moments not depending on energy.

In the next sections, I want to delve deeper into several of the properties shown here.

## 2.2 Chebyshev polynomials of the first kind

Chebyshev polynomials of the first kind feature in some of the most efficient numerical methods available. They can be defined most simply by

$$T_n(\cos(\theta)) = \cos(n\theta), \quad (2.1)$$

or, equivalently,

$$T_n(x) = \cos(n \arccos(x))$$

and so are only defined in the domain  $-1 \leq x \leq 1$ . Since  $n$  is an integer, this expression can be simplified to simple polynomials in  $x$ . The first few polynomials are:

$$\begin{aligned} T_0(x) &= 1 & T_3(x) &= 4x^3 - 3x \\ T_1(x) &= x & T_4(x) &= 8x^4 - 8x + 1 \\ T_2(x) &= 2x^2 - 1 & T_5(x) &= 16x^5 - 20x^3 + 5x \end{aligned}$$

and are represented in Fig. 2.1.

Because of eq. 2.1, Chebyshev polynomials have a deep connection to Fourier series and

## 2 Introduction to spectral methods

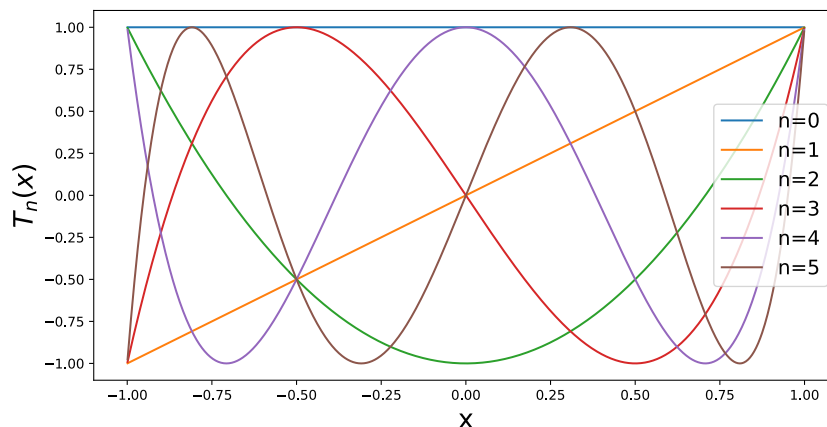


Figure 2.1: First few Chebyshev polynomials.

most of their properties derive precisely from them. For example, the cosine property

$$\cos((n+1)\theta) + \cos((n-1)\theta) = 2\cos(n\theta)\cos(\theta)$$

is directly responsible for their recurrence relation

$$T_{n+1}(x) = 2xT_n(x) - T_{n-1}(x)$$

where  $x$  can be recognized as  $T_1(x)$ . The orthogonality between cosines

$$\int_0^\pi d\theta \cos(n\theta) \cos(m\theta) = \frac{\pi}{2} \delta_{nm} (1 + \delta_{n0})$$

is responsible for the orthogonality relation between Chebyshev polynomials

$$\frac{2}{\pi} \int_{-1}^1 \frac{dx}{\sqrt{1-x^2}} T_n(x) T_m(x) dx = \delta_{nm} (1 + \delta_{n0}).$$

The orthogonality relation is what allows us to expand any integrable function defined in the  $-1 \leq x \leq 1$  domain as a series of Chebyshev polynomials:

$$f(x) = \sum_{n=0}^{\infty} a_n T_n(x) \quad (2.2)$$

where

$$a_n = \frac{2}{\pi} \frac{1}{1 + \delta_{n0}} \int_{-1}^1 \frac{dx}{\sqrt{1-x^2}} T_n(x) f(x). \quad (2.3)$$

Another common way to express this expansion is by factoring out the square root, for the so-called  $b$  coefficients

$$f(x) = \frac{1}{\sqrt{1-x^2}} \sum_{n=0}^{\infty} b_n T_n(x) \quad (2.4)$$

where

$$b_n = \frac{1}{1 + \delta_{n0}} \frac{2}{\pi} \int_{-1}^1 T_n(x) f(x) dx. \quad (2.5)$$

Both are equally valid and the choice of which to use comes down to a matter of convenience to find the coefficients.

## 2.3 Convergence

With regards to pointwise convergence, if  $f$  is differentiable at  $x$ , then the sum 2.2 converges. If  $f$  has a jump discontinuity but has right and left derivatives, then the sum converges to the average of  $f$  at the jump. However, it may not converge at the same rate for every point, and the series will in general converge slower in points closer to where its derivative is not continuous, or at discontinuities. This discrepancy in convergence speed is the origin of Gibbs oscillations when the sum is truncated at a finite number of terms  $M$ .

Gibbs oscillations are a manifestation of the lack of uniform convergence, and the conditions for their mitigation are important in several fields<sup>2</sup>. One of the simplest modifications that can be done to the truncated series is to tweak the expansion coefficients by the use of weights  $g_n$ , as such:

$$f_{\text{KPM}}(x) = \sum_{n=0}^N g_n a_n T_n(x) \quad (2.6)$$

This Chebyshev approximant  $f_{\text{KPM}}$  can be expressed as a convolution of  $f(x)$  with a kernel  $K(x, y)$ , and so in this sense the kernel polynomial method is understood as a controlled approximation: we know the exact form of the function that is being approximated. This kernel can be calculated by replacing the expression for  $a_n$  back into eq. 2.6 and factoring out the original function:

$$f_{\text{KPM}}(x) = \int_{-1}^1 \left[ \frac{2}{\pi} \frac{1}{\sqrt{1-t^2}} \sum_{n=0}^{\infty} g_n \frac{T_n(t) T_n(x)}{1 + \delta_{n0}} \right] f(t) dt.$$

The quantity inside brackets is the kernel

$$K(t, x) = \frac{2}{\pi} \frac{1}{\sqrt{1-t^2}} \sum_{n=0}^{\infty} g_n \frac{T_n(t) T_n(x)}{1 + \delta_{n0}}$$

and provides a way to calculate the approximant:

$$f_{\text{KPM}}(x) = \int_{-1}^1 K(t, x) f(t) dt.$$

---

<sup>2</sup>In the late 1800s, when analytical machines were used to sum Fourier series, they would often overshoot the curves they were supposed to represent because of the Gibbs phenomenon, but since this wasn't understood, it was instead attributed to malfunctioning.

## 2 Introduction to spectral methods

Different choices of weights  $g_n^N$  give rise to different kernels and therefore different approximants. The most common weights are the following

$$\text{Dirichlet } g_{D,n}^N = \begin{cases} 1 & \text{if } n \leq N \\ 0 & \text{if } n > N \end{cases} \quad (2.7)$$

$$\text{Féjer } g_{F,n}^N = 1 - n/N \quad (2.8)$$

$$\text{Jackson } g_{J,n}^N = \frac{(N - n + 1) \cos\left(\frac{\pi n}{N+1}\right) + \sin\left(\frac{\pi n}{N+1}\right) \cot\left(\frac{\pi}{N+1}\right)}{N + 1} \quad (2.9)$$

$$\text{Lorentz } g_{L,n}^N = \frac{\sinh(\lambda(1 - n/N))}{\sinh(\lambda)} \quad (2.10)$$

The Dirichlet weight is the one implicitly used when truncating the series at  $N$ . The Féjer weight [103] is of historical importance because its introduction to the partial sum ensures uniform convergence of the series if the function is continuous, and gets rid of the Gibbs oscillations at discontinuities. It is not necessarily the most useful one for KPM. In order to approximate the DoS, for example, the Féjer weight results in considerable tails from one peak to the other, so the Jackson weight is preferable. It ensures positivity and minimizes the tails of the peaks. The Lorentz weight is especially useful to approximate Green's functions, but since we are considering an explicit broadening instead of the more pathological  $i0^+$  limit, it is of no use here. See [95] a detailed analysis of the weights and the resulting kernels. In the next sections, we will proceed with a numerical analysis of the several weights in the relevant functions being approximated.

### 2.3.1 Comparison with Taylor series

To really appreciate the power of Chebyshev expansions, it is interesting to compare them against another popular expansion approach, the Taylor series. Consider the Cauchy curve  $f(x)$  defined between  $-1$  and  $1$  as defined by

$$f(x) = \frac{1}{x^2 + \sigma^2}$$

with  $\sigma = 1/2$ . This curve has poles in the complex plane when  $x = \pm i\sigma$ , which means that the Taylor series around  $x = 0$  has radius of convergence  $\sigma$ . This is problematic if we want to accurately approximate  $f(x)$  in the whole domain. Chebyshev series have no such problem, as can be seen from Fig. 2.2.

The Chebyshev series is able to accurately describe the Cauchy curve despite of its poles, unlike the Taylor series which is only able to do so within the radius of convergence. On the flip side, Chebyshev expansions are confined to the real axis. Attempting to approximate  $f(z)$  at points outside of the real axis between  $-1$  and  $1$  results in divergence, as shown in Fig. 2.3.

This example was specifically chosen for the Taylor series to fail, but the Cauchy curve

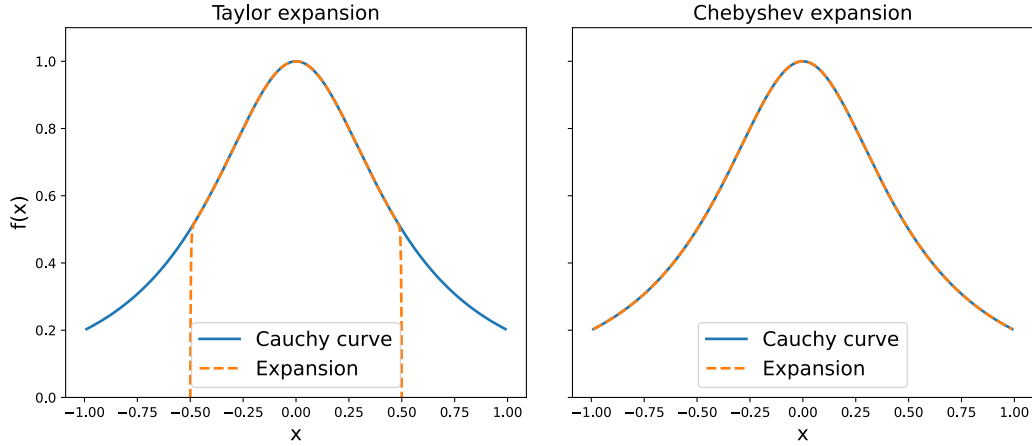


Figure 2.2: Comparison between a Taylor expansion and a Chebyshev expansion using  $N = 100$  polynomials for each.

is simply the imaginary part of the resolvent, so this is actually of practical importance for the calculation of the Green's functions. A similar problem would happen for discontinuous functions like the zero-temperature Fermi-Dirac distribution, since they are not analytical at the discontinuity.

## 2.4 Chebyshev expansion for operators

So far, the discussion has been focused on functions defined on the domain  $-1 \leq x \leq 1$ , which is where the Chebyshev polynomials are defined. For applications in quantum mechanics, we want to be able to extend this notion to operators. Namely, we want to express a function  $f$  of an operator  $H$  as a series of Chebyshev polynomials of this operator:

$$f(H) = \sum_{n=0}^{\infty} f_n T_n(H).$$

Usually, this operator is going to be the Hamiltonian, so we can assume that it is hermitian and diagonalizable. Then, we can use its eigenbasis  $|a\rangle$  with eigenvalues  $\varepsilon_a$  to understand how to perform this decomposition. In this basis,

$$f(H) = \sum_a \sum_{n=0}^{\infty} f_n T_n(\varepsilon_a) |a\rangle \langle a| \quad (2.11)$$

and so the same Chebyshev expansion that was used for regular functions can also be used for matrices, so long as their spectrum is real and within the interval  $-1 < \varepsilon_a < 1$ . Hermiticity makes sure that  $\varepsilon_a$  is real, but we have to rescale the matrix to ensure the bounds are correct. Let's assume that the smallest and the largest eigenvalues of the matrix are  $\varepsilon_A$  and  $\varepsilon_B$ , respectively. Usually, one has an estimate for these bounds, but if not, they can be found in a relatively efficient fashion with a Lanczos procedure. The spectral half-width is  $\Delta = (\varepsilon_B - \varepsilon_A) / 2$ , and their average is  $\delta = (\varepsilon_A + \varepsilon_B) / 2$ . Then, the

## 2 Introduction to spectral methods

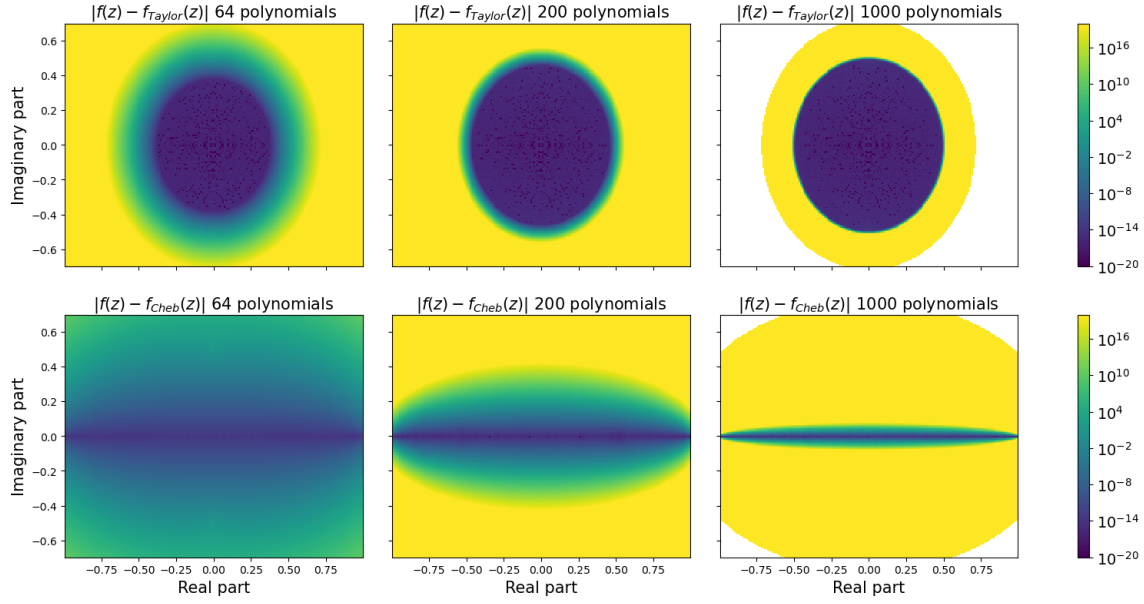


Figure 2.3: Comparison between a Taylor expansion and a Chebyshev expansion in the complex plane for different numbers of polynomials.

rescaled matrix

$$\tilde{H} = \frac{H - \delta}{\Delta}$$

has all eigenvalues between  $-1$  and  $1$ , necessarily including the boundaries. The boundaries are to be avoided, because small numerical instabilities can place the eigenvalues outside this interval, and compromising the Chebyshev expansion. Therefore, one should always use a slightly larger value for  $\Delta$ , defined as  $\Delta = (\varepsilon_B - \varepsilon_A) / 2 + \varepsilon$ , where  $\varepsilon$  should be a small number, of the order of  $0.01$ . This ensures that the spectrum lies within  $-1 + \varepsilon$  and  $1 - \varepsilon$ .

To see how this rescaling works in practice, let's analyze what happens to the Fermi operator. Let's assume that we want to compute the trace of the Fermi operator at a given inverse temperature  $\beta$  and chemical potential  $\mu$  for a Hamiltonian  $H$  that is to be rescaled:

$$\text{Tr}(f_{\beta,\mu}(H)) = \text{Tr} \left[ \frac{1}{1 + \exp(\beta(H - \mu))} \right].$$

Let the tilde  $\sim$  denote the rescaled quantities and define  $\tilde{\mu} = (\mu - \delta) / \Delta$  and  $\tilde{\beta} = \Delta\beta$  as the rescaled chemical potential and inverse temperatures, respectively. Then, the previous expression is equivalent to

$$\text{Tr}(f_{\beta,\mu}(H)) = \text{Tr} \left[ \frac{1}{1 + \exp(\tilde{\beta}(\tilde{H} - \tilde{\mu}))} \right] = \text{Tr}(f_{\tilde{\beta},\tilde{\mu}}(\tilde{H}))$$

which is the expression that should be expanded in Chebyshev polynomials.

## 2.5 Chebyshev expansion for known functions

In this section, I want to explain the Chebyshev expansions that are going to be required for the remainder of the thesis and go into some detail about their convergence properties.

### 2.5.1 Dirac delta

The Dirac delta is required in most of the spectral applications of KPM, like the DoS and the various variations of the Kubo formula. Let us look for an expansion of the form

$$\delta(x - y) = \sum_{n=0}^{\infty} \Delta_n(x) T_n(y) \quad (2.12)$$

Applying the orthogonality condition 2.3 and using the properties of the Dirac delta, we immediately find

$$\Delta_n(x) = \frac{2}{\pi\sqrt{1-x^2}} \frac{T_n(x)}{1 + \delta_{n0}}. \quad (2.13)$$

The alternative expansion is found in a similar way, but using 2.5

$$\begin{aligned} \delta(x - y) &= \frac{1}{\sqrt{1-y^2}} \sum_{n=0}^{\infty} \Delta_n^b(x) T_n(y) \\ \Delta_n^b(x) &= \frac{2}{\pi} \frac{T_n(x)}{1 + \delta_{n0}}. \end{aligned}$$

The only difference between the two is that the square root has a different variable in it. For applications to quantum mechanics, the first expansion is the most useful, because  $y$  is to be replaced by an operator. While a polynomial of this operator is simple to calculate, the inverse of the square root is not.

### 2.5.2 Complex exponential

The complex exponential features in the time evolution operator of time-independent Hamiltonians. We want to find the following decomposition

$$e^{izx} = \sum_{n=0}^{\infty} u_n(z) T_n(x) \quad (2.14)$$

for complex  $z$ . The  $u_n$  can be determined as per usual, using 2.2 alongside the change of variable  $x = \cos(\theta)$  and identifying the integral as the definition of the Bessel function, but there is another way. Consider the expansion of plane waves of wave vector  $\mathbf{k}$  into cylindrical ones

$$e^{i\mathbf{k}\cdot\mathbf{r}} = \sum_{n=-\infty}^{\infty} i^n J_n(kr) e^{in\theta}$$

## 2 Introduction to spectral methods

where  $\mathbf{k} \cdot \mathbf{r} = kr \cos(\theta)$ . Letting  $z = kr$  and using  $J_{-n}(t) = (-1)^n J_n(t)$ , we get the Jacobi-Anger expansion

$$e^{iz \cos(\theta)} = J_0(t) + 2 \sum_{n=1}^{\infty} i^n J_n(z) \cos(n\theta)$$

or

$$e^{iz \cos(\theta)} = \sum_{n=0}^{\infty} \frac{2}{1 + \delta_{n0}} i^n J_n(z) \cos(n\theta)$$

which is actually valid for complex  $z$ . From here, defining  $x = \cos(\theta)$ , this expression immediately provides the desired Chebyshev expansion, where

$$u_n(z) = \frac{2}{1 + \delta_{n0}} i^n J_n(z).$$

The properties of this expansion coefficient are therefore provided by the Bessel functions. Taking  $z$  to be real, we obtain the Chebyshev expansion of the imaginary exponential.

### 2.5.3 Green's function

The Green's function is very closely related to the previous two. Let  $z$  be a complex number and  $x$  a real number. We want to find the following expansion:

$$g(z) = \frac{1}{z - x} = \sum_{n=0}^{\infty} g_n(z) T_n(x).$$

where the coefficients  $g_n(z)$  can be found through

$$\begin{aligned} g_n(z) &= \frac{2}{\pi} \frac{1}{1 + \delta_{n0}} \int_{-1}^1 \frac{dx}{\sqrt{1 - x^2}} T_n(x) \frac{1}{z - x}. \\ &= \frac{1}{\pi} \frac{1}{1 + \delta_{n0}} \int_{-\pi}^{\pi} d\theta \frac{\cos(n\theta)}{z - \cos(\theta)}. \end{aligned}$$

This integral can be solved using the Residue Theorem, but here I want to present a different approach, which does not require knowledge of complex analysis. This integral can also be recognized from the Green's function of an infinite 1D tight-binding chain with hopping parameter  $t = 1/2$ . Let  $\varepsilon(k) = \cos(k)$  be its dispersion relation, with eigenfunctions indexed by  $k$

$$|k\rangle = \frac{1}{\sqrt{N}} \sum_k e^{ikn} |n\rangle$$

where  $-\pi \leq k < \pi$ . Since these functions are not normalizable, we can keep a finite number  $N$  of sites and take it to infinity in the end of the calculation. The matrix element of the Green's function which connects site 0 to site  $n$ ,  $\langle 0 | (z - H)^{-1} | n \rangle$  can be expressed in the eigenbasis of  $H$  as

$$G_{0,n} = \langle 0 | \frac{1}{z - H} | n \rangle = \int_{-\pi}^{\pi} \frac{dk}{2\pi} \frac{e^{-ikn}}{z - \cos(k)} = \int_{-\pi}^{\pi} \frac{dk}{2\pi} \frac{\cos(nk)}{z - \cos(k)}.$$

The last equality holds because the imaginary part of  $\exp(-ikn)$  integrates to zero. Therefore, upon the identification of  $\theta$  as  $k$ , the relation can be established as

$$g_n(z) = \frac{2}{1 + \delta_{n0}} G_{0,n}.$$

From this point on, Dyson's equations can be used to find  $G_{0,n}$  algebraically, avoiding integration in the complex plane which is quite cumbersome. To proceed, let's begin by labeling the lattice points from  $-\infty$  to  $\infty$  and separating the lattice into the right side, from site  $n$  to  $+\infty$  and the left side, from  $-\infty$  to  $n-1$ . This naturally defines a left and a right Hamiltonian  $H_L$  and  $H_R$ , which are connected by a hopping  $t$  connecting site  $n-1$  to  $n$ , encapsulated in an operator  $V$ . Let  $H_0 = H_L + H_R$  be the disconnected Hamiltonian. The total Hamiltonian is therefore  $H = H_0 + V$ . Let  $G$  and  $G^0$  be the Green operators of  $H$  and  $H_0$ , respectively. Then, Dyson's equation tells us that

$$G = G^0 + G^0 V G$$

which becomes

$$G_{0,n} = G_{0,n-1}^0 V_{n-1,n} G_{n,n}. \quad (2.15)$$

The expression for  $G_{n,n}$  is easy to obtain because it is proportional to the density of states due to the translation invariance of  $H$ , that is,

$$G_{n,n} = \frac{1}{\sqrt{z^2 - 4t^2}}.$$

$G_{0,n-1}^0$  is the Green's function which connects a site at the surface ( $n-1$ ) to a site in the interior (0) of the truncated lattice. Let's call it  $g_{0,n-1}$ . Then, what we need to find is

$$G_{0,n} = g_{0,n-1} t \frac{1}{\sqrt{z^2 - 4t^2}}$$

To find the formula for  $g_{0,n-1}$ , let  $H_n$  be the Hamiltonian of the single site at  $n$ , and redefine  $H_0$  and  $H$  such that  $H_0 = H_L + H_n$  and  $H = H_0 + V$ . With these new Hamiltonians, Dyson's equation retains the exact same form as before (2.15), but now  $G$  refers to the new  $H$  and  $G_0$  to the new  $H_0$ . With this identification, we recognize that  $G_{0,n}$  is the Green's function which connects a site at the surface ( $n$ ) to a site in the interior (0) of the lattice truncated at  $n$ , and  $G_{0,n-1}$  is the Green's function which connects a site at the surface ( $n-1$ ) to a site in the interior (0) of the lattice truncated at  $n-1$ . That is,  $g_{0,n}$  and  $g_{0,n-1}$  respectively. We have thus established a recursive relation between these functions:

$$g_{0,n} = g_{0,n-1} t g_S$$

where  $g_S = G_{nn} = G_{n-1,n-1}^0$  is the surface Green's function. Repeating this argument

## 2 Introduction to spectral methods

until we reach  $g_{0,0} = g_S$ , we obtain

$$g_{0,n} = g_S (tg_S)^n.$$

The last ingredient needed to calculate the Chebyshev coefficient is the surface Green's function  $g_S$  of the truncated lattice. To get it, let's consider the same  $H_0$  and  $H$  but let's look at different matrix elements of Dyson's equation, namely:

$$\begin{aligned} G_{nn} &= G_{n,n}^0 + G_{n,n}^0 V_{n,n-1} G_{n-1,n} \\ G_{n-1,n} &= G_{n-1,n-1}^0 V_{n-1,n} G_{n,n} \end{aligned}$$

Combining these together and again identifying  $g_S = G_{nn} = G_{n-1,n-1}^0$ , we obtain a second order equation for  $g_S$

$$g_S = \frac{1}{z} + \frac{1}{z} (tg_S)^2$$

which has the two solutions

$$g_S = \frac{z \pm \sqrt{z^2 - 4t^2}}{2t^2}.$$

The negative solution must be chosen to ensure  $g_S \rightarrow 0$  when  $|z| \rightarrow \infty$ . Putting everything together and setting  $t = 1/2$ , we get

$$g_n(z) = \frac{-2i}{1 + \delta_{n0}} \frac{\left(z - i\sqrt{1 - z^2}\right)^n}{\sqrt{1 - z^2}} \quad (2.16)$$

which are exactly the coefficients obtained in [94]. For practical purposes, it's useful to define separate coefficients for the advanced and retarded Green's functions:

$$g_n^{\sigma,\eta}(\epsilon) = -\frac{2\sigma i}{1 + \delta_{n0}} \frac{e^{-ni\sigma \arccos(\epsilon + i\sigma\eta)}}{\sqrt{1 - (\epsilon + i\sigma\eta)^2}} \quad (2.17)$$

where  $\sigma = +1$  corresponds to the retarded and  $\sigma = -1$  to the advanced Green's functions and  $\eta$  is the finite **positive** number corresponding to the broadening of the Green's function, such that  $z = \epsilon + i\sigma\eta$ .

### Convergence

Given that the Green's function varies very rapidly around its poles, it's useful to have an estimate of the number of polynomials required to accurately resolve it. The main factor responsible for the convergence rate of the series expansion is  $\eta$ , the imaginary part of  $z$ . Figure 2.4 shows how the Chebyshev expansion of the Green's function depends on  $\eta$  and the number of polynomials.

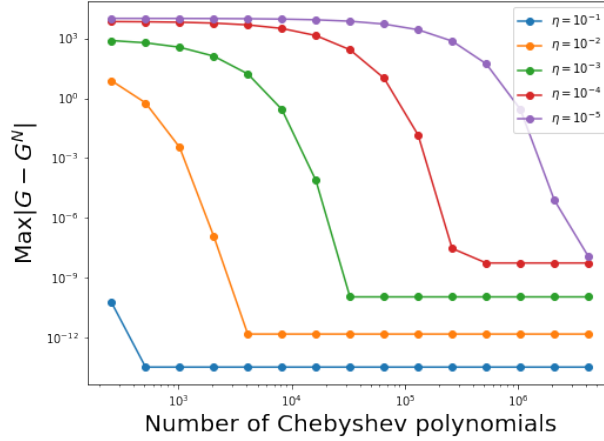


Figure 2.4: Convergence properties of the Chebyshev expansion of the Green's function, as a function of the number of polynomials used to expand it. Each curve represents a different value of the broadening parameter  $\eta$ .

The  $y$  axis is the maximum difference between the exact Green's function (centered at  $\varepsilon = 0$ ) and the expansion, that is,

$$\max_{\varepsilon} \left( \frac{1}{\varepsilon + i\eta} - \sum_{n=0}^M g_n(\varepsilon + i\eta) T_n(0) \right).$$

As a final note, it is common to expand the Green's function assuming the imaginary part of  $z$  to be an infinitesimal, and then to use the Lorentz weight to regularize the expansion. Since we have access to the expansion coefficients for a general complex  $z$  and since the convergence is more favorable for finite  $\eta$ , we decide not to use the Lorentz weight and to instead use the expansion for a small, but finite  $\eta$ . This is the core of the Chebyshev Polynomial Green's Function (CPGF) method [3, 94].

#### 2.5.4 Fermi-Dirac distribution

The Fermi-Dirac distribution at finite temperature and chemical potential also allows an expansion in terms of Chebyshev polynomials

$$f_{\beta,\mu}(\varepsilon) = \frac{1}{1 + e^{\beta(\varepsilon - \mu)}} = \sum_{n=0}^{\infty} f_n(\beta, \mu) T_n(\varepsilon) \quad (2.18)$$

but this expansion is not so common in the literature. More commonly, its expansion is avoided by convoluting it with the Dirac delta

$$f_{\beta,\mu}(x) = \int_{-\infty}^{\infty} d\varepsilon f_{\beta,\mu}(\varepsilon) \delta(\varepsilon - x)$$

and expanding the Dirac delta instead. In this section, I want to analyze the direct expansion of the Fermi-Dirac distribution.

## 2 Introduction to spectral methods

For finite temperature, there is no known closed form expression, but at zero temperature, there is. At zero temperature, the Fermi-Dirac distribution reduces to the shifted Heaviside function. The coefficients are given by

$$f_n(\infty, \mu) = \frac{2}{\pi} \frac{1}{1 + \delta_{n0}} \int_{-1}^{\mu} \frac{dx}{\sqrt{1-x^2}} T_n(x).$$

Let  $\cos(\theta_0) = \mu$  and use the standard change of variable  $x = \cos(\theta)$ . Then, the integral becomes easy to calculate

$$f_n(\infty, \mu) = \frac{2}{\pi} \frac{1}{1 + \delta_{n0}} \int_{\theta_0}^{\pi} d\theta \cos(n\theta)$$

and yields

$$f_n(\infty, \mu) = \begin{cases} \frac{2}{\pi n} [\sin(n\pi) - \sin(n \arccos(\mu))] & n > 0 \\ 1 - \frac{\arccos(\mu)}{\pi} & n = 0 \end{cases}$$

Because of the discontinuity, the Jackson weight is added to regularize the expansion. Figure 2.5 shows the effect of different weights on the approximant to the Fermi function at a cutoff of 100 polynomials and 1000 polynomials (top). The Gibbs phenomenon is clearly visible in the absence of a regularization (Dirichlet weight). On the bottom, convergence is analyzed more carefully at three different energy points, close and away from the discontinuity. The Jackson weight is clearly superior in every circumstance.

At finite temperature, the integral

$$f_n(\beta, \mu) = \frac{2}{\pi} \frac{1}{1 + \delta_{n0}} \int_0^{\pi} d\theta \cos(n\theta) f(\cos(\theta))$$

has to be evaluated numerically. The function is smooth everywhere, so a Gauss-Chebyshev quadrature method should give a good estimate for this integral. However, for smaller temperatures, the function varies very quickly close to the Fermi energy, and so it may be useful to split the integration domain into three sections to better capture this variation: one of them from  $-1$  to  $\mu - 1/\beta$ , another from  $-1/\beta$  to  $1/\beta$  and another from  $1/\beta$  to  $1$ . An alternative to this is to express the Fermi function as a Matsubara sum and to use contour integration.

### Effective temperature

Since the Fermi-Dirac distribution has a discontinuity at zero temperature, Gibbs oscillations are to be expected. For this reason, a kernel should be used to mitigate them, which will smoothen the discontinuity into a steep ramp. The size of this ramp can be interpreted as a Fermi-Dirac distribution at finite temperature. To estimate the size of the ramp, we can use the results we already have about the Dirac delta. The introduction of the Jackson kernel widens the Dirac delta into a gaussian-like curve of standard deviation  $\sigma = \pi/N$ , where  $N$  is the number of Chebyshev polynomials being used to approximate the curve.

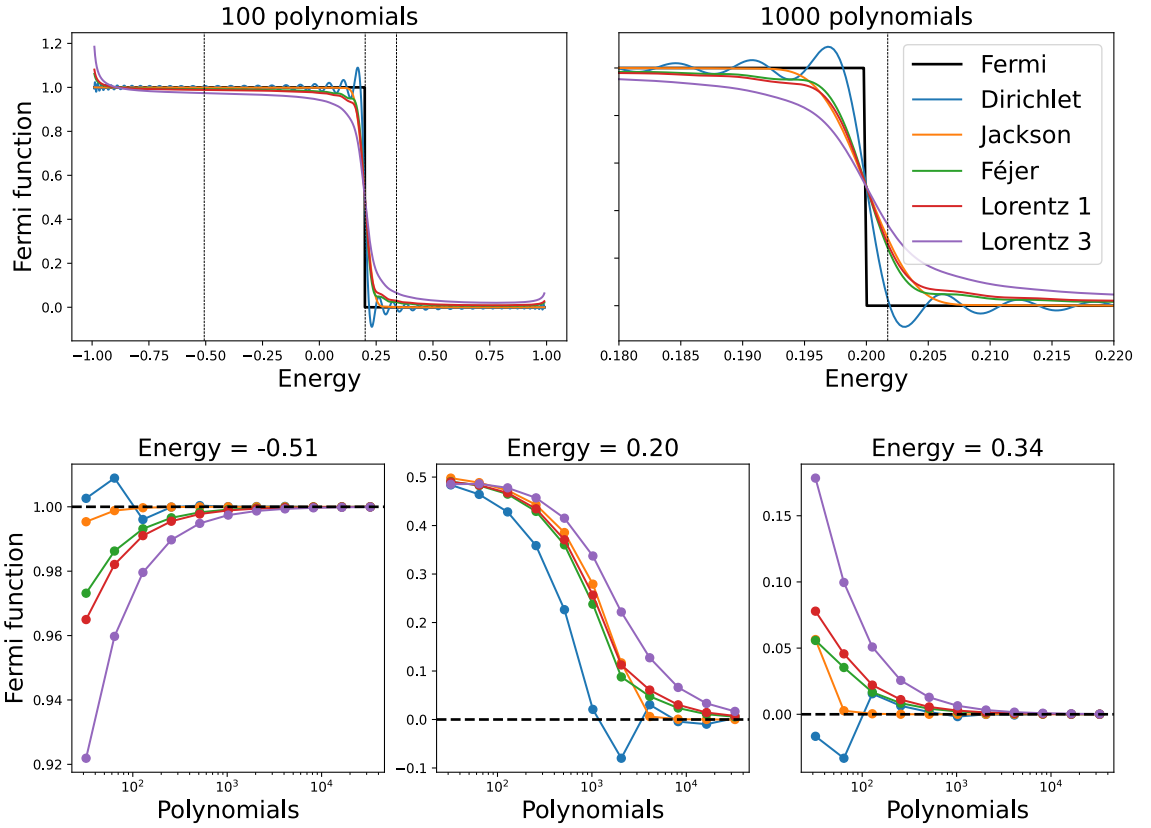


Figure 2.5: Convergence properties of the Fermi function of chemical potential  $\mu = 0.2$  at zero temperature.

The integral of this broadened Dirac delta is exactly the Fermi-Dirac distribution for the same number of polynomials and the same kernel. Therefore, the characteristic size of the ramp is also  $\pi/N$ , defining  $\beta_{\text{eff}} \approx N/\pi$  as the effective temperature of this approximation.

### Position of the eigen energies

As was noted in the beginning of this section, convergence around points of discontinuity is much slower. Coming back to the operator form of eq. 2.18,

$$f(\tilde{H}) = \sum_{n=0}^N f_n(\tilde{\beta}, \tilde{\mu}) T_n(\tilde{H}),$$

this can become problematic when there are eigenvalues of  $\tilde{H}$  close to  $\tilde{\mu}$ . To see this more clearly, let's use the eigenbasis of  $\tilde{H}$  to express  $f(\tilde{H})$  in terms of the eigenenergies  $\tilde{\epsilon}_m$ :

$$f(H) = \sum_{n=0}^N f_n(\tilde{\beta}, \tilde{\mu}) \sum_m T_n(\tilde{\epsilon}_m) |m\rangle \langle m|.$$

Each term  $\sum_{n=0}^N f_n(\tilde{\beta}, \tilde{\mu}) T_n(\tilde{\epsilon}_m)$  represents the approximation to  $f(\tilde{\epsilon}_m)$  with  $N$  Chebyshev polynomials. The closer the eigenenergy is to  $\tilde{\mu}$ , the slower the convergence. Therefore,

## 2 Introduction to spectral methods

the convergence of this series depends on the closest eigenvalue to  $\tilde{\mu}$ . As a consequence, it becomes very easy to converge when  $\mu$  is in a gap of the Hamiltonian's spectrum, but it can be very problematic when  $\mu$  lies inside a band, where in the thermodynamic limit there are states arbitrarily close to  $\mu$ .

### 2.6 Stochastic trace evaluation

At the heart of KPM is the stochastic trace evaluation, which is ultimately responsible for the efficiency of the method. Assume that we want to compute the trace of a hermitian matrix  $A$  of dimensions  $N \times N$  in a given basis  $|n\rangle$

$$T = \text{Tr}(A) = \sum_n \langle n| A |n\rangle = \sum_n A_{nn}.$$

This is a sum of many terms, and the usage of random numbers can in some allow us to perform many of these computations at once. Let  $\xi$  be a random number (possibly complex) taken from a certain distribution, with the only requirements being zero average  $\overline{\xi} = 0$ , unit variance  $\overline{|\xi|^2} = 1$ . An independent collection of  $N$  of these numbers satisfies  $\overline{\xi_n^* \xi_m} = \delta_{nm}$  and can be used to define a random vector in the basis  $|n\rangle$ :

$$|\xi\rangle = \sum_{n=1}^N \xi_n |n\rangle.$$

This vector gives us an estimator  $t$  for the trace

$$t = \langle \xi| A |\xi\rangle = \sum_{nm} \xi_m^* \xi_n \langle m| A |n\rangle. \quad (2.19)$$

It is easy to see that on average  $\bar{t} = T$ , in virtue of the properties imposed on the random numbers:

$$\bar{t} = \sum_{nm} \overline{\xi_m^* \xi_n} \langle m| A |n\rangle = \sum_n \langle n| A |n\rangle = T.$$

Since  $A$  is hermitian,  $t$  will be a real number. While the value of the average  $\bar{t}$  does not depend on the basis being used nor the distribution, the variance does. The average of the square can be calculated by considering all the correlations of four random numbers:

$$\overline{t^2} = \sum_{abcd} \overline{\xi_a^* \xi_b \xi_c^* \xi_d} A_{ab} A_{cd}.$$

The first thing to notice is that there can be no correlators with an odd number of terms because that would necessarily leave one correlator with just one term, and that is zero by construction. Therefore, we have to consider all the possible ways to correlate an even number of terms, and it is useful to separate into cases.

The first is the case  $a = b \neq c = d$ , which correlates the first two and the last two

numbers, but since these pairs are necessarily different, their correlation is zero:

$$\sum_{a \neq c} \overline{\xi_a^* \xi_a \xi_c^* \xi_c} A_{aa} A_{cc} = \sum_{a \neq c} \overline{\xi_a^* \xi_a} \overline{\xi_c^* \xi_c} A_{aa} A_{cc}$$

Since every random number follows the same distribution, the correlators factor out and we are left with a sum over  $a$  and  $c \neq a$ . This sum can be simplified by summing over  $a$  and  $c$  without restriction and then removing the case  $a = c$ , leading to

$$\sum_{a \neq c} \overline{\xi_a^* \xi_a \xi_c^* \xi_c} A_{aa} A_{cc} = \overline{\xi^* \xi} \overline{\xi^* \xi} \left[ \sum_a A_{aa} \sum_c A_{cc} - \sum_a A_{aa}^2 \right]$$

which finally simplifies to

$$\sum_{a \neq c} \overline{\xi_a^* \xi_a \xi_c^* \xi_c} A_{aa} A_{cc} = \text{Tr}(A) - \sum_a A_{aa}^2.$$

A similar reasoning can be used for the other two possibilities with two pairs. When  $a = c \neq b = d$ ,

$$\sum_{a \neq b} \overline{\xi_a^* \xi_b \xi_a^* \xi_b} A_{ab} A_{ab} = \left| \overline{\xi^2} \right|^2 \left[ \sum_{a,b} A_{ab}^2 - \sum_a A_{aa}^2 \right]$$

and when  $a = d \neq b = c$ ,

$$\sum_{a \neq b} \overline{\xi_a^* \xi_b \xi_b^* \xi_a} A_{ab} A_{ba} = \text{Tr}(A^2) - \sum_a A_{aa}^2.$$

Finally, when all the indices are the same, we get

$$\sum_a \overline{\xi_a^* \xi_a \xi_a^* \xi_a} A_{aa} A_{aa} = \left| \overline{\xi} \right|^4 \sum_a A_{aa}^2.$$

This exhausts all the possibilities for correlations. Putting this all together, the variance is

$$\sigma_t^2 = \text{Tr}(A^2) + \left| \overline{\xi^2} \right|^2 \text{Tr}(A^T A) + \left[ \left| \overline{\xi} \right|^4 - 2 - \left| \overline{\xi^2} \right|^2 \right] \sum_a A_{aa}^2. \quad (2.20)$$

At this point, it is worth noticing that if the complex random vector is chosen to lie on the unit complex circle, then  $\overline{\xi^2} = 0$ ,  $\left| \overline{\xi} \right|^4 = 1$  and the expression simplifies to

$$\sigma_t^2 = \text{Tr}(A^2) - \sum_a A_{aa}^2 \quad (2.21)$$

which is the more well-known form [95]. If the random vector is chosen to be real, then the expression also simplifies

$$\sigma_t^2 = \text{Tr}(A^2) + \text{Tr}(A^T A) + \left[ \overline{\xi^4} - 3 \right] \sum_a A_{aa}^2.$$

## 2 Introduction to spectral methods

This derivation was done assuming the trace estimator  $t$  to be real. Were this not the case,  $\sigma_t^2$  would be a complex number and would not have the intended meaning. In the more general case, instead of  $\overline{t^2}$ , one could look into  $\overline{|t|^2}$ . One important thing to notice about 2.20 is that it depends on the basis chosen to write the random vector  $|\xi\rangle$ . In the extreme case, if we use complex unit vectors in a basis where  $A$  is diagonal, eq. 2.21 tells us that  $\sigma_t^2 = 0$ . This is already obvious in eq. 2.19, because  $t = T$  in virtue of the fact that  $\xi_a^* \xi_a = 1$  for all  $a$  and the inexistence of nondiagonal elements. This would not happen for other distributions and seems to indicate that complex unit vectors have the optimal variance for sparse matrices. This is the same conclusion reached by Iitaka [104]. Indeed for many of the usual applications, they do yield the smallest variance, but this is not always the case. As we will see in chapter 5, using complex unit vectors for the stochastic evaluation of the expectation value of the current gives rise to a variance which can be upwards to 50 times larger than by using real vectors. This is such an example where the derivation for the variance used here is not valid, because the matrix being used is not hermitian.

Lastly, the most important property of the stochastic evaluation of the trace is the following. Assuming that the matrix is sufficiently sparse, the variance will scale as  $N$ , as will the trace. For this reason, the relative error  $\sigma_t/t$  will scale as  $1/\sqrt{N}$ . The same scaling will happen with the number  $N_R$  of random vectors due to the central limit theorem. Therefore, we can expect

$$\frac{\sigma_t}{t} \sim \frac{1}{\sqrt{N_R N}} \quad (2.22)$$

and this is really what makes KPM so powerful. The relative error goes down not just with  $N_R$  but also with  $N$ . The larger the system, the smaller the relative error, regardless of whether or not it has translational symmetry. For very large systems, the number of random vectors can be made as small as 1. In general, if the matrix is not sparse, however, then the first two terms of 2.20 should contribute as  $N^2$  and eq. 2.22 no longer holds.

### 2.6.1 Variance of Chebyshev moments

While the previous section is true for matrices  $A$  in general, this brings up an apparent inconsistency. In practice, the matrix which is getting traced over is a Chebyshev polynomial of the Hamiltonian. A sufficiently high-order polynomial should therefore be a dense matrix, so how does 2.22 hold? The answer to this subtle point lies with some properties of the Chebyshev polynomials and the fact that the spectrum is limited to the range  $-1 \leq x \leq 1$ .

The first term can be expressed in the eigenbasis of  $H$ . Since the eigenvalues  $\varepsilon_n$  are limited to the aforementioned range,  $\varepsilon_n^2 \leq 1$  and so we get that

$$\text{Tr}(T_m^2(H)) = \sum_n \cos^2(m \arccos(\varepsilon_n)) \leq \sum_n 1 \leq N$$

and the first term actually contributes as  $N$ , regardless of the sparsity of the matrix.

The second term contributes in a similar manner. Its absolute value is actually bounded by the first term. Using the Cauchy-Schwartz inequality for the Frobenius norm  $|A| = \sqrt{\sum_{ij} |A_{ij}|^2}$  we get

$$|\text{Tr}(A^T A)| = \left| \sum_{ij} A_{ij}^2 \right| \leq \sum_{ij} |A_{ij}|^2 = \sum_{ij} A_{ij} A_{ij}^* = \text{Tr}(A^2)$$

and so it also contributes as  $N$ . The last term follows a similar pattern

$$\left| \sum_a A_{aa}^2 \right| = \sum_a |A_{aa}^2| \leq \sum_{ab} |A_{ab}|^2 = \text{Tr}(A^2)$$

where we have used the fact that  $A_{aa}$  is real in virtue of  $A$  being Hermitian. Therefore,  $\sigma_t^2$  always scales as  $N$  when  $A$  is a Chebyshev matrix, even though it is in general a dense matrix.

## 2.7 Applications to quantum transport

The first known application of KPM in its current form was in 1994 by Silver [99], even though gaussian random vectors had already been used to compute polynomial moments of operators before [105–107]. Silver used it to calculate the DoS just like what was done in the beginning of this chapter. 10 years later, Weisse [69] applied it to response functions, using the Kubo formula for the real part of the optical conductivity:

$$\sigma(\omega) = \sum_{nm} \frac{|\langle n | J_x | m \rangle|^2}{\omega L^d} [f(E_m) - f(E_n)] \delta(\omega - (E_n - E_m)).$$

For the first time, this required a double Chebyshev expansion, but it was not obvious how to make the transition from here to a form suitable to expansion. The trick consisted on defining an auxiliary object

$$j(x, y) = \frac{1}{L^d} \sum_{nm} \langle m | J_x | n \rangle \delta(x - E_n) \langle n | J_x | m \rangle \delta(x - E_m)$$

such that now the conductivity could be written as an integral over this object:

$$\sigma(\omega) = \frac{1}{\omega} \int_{-\infty}^{\infty} j(x, x + \omega) [f(x) - f(x + \omega)] dx.$$

Now, each Dirac delta could be expanded in Chebyshev polynomials, defining a Chebyshev moment matrix, in analogy to the Chebyshev moments of the DoS. To make this clearer, note that  $j(x, y)$  can be written as a trace

$$j(x, y) = \frac{1}{L^d} \text{Tr} [J_x \delta(x - H) J_x \delta(x - H)]$$

## 2 Introduction to spectral methods

and each of the Dirac deltas can be expanded as in eq. 2.12,

$$\text{Tr} [J_x \delta(x - H) J_x \delta(x - H)] = \sum_{ab} \Delta_a(x) \Delta_b(y) \text{Tr} [J_x T_a(H) J_x T_b(H)]$$

where the terms of the trace are defined as the Chebyshev moments

$$\mu_{ab} = \frac{1}{L^d} \text{Tr} [J_x T_a(H) J_x T_b(H)].$$

The full current can be reconstructed from these

$$\sigma(\omega) = \sum_{ab} \mu_{ab} \int_{-\infty}^{\infty} \Delta_a(x) \Delta_b(x + \omega) \frac{f(x) - f(x + \omega)}{\omega} dx.$$

This was the first second-order Chebyshev expansion of the sort, and it enjoys several of the advantages that we've seen before. The calculation of  $\mu_{ab}$  is done with random vectors and is the most complicated part, but it does not depend on the frequency  $\omega$ , the inverse temperature  $\beta$  nor the chemical potential  $\mu$ . Once  $\mu_{ab}$  has been computed, the calculation for all these parameters becomes very quick. Just like what happened to the DoS, the optical conductivity has been factorized by the Chebyshev expansion. This marked the first use of spectral methods in modern transport equations and has set the trend for the future.

Expansions of the same sort have now been used in the several variants of Kubo's formula. One of the main issues while going from Kubo's formula to its KPM-ready form is how to express it as a trace. Terms like  $\delta(\omega - E_n + E_m)$ , which depend on two energies, can become problematic because they cannot directly be expressed in terms of the Hamiltonian matrix. The trick to deal with them is to factor out one of the energies with an auxiliary Dirac delta, as Weisse did in the example above. Defining  $\varepsilon = E_n$ , the Dirac delta can be expressed in terms of a convolution:

$$\delta(\omega - E_n + E_m) = \int_{-\infty}^{\infty} d\varepsilon \delta(\varepsilon - E_n) \delta(\omega - \varepsilon + E_m)$$

or, in terms of the Hamiltonian,

$$\delta(\omega - E_n + E_m) = \int_{-\infty}^{\infty} d\varepsilon \langle n | \delta(\varepsilon - H) | n \rangle \langle m | \delta(\omega - \varepsilon + H) | m \rangle.$$

Each of the Dirac deltas can now be expanded accordingly and this is the procedure responsible for the double expansion. This procedure is formalized in chap 4 for the nonlinear optical response.

### 2.7.1 Reducing the price of a double expansion

The double Chebyshev expansion is able to bring spectral methods to a broader class of problems by turning the numerical algorithm into complexity  $\mathcal{O}(N)$ . In fact, let us be more precise and introduce the average lattice coordination  $Z$ . The complexity is therefore more

accurately captured as  $\mathcal{O}(NZ)$ - Despite being of linear complexity in the Hilbert space, this characterization hides the fact that a double Chebyshev expansion is numerically costly. In this subsection, I want to get into some more detail about this process and when it's worth doing. Consider the Kubo-Greenwood formula at zero temperature, written as a trace

$$\sigma^{xx} = \frac{e\hbar}{L^d} \text{Tr} [v^x \delta(\varepsilon_F - H) v^x \delta(\varepsilon_F - H)] \quad (2.23)$$

where  $\varepsilon_F$  is the Fermi energy. The numerical evaluation of this trace with KPM would have complexity  $\mathcal{O}(NZM^2)$ , where  $M - 1$  is the highest order of Chebyshev polynomials being used to expand the Dirac deltas. Notice that the number of Fermi energies does not change the complexity of the algorithm. The resolution of this expansion with the Jackson kernel is roughly  $\pi/M$ , so attempting to obtain fine resolutions can rapidly incur in prohibitive numerical costs. With access to enough RAM, this can in part be mitigated. Suppose we want to calculate all the Chebyshev moments  $\mu_{nm} = \langle \xi | v^x T_n(H) v^x T_m(H) | \xi \rangle$  up to  $n = m = M - 1$ . Let  $|\xi'\rangle = v^x |\xi\rangle$ ,  $|n\rangle = T_n(H) |\xi\rangle$  and  $|n'\rangle = T_n(H) |\xi'\rangle$ . The moments can be written simply as

$$\mu_{nm} = \langle n' | v_x | m \rangle$$

where both the vectors on the left and the vectors on the right satisfy the recursion relation

$$\begin{aligned} |m+1\rangle &= 2H|m\rangle - |m-1\rangle \\ |n'+1\rangle &= 2H|n'\rangle - |n'-1\rangle \end{aligned}$$

when  $n', m > 1$ . The case  $= 0$  is omitted for simplicity and does not change the argument. Because of the double-step recurrence, only two vectors are required to be kept in memory at any given time,  $|m\rangle$  and  $|m-1\rangle$ . Then, for every  $|n'\rangle$ , all the  $|m\rangle$  have to be calculated every time in order to build the matrix  $\mu_{nm}$ . Immediately, we see a source of redundancy here. The process of calculating the  $|m\rangle$  is being repeated!

Suppose now that, as we calculate the  $|m\rangle$  from 0 to  $M - 1$ , we store every single vector in a matrix  $T_{im}$ , where  $i$  is the Hilbert space index and  $m$  is the Chebyshev index. This matrix has  $N \times M$  entries and requires the exact same complexity as the usual Chebyshev recursion scheme, so the numerical complexity to calculate  $T$  is  $\mathcal{O}(NMZ)$ . The exact same process can be repeated for the vector on the left. Let  $T'_{ni}$  be this matrix. The calculation of both  $T$  and  $T'$  adds up to a complexity of  $\mathcal{O}(2NMZ)$  and takes up RAM of order  $\mathcal{O}(2NM)$ . Finally, the matrix  $\mu_{nm}$  is built of these two matrices as

$$\mu_{nm} = \sum_i T'_{ni} T_{im},$$

which is matrix product on dense matrices, of complexity  $\mathcal{O}(NM^2)$  but which is highly

## 2 Introduction to spectral methods

vectorizable and does not depend on  $Z$ . Thus, given enough RAM, we are able to reduce the complexity of the algorithm from  $\mathcal{O}(NZM^2)$  to  $\mathcal{O}(2NMZ + NM^2)$ , while keeping in mind that the second part is much more efficient. Of course, this would have to be repeated for every random vector.

In practice, for very large systems, one will not have sufficiently RAM to store all these vectors, and so instead of two large  $T$  and  $T'$  matrices of dimensions  $N \times M$ , one could instead store just  $D$  vectors and construct  $\mu_{nm}$  by blocks. Suppose for the sake of the simplicity that  $D$  divides  $M$ . Then, each block of size  $D^2$  would have constructed individually and there are  $(M/D)^2$  such blocks. Since the first part of the algorithm would have to be repeated for every block, its complexity would be  $\mathcal{O}\left(2NDZ\left(\frac{M}{D}\right)^2\right)$ . The second part would also have to be repeated for every block, but the matrices would be of dimension  $N \times D$ , so the overall complexity  $\mathcal{O}\left(ND^2\left(\frac{M}{D}\right)^2\right)$  is unchanged. Assuming that the computation time can be factored in each of the two parts ( $\tau_A$  for the first and  $\tau_B$  for the second), the total computational time can be decomposed into two parts

$$\tau_{\text{CPU}} = 2NDZ \left(\frac{M}{D}\right)^2 \tau_A + NM^2 \tau_B = NM^2 \left(\tau_A \frac{2Z}{D} + \tau_B\right)$$

which makes it clear that the larger the amount of memory  $D$ , the better. However, if  $\tau_A$  and  $\tau_B$  are comparable, and  $Z$  is of the order of unity (as in graphene, for example, where  $Z = 3$ ), then going for massive memory increases will not decrease the computational time below the limit given by  $\tau_B$ .

In conclusion, storing  $D$  vectors in memory incurs into a larger memory footprint, but also allows for potentially large performance increases. If the algorithm is dominated by the first part, then the computational time is inversely proportional to  $D$ .

### 2.7.2 Avoiding a double expansion

One of the great advantages of a Chebyshev expansion is the fact that once the momenta have been calculated, they do not have to be recalculated for different Fermi energies or frequencies or temperatures. However, if one is only interested in one single set of parameters, this can reveal to be counterproductive. For example, in the previous section, if we are only interested in calculating the Kubo-Greenwood [2.23](#) formula at zero temperature for a small number  $N_F$  of Fermi energies, then it might be more favorable to avoid the double expansion altogether. To see how this can be done, consider again the Chebyshev expansion of the Kubo-Greenwood formula for one random vector

$$\sigma^{xx} = \frac{e\hbar}{Ld} \langle \xi | v^x \left[ \sum_n \Delta_n(\varepsilon_F) T_n(H) \right] v^x \left[ \sum_m \Delta_m(\varepsilon_F) T_m(H) \right] | \xi \rangle.$$

Using the notation of the previous section,

$$\begin{aligned} |R\rangle &= \sum_m \Delta_m(\varepsilon_F) |m\rangle \\ |L\rangle &= \sum_n \Delta_n(\varepsilon_F) |n'\rangle, \end{aligned}$$

the conductivity can be expressed in terms of these two vectors

$$\sigma^{xx} = \frac{e\hbar}{L^d} \langle L | v^x | R \rangle.$$

For a given Fermi energy, each of these vectors can be calculated by accumulating the sum of Chebyshev vectors sequentially, and so it has complexity  $\mathcal{O}(NMZ)$ . The final product  $\langle L | v^x | R \rangle$  contributes with  $2NZ$ . Therefore, the overall complexity of computing the conductivity for a set of  $N_F$  Fermi energies is dominated by the first part and is  $\mathcal{O}(2NMZN_F)$ . In contrast to the original double expansion, one factor of  $M$  is replaced by  $2N_F$ . So, if the number of Fermi energies to calculate is small, this route is preferable [94].

## 2.8 Further applications

Spectral methods have been used in several other contexts. The rest of this thesis is devoted to applying spectral methods in new scenarios, like the calculation of the disorder self-energy, linear-scaling computation of the conductance, nonlinear optical conductivity and a new efficient implementation for superconductivity.



## 3 Diagrammatics in disordered systems

As mentioned in the Introduction, the self-energy is an important object in the theory of quantum transport and it is the central object in disorder-averaged two-point correlation functions. It is also a complicated object to calculate. The diagrammatic methods discussed in the Introduction can be used to evaluate it perturbatively in the disorder strength, or nonperturbatively within some approximation. Notably, quantum interference processes are absent from these common approximation schemes due to the difficulty in evaluating these terms. In most cases of interest, these terms are not important, as they are subdominant for larger energies, but sometimes they can play a dominant role. In this chapter, we want to show that it is possible to calculate this operator exactly in a numerical fashion, and that the contribution coming from quantum interference can be extremely important in the correct context such as the Gade singularity problem in graphene.

To build towards this result, we will start with an intuitive introduction to diagrammatics, focusing exclusively on the two-point correlation functions required for the spectral function and discussing the importance of disorder averaging. Through the example of the spectral function of a disordered system, we want to intuitively justify the need and usefulness of diagrammatic methods while preserving the simplicity. From this point of view, the self-energy will appear naturally as the analytical object which describes the complete effect of disorder at the level of two-point correlation functions. This sets the stage for the main point of this chapter: the exact calculation of the disordered self-energy operator. Along the way, the approximation techniques mentioned in the Introduction will be explained. Once the method for the exact calculation of the disordered self-energy operator has been shown, it will be compared to these techniques in both graphene and the complex oxide perovskite SrRuO<sub>3</sub> (SRO).

### 3.1 Intuitive introduction to the disorder self-energy

To start our discussion, let's begin by exploring a simple model where the disorder self-energy appears naturally. Suppose that we want to obtain the spectral function of a simple one-dimensional tight-binding model (1D TB), described by a Hamiltonian  $H$ . Apart for some factors, the spectral function at wavevector  $k$  and energy  $\varepsilon$  can be expressed in terms of the retarded Green's functions

$$A(k, \varepsilon) \propto \text{Im} \langle k | G^R(\varepsilon) | k \rangle. \quad (3.1)$$

### 3 Diagrammatics in disordered systems

This is a straightforward calculation to do if the system has translation invariance:

$$A(k, \varepsilon) \propto \text{Im} \frac{1}{\varepsilon - \varepsilon_k + i0^+} \quad (3.2)$$

where  $\varepsilon_k$  is the dispersion relation of this one-band model. In the absence of translation invariance, however (such as a disordered system), eq. 3.2 is no longer valid and we have to find another way to evaluate eq. 3.1. One obvious way is through a Chebyshev expansion of the Green's function, which although simple and exact, does not provide much insight into the disorder-induced processes which lead to the modification of the spectral function.

At the same time, we notice that the physical manifestation of disorder in the spectral function is through a broadening and shift of the spectral lines (see Fig. 3.1), which can be represented as

$$A(k, \varepsilon) \propto \text{Im} \frac{1}{\varepsilon - \varepsilon_k + \Sigma^R(k, \varepsilon)} \quad (3.3)$$

through the introduction of the complex-valued function  $\Sigma^R(k, \varepsilon)$ , the retarded disorder self-energy. Here,  $\Sigma^R(k, \varepsilon)$  is a scalar, but later we will see how to define it in general. This dependency on  $k$  and  $\varepsilon$  means that the spectral function does not get modified in the same way everywhere. Figure 3.1 shows this clearly for the 1D TB model with Anderson disorder, as the spectral line gets broadened and shifted considerably more near the band edges.

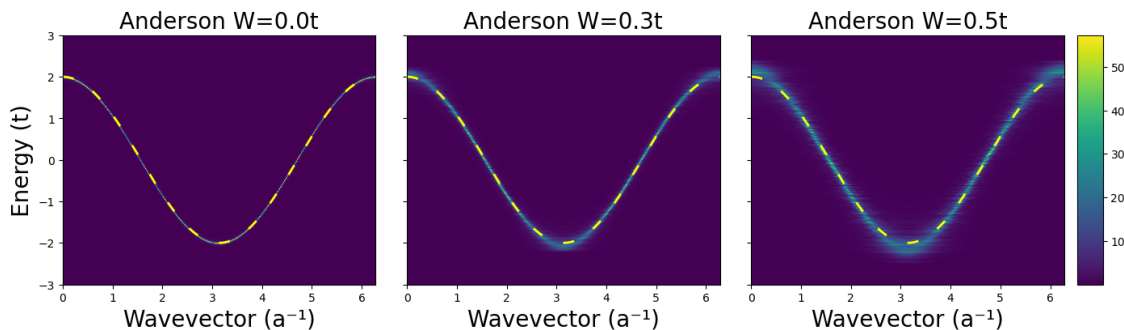


Figure 3.1: Spectral function of the 1D TB model of hopping  $t$  and lattice constant  $a$ , for several Anderson disorder strengths. The yellow dashed line represents the dispersion relation for the clean model.

The diagrammatic approach to disorder [11, 12] introduces a systematic way to compute this object, as well as providing insight about the processes at play. The self-energy is the central object of this chapter and so the next sections are devoted to understanding its relation to the disorder-averaged Green's function and to understanding the approximation schemes typically employed in its computation.

## 3.2 Self-energy and the disorder averaged Green's function

The diagrammatic approach to disorder relies on one crucial property: while a disordered system does not have translation symmetry, a disorder-averaged one does. Intuitively, since we expect the result not to depend on the specific realization of disorder, this procedure also makes physical sense.

It is important to be clear about the meaning of the term “disorder average” in this context, as well as the kind of disorder that we are talking about. To be concrete, only two kinds of disorder are going to be treated:

- Impurities/vacancies with a given concentration  $n$  (dilute disorder), where averaging over configurations of disorder means averaging over all possible impurity/vacancy positions with a fixed given concentration  $n$ , and
- Anderson disorder of strength  $W$ , where it means averaging over all possible Anderson disorder landscapes with strength  $W$ .

To proceed, let's assume that the Hamiltonian is composed of two parts: a translation invariant Hamiltonian  $H_0$  and the disordered part  $V$ , such that  $H = H_0 + V$ . Let

$$g(z) = \frac{1}{z\hat{\mathbf{1}} - H_0}$$

be the clean Green's function, where  $z = \varepsilon + i\eta$  is defined for notational simplicity. If  $\eta = 0^+$ ,  $g$  is a retarded Green's function. If  $\eta = 0^-$ , it is an advanced Green's function. The disorder-averaged Green's function  $\overline{G(z)}$  is obtained by averaging the complete Green's function

$$G(z) = \frac{1}{z\hat{\mathbf{1}} - H},$$

over all possible configurations of disorder. The self-energy operator is defined with respect to the disorder-averaged Green's function as such

$$\Sigma(z) = g^{-1}(z) - \overline{G(z)}^{-1}$$

and therefore contains all the information about disorder that  $\overline{G(z)}$  does. It is also a function of the energy  $\varepsilon$  and the broadening  $\eta$ , through the complex variable  $z$ . Just like with the Green's functions, if  $\eta = 0^+$ ,  $\Sigma(z)$  becomes the retarded self-energy, and if  $\eta = 0^-$ , it becomes the advanced self-energy, that is,

$$\begin{aligned}\Sigma(\varepsilon + i0^+) &= \Sigma^R(\varepsilon) \\ \Sigma(\varepsilon + i0^-) &= \Sigma^A(\varepsilon)\end{aligned}$$

which are both only functions of the energy, not  $\eta$ . If we know how to compute  $\overline{G(z)}$ , we can in principle invert it and use it to calculate the self-energy. Analytically, this is a difficult calculation to do, but it can be done perturbatively or with resort to some

approximation with diagrammatic methods. Later in this chapter, we will show how the self-energy can be obtained numerically without any approximation.

### 3.3 Diagrammatics

The starting point for a diagrammatic treatment of disorder is the complete Green's function  $G(z)$ . Using  $H = H_0 + V$ , the Green's function can be written as

$$G = \frac{1}{g^{-1} - V} = [g^{-1} (\hat{\mathbf{1}} - gV)]^{-1} = \frac{1}{\hat{\mathbf{1}} - gV} g$$

where the dependency on  $z$  in  $G$  and  $g$  has been omitted for the sake of notational simplicity. This expression can be readily expanded as a harmonic series

$$G = g + gVg + gVgVg + \dots$$

In momentum space, using the simplified notation  $G_{\alpha\beta}(\mathbf{k}, \mathbf{k}') = \langle \mathbf{k}, \alpha | G | \mathbf{k}', \beta \rangle$  for all operators, the above expression can be cast as

$$\begin{aligned} G_{\alpha\beta}(\mathbf{k}, \mathbf{k}') &= g_{\alpha\beta}(\mathbf{k}) \delta_{\mathbf{k}, \mathbf{k}'} + \sum_{\alpha_1 \alpha_2} g_{\alpha\alpha_1}(\mathbf{k}) V_{\alpha_1 \alpha_2}(\mathbf{k}, \mathbf{k}') g_{\alpha_2 \beta}(\mathbf{k}') \\ &+ \sum_{\mathbf{k}_1} \sum_{\alpha_1 \alpha_2 \alpha_3 \alpha_4} g_{\alpha\alpha_1}(\mathbf{k}) V_{\alpha_1 \alpha_2}(\mathbf{k}, \mathbf{k}_1) g_{\alpha_2 \alpha_3}(\mathbf{k}_1) V_{\alpha_3 \alpha_4}(\mathbf{k}_1, \mathbf{k}') g_{\alpha_4 \beta}(\mathbf{k}') + \dots \end{aligned}$$

where  $\mathbf{k}, \mathbf{k}'$  label the momentum vectors and  $\alpha, \beta$  label the remaining degrees of freedom unrelated to translation. Since  $g$  has the full translational symmetry of  $H_0$ , it does not connect different momentum vectors, hence  $g_{\alpha\beta}(\mathbf{k}, \mathbf{k}') = g_{\alpha\beta}(\mathbf{k}) \delta_{\mathbf{k}, \mathbf{k}'}$ .

Let us now introduce the diagrammatic representation of this expansion. Figure 3.2 represents the expansion up to third order in  $V$ , and the first three diagrams correspond to the first three terms on the right-hand side the expression above. The solid lines with arrows and indices represent the clean Green's function  $g$ , and the dashed lines with a cross at the end represent the disorder insertions  $V$ . The internal indices and labels are assumed to be summed over (that is, everything except  $\mathbf{k}, \mathbf{k}', \alpha, \beta$ ).

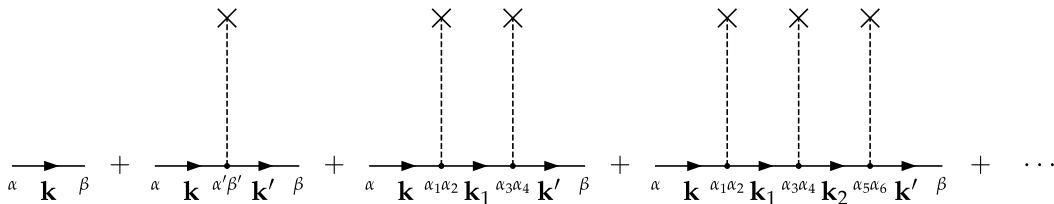


Figure 3.2: Diagrammatic representation of the disordered Green's function, before averaging over disorder configurations.

As mentioned before, we are not interested in the properties of a particular system, so let's average over disorder realizations:

$$\overline{G} = g + g\overline{V}g + g\overline{V}g\overline{V}g + \dots \quad (3.4)$$

Note that correlations are introduced because of terms with several disordered operators such as  $\overline{V}g\overline{V}$ . If we wanted to calculate these first few terms explicitly, the next step would be to choose a basis and evaluate the correlators. This would provide a controlled approximation, perturbative in the disorder strength (in the case of Anderson disorder) or in the concentration (in the case of impurities or vacancies). Even though this is not the most efficient way to compute as many terms as possible, it is still instructive to see how this evaluation is done. It will be useful later on and will clarify 1) how the translation invariance is reobtained and 2) how correlated disorder activates different matrix elements in the self-energy.

### 3.3.1 Correlators with Anderson disorder

For concreteness, let's see how to evaluate the averages  $\overline{V}$  and  $\overline{V}g\overline{V}$  when  $V$  represents Anderson disorder in a regular tight-binding lattice. In this situation, the disordered operator  $V$  is a diagonal operator in the position basis

$$V = \sum_{\mathbf{R}\alpha} V_{\mathbf{R},\alpha} |\mathbf{R}, \alpha\rangle \langle \mathbf{R}, \alpha|,$$

where the  $V_{\mathbf{R},\alpha}$  are a set of uncorrelated random numbers, each taken from a box distribution of average 0 and width  $W$ . Each realization of disorder is a different set of these numbers (see Fig. 3.3).

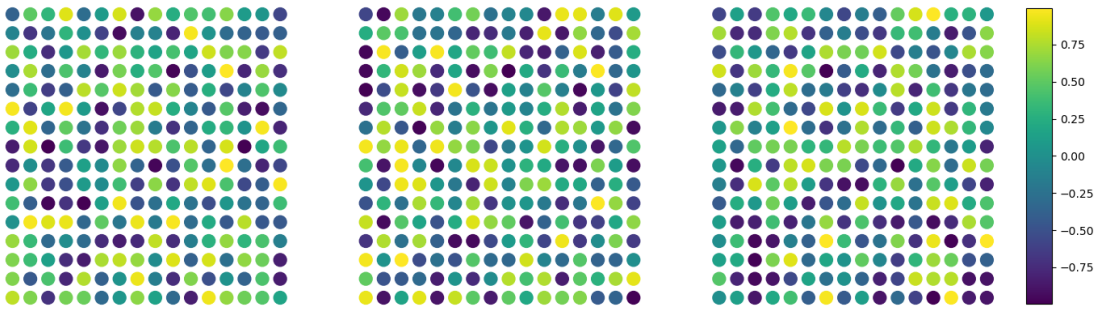


Figure 3.3: Example of different Anderson disorder configurations for a square lattice. The color represents the value of the local potential.

The moments of this distribution are

$$v_n = \begin{cases} \frac{1}{n+1} \left(\frac{W}{2}\right)^n & \text{if } n \text{ even} \\ 0 & \text{if } n \text{ odd} \end{cases}.$$

### 3 Diagrammatics in disordered systems

For the sake of generality, let's assume that the average can be nonzero. Now let's define the momentum basis as follows:

$$|\mathbf{k}, \alpha\rangle = \frac{1}{\sqrt{N}} \sum_{\mathbf{R}} e^{i\mathbf{k}\cdot\mathbf{R}} |\mathbf{R}, \alpha\rangle$$

where  $N$  is the number of unit cells, that is, the number of elements in the sum over  $\mathbf{R}$ . In this basis,  $V$  has the following form:

$$\langle \mathbf{k}, \alpha | V | \mathbf{k}', \beta \rangle = \frac{1}{N} \sum_{\mathbf{R}} V_{\mathbf{R},\alpha} e^{i(\mathbf{k}'-\mathbf{k})\cdot\mathbf{R}} \delta_{\alpha\beta}.$$

The average of  $V$  in this basis can be obtained from the statistics of the distribution

$$\begin{aligned} \overline{\langle \mathbf{k}, \alpha | V | \mathbf{k}', \beta \rangle} &= \frac{1}{N} \sum_{\mathbf{R}} \overline{V_{\mathbf{R},\alpha}} e^{i(\mathbf{k}'-\mathbf{k})\cdot\mathbf{R}} \delta_{\alpha\beta} \\ &= v_1 \frac{1}{N} \sum_{\mathbf{R}} e^{i(\mathbf{k}'-\mathbf{k})\cdot\mathbf{R}} \delta_{\alpha\beta} \\ &= v_1 \delta_{\mathbf{k},\mathbf{k}'} \delta_{\alpha\beta}. \end{aligned}$$

For the next applications, we're going to require the correlator of the disorder between two sites. Using the fact that the disorder is uncorrelated,

$$\overline{V_{\mathbf{R},\alpha} V_{\mathbf{R}',\beta}} = \begin{cases} v_2 & \text{if } \mathbf{R} = \mathbf{R}' \text{ and } \alpha = \beta \\ v_1^2 & \text{otherwise} \end{cases},$$

the average of a product of disorder operators becomes

$$\begin{aligned} \overline{\langle \mathbf{k}_1, \alpha_1 | V | \mathbf{k}_2, \alpha_2 \rangle \langle \mathbf{k}_3, \alpha_3 | V | \mathbf{k}_4, \alpha_4 \rangle} & \quad (3.5) \\ &= \frac{1}{N} (v_2 - v_1^2) \delta_{\mathbf{k}_2-\mathbf{k}_1, \mathbf{k}_3-\mathbf{k}_4} \delta_{\alpha_3\alpha_4} \delta_{\alpha_1\alpha_2} \delta_{\alpha_1\alpha_3} + v_1^2 \delta_{\mathbf{k}_2\mathbf{k}_1} \delta_{\alpha_1\alpha_2} \delta_{\mathbf{k}_3\mathbf{k}_4} \delta_{\alpha_3\alpha_4}. \end{aligned}$$

The first term is composed of the second cumulant and consists of a single restriction on the momenta, while the second term has two restrictions on the momenta. This specific form was due to the fact that the disorder is uncorrelated by construction.

Let's now look at what happens when some correlation is allowed. In general, if the disorder is correlated, then a correlation matrix has to be defined for all unit cells and orbitals:  $\overline{V_{\mathbf{R},\alpha} V_{\mathbf{R}',\beta}} = C_{\mathbf{R}\mathbf{R}'}^{\alpha\beta}$ . For the purposes of this thesis, however, we will only consider disorder which correlates different orbitals within the same unit cell, so we can consider the following, simpler correlation matrix:

$$\overline{V_{\mathbf{R},\alpha} V_{\mathbf{R}',\beta}} = \begin{cases} C_{\alpha\beta} & \text{if } \mathbf{R} = \mathbf{R}' \\ v_1^2 & \text{otherwise} \end{cases}.$$

With this in mind, the previous expression gets modified slightly to

$$\begin{aligned} & \overline{\langle \mathbf{k}_1, \alpha_1 | V | \mathbf{k}_2, \alpha_2 \rangle \langle \mathbf{k}_3, \alpha_3 | V | \mathbf{k}_4, \alpha_4 \rangle} \\ &= \frac{1}{N} (C_{\alpha_1 \alpha_3} - v_1^2 \delta_{\alpha_1 \alpha_3}) \delta_{\mathbf{k}_2 - \mathbf{k}_1, \mathbf{k}_3 - \mathbf{k}_4} \delta_{\alpha_3 \alpha_4} \delta_{\alpha_1 \alpha_2} + v_1^2 \delta_{\mathbf{k}_2, \mathbf{k}_1} \delta_{\mathbf{k}_3, \mathbf{k}_4} \delta_{\alpha_1 \alpha_2} \delta_{\alpha_3 \alpha_4}. \end{aligned} \quad (3.6)$$

The only difference relative to the previous expression is the presence of  $C_{\alpha_1 \alpha_3}$  instead of  $v_2 \delta_{\alpha_1 \alpha_3}$ . The existence of this correlation may be a mechanism behind disorder-enabled processes by activating off-diagonal matrix elements of the self-energy. This will be useful to understand the structure of the self-energy matrix in section 3.7.2.

### 3.3.2 Correlators with impurity disorder

For the purposes of this subsection, let's define impurity disorder as a set of  $N_I$  sites  $\Omega_I = \{\mathbf{R}_i : i = 1, \dots, N_I\}$  in the lattice which have a different value for the local energy than the rest of the lattice. The disordered operator  $V$  for this kind of disorder is

$$V = \sum_{\alpha} \sum_{\mathbf{R}_i \in \Omega_I} \varepsilon_{i, \alpha} |\mathbf{R}_i, \alpha\rangle \langle \mathbf{R}_i, \alpha|$$

where the sum is over all impurity sites  $\mathbf{R}_i$  and orbital degrees of freedom within that site. Each configuration of disorder consists of a different set of  $N_I$  impurity sites  $\Omega'_I$  (see top row of Fig. 3.4).

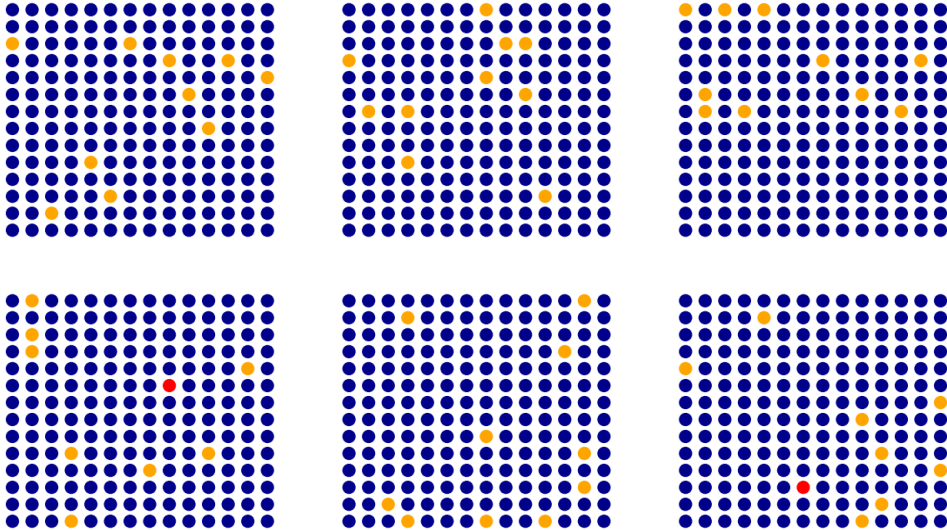


Figure 3.4: Different configurations of mutually exclusive impurities (top row) and non-mutually exclusive impurities (bottom row) in a square lattice. Sites in yellow (red) have local energy  $\varepsilon$  ( $2\varepsilon$ ). The remaining sites have local energy zero.

For the sake of generality, we can allow hoppings between orbitals in the impurity sites,

### 3 Diagrammatics in disordered systems

defining the more general operator

$$V = \sum_{\alpha\beta} \sum_{\mathbf{R}_i \in \Omega_I} h_{\alpha\beta} |\mathbf{R}_i, \alpha\rangle \langle \mathbf{R}_i, \beta|.$$

Defining the structure factor

$$\varrho_{\mathbf{q}} = \frac{1}{N} \sum_{\mathbf{R}_i \in \Omega_I} e^{i\mathbf{q} \cdot \mathbf{R}_i},$$

we express the matrix element in momentum space as

$$\langle \mathbf{k}, \alpha | V | \mathbf{k}', \beta \rangle = h_{\alpha\beta} \frac{1}{N} \sum_{\mathbf{R}_i \in \Omega_I} e^{i(\mathbf{k}' - \mathbf{k}) \cdot \mathbf{R}_i} = h_{\alpha\beta} \varrho_{\mathbf{k}' - \mathbf{k}}.$$

Consequently, it becomes clear that  $\varrho$  is the object that needs to be averaged over. The averaging procedure is done by averaging over all possible positions for the  $N_I$  impurities and therefore it is important to understand exactly how this is done. The first option is to force there to be exactly  $N_I$  impurities in the lattice which cannot be in the same place (top row of Fig. 3.4). The second option is to lift this restriction and allow impurities to be in the same position. If these impurities consist of a change to local energies, then two impurities in the same place would each contribute with an identical change to the local energy, doubling it (bottom row of Fig. 3.4). If  $n = N_I/N$  is the concentration of impurities, this is a correction proportional to  $n^2$ , but it could become relevant when higher-order processes are taken into account. In the case of vacancies, which in many cases can be assumed to be infinite local energies, this would be essentially the same as having a variable number of vacancies. For illustrative purposes, let's calculate the average of  $\varrho_{\mathbf{q}}$  and  $\varrho_{\mathbf{q}}\varrho_{\mathbf{q}'}$  in both situations.

#### Mutually exclusive impurities

If the impurities are not allowed to be in the same position, then this imposes a restriction  $\mathbf{R}_1 \neq \mathbf{R}_2 \neq \dots \neq \mathbf{R}_{N_I}$ . The average that needs to be evaluated is

$$\overline{\varrho_{\mathbf{q}}} = \frac{\frac{1}{N_I!} \sum_{\mathbf{R}_1 \neq \mathbf{R}_2 \neq \dots \neq \mathbf{R}_{N_I}} \frac{1}{N} [e^{i\mathbf{q} \cdot \mathbf{R}_1} + e^{i\mathbf{q} \cdot \mathbf{R}_2} + \dots + e^{i\mathbf{q} \cdot \mathbf{R}_{N_I}}]}{\frac{1}{N_I!} \sum_{\mathbf{R}_1 \neq \mathbf{R}_2 \neq \dots \neq \mathbf{R}_{N_I}} 1}$$

where the sum  $\sum_{\mathbf{R}_1 \neq \mathbf{R}_2 \neq \dots \neq \mathbf{R}_{N_I}}$  stands for a  $N_I$  individual sums over unit cells  $\mathbf{R}_1, \dots, \mathbf{R}_{N_I}$  such that  $\mathbf{R}_1 \neq \mathbf{R}_2 \neq \dots \neq \mathbf{R}_{N_I}$ . The denominator is simply the number of combinations of  $N_I$  objects in  $N$  slots

$$\frac{1}{N_I!} \sum_{\mathbf{R}_1 \neq \mathbf{R}_2 \neq \dots \neq \mathbf{R}_{N_I}} = \frac{N(N-1) \dots (N-N_I+1)}{N_I!} = \frac{N!}{N_I!(N-N_I)!}.$$

The numerator simplifies because every term in the sum of exponentials will contribute identically (this can be seen by rearranging the indices)

$$\frac{1}{N_I!} \sum_{\mathbf{R}_1 \neq \mathbf{R}_2 \neq \dots \neq \mathbf{R}_{N_I}} \frac{1}{N} [e^{i\mathbf{q} \cdot \mathbf{R}_1} + e^{i\mathbf{q} \cdot \mathbf{R}_2} + \dots + e^{i\mathbf{q} \cdot \mathbf{R}_{N_I}}] = \frac{N_I}{N} \frac{1}{N_I!} \sum_{\mathbf{R}_1 \neq \mathbf{R}_2 \neq \dots \neq \mathbf{R}_{N_I}} e^{i\mathbf{q} \cdot \mathbf{R}_1}$$

so all that is left is to separate the sum over  $\mathbf{R}_1$  from the rest. Fixing  $\mathbf{R}_1$ , there will be  $N - 1$  slots to put the remaining  $N_I - 1$  objects, so the expression becomes

$$\frac{1}{N_I!} \sum_{\mathbf{R}_1 \neq \mathbf{R}_2 \neq \dots \neq \mathbf{R}_{N_I}} e^{i\mathbf{q} \cdot \mathbf{R}_1} = \frac{(N - 1)!}{N_I! (N - N_I)!} \sum_{\mathbf{R}_1} e^{i\mathbf{q} \cdot \mathbf{R}_1} = \frac{N!}{N_I! (N - N_I)!} \delta_{\mathbf{q}, \mathbf{0}}.$$

Putting it all together, the average of  $\varrho_{\mathbf{q}}$  is proportional to the concentration of impurities:

$$\overline{\varrho_{\mathbf{q}}} = \frac{\frac{1}{N_I!} \frac{N_I}{N} \delta_{\mathbf{q}, \mathbf{0}} \frac{N!}{(N - N_I)!}}{\frac{N!}{N_I! (N - N_I)!}} = \frac{N_I}{N} \delta_{\mathbf{q}, \mathbf{0}} = n \delta_{\mathbf{q}, \mathbf{0}}.$$

Next, we need to calculate the first correlator  $\overline{\varrho_{\mathbf{q}} \varrho_{\mathbf{q}'}}$  following the same ideas. The result is

$$\overline{\varrho_{\mathbf{q}} \varrho_{\mathbf{q}'}} = \frac{n}{N} (1 - n) \delta_{\mathbf{q} + \mathbf{q}', \mathbf{0}} + n^2 \delta_{\mathbf{q}, \mathbf{0}} \delta_{\mathbf{q}', \mathbf{0}}, \quad (3.7)$$

which is valid in the thermodynamic limit  $N_I, N \gg 1$ .

### Non mutually exclusive impurities

Assuming that multiple impurities can occupy the same place, the calculation is slightly different, but simpler. The sums over positions are now unrestricted

$$\overline{\varrho_{\mathbf{q}}} = \frac{\sum_{\mathbf{R}_1} \dots \sum_{\mathbf{R}_{N_I}} \frac{1}{N} [e^{i\mathbf{q} \cdot \mathbf{R}_1} + e^{i\mathbf{q} \cdot \mathbf{R}_2} + \dots + e^{i\mathbf{q} \cdot \mathbf{R}_{N_I}}]}{\sum_{\mathbf{R}_1} \dots \sum_{\mathbf{R}_{N_I}} 1}.$$

The denominator immediately becomes  $N^{N_I}$  and the numerator is calculated in a similar fashion. All the exponentials contribute in the same way, and the sums can now be factored

$$\begin{aligned} & \sum_{\mathbf{R}_1} \dots \sum_{\mathbf{R}_{N_I}} \frac{1}{N} [e^{i\mathbf{q} \cdot \mathbf{R}_1} + e^{i\mathbf{q} \cdot \mathbf{R}_2} + \dots + e^{i\mathbf{q} \cdot \mathbf{R}_{N_I}}] \\ &= N^{N_I - 1} \frac{N_I}{N} \sum_{\mathbf{R}_1} e^{i\mathbf{q} \cdot \mathbf{R}_1} \\ &= N^{N_I - 1} \frac{N_I}{N} N \delta_{\mathbf{q}, \mathbf{0}} \\ &= N^{N_I} n \delta_{\mathbf{q}, \mathbf{0}}. \end{aligned}$$

### 3 Diagrammatics in disordered systems

Putting it together, we get the same result as before

$$\overline{\varrho_{\mathbf{q}}} = \frac{N^{N_I} n \delta_{\mathbf{q}, \mathbf{0}}}{N^{N_I}} = n \delta_{\mathbf{q}, \mathbf{0}}.$$

However, the similarities end here, because the correlator  $\overline{\varrho_{\mathbf{q}} \varrho_{\mathbf{q}'}}$  has a slight difference

$$\overline{\varrho_{\mathbf{q}} \varrho_{\mathbf{q}'}} = \frac{n}{N} \delta_{\mathbf{q}+\mathbf{q}', \mathbf{0}} + n^2 \delta_{\mathbf{q}, \mathbf{0}} \delta_{\mathbf{q}', \mathbf{0}}. \quad (3.8)$$

Comparing eqs. 3.7 and 3.8, we note that when impurities cannot be in the same position, the correlator is affected by a correction of order  $n^2$ . If one is only interested in results which are correct up to linear order in  $n$ , then this difference is irrelevant. Such is the case for the T-matrix approximation, which will be discussed later in section 3.5.3. However, if higher orders in  $n$  are required, then this difference has to be considered. This would affect, for example, the self-consistent T-matrix approximation.

With this in mind, here are the lowest-order contributions to all the correlators:

$$\begin{aligned} \overline{\varrho_{\mathbf{q}_1}} &= n \delta_{\mathbf{q}_1, \mathbf{0}} \\ \overline{\varrho_{\mathbf{q}_1} \varrho_{\mathbf{q}_2}} &= \frac{n}{N} \delta_{\mathbf{q}_1 + \mathbf{q}_2, \mathbf{0}} + \mathcal{O}(n^2) \\ \overline{\varrho_{\mathbf{q}_1} \varrho_{\mathbf{q}_2} \varrho_{\mathbf{q}_3}} &= \frac{n}{N^2} \delta_{\mathbf{q}_1 + \mathbf{q}_2 + \mathbf{q}_3, \mathbf{0}} + \mathcal{O}(n^2) \\ &\dots \\ \overline{\varrho_{\mathbf{q}_1} \dots \varrho_{\mathbf{q}_M}} &= \frac{n}{N^{M-1}} \delta_{\mathbf{q}_1 + \dots + \mathbf{q}_M, \mathbf{0}} + \mathcal{O}(n^2). \end{aligned} \quad (3.9)$$

These will be useful when evaluating the T-matrix approximation. Finally, let's see what the product of disorder matrix elements look like after averaging over impurity positions. The average of one matrix element is

$$\overline{\langle \mathbf{k}_1, \alpha_1 | V | \mathbf{k}_2, \alpha_2 \rangle} = h_{\alpha_1 \alpha_2} \overline{\varrho_{\mathbf{k}_1 - \mathbf{k}_2}} = h_{\alpha_1 \alpha_2} n \delta_{\mathbf{k}_1, \mathbf{k}_2}$$

and the average of the product of two matrix elements is

$$\begin{aligned} &\overline{\langle \mathbf{k}_1, \alpha_1 | V | \mathbf{k}_2, \alpha_2 \rangle \langle \mathbf{k}_3, \alpha_3 | V | \mathbf{k}_4, \alpha_4 \rangle} \\ &= h_{\alpha_1 \alpha_2} h_{\alpha_3 \alpha_4} \left[ \frac{n}{N} (1 - n) \delta_{\mathbf{k}_2 - \mathbf{k}_1, \mathbf{k}_3 - \mathbf{k}_4} + n^2 \delta_{\mathbf{k}_1, \mathbf{k}_2} \delta_{\mathbf{k}_3, \mathbf{k}_4} \right]. \end{aligned} \quad (3.10)$$

Comparing with the previous case of Anderson disorder, the average of disorder matrix elements 3.6, we see that the general structure is still the same: there is a term which imposes  $\mathbf{k}_2 - \mathbf{k}_1 = \mathbf{k}_3 - \mathbf{k}_4$  and another which imposes  $\mathbf{k}_2 = \mathbf{k}_1$  and  $\mathbf{k}_3 = \mathbf{k}_4$ . The particular numerical prefactors depend on the type of disorder and on the presence of correlations. It is worthwhile to notice that none of the numerical prefactors to the Kronecker deltas depends on  $\mathbf{k}$ . This happened because we chose the disorder not to connect different unit cells. Were this not the case, an additional momentum dependency would exist. Therefore,

for the remainder of this chapter, we will keep assuming that the average of products of matrix elements follows the form

$$\overline{\langle \mathbf{k}_1, \alpha_1 | V | \mathbf{k}_2, \alpha_2 \rangle} = A_{\alpha_1 \alpha_2} \delta_{\mathbf{k}_1, \mathbf{k}_2}$$

for one single matrix element of  $V$ ,

$$\begin{aligned} & \overline{\langle \mathbf{k}_1, \alpha_1 | V | \mathbf{k}_2, \alpha_2 \rangle \langle \mathbf{k}_3, \alpha_3 | V | \mathbf{k}_4, \alpha_4 \rangle} \\ &= \frac{1}{N} B_{\alpha_1 \alpha_2 \alpha_3 \alpha_4} \delta_{\mathbf{k}_2 - \mathbf{k}_1, \mathbf{k}_3 - \mathbf{k}_4} + A_{\alpha_1 \alpha_2} A_{\alpha_3 \alpha_4} \delta_{\mathbf{k}_1, \mathbf{k}_2} \delta_{\mathbf{k}_3, \mathbf{k}_4} \end{aligned}$$

for the product of two, and so on. This form will be assumed for any operator  $V$  used in the remainder of this chapter. The specific form of the objects  $A$  and  $B$  will be the only difference between them.

### 3.3.3 Diagrammatic representation

Now that we know how to evaluate the correlators, let's go back to the disorder average of the expansion of the full Green's function (eq. 3.4). The first term is trivial, but the second term of this expression becomes

$$\begin{aligned} \langle \mathbf{k}, \alpha | g \bar{V} g | \mathbf{k}', \beta \rangle &= \sum_{\alpha_1 \alpha_2} g_{\alpha \alpha_1}(\mathbf{k}) \overline{\langle \mathbf{k}, \alpha_1 | V | \mathbf{k}', \alpha_2 \rangle} g_{\alpha_2 \beta}(\mathbf{k}') \\ &= \sum_{\alpha_1 \alpha_2} g_{\alpha \alpha_1}(\mathbf{k}) [A_{\alpha_1 \alpha_2} \delta_{\mathbf{k}, \mathbf{k}'}] g_{\alpha_2 \beta}(\mathbf{k}) \end{aligned}$$

which is diagonal in  $\mathbf{k}$ -space in virtue of the disorder average. The diagrammatic representation of this process is shown in diagram a2 of Fig. 3.5. When the disorder average is performed, the crosses become circles that connect several disorder insertions and the combinations of these connections represent all the possible correlations between operators. In this particular case, there is only one disorder operator and so no correlations exist between operators. The vertical line connecting the circle to the main horizontal line means that a term  $A_{\alpha_1 \alpha_2}$  representing the vertex is to be inserted into the equation in the middle of the two clean Green's functions and summed over its indices. The only momentum dependency of this object comes trivially from the external propagators  $g_{\alpha \alpha_1}(\mathbf{k})$  and  $g_{\alpha_2 \beta}(\mathbf{k})$ .

### 3 Diagrammatics in disordered systems

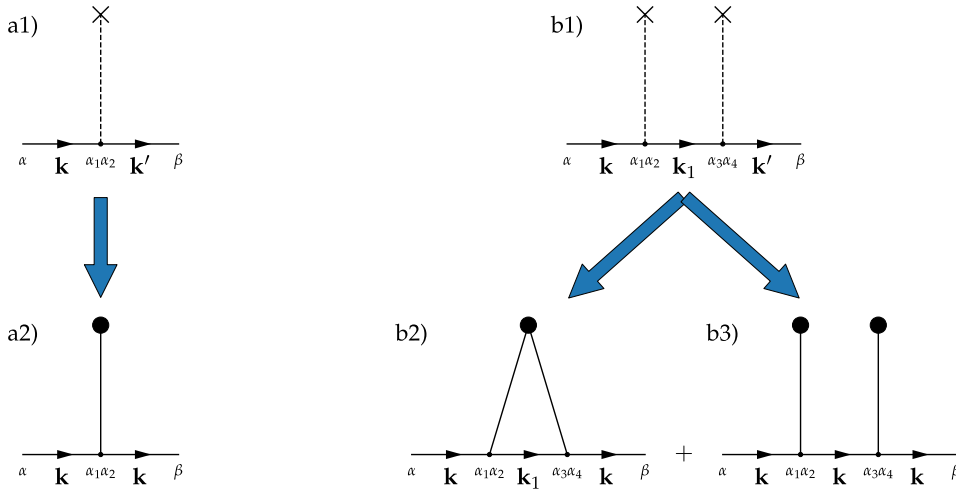


Figure 3.5: Diagrammatic representation of the process of disorder averaging with one disorder insertion (left) and two disorder insertions (right).

The next term in eq. 3.4 has a more interesting structure

$$\begin{aligned}
 & \langle \mathbf{k}, \alpha | g \overline{V} g \overline{V} g | \mathbf{k}', \beta \rangle \\
 &= \sum_{\alpha_1 \alpha_2 \alpha_3 \alpha_4} g_{\alpha \alpha_1}(\mathbf{k}) B_{\alpha_1 \alpha_2 \alpha_3 \alpha_4} \left( \frac{1}{N} \sum_{\mathbf{k}_1} g_{\alpha_2 \alpha_3}(\mathbf{k}_1) \right) g_{\alpha_4 \beta}(\mathbf{k}) \\
 &+ \sum_{\alpha_1 \alpha_2 \alpha_3 \alpha_4} g_{\alpha \alpha_1}(\mathbf{k}) A_{\alpha_1 \alpha_2} g_{\alpha_2 \alpha_3}(\mathbf{k}) A_{\alpha_3 \alpha_4} g_{\alpha_4 \beta}(\mathbf{k})
 \end{aligned}$$

and accordingly, its diagrammatic representation (shown in diagrams b2 and b3 of Fig. 3.5) is more complex than the previous case. As before, the disorder average is represented by turning the crosses into circles, but the correlations are now represented by the way in which the dashed lines connect to each other. The second term in the expression above is represented by diagram b3, with the same interpretation as in diagram a2. Since the term factors into a product of terms, the diagram is called *reducible*, meaning that it can be pictorially separated into two diagrams like a2 by “cutting” it in the middle.

The first term of the expression above correlates two disordered operators, and therefore its diagram (b2) connects the two lines. The circle going into two lines gives rise to a term  $B_{\alpha_1 \alpha_2 \alpha_3 \alpha_4}$  which is to be summed over all its indices. This forms an internal loop which represents the integral over  $\mathbf{k}_1$ . Unlike the other diagram, this one cannot be factorized, and is called a *one-particle irreducible* diagram.

Note that, like before, all the momentum dependency for this term comes trivially from the external propagators. This time, there is also a different momentum label inside the expression, but since it is integrated over, it becomes independent of momentum.

Higher-order terms follow a similar pattern, and all the possible correlations are obtained

by combining the crosses into circles in all possible ways. Different kinds of disorder have different expressions for the vertices (that is, different forms for the objects  $A$ ,  $B$ , etc), but the diagrams all have the same structure.

Finally, some of the diagrams simplify, because if  $\overline{V} = 0$ , then all the diagrams with circles which only have one line coming out of them will not contribute. If the average of an odd product of  $V$  operators is zero, all the diagrams with an odd number of lines coming out of the circles will also be zero. Such is the case for Anderson disorder, but not for dilute impurities or vacancies.

### 3.3.4 Fourth order diagrams

Diagrammatics allows us to do calculations in systems with disorder through objects defined in momentum space. The diagrams discussed so far are particularly easy to calculate, but if we keep going to higher orders, we will come across diagrams which provide a serious challenge. For example, the disorder average of the fourth order term

$$\langle \mathbf{k}, \alpha | \overline{VgVgVgV} | \mathbf{k}', \beta \rangle \quad (3.11)$$

produces several subterms with different correlations between the  $V$ , just as happened for the second order case. For simplicity, let's assume that we're dealing with Anderson disorder and all the odd moments of the disorder distribution are zero. Figure 3.6 shows all the nonzero diagrams in this case.

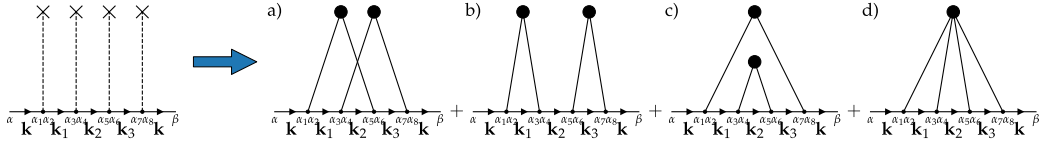


Figure 3.6: Diagrams appearing in fourth order when the odd moments are zero.

Diagrams b), c) and d) have an easy expression to calculate, but diagram a) is special. Its expression is

$$\begin{aligned} \text{Diagram a)} &= \sum_{\alpha_1 \dots \alpha_8} B_{\alpha_1 \alpha_2 \alpha_5 \alpha_6} B_{\alpha_3 \alpha_4 \alpha_7 \alpha_8} g_{\alpha \alpha_1}(\mathbf{k}) \times \\ &\times \frac{1}{N^2} \sum_{\mathbf{k}_1} \sum_{\mathbf{k}_3} g_{\alpha_1 \alpha_2}(\mathbf{k}_1) g_{\alpha_4 \alpha_5}(\mathbf{k}_3 + \mathbf{k}_1 - \mathbf{k}) g_{\alpha_6 \alpha_7}(\mathbf{k}_3) g_{\alpha_8 \beta}(\mathbf{k}) \end{aligned}$$

which involves two sums, and the summand depends explicitly on  $\mathbf{k}$ . This is a manifestation of the two lines crossing and the impossibility of untangling them. These integrals cannot be factorized, making this a potentially complicated term to evaluate. For large momenta and energies, this diagram (and crossing diagrams like it) is negligible [13], but it can play

### 3 Diagrammatics in disordered systems

a big role at low energies as we will see later. For the kinds of disorder that are being considered in this thesis, this diagram represents the lowest-order instance of a nontrivial momentum dependency on the disorder-averaged Green's function. The trivial momentum dependency comes from the external propagators  $g_{\alpha\alpha_1}(\mathbf{k})$  and  $g_{\alpha_8\beta}(\mathbf{k})$ , which is always present in every diagram, but the explicit momentum dependency on  $\mathbf{k}$  inside the summand is responsible for a nontrivial contribution.

This momentum dependency means that the summand has to be evaluated once for every single value of  $\mathbf{k}$  that we want to analyze. Furthermore, the double sum over momenta makes this a rather heavy calculation. Spectral methods can offer an alternative way to compute this diagram by making explicit use of the correlation between operators.

## 3.4 Diagrammatics with spectral methods

To get the previous expression with spectral methods, we need to evaluate eq. 3.11 while making sure that the first disorder operator only correlates with the third and that the second disorder operator only correlates with the fourth. To achieve this, define the operators  $V$  and  $V'$ , taken from the same distribution. Then, evaluating the average  $\overline{gVgV'gVgV'g}$  automatically produces the desired correlations. The diagram can be evaluated at each individual  $\mathbf{k}$  as such:

$$\text{Diagram a)} = \langle \mathbf{k}, \alpha | \overline{VgV'gVgV'} | \mathbf{k}, \beta \rangle$$

and averaging over realizations of disorder  $V$  and  $V'$ .

In a similar spirit, other contributions can be estimated in the same way, simply by changing the positions of the  $V'$  and  $V$  operators. In practice, though, the other contributions do not require a double sum over the momenta, and so it is not useful to pursue this method. One exception to this is diagram 3.6d), which correlates all four operators. It can be obtained indirectly by using  $V$  everywhere and subtracting the other terms:

$$\overline{VgVgVgV} - \overline{VgV'gVgV'} - \overline{V'gV'gVgV} - \overline{V'gVgVgV'}.$$

However, if one wants to go to higher order terms, things can get very complicated easily and so it becomes imperative to find more efficient ways to proceed. This is the purpose of the next section.

## 3.5 Self-energy and approximation techniques

The expansion of  $\overline{G(z)}$  in powers of  $V$  can be carried out to any desired order given enough computational time, but there are better ways of summing this series. The first point to notice is that there is a lot of redundancy in calculations of the previous sections. Many terms can in fact be factorized by looking just at the irreducible diagrams. These form the self-energy  $\Sigma(z)$ . It is the sum of all one-particle irreducible diagrams without external

propagators, represented in Fig. 3.7 a). Then, the exact disorder-averaged Green's function  $\overline{G}(z)$  can be expressed as a sum over these objects as in Fig. 3.7 b). This is no more than a reordering of the series of  $\overline{G}(z)$ .

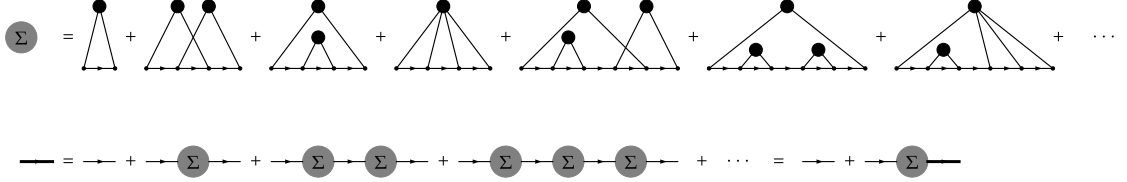


Figure 3.7: Self-energy operator (a) as a sum of one-particle irreducible diagrams, and the disorder-averaged Green's function as a sum over self-energy operators (b). Note that these diagrams do not have the external propagators.

Mathematically, this can be seen as a self-consistent equation (the explicit dependency of  $\Sigma$  on  $z$  has been omitted, in conformity with  $g$  and  $G$ )

$$\overline{G} = g + g\Sigma g + g\Sigma g\Sigma g + \dots = g + g\Sigma\overline{G}$$

which can be formally summed as a geometric series:

$$\overline{G} = g \frac{1}{\mathbf{1} - \Sigma g} = \frac{1}{g^{-1} - \Sigma}.$$

It then becomes clear that the real part of  $\Sigma$  is responsible for the shift of the original Green's function's poles and the imaginary part is responsible for their broadening. This gives direct access to the quasiparticles' lifetimes and herein lies the usefulness of the self-energy operator.

For the reasons stated in the beginning of section 3.2, the average over disorder also renders the self-energy diagonal in  $\mathbf{k}$ -space. Therefore, the previous equation can be written in the subspace spanned by the subbasis  $|\mathbf{k}, \alpha\rangle$ , for all  $\alpha$ :

$$\overline{G}(\mathbf{k}, z) = \frac{1}{z\hat{\mathbf{1}} - H_0(\mathbf{k}) - \Sigma(\mathbf{k}, z)},$$

where  $H_0(\mathbf{k})$  is the momentum representation of the translation invariant part of the Hamiltonian,  $H_0$  and all these three objects are understood to be matrices in this subspace of momentum  $\mathbf{k}$ .

By construction, each term of  $\Sigma$  that has been calculated translates into an infinite series of terms calculated for  $\overline{G}$ . By doing approximations on  $\Sigma$  instead of on  $\overline{G}$  directly, we get a much better and more efficient approximation for  $\overline{G}$ . In the following subsections, a few useful approximation schemes will be described before showing a way to compute  $\Sigma$  exactly.

### 3.5.1 Born approximation

The simplest and most used approximation is the Born approximation, which consists of keeping just the triangle diagram (Fig. 3.8 a)).

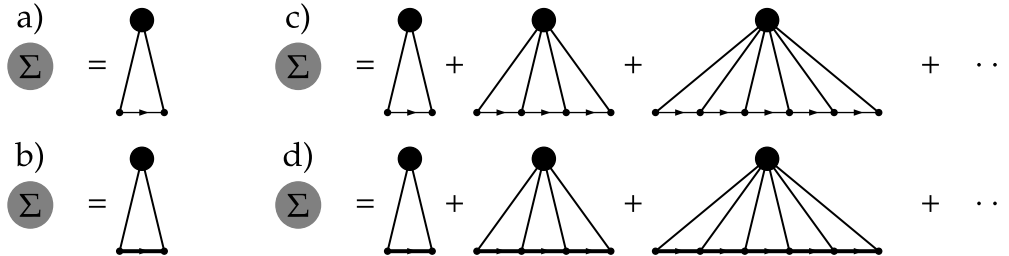


Figure 3.8: a) Born approximation (BA), b) Self-consistent Born approximation (SCBA), c) T-matrix approximation (TMA) and d) self-consistent T-matrix approximation (SCTMA). The thin lines with arrows represent the clean Green's function  $g$  and the thick lines with arrows the disorder-averaged complete Green's function  $\bar{G}$ .

The expression for the self-energy under the Born approximation is

$$\Sigma_{\alpha\beta}^{\text{BA}}(\mathbf{k}, z) = \langle \mathbf{k}, \alpha | \overline{Vg(z)V} | \mathbf{k}, \beta \rangle = A_{\alpha\beta} \frac{1}{N} \sum_{\mathbf{k}_1} g_{\alpha\beta}(\mathbf{k}_1, z). \quad (3.12)$$

In the case of Anderson disorder with zero mean, (with  $A_{\alpha\beta} = v_2 \delta_{\alpha\beta}$  for uncorrelated disorder and  $A_{\alpha\beta} = C_{\alpha\beta}$  for correlated disorder), this approximation is actually the lowest order approximation to the self-energy. We can see immediately that correlation is responsible for activating the nondiagonal elements of the disorder self-energy, at least at the level of the Born approximation.

For the case of dilute impurities and vacancies, or a type of disorder with  $\bar{V} \neq 0$ , the lowest order term would actually be just a single circle with one line coming out. This term may possess some matrix structure, but no momentum or energy dependency, and is just usually ignored. While this is justified when it has a scalar structure (as its real part can be absorbed into the definition of the Fermi energy), this is not the case for a more general structure. In any case, this term is not included in the Born approximation - that is reserved for the triangle diagram.

### 3.5.2 Self-consistent Born approximation

A much better approximation can be done by choosing a specific subset of diagrams for the self-energy, the nonintersecting diagrams that only have two lines coming out of each circle, corresponding to ignoring higher-order correlators. This is represented in Fig. 3.8 b) as a self-consistent equation. The Green's function used in this self-energy is the one determined by this self-energy, thus establishing a self-consistent equation to determine

both  $\Sigma$  and  $\overline{G}$ :

$$\overline{G}^{\text{SCBA}}(\mathbf{k}, z) = \frac{1}{z\hat{\mathbf{1}} - H_0(\mathbf{k}) - \Sigma^{\text{SCBA}}(\mathbf{k}, z)} \quad (3.13)$$

and

$$\Sigma_{\alpha\beta}^{\text{SCBA}}(\mathbf{k}, z) = A_{\alpha\beta} \frac{1}{N} \sum_{\mathbf{q}} \overline{G}_{\alpha\beta}^{\text{SCBA}}(\mathbf{q}, z). \quad (3.14)$$

This is the self-consistent Born approximation (SCBA). Even though there is a momentum label in the self-energy operator of the two previous equations, it actually does not depend on  $\mathbf{k}$ , as the momentum of the disorder-averaged Green's function is being integrated. Therefore, eqs. 3.13 and 3.14 can be solved simultaneously by replacing 3.14 in 3.13, and repeating the procedure to convergence. This procedure takes into account every single diagram which does not have crossings or higher-order correlators.

### 3.5.3 T-matrix

The T-matrix approximation (TMA) consists of the sum of all single-impurity scattering diagrams and is a very good approximation in the dilute limit. In fact, it is exact in the limit of a single impurity. Perturbatively, it is the linear order term in the impurity concentration  $n$ . Diagrammatically, this is represented in Fig. 3.8 c) as a sum over all diagrams with just one circle. In some particular cases, it is possible to find a closed form expression for the T-matrix. Such is the case for dilute impurities. To see this, let's begin by writing the T-matrix self-energy  $\Sigma^{\text{T}}$  as a sum of one-impurity diagrams (the diagrams with just one circle, denoted by an overline with a T)

$$\Sigma_{\alpha\beta}^{\text{T}}(\mathbf{k}, z) = \langle \mathbf{k}, \alpha | \overline{V}^{\text{T}} | \mathbf{k}, \beta \rangle + \langle \mathbf{k}, \alpha | \overline{VgV}^{\text{T}} | \mathbf{k}, \beta \rangle + \dots$$

As we have seen in sec 3.3.2, the average falls onto the structure factor  $\varrho$ . Defining  $\hat{h}$  as the operator constructed from  $h_{\alpha\beta}$  (the hoppings associated with the impurity) as

$$h_{\alpha\beta} = \langle \mathbf{k}, \alpha | \hat{h} | \mathbf{k}', \beta \rangle,$$

the T-matrix approximation can be expressed as

$$\Sigma_{\alpha\beta}^{\text{T}}(\mathbf{k}, z) = \langle \mathbf{k}, \alpha | \hat{h} | \mathbf{k}', \beta \rangle \overline{\varrho_0}^{\text{T}} + \sum_{\mathbf{q}} \langle \mathbf{k}, \alpha | \hat{h}g(\mathbf{q}) \hat{h} | \mathbf{k}', \beta \rangle \overline{\varrho_{\mathbf{q}-\mathbf{k}}\varrho_{\mathbf{k}-\mathbf{q}}}^{\text{T}} + \dots$$

The structure factors we need were already specified in eq. 3.9, and when the sum of the momenta is zero  $\mathbf{q}_1 + \dots + \mathbf{q}_M = 0$  (such as in this case), they simplify to

$$\overline{\varrho_{\mathbf{q}_1} \dots \varrho_{\mathbf{q}_M}}^{\text{T}} = \frac{n}{N^{M-1}}$$

### 3 Diagrammatics in disordered systems

and so the expression for the self-energy simplifies

$$\begin{aligned}\Sigma_{\alpha\beta}^T(\mathbf{k}, z) &= \langle \mathbf{k}, \alpha | \hat{h} | \mathbf{k}, \beta \rangle n + \langle \mathbf{k}, \alpha | \hat{h} \left[ \frac{1}{N} \sum_{\mathbf{q}} g(\mathbf{q}) \right] \hat{h} | \mathbf{k}', \beta \rangle n + \\ &+ \langle \mathbf{k}, \alpha | \hat{h} \left[ \frac{1}{N} \sum_{\mathbf{q}} g(\mathbf{q}) \right] \hat{h} \left[ \frac{1}{N} \sum_{\mathbf{q}} g(\mathbf{q}) \right] \hat{h} | \mathbf{k}', \beta \rangle n + \dots\end{aligned}$$

Because of the sums over internal momenta  $\mathbf{q}$ , the operator  $\sum_{\mathbf{q}} g(\mathbf{q})$  does not depend on the momentum. For notational simplicity, let  $\hat{\mathcal{G}} = \frac{1}{N} \sum_{\mathbf{q}} g(\mathbf{q})$ . then, the self-energy takes the form

$$\Sigma_{\alpha\beta}^T(\mathbf{k}, z) = n \langle \mathbf{k}, \alpha | \hat{h} \left( \hat{\mathbf{1}} + \hat{\mathcal{G}}\hat{h} + \left( \hat{\mathcal{G}}\hat{h} \right)^2 + \dots \right) | \mathbf{k}, \beta \rangle$$

which can be summed as a harmonic series

$$\Sigma_{\alpha\beta}^T(\mathbf{k}, z) = n \langle \mathbf{k}, \alpha | \hat{h} \frac{1}{\hat{\mathbf{1}} - \hat{\mathcal{G}}\hat{h}} | \mathbf{k}, \beta \rangle.$$

Just like in the previous sections, the self-energy does not depend on  $\mathbf{k}$ . Under certain circumstances, assuming that  $\hat{h}$  is very large and invertible, the previous equation becomes

$$\Sigma_{\alpha\beta}^T(\mathbf{k}, z) = -n \langle \mathbf{k}, \alpha | \hat{\mathcal{G}}^{-1} | \mathbf{k}, \beta \rangle. \quad (3.15)$$

This typically happens when  $\hat{h}$  represents vacancies. Finally, note that by replacing  $g$  with the disorder-averaged Green's function determined by the TMA, we can get an even better approximation, the self-consistent T-matrix approximation (SCTMA)). The SCTMA takes into account every single diagram without crossings.

#### 3.5.4 T-matrix in graphene with vacancies

In order to apply the previous section to graphene with vacancies, one extra step needs to be done. In a tight-binding description, graphene can be described in terms of two sublattices, and there can be vacancies in either of them. This does not fit the previous framework well, but it can be fixed at the level of the first order in the concentration of vacancies. Consider  $V_A$  ( $V_B$ ) to be the operator which describes vacancies in sublattice  $A$  ( $B$ ). In this description, vacancies are expressed as local impurities with a very large local energy  $\varepsilon \gg 1$ :

$$V_A = \sum_{\mathbf{R}_i \in \Omega_A} \varepsilon | \mathbf{R}_i, A \rangle \langle \mathbf{R}_i, A |$$

where the sum is over the set  $\Omega_A$  of unit cells which have vacancies in the sublattice  $A$ .  $V_B$  has an identical definition. Then, the full Hamiltonian is

$$H = H_0 + V_A + V_B.$$

The fact that two operators are required instead of just one makes the analysis slightly more complicated. Just like in sec. 3.3.2, define the structure factors for the impurities in each sublattice:

$$\begin{aligned}\varrho_{\mathbf{q}}^A &= \frac{1}{N} \sum_{\mathbf{R}_i \in \Omega_A} e^{i\mathbf{q} \cdot \mathbf{R}_i} \\ \varrho_{\mathbf{q}}^B &= \frac{1}{N} \sum_{\mathbf{R}_i \in \Omega_B} e^{i\mathbf{q} \cdot \mathbf{R}_i}.\end{aligned}$$

The vacancies' positions in different sublattices are uncorrelated, so that automatically means that  $\overline{\varrho_{\mathbf{q}}^B \varrho_{\mathbf{q}'}^A} = \overline{\varrho_{\mathbf{q}}^B} \overline{\varrho_{\mathbf{q}'}^A}$  and also that  $\overline{V_A V_B} = \overline{V_A} \overline{V_B}$ . Let  $n_A$  ( $n_B$ ) be the concentration of vacancies in sublattice  $A$  ( $B$ ). To keep the computation of  $\Sigma_T$  to first order in the concentration of vacancies, we can never get a product of  $\overline{V_A}$  and  $\overline{V_B}$ . Each of these would be proportional to  $n_A$  and  $n_B$ , respectively, and if both are comparable, then this would be of order  $n_A^2$ . This means that in a term like

$$\langle \mathbf{k}, \alpha | \overline{V g V^T} | \mathbf{k}, \beta \rangle = \langle \mathbf{k}, \alpha | \overline{(V_A + V_B) g (V_A + V_B)^T} | \mathbf{k}, \beta \rangle,$$

the only surviving terms to first order are

$$\langle \mathbf{k}, \alpha | \overline{V_A g V_A^T} | \mathbf{k}, \beta \rangle + \langle \mathbf{k}, \alpha | \overline{V_B g V_B^T} | \mathbf{k}, \beta \rangle.$$

The same can be said of any term, so in fact we get a separate T-matrix approximation for each sublattice:

$$\Sigma_{\alpha\beta}^T(\mathbf{k}, z) = n_A \langle \mathbf{k}, A | \epsilon \frac{1}{\mathbf{1} - \hat{\mathcal{G}}_\epsilon} | \mathbf{k}, A \rangle \delta_{\alpha A} \delta_{\beta A} + n_B \langle \mathbf{k}, B | \epsilon \frac{1}{\mathbf{1} - \hat{\mathcal{G}}_\epsilon} | \mathbf{k}, B \rangle \delta_{\alpha B} \delta_{\beta B}.$$

Considering  $n_A = n_B = n$  and letting  $\epsilon \rightarrow \infty$ , we get a very simple formula for the T-matrix

$$\Sigma_{\alpha\beta}^T(\mathbf{k}, z) = -n \langle \mathbf{k}, A | \hat{\mathcal{G}}^{-1} | \mathbf{k}, A \rangle \delta_{\alpha A} \delta_{\beta A} - n \langle \mathbf{k}, B | \hat{\mathcal{G}}^{-1} | \mathbf{k}, B \rangle \delta_{\alpha B} \delta_{\beta B}.$$

Because the matrix elements are identical, the formula simplifies even further:

$$\Sigma_{\alpha\beta}^T(\mathbf{k}, z) = -n \langle \mathbf{k}, A | \hat{\mathcal{G}}^{-1} | \mathbf{k}, A \rangle \delta_{\alpha\beta}. \quad (3.16)$$

Therefore, we find that the T-matrix approximation for the self-energy in graphene is a diagonal matrix. As we will learn in the next section, this is not the complete picture. The T-matrix approximation is a very powerful tool, but it is only able to capture one subset of diagrams.

### 3.5.5 A different T-matrix for graphene

Upon reading these previous four sections, the reader might come under the impression that the approximations existing in the literature are incapable of dealing with a  $\mathbf{k}$ -dependent self-energy. This is the case for the purposes of this thesis because all the disorder types considered here make it so, but this is not the case in general. If the disorder connects different unit cells, then a momentum dependency automatically appears.

One particularly interesting case is an alternate way to describe vacancies. Instead of a very high local energy, vacancies can also come from removing all the hoppings to a given site. In practice, this translates to a disordered operator with symmetrical hoppings to those of the clean Hamiltonian  $H_0$ , which when summed to  $H_0$ , puts those hoppings to zero. Since this can connect different unit cells, a  $\mathbf{k}$ -dependency appears already at the level of the Born approximation. For practical purposes, though, this also makes it more difficult to find a closed form expression for the T-matrix approximation. Another point that has to be kept in mind is the fact that this kind of description cannot be accurate to higher order in the concentration of vacancies.

To understand this, imagine the effect of putting two of these vacancies together. Then, all the hoppings to those sites get cancelled out except the ones that connect the two sites, which get subtracted twice. The result is a set of two sites connected among themselves but isolated from the rest of the lattice. The probability of this happening is of order  $n^2$ . Furthermore, if several disorder sites are allowed to sit in the same place like in section 3.3.2, then the hoppings get subtracted several times and this no longer describes a vacancy. This is also an effect of order  $n^2$ .

## 3.6 Exact calculation of the self-energy operator

Up until this point, the self-energy has been calculated with resort to a diagrammatic expansion, which at best can provide the sum of an infinite subset of diagrams, but a complete sum of all the diagrams is hopeless. In particular, crossing diagrams are notoriously difficult to calculate because of the multiple integrals over the FBZ. Furthermore, all the popular techniques described so far fail to capture any kind of  $\mathbf{k}$  dependency on the self-energy. In order to better understand the processes (diagrams) which are relevant or not, it is important to have a more flexible approach to getting the self-energy, with which we can compare the approximations above. In order to do this, we have to go back to the definition of the self-energy:

$$\Sigma(\mathbf{k}, z) = g^{-1}(\mathbf{k}, z) - \overline{G(\mathbf{k}, z)}^{-1}.$$

The first term  $g^{-1}(\mathbf{k}, z)$  is simply  $z - H_0(\mathbf{k})$ , but the second has to be done with care. Starting with the exact Green's function, with disorder included, we begin by evaluating

it in the subspace of momentum  $\mathbf{k}$

$$\langle \mathbf{k}, \alpha | G(z) | \mathbf{k}, \beta \rangle. \quad (3.17)$$

At this point, it should be pointed out that  $G$  is not diagonal in  $\mathbf{k}$ -space, and so inverting the matrix in this subspace is meaningless. However, averaging over disorder, we know that translation invariance is recovered, and so  $\overline{G(\mathbf{k}, z)}$  is diagonal and can be inverted safely within this  $\mathbf{k}$ -subspace. To achieve this goal, one can evaluate eq. 3.17 for a given realization of disorder, and then repeat the process for other configurations until the average converges to desired precision. Under these circumstances, the direct matrix inversion of the matrix 3.17 is justified.

Alternatively, instead of performing many averages over disorder, one may use larger systems. This has two advantages: 1) mitigates finite-size effects and 2) reduces statistical fluctuations of the underlying process of evaluating the exact Green's function. At first, it may be unclear why this self-averaging property exists, but we justify it through a thorough convergence analysis later on and an analytical proof for a few particular cases, which can be found in the appendix 8.1.

### 3.6.1 Numerical procedure

In this section, more detail is given about the numerical procedure used to calculate the exact self-energy operator, highlighting some important aspects along the way. We begin by using the CPGF method to expand the full Green's function as a series of Chebyshev polynomials

$$G(z) = \sum_{n=0}^{\infty} g_n(z) T_n(H)$$

where the expression for  $g_n$  is found in section 2.16. Recall that a small but finite  $\eta$  is required for numerical convergence. The smaller the  $\eta$ , the more Chebyshev polynomials are required for convergence. Then, evaluate all the matrix elements  $\alpha\beta$  for a given  $\mathbf{k}$ . This defines the matrix  $G(\mathbf{k}, \mathbf{k})$  in the  $\mathbf{k}$ -subspace, as defined previously. Each of these matrix elements has to be calculated individually through this Chebyshev expansion, and the corresponding Chebyshev moments are codified in the momenta matrix  $\mathcal{T}(\mathbf{k}, n)$ , defined as  $\mathcal{T}_{\alpha\beta}(\mathbf{k}, n) = \langle \mathbf{k}, \alpha | T_n(H) | \mathbf{k}, \beta \rangle$

$$G_{\alpha\beta}(\mathbf{k}, \mathbf{k}) = \sum_{n=0}^{\infty} g_n(z) \langle \mathbf{k}, \alpha | T_n(H) | \mathbf{k}, \beta \rangle = \sum_{n=0}^{\infty} g_n(z) \mathcal{T}_{\alpha\beta}(\mathbf{k}, n). \quad (3.18)$$

or, more compactly,

$$G(\mathbf{k}, \mathbf{k}) = \sum_{n=0}^{\infty} g_n(z) \mathcal{T}(\mathbf{k}, n). \quad (3.19)$$

### 3 Diagrammatics in disordered systems

Starting with  $|\mathbf{k}, \beta\rangle$ , all the higher-order moments can be calculated through the Chebyshev recursion

$$\begin{aligned} |\mathbf{k}, \beta, 1\rangle &= T_1(H) |\mathbf{k}, \beta\rangle = H |\mathbf{k}, \beta\rangle \\ |\mathbf{k}, \beta, n+1\rangle &= T_n(H) |\mathbf{k}, \beta\rangle = 2H |\mathbf{k}, \beta, n\rangle - |\mathbf{k}, \beta, n-1\rangle \end{aligned}$$

As each  $|\mathbf{k}, \beta, n\rangle$  is calculated, a whole column of  $\mathcal{T}(\mathbf{k}, n)$  can be obtained at once by projecting this vector into every  $\langle \mathbf{k}, \alpha|$ . This has to be repeated for every  $\beta$ . Therefore, for a unit cell with  $N_o$  orbitals, there are  $N_o^2$  matrix elements to be calculated, but only  $N_o$  operations are required. Even though this method is closely related to the stochastic trace evaluation (STE) as discussed in 2.6, there are no random vectors here. The only source of randomness comes from the realization of disorder. It is very important to make sure that the same realization of disorder is used for every matrix element of  $\mathcal{T}(\mathbf{k}, n)$ . Otherwise, the self-energy matrix will have a much larger error bar.

Once  $\mathcal{T}(\mathbf{k}, n)$  has been calculated for every  $n$ , the matrix elements of the Green's function can be reconstructed using eq. 3.18. Then, the process is repeated for several realizations of disorder to get  $\overline{G(\mathbf{k}, z)}$  and the self-energy is directly obtained by inverting it:

$$\Sigma(\mathbf{k}, z) = z - H_0(\mathbf{k}) - \overline{G(\mathbf{k}, z)}^{-1}.$$

If the system possesses self-averaging properties, then  $\overline{G(\mathbf{k}, z)}$  is very well approximated by  $G(\mathbf{k}, \mathbf{k})$ , that is to say that only one average is required to get a satisfactory result. Consequently, instead of performing averages over disorder, one can instead spend the computational effort into simulating larger systems. Besides mitigating finite-size effects, this has the added bonus of further decreasing the error bar. All the cases studied in this chapter possess this property.

Before showing the power of this method and its applications to some interesting physical problems, it is important to keep in mind some considerations on convergence.

#### 3.6.2 Considerations on convergence

The process of subtracting  $\overline{G(\mathbf{k}, z)}^{-1}$  from  $g^{-1}$  can yield a very small result if the disorder is weak. This means that any imprecision in calculating  $G(\mathbf{k}, \mathbf{k})$  can propagate towards a big imprecision in  $\Sigma(\mathbf{k}, z)$ . A careful convergence analysis is therefore warranted for every self-energy operator that is calculated. The main points to keep in mind are the following:

1. For a given  $\eta$ , the number of polynomials used must be enough to ensure the complete convergence of not just  $G$  but also  $\Sigma$ . Even if  $G$  seems completely converged,  $\Sigma$  might not be because of the propagation of small imprecisions. This is why in the examples shown below, a convergence analysis was performed on  $\Sigma$  and not  $G$ .
2. For self-averaging systems, it has to be checked that the system is sufficiently large for the self-averaging to take place. When this happens, we expect the error bar of

$\Sigma$  to be proportional to  $D^{-1/2}$ , where  $D$  is the size of the Hilbert space.

3. The small broadening  $\eta$  has to be sufficiently small for  $G(z)$  to accurately represent the exact Green's function, for  $\eta = 0^\pm$ . As we will see in the next examples, this is not always an easy task and  $G(z)$  might not be an accurate representation across the entire spectrum.

### 3.7 Self-energy in SRO

As a first application of the exact calculation of the self-energy operator, it's important to compare it against the known approximation schemes [5]. The model should have a sufficiently complicated band structure for the matrix structure of the self-energy to become relevant.

We expect the exact calculation to match the approximation schemes for weak disorder, but to deviate from them when disorder becomes sufficiently strong. For this purpose, we chose to analyze the self-energy matrix of the spin-polarized two-dimensional electron gas that is formed in SrRuO<sub>3</sub> embedded in a SrTiO<sub>3</sub> [108] matrix (see Fig. 3.9) due to the effect of 1) Anderson disorder and 2) vacancies.

The complex oxide perovskite SrRuO<sub>3</sub> (also known as SRO) [109, 110] has been studied extensively for the last fifty years, having originated well over one thousand papers on the subject by now. It is chemically inert and is one of the oxide materials with the highest conductivity, but it is especially famous for its itinerant ferromagnetism and unusual transport properties without the need for doping.

At the same time, the prospect of two-dimensional ferromagnetic conductors whose properties can be activated by magnetic and electric fields has led to considerable interest in this area. Even though SRO loses its ferromagnetic properties when its thickness goes below three unit cells, it has been proposed [111, 112] and subsequently experimentally verified [108] that an atomically thin layer of SRO embedded in a SrTiO<sub>3</sub> matrix can display these properties.

Despite the theoretical and experimental advances, the role of disorder in this complex interfacial behavior remains essentially unexplored. In what follows, we analyze the effect of vacancies and Anderson disorder by modeling the emergent two-dimensional electron gas with a first-principles parameterized multi-orbital TB model, as found in the supplementary material of [113]. The lattices used had dimensions  $4096 \times 4096$ , and 16384 Chebyshev

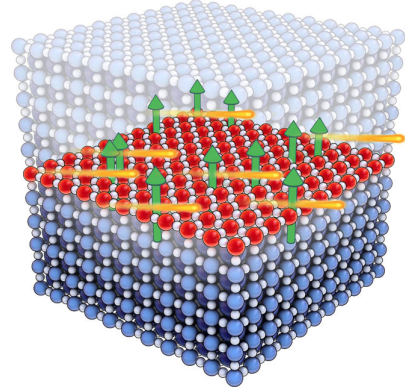


Figure 3.9: SrRuO<sub>3</sub> embedded in a SrTiO<sub>3</sub> matrix.

polynomials were used for all the simulations.

### 3.7.1 Tight-binding Hamiltonian and band structure

The underlying lattice for this model is a square lattice, which supports a six-orbital tight-binding Hamiltonian comprising of the spinful 4d orbitals of Ru in the SRO layer. This Hamiltonian is composed of four terms:

$$H = H_1 + H_2 + H_3 + H_4.$$

The first term represents the nearest neighbor interaction in the  $x$  and  $y$  directions, separately,

$$H_1 = \sum_{a,\sigma,\langle ij \rangle_x} t^{a,x} d_{ia\sigma}^\dagger d_{ja\sigma} + \sum_{a,\sigma,\langle ij \rangle_y} t^{a,y} d_{ia\sigma}^\dagger d_{ja\sigma},$$

with  $t^{1,x} = t^{2,y} = t_2$ ,  $t^{2,x} = t^{3,x} = t^{1,y} = t^{3,y} = t_1$ . The operator  $d_{ia\sigma}^\dagger$  creates an electron in site  $i$  orbital  $a$  ( $yz = 1$ ,  $xz = 2$ ,  $xy = 3$ ) and spin  $\sigma$ . The notation  $\langle i, j \rangle_{x(y)}$  indicates nearest neighbors in the  $x$  ( $y$ ) direction. The second term

$$H_2 = \sum_{a,b,\sigma,\langle\langle i,j \rangle\rangle} f_{ij}^{ab} d_{ia\sigma}^\dagger d_{jb\sigma} + \sum_{a,\sigma,\langle\langle i,j \rangle\rangle} g^a d_{ia\sigma}^\dagger d_{ja\sigma}$$

represents the second-nearest-neighbor interaction with  $g^1 = g^2 = t_3$ ,  $g^3 = t_4$  and  $f_{ij}^{12} = f_{ij}^{21} = f$  if  $i$  and  $j$  are along a diagonal and  $f_{ij}^{12} = f_{ij}^{21} = -f$  if they are along an anti-diagonal. The terms  $H_3$  and  $H_4$  represent the Zeeman interaction and spin-orbit coupling (SOC), respectively, with the following expressions:

$$\begin{aligned} H_3 &= -m \sum_{a,\sigma,i} \tau_{\sigma\sigma}^z d_{ia\sigma}^\dagger d_{ia\sigma} \\ H_4 &= i\lambda \sum_{a,\sigma,\sigma',i} \varepsilon^{abc} \tau_{\sigma\sigma'}^c d_{ia\sigma}^\dagger d_{ia\sigma'}. \end{aligned}$$

Here,  $m$  is the amplitude of the Zeeman interaction,  $\lambda$  is the amplitude of the SOC,  $\tau^i$  is a Pauli matrix and  $\varepsilon^{abc}$  is the Levi-Civita symbol. The SOC term was calculated by evaluating the matrix elements  $\hat{\mathbf{L}} \cdot \hat{\mathbf{S}}$  in the angular momentum basis with  $\ell = 2$  restricted to the Cartesian set  $xy, xz, yz$ .

In momentum space, the Hamiltonian is [114]

$$H = \sum_{\mathbf{k}} \left[ \varepsilon_{\mathbf{k}\sigma}^a \delta_{ab} \delta_{\sigma\sigma'} + f_{\mathbf{k}}^{ab} \delta_{\sigma\sigma'} + i\lambda \varepsilon^{abc} \tau_{\sigma\sigma'}^c \right] d_{\mathbf{k}a\sigma}^\dagger d_{\mathbf{k}b\sigma}$$

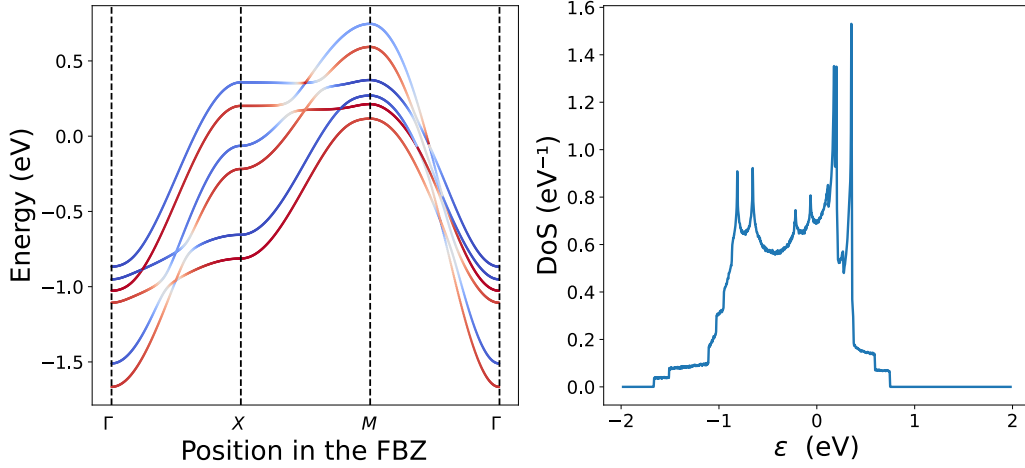


Figure 3.10: Band structure (left) and density of states (right) of SRO.

where

$$\begin{aligned}
\varepsilon_{\mathbf{k}\sigma}^{1=yz} &= -2t_1 \cos(k_y) - 2t_2 \cos(k_x) - 4t_3 \cos(k_x) \cos(k_y) - m\tau_{\sigma\sigma}^z \\
\varepsilon_{\mathbf{k}\sigma}^{2=xz} &= -2t_1 \cos(k_x) - 2t_2 \cos(k_y) - 4t_3 \cos(k_x) \cos(k_y) - m\tau_{\sigma\sigma}^z \\
\varepsilon_{\mathbf{k}\sigma}^{3=xy} &= -2t_1 (\cos(k_x) + \cos(k_y)) - 4t_4 \cos(k_x) \cos(k_y) - m\tau_{\sigma\sigma}^z \\
f_{\mathbf{k}}^{12} &= -4f \sin(k_x) \sin(k_y) \\
f_{\mathbf{k}}^{21} &= f_{\mathbf{k}}^{12}
\end{aligned}$$

This model possesses a rich band structure. In Fig. 3.10, the band structure is shown along the path  $\Gamma XM\Gamma$ . In the absence of SOC, nodal loops are formed when the minority and majority bands intersect. The majority and minority spin bands are hybridized when SOC is included, leading to a modulation of the equilibrium  $\mathbf{k}$ -space spin-polarization density and an enhanced Berry curvature near the avoided anti-crossings [115].

### 3.7.2 Anderson disorder

The first model of disorder under consideration is Anderson disorder. The on-site energies  $\varepsilon_i$  for every orbital in each unit cell are taken from a uniform distribution of average 0 and width  $W$ .

In other words, this means that the on-site disorder is locally correlated since the local energies are identical for all the  $4d$  orbitals within each unit cell, but different among different unit cells. This puts us exactly in the situation of section 3.3.1, where the Anderson correlator is given by eq. 3.6. Every matrix element of the correlation matrix  $C_{\alpha\beta}$  becomes identical to the second moment of the box distribution and so has the simple form  $C_{\alpha\beta} = v_2$  for all  $\alpha, \beta = 1, \dots, 6$ . At the level of the Born approximation 3.12

$$\Sigma_{\alpha\beta}^{\text{BA}}(\mathbf{k}, z) = v_2 \frac{1}{N} \sum_{\mathbf{q}} g_{\alpha\beta}(\mathbf{q})$$

### 3 Diagrammatics in disordered systems

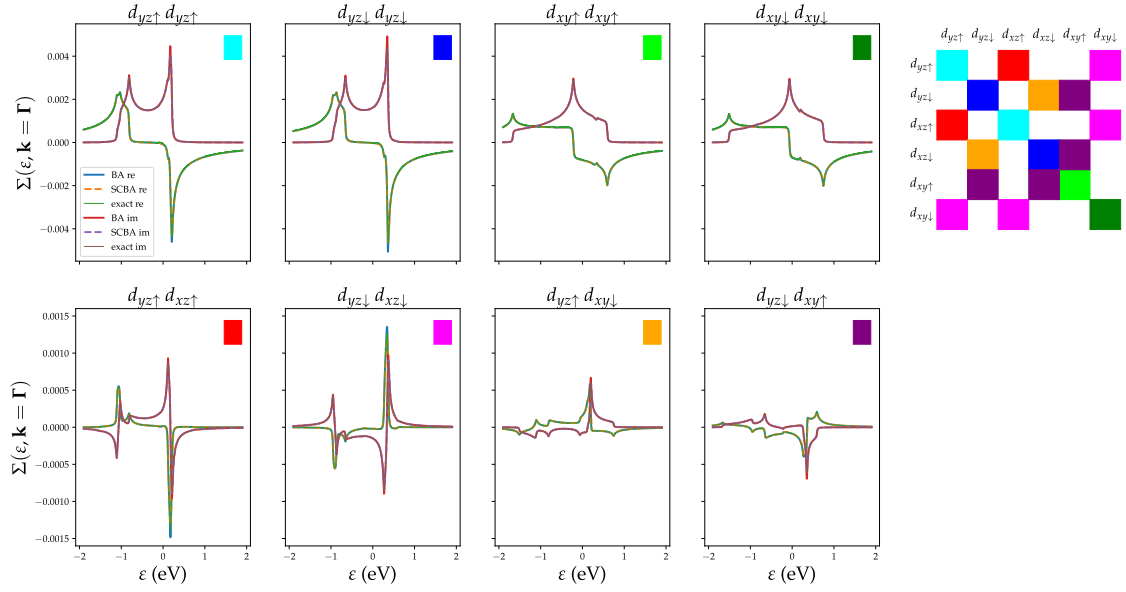


Figure 3.11: Independent matrix elements of the self-energy operator for weak correlated Anderson disorder of strength  $W = 0.1\text{eV}$  in SRO. Each matrix element is color coded. The complete matrix is displayed on the right. Matrix elements with the same color are related to each other by a factor of  $1, -1, i$  or  $-i$ .

we expect all matrix elements to be allowed, but only those stemming from the matrix structure of the clean Green's function will appear. In this section, and the next, what is represented is the self-energy as a function of the energy  $\varepsilon$ , not the complex variable  $z = \varepsilon + i\eta$ . Figure 3.11 shows the matrix elements of the disorder self-energy for weak disorder  $W = 0.1\text{eV}$  evaluated at the  $\mathbf{k} = \Gamma$  point, compared with the Born approximation (BA) and the self-consistent Born approximation (SCBA). The agreement is perfect for every matrix element, showing that the exact calculation of the self-energy is able to reproduce the self-energy obtained by diagrammatic approximations. The energy resolution is set to  $\eta = 1\text{meV}$  and excellent spectral convergence is reached at 16384 Chebyshev polynomials. These results challenge conventional wisdom, which considers the self-energy as a scalar:  $\Sigma \approx -i\Gamma$ . Not only is it not a scalar, it is not even diagonal. The direct access to the full matrix structure allows one to make more controlled approximations to this operator.

Increasing the  $W$  to  $0.5\text{eV}$ , some deviations to the BA and SCBA should start to appear. The BA is only valid up to order  $W^2$ , but the SCBA is nonperturbative. It contains diagrams up to any order, but already fails to capture two of the three diagrams at order  $W^4$ . Therefore, we expect the SCBA to be a better, despite limited, approximation.

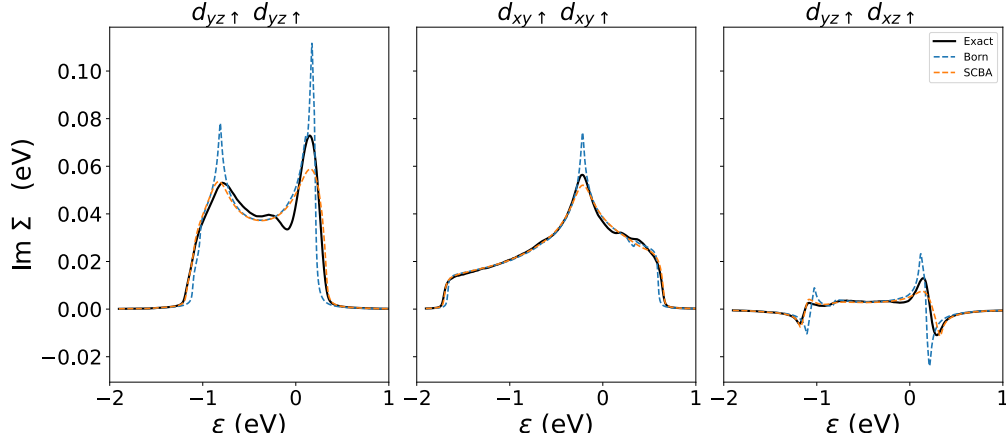


Figure 3.12: Three selected matrix elements of the self-energy operator for stronger correlated Anderson disorder of strength  $W = 0.5$  eV in SRO. The other matrix elements have been omitted for clarity, and the self-energy matrix still follows the same structure as in Fig. 3.11.

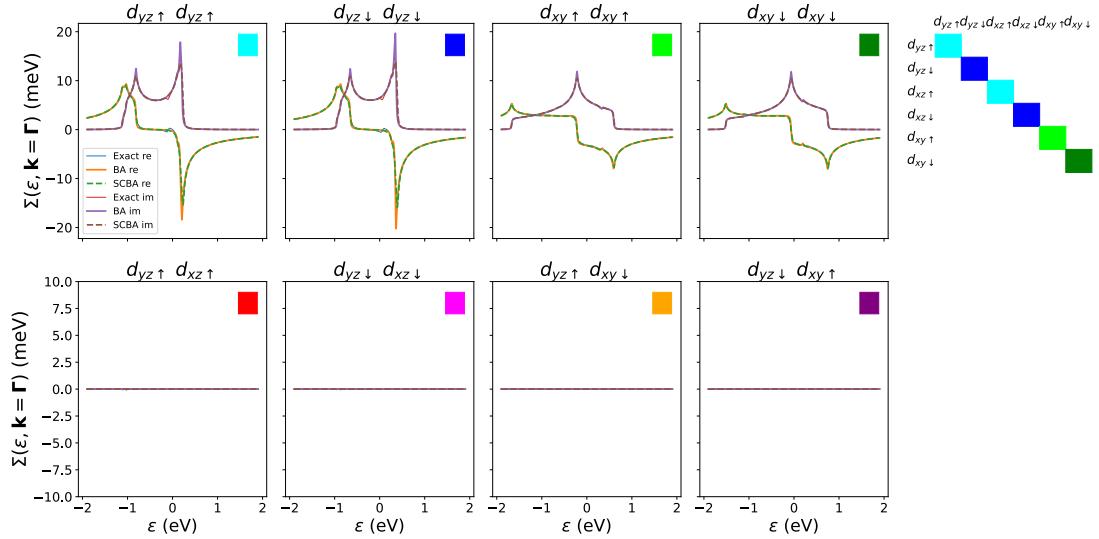


Figure 3.13: Independent matrix elements of the self-energy operator for uncorrelated Anderson disorder  $W = 0.2$  eV in SRO.

Looking at Fig. 3.12, the SCBA does in fact seem to provide a better approximation, but it is not able to capture the finer details of the exact self-energy such as the dip close to  $\varepsilon = 0$ . Ultimately, all methods still agree reasonably well on a quantitative scale.

Next, let's try a different kind of Anderson disorder. This time, the on-site energies are also uncorrelated among different orbitals, which results in a correlation matrix  $C_{\alpha\beta} = \delta_{\alpha\beta}v_2$ . At the level of the Born approximation, the self-energy is diagonal

$$\Sigma_{\alpha\beta}^{\text{BA}}(\mathbf{k}, z) = v_2 \delta_{\alpha\beta} \frac{1}{N} \sum_{\mathbf{q}} g_{\alpha\beta}(\mathbf{q}).$$

This is exactly what we see in the exact self-energy. Repeating the first analysis, we get Fig. 3.13. As predicted from section 3.3.1, only the diagonal matrix elements are nonzero. This was only proven at the level of the Born approximation, but the pattern seems to hold even at stronger disorders, which is indicative of a deeper connection.

### 3.7.3 Vacancies

Vacancies can be thought of as very strong correlated impurities. When a lattice site is vacant, then all the orbitals of that site disappear, so this kind of disorder correlates all the orbitals.

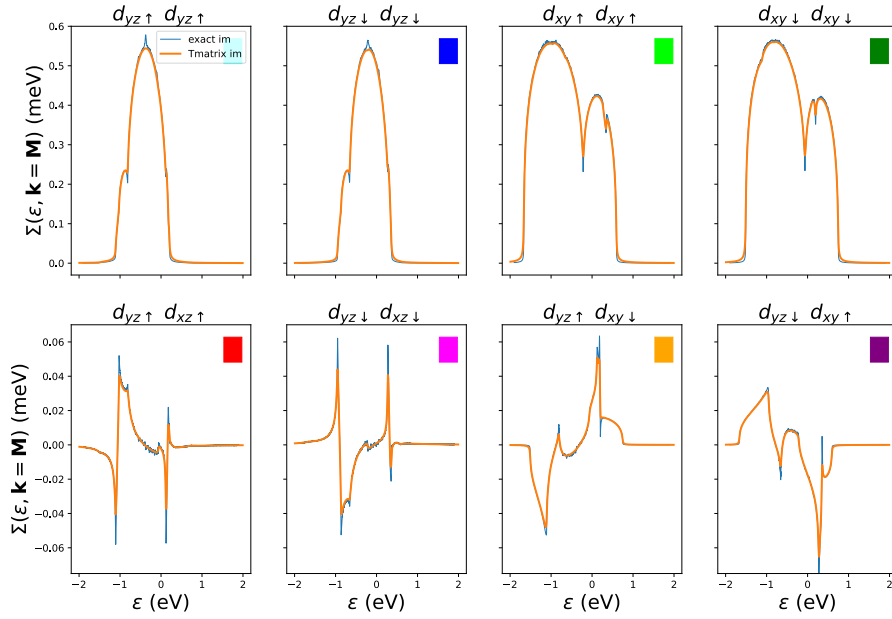


Figure 3.14: Independent matrix elements of the self-energy operator at  $\mathbf{k} = \mathbf{M}$  for a 0.1% concentration of vacancies in SRO.

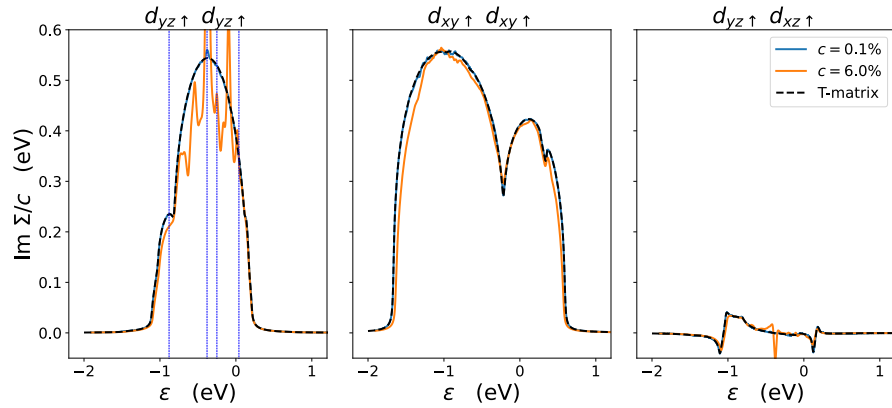


Figure 3.15: Comparison between the T-matrix approximation (normalized to the concentration of vacancies) and the exact self-energy operator for two concentrations of vacancies (0.1% and 6%) in SRO.

Just like the correlated Anderson disorder case, we expect there to be no restriction on the self-energy matrix elements. Since this is a kind of dilute disorder, the T-matrix approximation is the most natural approximation scheme for this case, and should provide a very good approximation when the concentration of vacancies is low.

In the language of section 3.5.3, vacancies can be expressed with  $h_{\alpha\beta} = \varepsilon\delta_{\alpha\beta}$  for a very large  $\varepsilon$ . This matrix is invertible, and so eq. 3.15 is valid. Figure 3.14 shows that the T-matrix is a fantastic approximation for small concentrations and the same matrix elements as before are activated, when correlated Anderson disorder was used.

When the concentration of impurities becomes sufficiently large, the T-matrix approximation starts to deviate significantly from the exact self-energy (Fig. 3.15). In broad terms, the self-energy is proportional to the concentration of impurities in accord with the T-matrix result, but at higher concentrations, we start to see discrepancies which scale as  $\sim c^{-1.4}$  near the peak (Fig. 3.16), which signals the onset of non-perturbative disorder corrections. We note that such peaks cannot be attributed to van Hove singularities because they are absent at low defect concentration and there is no correlation between the position of the peaks and the position of the singularities. We attribute them to resonances induced by multi-vacancy clusters, which only start to form at higher defect concentrations.

### 3.8 Self-energy in graphene with vacancies

This next example is one case where diagrammatics fail on a more fundamental level. Intuitively, the diagrammatic approach is expected to be valid for low concentrations of impurities/vacancies, where the self-energy is constant in the FBZ. What we will see in this section challenges this notion. In graphene, the self-energy is found to have a very strong momentum dependency and a nontrivial matrix structure, neither of which can be captured with any of the diagrammatic approaches discussed so far.

As a relatively new material, graphene has originated a flurry of research since its first successful isolation in 2004 [116–118]. The possibility of a condensed matter realization of two-dimensional Dirac fermions made graphene a strong candidate for a wide variety of exotic phenomena, such as Klein tunneling, the anomalous integer quantum Hall effect

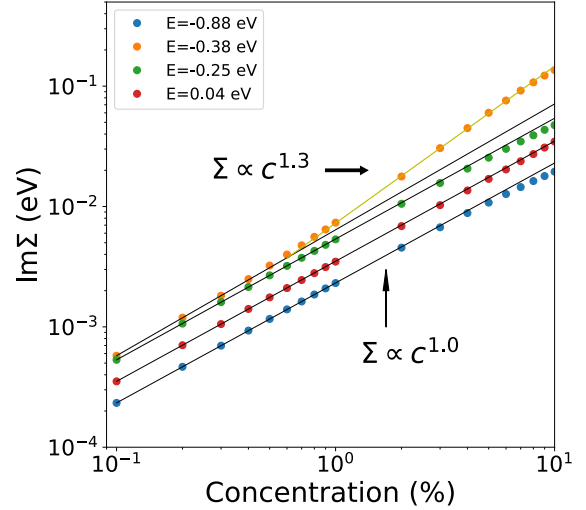


Figure 3.16:  $d_{yz\uparrow}d_{yz\uparrow}$  component of the self-energy as a function of concentration for several values of the energy in SRO (dotted lines in Fig. 3.15).

### 3 Diagrammatics in disordered systems

and exceptional higher-harmonic generation [117].

For these phenomena to be experimentally relevant, it is important to understand whether they are robust to defects, which arise naturally in the fabrication process. Vacancy defects in graphene are one particularly interesting kind of disorder to look at, because they preserve the sublattice symmetry of the lattice. Vacancies can arise directly from missing lattice sites, but effective vacancies also appear in other situations. For example, in graphene, an adsorbed hydrogen atom can increase the local potential so much that electrons no longer hop to that site. Adsorbed molecules can also bind chemically to the carbon atoms, changing the  $sp_2$  hybridization to  $sp_3$  and removing one  $p_z$  orbital from the  $p_z$  band which comprises the TB model of graphene [119, 120].

A lot of research has been done on the effect of vacancies in graphene [121], but of particular interest is the effect they have around the Dirac point. If the disorder is weak and preserves the chiral symmetry, this model represents a special universality class of the Anderson localization behavior, characterized by the existence of extended states at the band center accompanied by a divergence in the density of states [14, 15]. Vacancies are part of this class of disorder, but they cannot be considered to be weak scatterers. A nonperturbative analysis of the same model [122] finds that the low-energy DoS scaling predicted by Gade [14] gets modified from

$$\rho(\varepsilon) \sim \frac{1}{\varepsilon \exp(|\log(\varepsilon)|^{-1/x})}$$

to the stronger diverging

$$\rho(\varepsilon) \sim \frac{1}{\varepsilon \tau_n |\log(\varepsilon \tau_n)|^{3/2}}$$

at even lower energies. Here,  $\tau_n \sim 1/n$  is simply a time scale related to the vacancy concentration. Both these regimes have been verified numerically [16] and compared against the SCTMA. Concretely, the SCTMA allowed the evaluation of the self-energy in two specific limits in the continuum and predicts a scalar self-energy [123]

$$\text{Im}\Sigma(\varepsilon) \propto \begin{cases} \Gamma & \varepsilon \ll \Gamma \\ -n/|\varepsilon| \log(|\varepsilon|) & \varepsilon \gg \Gamma \end{cases}$$

where  $\Gamma = \Lambda \sqrt{-n/\log(n)}$ ,  $n$  is the concentration of vacancies and  $\Lambda$  is a cutoff. The SCTMA should provide a good approximation for large energies  $\varepsilon \gg \Gamma$  because the diagrams representing quantum coherent multiple scatterings are negligible in this regime [13]. Since the SCTMA ignores multi-impurity scattering events, quantum-interference processes are absent, and so it was unable to capture the DoS divergence when  $\varepsilon \ll \Gamma$ . One might wonder if the continuum approximation could be a limiting factor here, but an analysis using the exact lattice Green's functions does not change the qualitative picture as will be shown later on. This analysis shows that so far, a reliable way to capture quantum-interference processes with diagrammatics remained elusive.

From the transport point of view, these zero-energy modes (ZEM) are predicted to possess remarkable properties: their conductivity at zero temperature is independent of the concentration of vacancies and is equal to the universal value  $\sigma_0 = (4/\pi) e^2/h$  [94]. This striking property is just another piece of the puzzle which is the nature of the ZEM. The self-energy is an object of particular interest because it codifies the statistical properties of the disorder, and so it might provide clues into the nature and properties of the ZEM if the quantum interference processes are able to be included in it.

To tackle this problem with our method, we begin by specifying the graphene Hamiltonian

$$H = - \sum_{\langle i,j \rangle} t_{ij} c_i^\dagger c_j$$

where  $c_i^\dagger$  ( $c_i$ ) creates (removes) an electron at the  $i$ -th site and  $\langle i, j \rangle$  denotes nearest-neighbors. If both sites  $i$  and  $j$  are regular sites, then  $t_{ij} = t$ . If at least one of them is a vacancy, then  $t_{ij} = 0$ . Figure 3.17 shows the lattice setup. The red arrows are the primitive vectors and the highlighted blue diamond is the unit cell. The region inside the black dashed diamond represents the whole lattice, which is repeated with periodic boundary conditions. The lattices used for this section consist of systems with several millions of unit cells. With this model, we simply apply the prescription of section 3.6.1: we use CPGF to obtain the exact green's function and invert it to get the self-energy. All the ensuing graphs were produced with a lattice of  $10^7$  sites and a Green's function resolved with  $M = 65536$  Chebyshev polynomials, for a sub-meV resolution of  $\eta = 0.8$  meV.

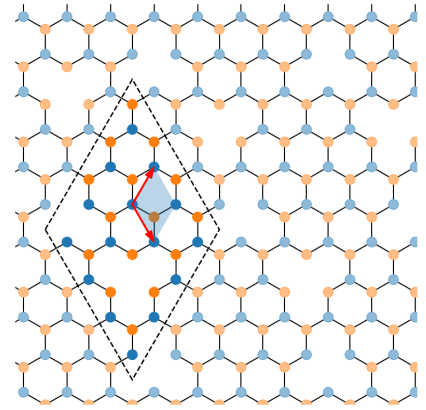


Figure 3.17: Graphene lattice with vacancies.

### 3.8.1 Self-energy

The self-energy was computed for several values of  $\mathbf{k}$ , specified by color in the FBZ depicted in Fig. 3.18. Panel a) represents the imaginary part of the low-energy  $AA$  component of the self-energy for a 0.3% vacancy concentration. Panel b) is the same, but for the  $AB$  component. The first striking feature here is the prominent momentum dependency. While the TM predicts a divergence, our method reveals that  $\Sigma$  appears bounded and surprisingly seems to go to zero at  $\varepsilon = 0$  at the Dirac point  $\mathbf{k} = \mathbf{K}$ , where the Gade singularity is located. The divergence is in fact a set of twin peaks. The second striking feature is the realization that  $\Sigma$  does not have a scalar structure, in disagreement to what the TM and SCTM predict. This rich structure is present for the majority of the FBZ, where both components are of comparable size, but near the Dirac point  $\Sigma$  becomes a scalar. Panels

### 3 Diagrammatics in disordered systems

c) and d) show the same qualitative picture still holds for a 1% vacancy concentration.

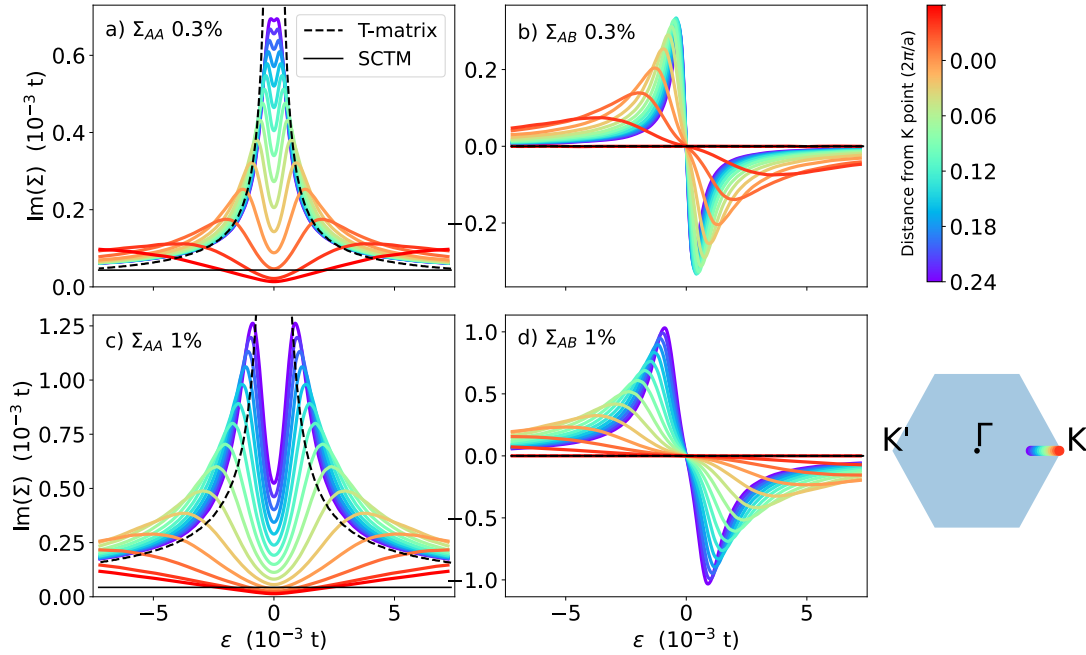


Figure 3.18: Components of the imaginary part of the self-energy operator as a function of energy for a vacancy concentration of 0.3% (top) and 1% (bottom) in graphene. Each color represents a different point in the Brillouin zone (bottom right hexagon). The T-matrix and the self-consistent T-matrix approximations are represented by black curves.

This rich behavior becomes even more interesting when one analyzes  $\Sigma$  as a function of the concentration at the Dirac point in Fig. 3.19. Instead of being proportional to the concentration (as a TMA would suggest), the self-energy instead displays a highly anomalous behavior with the concentration. The curves seem to be collapsing into one main curve as the concentration is increased. Remarkably,  $\Sigma$  approaches zero at  $\varepsilon = 0$ , regardless of the concentration (see next section for a scaling analysis). This exceedingly large quasiparticle lifetime in the long wavelength limit sheds new light into the “mysterious” ZEM resilience observed in large-scale simulations of the dc conductivity [94]. The last panel shows that the self-energy can be approximately collapsed into one curve by following the scaling law  $\Sigma(\varepsilon) = c^\alpha f(\varepsilon c^\alpha)$  with  $\alpha = 0.56 \pm 0.02$ .

This analysis suggests a classification into three regimes: 1) large energies, where the TMA provides an excellent approximation and  $\Sigma$  is  $\mathbf{k}$ -independent. 2), an intermediate region where  $\Sigma$  follows the scaling law and 3) the region near  $\varepsilon = 0$  where  $\Sigma$  is independent of the concentration. The anomalous behavior at zero energy coincides with the region with the strongest momentum variation, which seems to indicate that both effects stem from higher-order multi-impurity scattering processes. These are precisely the kinds of processes which cannot be captured by either the TMA or the SCTMA and which are typically ignored in the semiclassical limit where the crossing diagrams have a small contribution. In this case, they seem to be dominant.

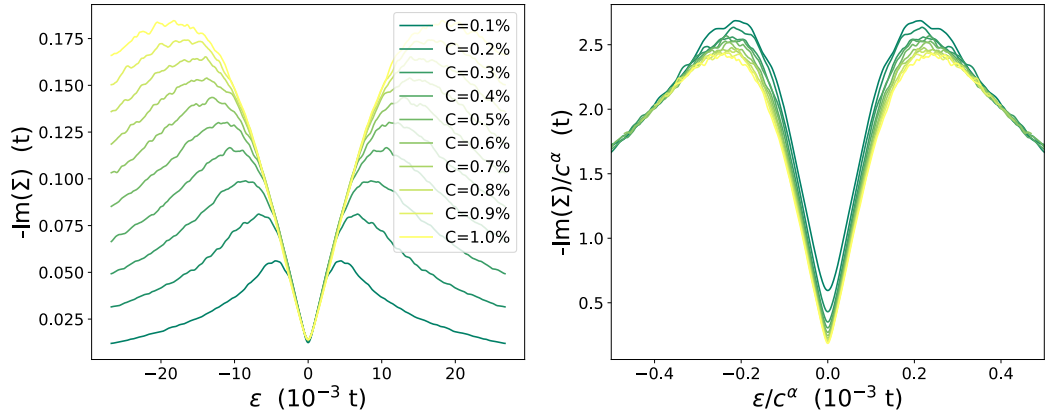


Figure 3.19: AA component of the imaginary part of the self-energy operator at the Dirac point for several concentrations in graphene. The right panel shows the collapsed self-energy matrix using the ansatz  $\Sigma(\epsilon) = c^\alpha f(\epsilon c^\alpha)$  with  $\alpha \approx 0.56$ .

### 3.8.2 Convergence study

As noted in section 3.6.2, it is important to ascertain the convergence of the self-energy matrix, and several factors have to be carefully assessed:

1. The phenomenological broadening  $\eta$  used for the numerical resolution of the Green's functions has to be as small as possible to accurately capture the singular nature of the Green's functions.
2. For any  $\eta$ , the number of polynomials has to be sufficiently large for the series to converge, keeping in mind that a converged Green's function does not necessarily mean a converged self-energy.
3. The (linear) system size  $L$  has to be large enough for the mean-level spacing to be smaller than the resolution being used.
4. The statistical fluctuations due to the variations in vacancy positions from one realization of disorder to the other have to be low enough for the results to be meaningful. Due to the self-averaging properties of the disorder in this case, a larger system size will also mean a smaller error bar.
5. The simulations of this section relied heavily on the assumption of self-averaging. This also has to be checked. A system with self-averaging properties should yield an error bar which scales as  $D^{-1/2}$ , where  $D$  is the size of the Hilbert space. In this case, since  $D = 2L^2$ , the error bar should scale as  $1/L$ .

In this section we address each of these points in detail for a 0.3% vacancy concentration with the help of Fig. 3.20. The inset is the self-energy at  $\epsilon = 0$  as a function of the broadening, indicating that  $\Sigma(\epsilon = 0) = 0$ . Panel b) shows the standard deviation of  $\text{Im}(\Sigma_{AA})$  as a function of the system size for several energies. The slope is  $-1$ , indicating self-averaging behavior. Now let's address each of the previous points:

### 3 Diagrammatics in disordered systems

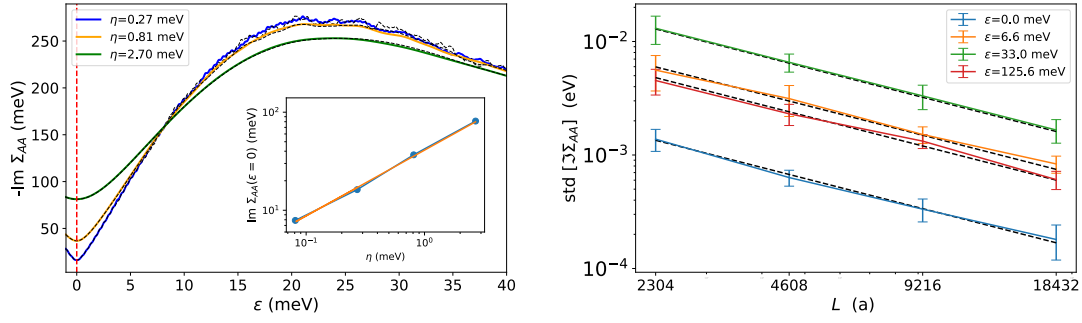


Figure 3.20: Convergence study for the imaginary part of the  $AA$  component of the disorder self-energy operator in graphene.

1. The phenomena tackled in the previous section are characterized by fine features that require a very small resolution to be accurately resolved. Furthermore, due to the singular nature of the Green's functions at zero energy, convergence with  $\eta$  is very difficult to achieve in that region. This is evident from Fig. 3.20a), where the curves seem close to convergence for  $|\varepsilon| > 5$  meV, but far from that otherwise. Nevertheless, the tendency can be estimated. The inset shows the self-energy at zero energy as a function of  $\eta$  and it is well fitted by  $\text{Im}\Sigma = \eta^{2/3}$  (orange line), which extrapolates to zero at  $\eta = 0$ .
2. The curves no longer change when the number of polynomials is increased. This has been checked by doubling and halving the number of polynomials and indicates that both the Green's function and the self-energy have converged.
3. Figure 3.20 a) displays  $\Sigma$  for two different system sizes and several values of  $\eta$ . The colored curves have  $L = 36864$ , and the superimposed black dashed curves have  $L = 18432$ . Close to zero energy where the focus of previous section lies, the curves do not change at all when  $L$  is changed, corroborating that the mean level spacing is very small due to the diverging DoS. In contrast, for larger energies, the discreteness of the spectrum becomes visible for  $\eta \lesssim 1$  meV, which is very close to the estimated mean level spacing of 1.4 meV
4. Figure 3.20 b) shows that for several energies, the error bar follows the self-averaging behavior  $1/L$ . The black dashed lines have slope  $-1$ .
5. Figure 3.20 b) also shows that the statistical fluctuations are very small, of the order of 2meV when  $L = 18432$  and therefore do not influence our results.

## 4 Nonlinear optical conductivity

In this chapter, a general perturbation procedure is developed to deal with non-interacting fermion systems at finite temperature coupled to a time-dependent external field. In [69], Weisse proposed an advanced Chebyshev expansion method to compute linear response functions. This Chapter comes as the next logical step, by providing the generalization to all orders in perturbation theory. Through careful categorization of all these contributions, we provide a systematic procedure to find the objects needed to calculate the conductivity at any order. These objects are expressed with no reference to a specific basis. The critical point here is that the mathematical objects provided by our perturbation expansion are precisely the ones required by the numerical spectral methods we use. This fact, combined with our diagrammatic approach, provides a straightforward way to implement the numerical calculation of the nonlinear optical conductivity for a wide range of materials.

### 4.1 Keldysh Formalism

The Keldysh formalism [32] is a general perturbation scheme describing the quantum mechanical time evolution of non-equilibrium interacting systems at finite temperature. It provides a concise diagrammatic representation of the average values of quantum operators. This formalism does not rely on any particular basis, which is a critical feature for this Chapter. In this section we will introduce the definitions of the objects used throughout the Chapter and show how to expand the Green's functions for fermions [124] with this formalism.

#### 4.1.1 Definitions

##### Green's functions

To use the Keldysh formalism for fermions, we need the definitions of the time-ordered, lesser, greater and anti-time-ordered Green's functions. Respectively,

$$iG_{ab}^T(t, t') = \left\langle T \left[ c_a(t) c_b^\dagger(t') \right] \right\rangle \quad (4.1)$$

$$iG_{ab}^<(t, t') = -\left\langle c_b^\dagger(t') c_a(t) \right\rangle \quad (4.2)$$

$$iG_{ab}^>(t, t') = \left\langle c_a(t) c_b^\dagger(t') \right\rangle \quad (4.3)$$

$$iG_{ab}^{\tilde{T}}(t, t') = \left\langle \tilde{T} \left[ c_a(t) c_b^\dagger(t') \right] \right\rangle. \quad (4.4)$$

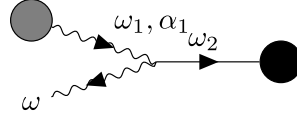


Figure 4.1: Diagrammatic representation of the expected value of the current operator in Fourier space. The horizontal straight line ending in a circle is the lesser Green's function and the wavy line beginning in a circle represents the current operator.

All the creation and annihilation operators are in the Heisenberg picture and the labels  $a$  and  $b$  denote states belonging to a complete single-particle basis.  $T$  is the time-ordering operator and  $\tilde{T}$  the anti-time-ordering operator. The average  $\langle \dots \rangle$  stands for  $\text{Tr}[\rho(t_0) \dots] / \text{Tr}[\rho(t_0)]$  in the grand canonical ensemble,  $\rho$  is the density matrix and  $t_0$  denotes the time at which the external perturbation has been switched on. These are the building blocks of the Keldysh formalism. The advanced and retarded Green's functions are a simple combination of the previous objects:

$$\begin{aligned} G^R &= G^T - G^< \\ G^A &= -G^{\tilde{T}} + G^<. \end{aligned}$$

The non-perturbed versions of these Green's functions are denoted by a lowercase  $g$ .

### Expected value of an operator

The expected value of the current  $\mathbf{J}(t)$  (or any one-particle operator) may be evaluated with resort to these Green's functions by tracing over its product with the perturbed lesser Green's function:

$$\mathbf{J}(t) = \langle \hat{\mathbf{J}}(t) \rangle = -\text{Tr} \left[ \hat{\mathbf{J}}(t) iG^<(t, t) \right]. \quad (4.5)$$

The Fourier transform <sup>1</sup> of  $\mathbf{J}(t)$  is shown diagrammatically in Fig. 4.1. The circles stand for the full, perturbed operators in the presence of an external field.

### Conductivity

We use the same definition for the nonlinear optical conductivity as in [63, 64]:

$$\begin{aligned} J^\alpha(\omega) &= \sigma^{\alpha\beta}(\omega) E^\beta(\omega) + \int \frac{d\omega_1}{2\pi} \int \frac{d\omega_2}{2\pi} \times \\ &\sigma^{\alpha\beta\gamma}(\omega_1, \omega_2) E^\beta(\omega_1) E^\gamma(\omega_2) 2\pi\delta(\omega_1 + \omega_2 - \omega) + \dots \end{aligned} \quad (4.6)$$

where  $E^\alpha$  is the component of the electric field along the  $\alpha$  direction and the repeated indices are assumed to be summed over. The coefficients of this expansion are the con-

<sup>1</sup>Fourier convention:  $f(t) = (2\pi)^{-1} \int d\omega e^{-i\omega t} \tilde{f}(\omega)$ , where the tilde is used to denote the Fourier transformed function.

ductivities at each order in the expansion. The next section is devoted to finding the perturbation expansion of  $G^<$ . In this chapter we are dealing with tight-binding models, in which case the current operator will itself be a power series of the external field.

### 4.1.2 Non-interacting electronic systems

Our system is described by the many-particle time-dependent Hamiltonian

$$\mathcal{H}(t) = \mathcal{H}_0 + \mathcal{H}_{\text{ext}}(t).$$

where  $\mathcal{H}_0$  is an Hamiltonian that we can solve exactly and  $\mathcal{H}_{\text{ext}}(t)$  is the time-dependent external perturbation. Here we restrict ourselves to non-interacting Hamiltonians since we're dealing with non-interacting electrons. These operators are expressed in terms of their single-particle counterparts as

$$\begin{aligned}\mathcal{H}_{\text{ext}}(t) &= \sum_{ab} [H_{\text{ext}}(t)]_{ab} c_a^\dagger(t) c_b(t) \\ \mathcal{H}_0 &= \sum_{ab} [H_0]_{ab} c_a^\dagger(t) c_b(t).\end{aligned}$$

The expansion of the perturbed lesser Green's function  $G^<$  will be expressed in terms of the unperturbed Green's functions  $g^>$ ,  $g^<$ ,  $g^R$  and  $g^A$  in Fourier space (denoted with tildes):

$$\begin{aligned}i\tilde{g}^<(\omega) &= -2\pi f(\hbar\omega) \delta(\omega - H_0/\hbar) \\ i\tilde{g}^>(\omega) &= 2\pi [1 - f(\hbar\omega)] \delta(\omega - H_0/\hbar) \\ i\tilde{g}^R(\omega) &= \frac{i}{\omega - H_0/\hbar + i0^+} \\ i\tilde{g}^A(\omega) &= \frac{i}{\omega - H_0/\hbar - i0^+},\end{aligned}\tag{4.7}$$

where  $f(\epsilon) = (1 + e^{\beta(\epsilon - \mu)})^{-1}$  is the Fermi-Dirac distribution,  $\beta$  is the inverse temperature and  $\mu$  is the chemical potential. The Keldysh formalism and Langreth's rules provide the perturbation expansion of  $G^<$  [125]. Defining  $V(t) = (i\hbar)^{-1} H_{\text{ext}}(t)$ , the zeroth-order term in the expansion is

$$i\tilde{G}^{<(0)}(\omega) = \int d\omega_1 i\tilde{g}^<(\omega_1) \delta(\omega)$$

and the first-order one is

$$\begin{aligned}i\tilde{G}^{<(1)}(\omega) &= \int \frac{d^3\omega_{123}}{(2\pi)^3} (2\pi)^2 \delta(\omega_1 - \omega_2 - \omega_3) \delta(\omega + \omega_3 - \omega_1) \\ &\times \left[ i\tilde{g}^R(\omega_1) \tilde{V}(\omega_2) i\tilde{g}^<(\omega_3) + i\tilde{g}^<(\omega_1) \tilde{V}(\omega_2) i\tilde{g}^A(\omega_3) \right].\end{aligned}$$

#### 4 Nonlinear optical conductivity

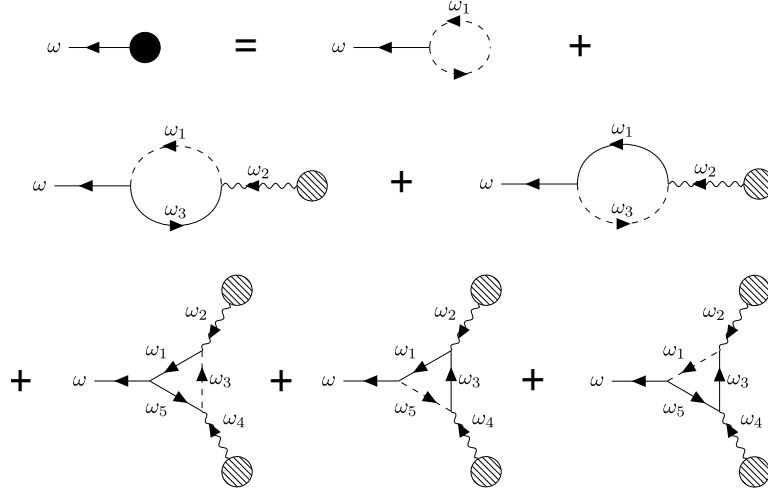


Figure 4.2: Diagrammatic representation of the lesser Green's function.

$\int d^n \omega_{1\dots n}$  is a shorthand for  $\int \dots \int d\omega_1 \dots d\omega_n$ . The second-order term is

$$\begin{aligned}
 i\tilde{G}^{<(2)}(\omega) &= \int \frac{d^5 \omega_{1\dots 5}}{(2\pi)^5} (2\pi)^3 \delta(\omega_5 + \omega - \omega_1) \times \\
 &\delta(\omega_1 - \omega_2 - \omega_3) \delta(\omega_3 - \omega_4 - \omega_5) \times \\
 &\left[ i\tilde{g}^R(\omega_1) \tilde{V}(\omega_2) i\tilde{g}^R(\omega_3) \tilde{V}(\omega_4) i\tilde{g}^<(\omega_5) \right. \\
 &+ i\tilde{g}^R(\omega_1) \tilde{V}(\omega_2) i\tilde{g}^<(\omega_3) \tilde{V}(\omega_4) i\tilde{g}^A(\omega_5) \\
 &\left. + i\tilde{g}^<(\omega_1) \tilde{V}(\omega_2) i\tilde{g}^A(\omega_3) \tilde{V}(\omega_4) i\tilde{g}^A(\omega_5) \right].
 \end{aligned}$$

Diagrammatically, the expansion of  $iG^<(\omega)$  is represented by Fig. 4.2. Each wavy line ending in a circle represents an external perturbation  $\tilde{V}$ . There are three different types of Green's functions that may appear in these expansions, with a certain regularity: a lesser Green's function  $\tilde{g}^<$ , which is always present, retarded Green's functions  $\tilde{g}^R$  and advanced Green's functions  $\tilde{g}^A$ . Diagrammatically,  $\tilde{g}^<$  is represented by a dashed line while the solid lines represent retarded or advanced Green's functions. To identify whether a line represents a retarded or advanced Green's function, one needs to read the diagram and identify the position of the lesser Green's function and the outgoing line. Reading clockwise (anti-clockwise) until finding the outgoing line, there can only be advanced (retarded) Green's functions. In each intersection, the corresponding external perturbation  $\tilde{V}$  is inserted. An exception is made for the intersection with the line representing  $\omega$ , as it still needs to be contracted.

If the external perturbation were a simple external field  $\mathbf{E}(t)$ , then the coupling would be  $H_{\text{ext}}(t) = e\mathbf{E}(t) \cdot \mathbf{r}$  and the previous expressions coupled with eq. (4.5) would suffice. Now we will turn to tight-binding Hamiltonians, for which the external coupling is actually an infinite series of operators due to the way the electromagnetic field is introduced. This affects not only the  $V$  operators but also the expression for the current operator.

## 4.2 Tight-binding Hamiltonian with external electric field

Tight-binding models provide a simple framework with which to calculate transport quantities. This framework can be used to express structural disorder in the system, whilst Peierls' substitution [126] adds an electromagnetic field as an external perturbation. Despite the simplicity of this procedure, the addition of an electromagnetic field through a phase factor yields an infinite series of  $H_{\text{ext}}$ . In this section, we obtain the expression for  $H_{\text{ext}}$  and show how the expansions of the previous sections may be used to obtain the non-linear optical conductivity. This is entirely analogous to the way the external perturbation is introduced with the velocity gauge in the work of Passos et al [63].

### 4.2.1 Series expansion

Let's consider the following tight-binding Hamiltonian:

$$\mathcal{H}_0 = \sum_{\mathbf{R}_i, \mathbf{R}_j} \sum_{\sigma_1, \sigma_2} t_{\sigma_1 \sigma_2}(\mathbf{R}_i, \mathbf{R}_j) c_{\sigma_1}^\dagger(\mathbf{R}_i) c_{\sigma_2}(\mathbf{R}_j). \quad (4.8)$$

The  $\mathbf{R}_i$  represent the lattice sites and the  $\sigma_i$  the other degrees of freedom unrelated to the position, such as the orbitals and spin. The electromagnetic field is introduced through Peierls' substitution:

$$t_{\sigma_1 \sigma_2}(\mathbf{R}_i, \mathbf{R}_j) \rightarrow e^{-\frac{ie}{\hbar} \int_{\mathbf{R}_j}^{\mathbf{R}_i} \mathbf{A}(\mathbf{r}', t) \cdot d\mathbf{r}'} t_{\sigma_1 \sigma_2}(\mathbf{R}_i, \mathbf{R}_j). \quad (4.9)$$

To introduce both a static magnetic field and a uniform electric field, we use the following vector potential:

$$\mathbf{A}(\mathbf{r}, t) = \mathbf{A}_1(\mathbf{r}) + \mathbf{A}_2(t).$$

The electric and magnetic fields are obtained from  $\mathbf{E}(t) = -\partial_t \mathbf{A}_2(t)$  and  $\mathbf{B}(\mathbf{r}) = \nabla \times \mathbf{A}_1(\mathbf{r})$ . The introduction of the magnetic field only changes the  $t_{\sigma_1 \sigma_2}(\mathbf{R}_i, \mathbf{R}_j)$  without introducing a time dependency. Therefore, we may assume that a magnetic field is always present without any loss of generality for the following discussion while keeping in mind that its introduction broke translation invariance. Since the magnetic field only affects the hopping parameters, from now on, the term in the vector potential that provides the electric field will be denoted by  $\mathbf{A}(t)$ . The external perturbation is obtained by expanding the exponential in eq. 4.9 and identifying the original Hamiltonian.

### Expansion of the external perturbation

Expanding the exponential in eq. 4.9 yields an infinite series of operators for the full Hamiltonian:

$$H_{\mathbf{A}}(t) = H_0 + H_{\text{ext}}(t)$$

#### 4 Nonlinear optical conductivity

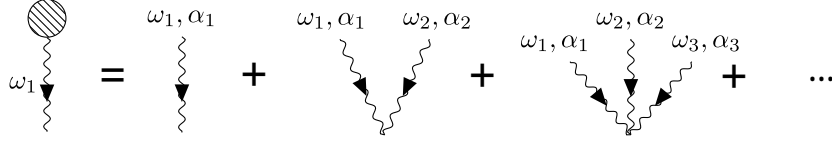


Figure 4.3: Diagrammatic representation of the external perturbation.

from which we identify, after a Fourier transform,

$$\begin{aligned} \tilde{V}(\omega) &= \frac{e}{i\hbar} h^\alpha \tilde{A}^\alpha(\omega) + \frac{e^2}{i\hbar} \frac{h^{\alpha\beta}}{2!} \int \frac{d\omega'}{2\pi} \int \frac{d\omega''}{2\pi} \times \\ &\tilde{A}^\alpha(\omega') \tilde{A}^\beta(\omega'') 2\pi\delta(\omega' + \omega'' - \omega) + \dots \end{aligned}$$

Repeated spatial indices are understood to be summed over. We have defined

$$\hat{h}^{\alpha_1 \dots \alpha_n} = \frac{1}{(i\hbar)^n} [\hat{r}^{\alpha_1}, [\dots [\hat{r}^{\alpha_n}, H_0]]] \quad (4.10)$$

where  $\hat{r}$  is the position operator. In first order,  $\hat{h}^\alpha$  is just the single-particle velocity operator. Under periodic boundary conditions (PBC), the position operator  $\hat{r}$  is ill-defined but its commutator with the Hamiltonian is not. In real space, this commutator is simply the Hamiltonian matrix element connecting the two sites  $i$  and  $j$  multiplied by the distance vector  $\mathbf{d}_{ij}$  between them. If we define this distance vector as the distance between neighbors instead of the difference of the two positions, it will be well defined in PBC. Using this strategy, all the  $\hat{h}$  operators may be evaluated in position space by assigning to each bond the Hamiltonian matrix element multiplied by the required product of difference vectors  $h_{ij}^{\alpha_1 \dots \alpha_n} = (i\hbar)^{-n} H_{ij} d_{ij}^{\alpha_1} \dots d_{ij}^{\alpha_n}$ .

In Fig. 4.3, we see how the diagrammatic representation of the external perturbation unfolds into an infinite series of external fields. The wavy line represents  $\tilde{\mathbf{A}}$  and the number of external fields connected to the same point is the number of commutators in eq. 4.10.

#### Expansion of the current

The current operator is calculated directly from the Hamiltonian, using  $\hat{J}^\alpha = -\Omega^{-1} \partial H / \partial A^\alpha$  ( $\Omega$  is the volume of the sample), which also follows a series expansion due to the presence of an infinite number of  $\mathbf{A}(t)$  in  $H_{\text{ext}}$ :

$$\hat{J}^\alpha(t) = -\frac{e}{\Omega} \left( \hat{h}^\alpha + e \hat{h}^{\alpha\beta} A^\beta(t) + \frac{e^2}{2!} \hat{h}^{\alpha\beta\gamma} A^\beta(t) A^\gamma(t) + \dots \right).$$

Figure 4.4 depicts the diagrammatic representation of this operator in Fourier space.

The complexity of this expansion becomes clear. In eq. 4.5, both the current operator and the Green's functions follow a perturbation expansion. Furthermore, each interaction operator in every one of the terms in the Green's function expansion also follows a similar

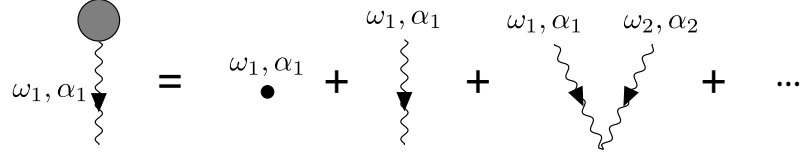


Figure 4.4: Diagrammatic representation of the current operator. The single small circle is to be understood as a Dirac delta.

expansion. We now have all the objects needed for the perturbative expansion of the conductivity.

#### 4.2.2 Perturbative expansion of the conductivity

In the previous sections we laid out the expressions for each individual operator in our expansion and represented their corresponding diagrammatic depictions. In this subsection, we put together all the elements of the previous sections to provide the full diagrammatic representation of the first and second-order conductivities. This expansion closely resembles that of [127] but has several differences due to the usage of these specific Green's functions. The only thing left to do is to replace the perturbed objects in the diagrammatic representation of the expected value of the current operator by their expansions. It is straightforward to see how the diagrams fit together in Fig. 4.5, which shows all the contributing diagrams up to second order.

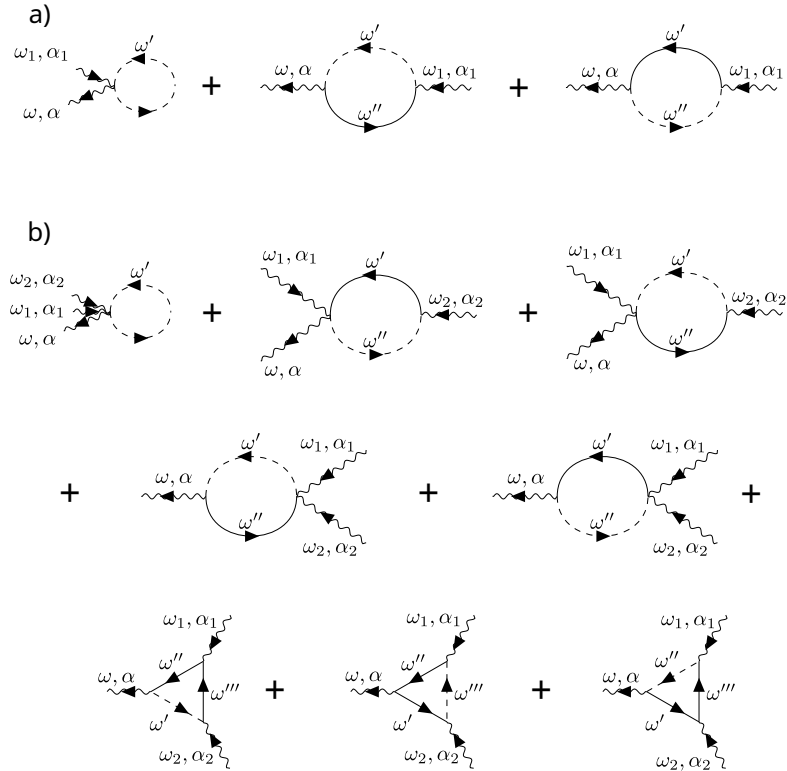


Figure 4.5: Expansion of the expected value of the conductivity in (a) first and (b) second order.

#### 4 Nonlinear optical conductivity

Obtaining the conductivity from the current is a matter of expressing the frequencies  $\omega'$ ,  $\omega''$  and  $\omega'''$  in terms of  $\omega_1$ ,  $\omega_2$  and  $\omega$  and using  $\mathbf{E}(\omega) = i\omega\mathbf{A}(\omega)$ . The Dirac delta in eq. 4.6 simply means that  $\omega$  is to be replaced by the sum of external frequencies entering the diagram. Thus, the  $n$ -th order conductivity may be found using the following rules:

1. Draw all the diagrams with  $n$  wavy lines coming in the diagram, one going out and one dashed interconnecting line. Integrate over the internal frequencies and ignore the conservation of momentum in the vertex containing  $\omega$ , as that is already taken into account by the Dirac delta in the definition of the conductivity.
2. Reading clockwise starting from the vertex containing  $\omega$ , insert, by order, a generalized velocity operator  $\hat{h}^{\alpha_1 \dots \alpha_k}$  at each vertex and a Green's function at each edge. Each  $\alpha_i$  is the label of a frequency line connecting to the vertex. If the edge is a dashed line, the Green's function is  $ig^<$ . All the edges before that correspond to  $ig^R$  and the ones after it to  $ig^A$ . Trace over the resulting operator.
3. Multiply by  $\Omega^{-1}e^{n+1} \prod_{k=1}^n (i\omega_k)^{-1} (i\hbar)^{1-N}$ , where  $n$  is the number of dashed lines and  $N$  is the number of interconnecting lines. For each vertex, divide by the factorial of the number of outgoing lines.

Following these rules and replacing  $ig^<$  by eq. 4.7, the first-order conductivity is found:

$$\begin{aligned} \sigma^{\alpha\beta}(\omega) &= \frac{ie^2}{\Omega\omega} \int_{-\infty}^{\infty} d\epsilon f(\epsilon) \text{Tr} \left[ \hat{h}^{\alpha\beta} \delta(\epsilon - H_0) + \frac{1}{\hbar} \hat{h}^{\alpha} g^R(\epsilon/\hbar + \omega) \hat{h}^{\beta} \delta(\epsilon - H_0) \right. \\ &\quad \left. + \frac{1}{\hbar} \hat{h}^{\alpha} \delta(\epsilon - H_0) \hat{h}^{\beta} g^A(\epsilon/\hbar - \omega) \right]. \end{aligned}$$

Similarly, for the second-order conductivity:

$$\sigma^{\alpha\beta\gamma}(\omega_1, \omega_2) = \frac{1}{\Omega} \frac{e^3}{\omega_1 \omega_2} \int_{-\infty}^{\infty} d\epsilon f(\epsilon) \text{Tr} \left[ \sum_{i=1}^8 \mathcal{O}_i^{\alpha\beta\gamma}(\omega_1, \omega_2) \right] \quad (4.11)$$

where

$$\begin{aligned} \mathcal{O}_1^{\alpha\beta\gamma}(\omega_1, \omega_2) &= \frac{1}{2} \hat{h}^{\alpha\beta\gamma} \delta(\epsilon - H_0) \\ \mathcal{O}_2^{\alpha\beta\gamma}(\omega_1, \omega_2) &= \frac{1}{\hbar} \hat{h}^{\alpha\beta} g^R(\epsilon/\hbar + \omega_2) \hat{h}^{\gamma} \delta(\epsilon - H_0) \\ \mathcal{O}_3^{\alpha\beta\gamma}(\omega_1, \omega_2) &= \frac{1}{\hbar} \hat{h}^{\alpha\beta} \delta(\epsilon - H_0) \hat{h}^{\gamma} g^A(\epsilon/\hbar - \omega_2) \\ \mathcal{O}_4^{\alpha\beta\gamma}(\omega_1, \omega_2) &= \frac{1}{2\hbar} \hat{h}^{\alpha} g^R(\epsilon/\hbar + \omega_1 + \omega_2) \hat{h}^{\beta\gamma} \delta(\epsilon - H_0) \\ \mathcal{O}_5^{\alpha\beta\gamma}(\omega_1, \omega_2) &= \frac{1}{2\hbar} \hat{h}^{\alpha} \delta(\epsilon - H_0) \hat{h}^{\beta\gamma} g^A(\epsilon/\hbar - \omega_1 - \omega_2) \\ \mathcal{O}_6^{\alpha\beta\gamma}(\omega_1, \omega_2) &= \frac{1}{\hbar^2} \hat{h}^{\alpha} g^R(\epsilon/\hbar + \omega_1 + \omega_2) \hat{h}^{\beta} g^R(\epsilon/\hbar + \omega_2) \hat{h}^{\gamma} \delta(\epsilon - H_0) \\ \mathcal{O}_7^{\alpha\beta\gamma}(\omega_1, \omega_2) &= \frac{1}{\hbar^2} \hat{h}^{\alpha} g^R(\epsilon/\hbar + \omega_1) \hat{h}^{\beta} \delta(\epsilon - H_0) \hat{h}^{\gamma} g^A(\epsilon/\hbar - \omega_2) \\ \mathcal{O}_8^{\alpha\beta\gamma}(\omega_1, \omega_2) &= \frac{1}{\hbar^2} \hat{h}^{\alpha} \delta(\epsilon - H_0) \hat{h}^{\beta} g^A(\epsilon/\hbar - \omega_1) \hat{h}^{\gamma} g^A(\epsilon/\hbar - \omega_1 - \omega_2). \end{aligned}$$

The procedure is exactly the same for the  $n$ -th order conductivity, which will have  $2^{n-1}(n+2)$  diagrams. The higher-order expansions will not be obtained because a realistic computation of physical quantities with those formulas using spectral methods would require tremendous computational power. This point will be further explained in the next section.

### 4.3 Spectral methods

From the previous section, it becomes clear that the only objects needed to calculate the conductivity up to any order are the retarded and advanced Green's functions, Dirac deltas and the generalized velocity operators. As we have seen in chapter 2, both the Dirac deltas and the Green's functions can be expanded in terms of Chebyshev polynomials, and then the trace evaluated using STE. The Green's function expansion can be done either with the Lorentz weight 2.10 or with a finite imaginary part  $\eta$ . We choose the latter because the approximation is better controlled, even though both must yield the same result in the limit of infinite polynomials. For a finite  $\eta$ , the function is no longer singular and so we can expect the expansion to converge within a given accuracy after enough polynomials have been added. In this chapter, we will use the exact decomposition of the Green's function 2.17 in terms of Chebyshev polynomials in order to be able to evaluate the convergence of our method. The term  $\hbar/\eta$  may also be interpreted as a phenomenological relaxation time due to inelastic scattering processes and therefore may be adjusted to reflect this fact.

#### 4.3.1 Expansion in Chebyshev polynomials

The Dirac deltas are expanded using 2.13 and the advanced and retarded Green's functions using 2.17. As is typical with this kind of expansions, the operator part has been completely separated from its other arguments. All the Dirac deltas and Green's functions may therefore be separated into a term with only Chebyshev polynomials of  $H_0$  and another with only coefficients which encapsulate the frequency and energy parameters. The trace in the conductivity now becomes a trace over a product of polynomials and  $\hat{h}$  operators, which can be encapsulated in a new object, the  $\Gamma$  matrix:

$$\Gamma_{n_1 \dots n_m}^{\alpha_1, \dots, \alpha_m} = \frac{\text{Tr}}{N} \left[ \tilde{h}^{\alpha_1} T_{n_1}(H_0) \dots \tilde{h}^{\alpha_m} T_{n_m}(H_0) \right].$$

The upper indices in bold stand for any number of indices:  $\alpha_1 = \alpha_1^1 \alpha_1^2 \dots \alpha_1^{N_1}$ . Here we have used  $\tilde{h}^{\alpha_1} = (i\hbar)^{N_1} \hat{h}^{\alpha_1}$  rather than  $\hat{h}$  to avoid using complex numbers when the Hamiltonian matrix is purely real in our numerical simulations.

#### 4 Nonlinear optical conductivity

It's very important to keep in mind that these new operators are no longer hermitian. The commas in  $\Gamma$  separate the various  $\tilde{h}$  operators.  $N$  is the number of unit cells in the sample being studied and ensures that  $\Gamma$  is an intensive quantity. Some examples are:

$$\begin{aligned}\Gamma_{nm}^{\alpha,\beta,\gamma} &= \frac{\text{Tr}}{N} \left[ \tilde{h}^\alpha T_n(H_0) \tilde{h}^{\beta\gamma} T_m(H_0) \right] \\ \Gamma_n^{\alpha\beta} &= \frac{\text{Tr}}{N} \left[ \tilde{h}^{\alpha\beta} T_n(H_0) \right] \\ \Gamma_{nmp}^{\alpha,\beta,\gamma} &= \frac{\text{Tr}}{N} \left[ \tilde{h}^\alpha T_n(H_0) \tilde{h}^\beta T_m(H_0) \tilde{h}^\gamma T_p(H_0) \right].\end{aligned}$$

The  $\Gamma$  matrix only depends on the physical system itself as it is merely a function of the Hamiltonian and the  $\tilde{h}$  operators. The coefficients of the Chebyshev expansion may similarly be aggregated into a matrix, which we denote by  $\Lambda$ . Some examples:

$$\begin{aligned}\Lambda_n &= \int_{-\infty}^{\infty} d\epsilon f(\epsilon) \Delta_n(\epsilon) \\ \Lambda_{nm}(\omega) &= \hbar \int_{-\infty}^{\infty} d\epsilon f(\epsilon) \left[ g_n^R(\epsilon/\hbar + \omega) \Delta_m(\epsilon) + \Delta_n(\epsilon) g_m^A(\epsilon/\hbar - \omega) \right] \\ \Lambda_{nmp}(\omega_1, \omega_2) &= \hbar^2 \int_{-\infty}^{\infty} d\epsilon f(\epsilon) \left[ g_n^R(\epsilon/\hbar + \omega_1 + \omega_2) g_m^R(\epsilon/\hbar + \omega_2) \Delta_p(\epsilon) \right. \\ &\quad \left. + g_n^R(\epsilon/\hbar + \omega_1) \Delta_m(\epsilon) g_p^A(\epsilon/\hbar - \omega_2) \right. \\ &\quad \left. + \Delta_n(\epsilon) g_m^A(\epsilon/\hbar - \omega_1) g_p^A(\epsilon/\hbar - \omega_1 - \omega_2) \right].\end{aligned}$$

In terms of these new objects, the conductivities become

$$\sigma^{\alpha\beta}(\omega) = \frac{-ie^2}{\Omega_c \hbar^2 \omega} \left[ \sum_n \Gamma_n^{\alpha\beta} \Lambda_n + \sum_{nm} \Lambda_{nm}(\omega) \Gamma_{nm}^{\alpha,\beta} \right]$$

in first order and

$$\begin{aligned}\sigma^{\alpha\beta\gamma}(\omega_1, \omega_2) &= \frac{ie^3}{\Omega_c \omega_1 \omega_2 \hbar^3} \left[ \frac{1}{2} \sum_n \Lambda_n \Gamma_n^{\alpha\beta\gamma} + \sum_{nm} \Lambda_{nm}(\omega_2) \Gamma_{nm}^{\alpha\beta,\gamma} \right. \\ &\quad \left. + \frac{1}{2} \sum_{nm} \Lambda_{nm}(\omega_1 + \omega_2) \Gamma_{nm}^{\alpha,\beta\gamma} + \sum_{nmp} \Lambda_{nmp}(\omega_1, \omega_2) \Gamma_{nmp}^{\alpha,\beta,\gamma} \right]\end{aligned}$$

in second order.  $\Omega_c$  is the volume of the unit cell.

#### 4.3.2 Considerations on the numerical storage of $\Gamma$

Naturally, one cannot expect to sum the entire Chebyshev series, so it has to be truncated at a certain number of polynomials  $N_{\text{max}}$ . Each of the entries in a  $\Gamma$  matrix represents a complex number. Numerically, this is represented as two double-precision floating-point numbers, each taking up 8 bytes of storage. The amount of storage needed to store a  $\Gamma$  matrix of dimension  $n$  is  $16N_{\text{max}}^n$ . The number of Chebyshev polynomials needed to obtain

a decent resolution depends heavily on the problem at hand, but a typical number may be  $N_{\max} = 1024$ . A one-dimensional  $\Gamma$  matrix would take up 16 KiB of storage, a two-dimensional matrix 16 MiB and a three-dimensional matrix 16 GiB. Three-dimensional matrices appear in the second-order conductivity. The third-order conductivity would require a four-dimensional matrix and as such, 16 TiB of storage. Numbers like these make it unrealistic to go beyond second order conductivity.

## 4.4 Numerical results

In this section we showcase several examples, of increasing complexity, to compare our formalism with the literature. Starting with graphene, we compute the linear optical conductivity and verify that it agrees perfectly with the  $\mathbf{k}$ -space formalism. Breaking the sublattice symmetry with gapped graphene, we are able to obtain the second-order conductivity and check that it too agrees perfectly. This proves that our method is able to accurately reproduce the existing results. Then, we show two examples that cannot be reproduced easily with the  $\mathbf{k}$ -space formalism: second harmonic generation in gapped graphene with Anderson disorder and vacancies of varying concentration. Finally, the convergence properties are evaluated and the efficiency of the method is discussed.

### 4.4.1 Linear optical response in graphene

Let  $a$  be the distance between consecutive atoms in the honeycomb lattice. Then, the primitive vectors between unit cells are (see Fig. 4.6)

$$\begin{aligned}\mathbf{a}_1 &= a \left( \sqrt{3}, 0 \right) \\ \mathbf{a}_2 &= a \left( \frac{\sqrt{3}}{2}, \frac{3}{2} \right)\end{aligned}$$

and the distance vectors between nearest neighbors are

$$\begin{aligned}\boldsymbol{\delta}_1 &= \frac{a}{2} \left( \sqrt{3}, -1 \right) \\ \boldsymbol{\delta}_2 &= a \left( 0, 1 \right) \\ \boldsymbol{\delta}_3 &= \frac{a}{2} \left( -\sqrt{3}, -1 \right).\end{aligned}$$

The area of the unit cell is  $\Omega_c = \frac{3\sqrt{3}}{2}a^2$ . Starting from eq. 4.8, the graphene Hamiltonian is obtained by invoking translational invariance of the unit cell  $t_{\mu\nu}(\mathbf{R}_m, \mathbf{R}_n) = t_{\mu\nu}(\mathbf{R}_m - \mathbf{R}_n)$  and

$$t_{AB}(\boldsymbol{\delta}_1) = t_{AB}(\boldsymbol{\delta}_2) = t_{AB}(\boldsymbol{\delta}_3) = -t.$$

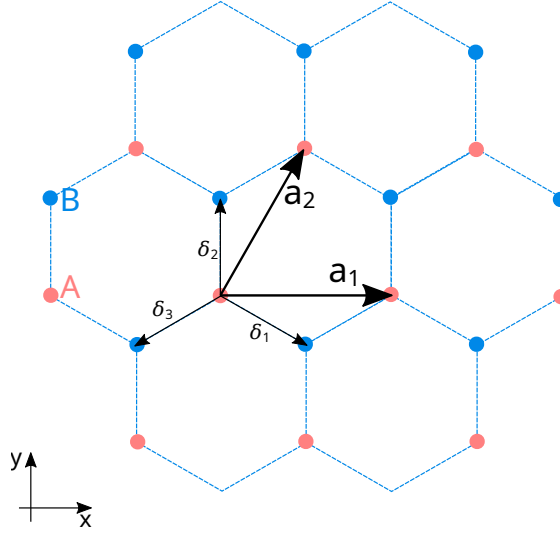


Figure 4.6: Honeycomb lattice and choice of primitive vectors.

The remaining non-zero hopping integrals are found by using  $t_{AB} = t_{BA}$ . The on-site energies  $t_{AA}(\mathbf{0})$  and  $t_{BB}(\mathbf{0})$  are taken to be zero. A factor of two is included due to spin degeneracy.

These parameters were used to obtain the first-order optical conductivity for graphene, as seen in Fig. 4.7. We used a lattice with 4096 unit cells in each direction and 2048 Chebyshev moments in the expansion. The resulting plot is compared to the results obtained in [64] through  $\mathbf{k}$ -space integration of a translation-invariant system. The curves are indistinguishable.

#### 4.4.2 Gapped graphene

The only difference relative to regular graphene is found in the on-site energies. Let  $t_{AA}(\mathbf{0}) = \Delta/2$  and  $t_{BB}(\mathbf{0}) = -\Delta/2$ . With the opening of a sizeable gap, the effects of excitons become relevant. In this simplified model, we ignore these effects to focus on the intrinsic second-order response of the material. In these conditions, the one- and three-dimensional  $\Gamma$  matrices are identically zero<sup>2</sup>, so the second-order conductivity may be calculated resorting only to two-dimensional  $\Gamma$  matrices. The calculation is thus simplified tremendously because the second-order conductivity reduces to

$$\sigma^{\alpha\beta\gamma}(\omega_1, \omega_2) = \frac{ie^3}{\Omega_c \omega_1 \omega_2 \hbar^3} \left[ \sum_{nm} \Lambda_{nm}(\omega_2) \Gamma_{nm}^{\alpha\beta,\gamma} + \frac{1}{2} \sum_{nm} \Lambda_{nm}(\omega_1 + \omega_2) \Gamma_{nm}^{\alpha,\beta\gamma} \right].$$

The indices  $n, m$  are understood to be summed over. The photogalvanic effect may be reproduced from this formula by setting  $\omega_1 = \omega = -\omega_2$  and the numerical results are shown in Fig. 4.4.2. Again, we used 4096 unit cells in each lattice direction and 2048 Chebyshev moments and compare the results with the ones obtained by integrating in  $\mathbf{k}$ -space, just

<sup>2</sup>These matrices were explicitly calculated in the  $\mathbf{k}$  basis and shown to be exactly zero.

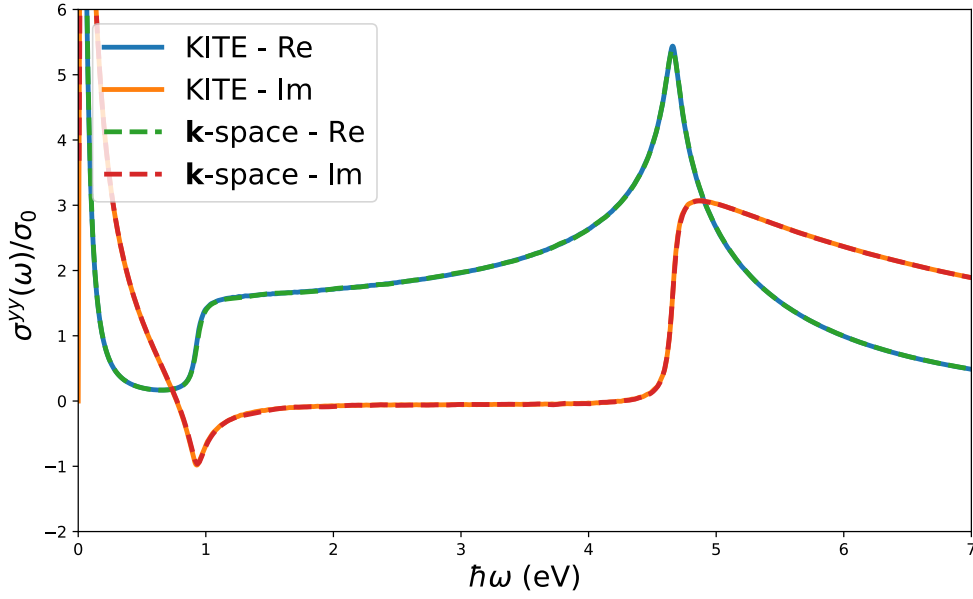


Figure 4.7: First-order longitudinal  $yy$  conductivity for graphene in units of  $\sigma_0 = e^2/\hbar$ . Hopping parameter:  $t = 2.33\text{eV}$ , temperature:  $T = 2.33\text{mK}$ , chemical potential:  $\mu = 0.466\text{eV}$ , broadening parameter:  $\eta = 38.8\text{meV}$ , number of Chebyshev moments used:  $M = 2048$ , lattice size:  $L = 4096 \times 4096$ . The solid curves represent the optical conductivity obtained by KITE (real part in green, imaginary in blue). The superimposed dashed lines are obtained in [64].

like in the previous subsection. For convenience, we define the constant  $\sigma_2 = e^3 a / 4t\hbar$  [128] in terms of the hopping integral  $t$  and the lattice parameter  $a$ .

This particular example benefits considerably from the cancellation of the most complicated objects that needed to be calculated. In the next section, we present an example with less symmetry that confirms the complete agreement between our method and the  $\mathbf{k}$ -space formalism.

#### 4.4.3 Sublattice displacement

The calculation of the photogalvanic effect for gapped graphene was very efficient due to the cancellation of the three-dimensional  $\Gamma$  matrices. In this appendix, we provide an extra example, which does not benefit from that property. By changing the relative position of the two sublattices, we are able to obtain non-zero values in all the  $\Gamma$  matrices, which enables us to test the remainder of the formula. All the hopping parameters in this system are exactly the same as in regular gapped graphene. The only difference is in the distance between atoms, which changes the velocity operators while keeping the Hamiltonian intact (See Fig. 4.9).

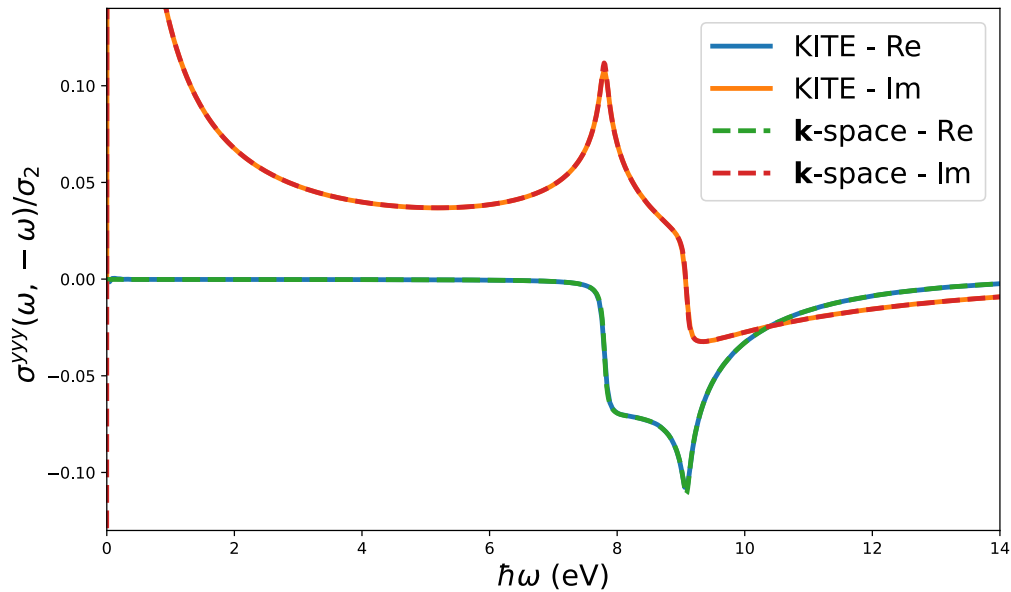


Figure 4.8: Second-order  $yyy$  photogalvanic effect for gapped graphene. Hopping parameter:  $t = 2.33\text{eV}$ , temperature:  $T = 0\text{K}$ , chemical potential:  $\mu = 0\text{eV}$ , gap  $\Delta = 7.80\text{eV}$  broadening parameter:  $\eta = 39\text{meV}$ , number of Chebyshev moments used:  $M = 2048$ , lattice size:  $L = 4096 \times 4096$ . The imaginary part disappears after the result is properly symmetrized.

The primitive vectors are identical, but the nearest-neighbor vectors are different:

$$\begin{aligned}\boldsymbol{\delta}_1 &= a \left( \frac{\sqrt{3}}{2}, -1 \right) \\ \boldsymbol{\delta}_2 &= a \left( 0, \frac{1}{2} \right) \\ \boldsymbol{\delta}_3 &= a \left( -\frac{\sqrt{3}}{2}, -1 \right).\end{aligned}$$

One of the sublattices was translated in the  $y$  direction by  $a/2$ . The second-order  $xxx$  conductivity remains zero, but now the  $xy$  photogalvanic effect is no longer zero and can be seen in Fig. 4.4.3. The lattice size and number of polynomials used was reduced to 1024 and 512 respectively, due to the greatly increased computational cost. At lower frequencies, the results start to diverge because there are not enough polynomials to resolve this region. The results are in great agreement with the ones obtained by  $\mathbf{k}$ -space integration. The small oscillations in the imaginary part are expected to disappear as the number of polynomials is increased.

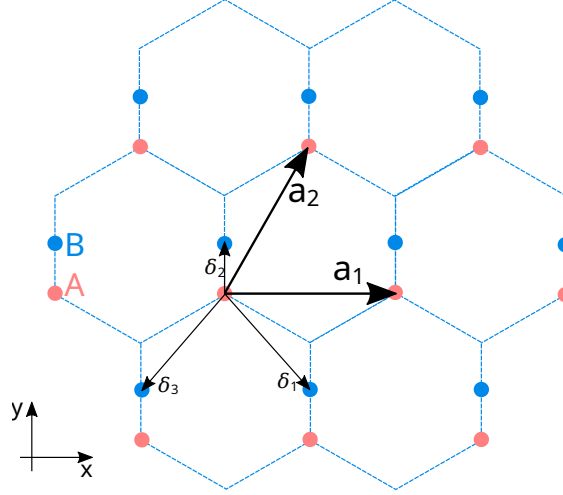


Figure 4.9: Displaced honeycomb lattice and choice of primitive vectors.

#### 4.4.4 Photogalvanic effect in gapped graphene with Anderson disorder

Our formalism does not rely on translation invariance, and so may be used to study disordered systems. To show this, we now introduce to gapped graphene a simple model for disorder by letting each atomic site have a random local energy taken from a uniform distribution  $[-W/2, W/2]$  (Anderson disorder [10]):

$$\mathcal{H}_W = \sum_{\mathbf{R}} \sum_{\sigma} W_{\sigma}(\mathbf{R}) c_{\sigma}^{\dagger}(\mathbf{R}) c_{\sigma}(\mathbf{R})$$

where  $\mathbf{R}$  is the position of the unit cell and  $\sigma$  labels the atoms inside each unit cell. The presence of disorder is expected to smooth out the sharp features of the optical response. As disorder increases, we should see a decrease in conductivity due to Anderson localization. This is the exact behavior that is seen in Fig. 4.11 where we plot the photogalvanic effect in gapped graphene in the presence of Anderson disorder of varying strength. Some fluctuations exist at the features, which are expected to disappear as the system size approaches the thermodynamic limit.

As expected, the introduction of Anderson disorder produces a broadening of the sharp features of the nonlinear optical conductivity. This broadening also means that there will be a larger response to the external electric field at frequencies smaller than the gap.

The large oscillations near the origin reveal something interesting about the numerical details of our formalism. Equation 4.11 is comprised of a complicated sum of several terms. Individually, some of these terms may be very large, but there may be cancellations among them. For each of these terms, the Chebyshev expansion is exact in the limit of infinite polynomials. For a finite number of polynomials, there will be slight differences between the exact result and the expansion, and if the exact result is very large, this difference will be considerable. It is highly unlikely that this difference will be the same for each term, and so their sum may not cancel out in the end. This is the typical behavior at

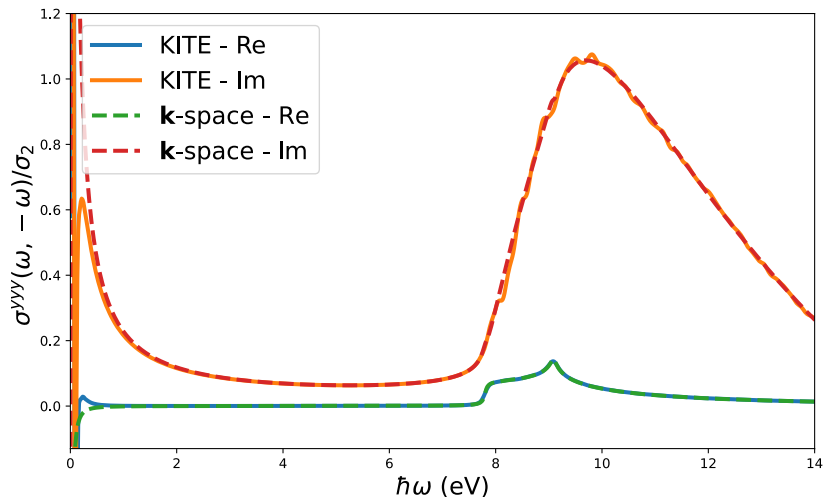


Figure 4.10: Second-order  $xy$  photogalvanic effect for displaced gapped graphene. Hopping parameter:  $t = 2.33\text{eV}$ , temperature:  $T = 0\text{K}$ , chemical potential:  $\mu = 0\text{eV}$ , gap  $\Delta = 7.8\text{eV}$  broadening parameter:  $\eta = 39\text{meV}$ , number of Chebyshev moments used:  $M = 512$ , lattice size:  $L = 1024 \times 1024$ .

the lower-frequency regime that is related to the singularities that plagued the velocity gauge approach. This has been discussed since the early work of Sipe and challenged for a long time the equivalence between the velocity and length gauges [55, 63, 64]. This effect could be fully mitigated by greatly increasing the number of polynomials, but here we are interested in the finite frequency behavior.

#### 4.4.5 Second-harmonic generation of gapped graphene with vacancies

In realistic samples, vacancies and impurities may exist due to imperfections in the fabrication process, as well as other more complex structural defects. In this section, we show that our method allows us to obtain the second-harmonic generation of a system with structural disorder. Using eq. 4.11, we show in Fig. 4.12 the effect of vacancies of varying concentration in the SHG of gapped graphene. Unlike Anderson disorder, the addition of vacancies to the system does not change the gap. Their most noticeable effect is to flatten the features of the second-harmonic generation. As discussed in the previous section, the lower frequencies are dominated by oscillations and would require many more polynomials to fully converge. Therefore, we omit that region and only represent the remaining regions, which have already converged within the desired accuracy.

#### 4.4.6 Considerations on convergence and accuracy

In this section, we briefly discuss some convergence properties of our method. For a more thorough discussion, see [95]. The convergence to the exact value depends on several factors:

1. Spectral methods rely on the self-averaging properties of random vectors, yielding an

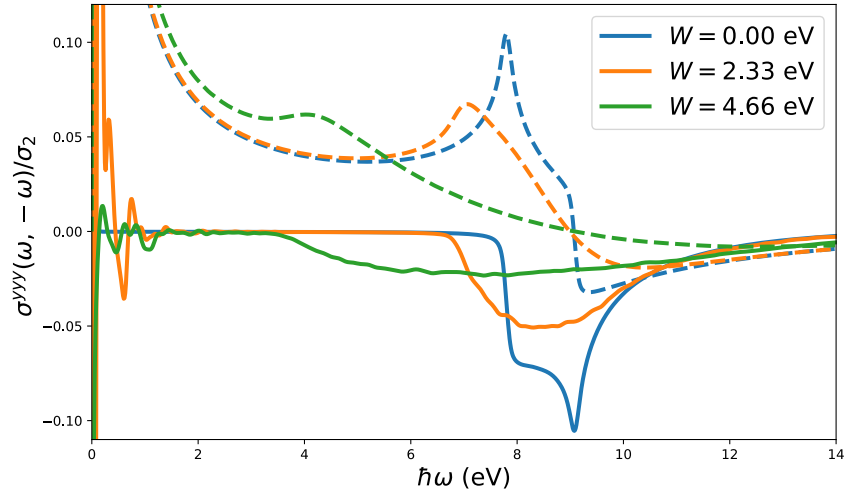


Figure 4.11: Photogalvanic effect for gapped graphene in the presence of Anderson disorder of varying strength  $W$  and a broadening parameter of  $\eta = 23\text{meV}$ . The parameters are the same as for Fig. 4.4.2 except for the number of polynomials, which is  $M = 512$ . The dashed lines represent the imaginary part of the conductivity.

associated variance. The error bar decreases as  $1/\sqrt{N_R N}$ , where  $N_R$  is the number of random vectors and  $N$  is the size of the sample, as described in section 2.6.

2. In the thermodynamic limit of an infinite lattice, the spectrum becomes continuous and so we expect the conductivity curve to be smooth. However, the systems used in simulations are finite and so have a typical energy level spacing, which we denote by  $\delta\varepsilon$ . This has important consequences for the resolution. Details characterized by a smaller energy scale than that of  $\delta\varepsilon$  are meaningless because they cannot be distinguished from the contribution of individual energy levels. The maximum resolution is therefore limited by the energy level spacing. For our concrete examples with the honeycomb lattice, we use  $\delta\varepsilon = 3\pi t/L$ , the energy level spacing at the Dirac point in graphene for a system of linear dimension  $L$ .
3. The resolution may be controlled through  $\eta$ , the broadening parameter of the Green's functions. Energy differences smaller than  $\lambda$  become indistinguishable from one another. On the one hand, a small  $\lambda$  is required in order to resolve the sharp features of the curve accurately. On the other hand, when  $\eta \lesssim \delta\varepsilon$ , the discrete nature of the spectrum starts to become visible through the roughness of the curve. For sufficiently small  $\eta$ , the expected sharp features of the curve become indistinguishable from the contributions of the individual energy levels. If these issues are not solved, they become a major source of systematic error in the final results. Therefore, if we want to see the expected thermodynamic limit, we have to ensure  $\eta \gtrsim \delta\varepsilon$ .

In Fig. 4.13, the  $yy$  optical conductivity of graphene is represented for several values of  $\eta$ . In this example,  $\delta\varepsilon = 5.3\text{meV}$ . As  $\eta$  is decreased, the curve becomes sharper, but

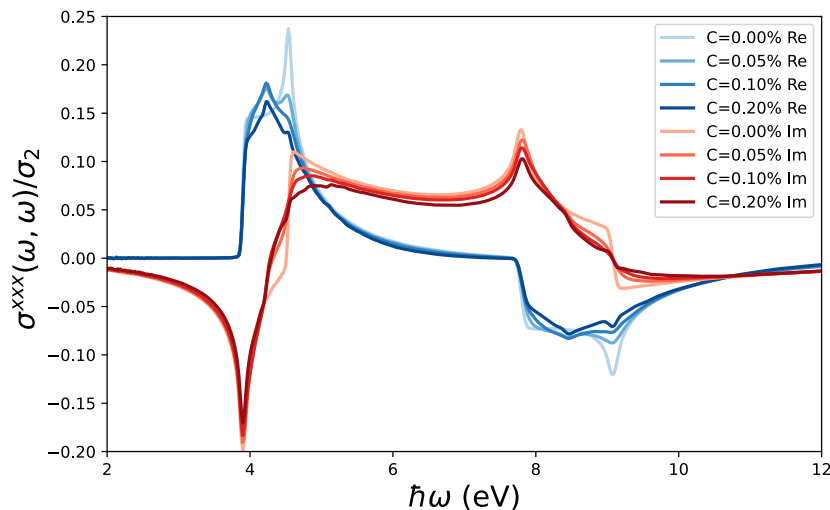


Figure 4.12: Second-harmonic generation in gapped graphene for a varying concentration of vacancies and  $\eta = 2.3\text{meV}$ . The blue (red) curves represent the real (imaginary) part of the conductivity. The darker curves have a higher concentration of vacancies. System size:  $L = 2048$ , number of polynomials:  $M = 512$ . All the other parameters are the same as in Fig. 4.11.

when  $\eta = 2.3\text{meV}$  the discreteness of the spectrum starts to become noticeable through the roughness of the curve. It is starting to diverge from the expected smooth curve of the thermodynamic limit.

In the lower inset, we study the convergence as a function of the number of polynomials at  $\hbar\omega = 4.66\text{eV}$ , a region of rapidly changing conductivity. The smaller the  $\eta$ , the more polynomials are required in order to have a fully converged result. Within the accuracy  $\delta\sigma/\sigma_0 \simeq 0.1$ , all the curves have already converged at  $1.6 \times 10^4$  polynomials. These calculations were repeated for several different initial random vectors. In the plot we show only one of these calculations. The error bar associated with the random vectors is too small to be distinguished from the curves themselves.

In the upper inset, we do the same thing, but now in a very small region around  $\hbar\omega = 2.33\text{eV}$ , a region of slowly increasing conductivity. The plot shows three sets of curves with different colors. Inside each set, we represent a collection of frequencies, ranging from  $\hbar\omega = 2.3300\text{eV}$  to  $\hbar\omega = 2.3316\text{eV}$ . The darker curves correspond to higher frequencies. The main graph shows that all these curves have converged to the same value in a region of slowly increasing conductivity. The inset, however, shows a different picture. The red ( $\eta = 23\text{meV}$ ) and black ( $\eta = 230\text{meV}$ ) sets of curves show a variation consistent with the expected increasing conductivity. If one zooms in to those sets of curves, it is possible to check that they are indeed increasing in value as  $\omega$  increases. The green curve ( $\eta = 2.3\text{meV}$ ) is not only changing in a scale much larger than expected, but it is also decreasing. This variation comes from the individual contribution of the energy levels, not from features of the conductivity and is therefore artificial. Within the accuracy  $\delta\sigma/\sigma_0 \simeq 10^{-3}$  each of these curves has completely converged at  $1.6 \times 10^4$  polynomials but this level of accuracy

is meaningless for  $\eta = 2.3\text{meV}$ . The error bars are not shown for clarity, but their values are the following: at  $\eta = 230\text{meV}$ ,  $\delta\sigma/\sigma_0 = 10^{-3}$ ; at  $\eta = 23\text{meV}$ ,  $\delta\sigma/\sigma_0 = 3 \times 10^{-3}$ ; at  $\eta = 2.3\text{meV}$ ,  $\delta\sigma/\sigma_0 = 5 \times 10^{-3}$ . At this scale, the error bars are comparable to the variation due to the number of polynomials and to the value of  $\eta$ .

These frequencies were chosen to compare the conductivity in a place where it is expected to converge quickly and another where it is expected to converge slowly. Looking at these graphs, it is possible to estimate how many polynomials are required to converge to the final value of the conductivity for the specified parameter  $\eta$  within a given accuracy. A rough estimate of the scaling is given by  $N \sim \eta^{-1}$ .

In sum, given a fixed resolution  $\eta$ , the number of polynomials should be large enough to ensure that the curves have converged, and the system size  $L$  should be large enough to ensure that the discreteness of the spectrum cannot be seen.

A similar analysis may be done for the second-order conductivity. We will not present it here for two reasons. Firstly, the main points of the previous paragraphs remain the same. Secondly, we cannot do such an analysis because the computational cost would be tremendously higher.

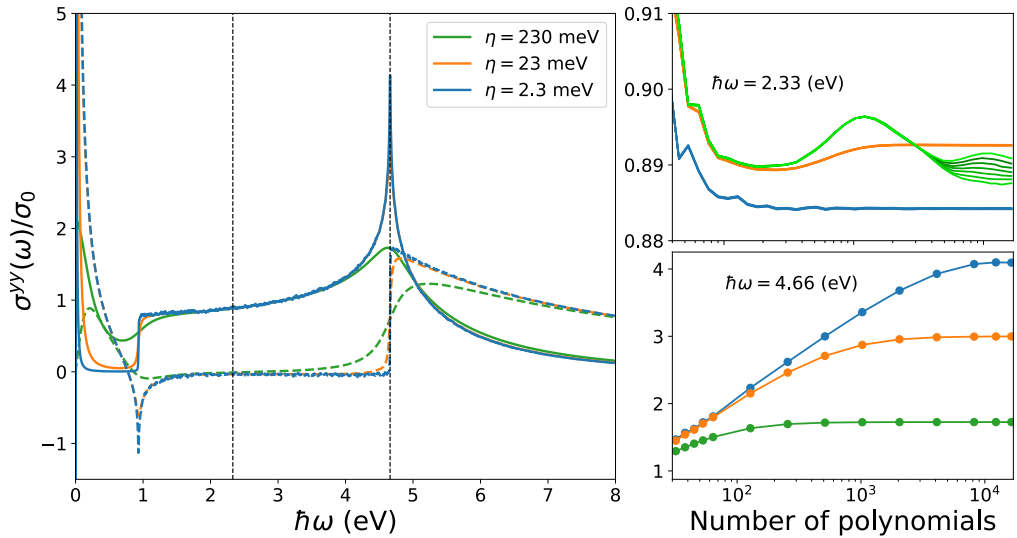


Figure 4.13: First-order optical  $yy$  conductivity per spin of graphene for  $M = 16384$  and  $L = 2048$  now as a function of the broadening parameter  $\eta$ . The remaining parameters remain the same as for Fig. 4.7. The solid (dashed) curves represent the real (imaginary) part of the conductivity. The legend shows the values for the broadening parameter. The lower inset shows the evolution of the value of the conductivity for each  $\eta$  as the number of polynomials is increased for  $\hbar\omega = 2.33\text{eV}$ . The upper inset shows the same thing but for several very close frequencies around  $\hbar\omega = 4.66\text{eV}$ . The darker curves correspond to higher frequencies.

#### 4.4.7 Considerations on efficiency

Our formalism provides a very general framework with which to compute the nonlinear optical response up to any order. Once the formulas were obtained, we chose to use spectral methods to perform the computation. This is not always the most efficient approach: for systems with translation invariance and periodic boundary conditions, we can specify the formulas for  $\mathbf{k}$ -space and then perform the explicit integration. Then, for a given set of parameters (temperature, broadening, Fermi energy) the computation time will scale as  $L^D N_\omega$  where  $L^D$  is the number of points in the Brillouin zone (which is also the number of lattice sites),  $D$  is the dimensionality and  $N_\omega$  is the number of frequencies we want to compute. For each  $\mathbf{k}$  and each frequency, this method comes down to diagonalizing the Bloch Hamiltonian  $H_{\mathbf{k}}$ , and then summing over the whole set of  $\mathbf{k}$  points. This method is extremely efficient at computing the optical conductivity at any order using the velocity gauge.

Using spectral methods, the computation is split into the calculation of the Chebyshev moments and the final matrix product of the  $\Gamma$  matrices with the  $\Lambda$  matrices. The first part is the most demanding and is independent of the parameters mentioned above. Its computation time scales as  $L^D N^{n+1}$ , where  $n$  is the order of the conductivity and  $N$  is the number of Chebyshev polynomials. More concretely, if we want to calculate the conductivity for a certain  $\eta$ , using  $N \sim \lambda^{-1} \sim N_\omega$ , we find that the  $\mathbf{k}$ -space calculation scales much more favorably.

If the system has no translation invariance,  $\mathbf{k}$ -space integration is no longer useful and we would need to numerically diagonalize the full Hamiltonian. This method scales as  $L^{3D} N_\omega$  which is highly unfavorable and because of that we would be limited to very small systems. In this context, spectral methods become the preferred choice.

For the examples used in this chapter, the computation of the second-order conductivity with the  $\mathbf{k}$ -space formalism in a system with  $L = 2048$  took around 2 minutes on a Xeon E5-2650 with 16 threads. In comparison, the same computation took 3 hours for translation-invariant gapped graphene with 2048 polynomials, and 70 hours for gapped graphene with Anderson disorder/vacancies and 512 polynomials. Despite the discrepancy in computational efficiency, we know of no other more efficient way to compute the nonlinear optical conductivity for disordered systems.

# 5 Stochastic conductance

In this chapter, we will see how to compute the conductance of a sample attached to finite leads by using a unitary time evolution. This process is numerically very different from the standard techniques to obtain the conductance. Using finite leads brings the problem down to a conceptually simple unitary time evolution which nevertheless yields the correct Landauer plateau as a quasi steady-state. Following Pires [50], we have generalized the method to higher dimensions and arbitrary lattices, and introduced the average over cross sections. This average allows us to express the current across the device as a trace over several sites, which then becomes amenable to using random vectors for a stochastic evaluation of the trace. Just like what was done for Kubo's formula, this single process brings the algorithm's complexity down to  $\mathcal{O}(N)$  and is highly parallelizable in real space. Since the object of study is the time-dependent current, transient and optical processes are able to be studied naturally. Besides the study of time-dependent processes, this also brings up the possibility of simulating real diffusive regimes in a wider range of disorder parameters. The open source code for this is on [github](#) and is also implemented in KITE [3], to be publicly released in a later version.

## 5.1 Setup

To begin exploring the problem, we first need to characterize the system and calculate some preliminary objects. Ultimately, we want to determine the current across a sample which is connected to two leads. The leads are understood as perfectly periodic metallic contacts that connect to the sample, and the sample is the system we want to study. This could be, for example, a graphene flake, a quantum dot, etc. For simplicity though, we always assume that both the sample and the leads are part of the same underlying lattice and that the width (cross-section) is always the same across the whole system. The more general case of arbitrary leads and sample is obtained through a straightforward generalization but will not be treated here. Unless stated otherwise, the leads are finite but sufficiently large for the results not to depend on their size.

This is intrinsically a non-equilibrium process, driven by a perturbation applied to a system in thermal equilibrium. The formal treatment of this setup is typically done in one of two different ways:

1. The partition-free (see Fig. 5.1), where the chemical potential is fixed across the whole system. The perturbation is an applied static electric field which manifests itself as a local electric potential in the Hamiltonian.

2. The partitioned approach, where each lead is initially detached from the sample and has a different chemical potential (see Fig. 5.2). The perturbation consists of connecting the leads to the sample.

Both approaches yield the same equilibrium current [50], but the transient regimes are different. In this section both will be briefly discussed, but only the partition-free one will be used throughout the chapter for the sake of simplicity.

### 5.1.1 Partition-free

In equilibrium, there is no electric field applied to the sample and the net current through the sample is zero. This does not necessarily mean that the local current is zero (for example, the presence of a magnetic field would change this picture), it only means that there is no net charge flux from one lead to the other. The Hamiltonian of this unperturbed system does not need to discriminate between leads and sample and is in general

$$\mathcal{H}_0 = \sum_{ij} H_{ij}^0 c_i^\dagger c_j$$

where  $i, j$  can either be part of the sample or the lead. Fixing the chemical potential  $\mu$  and working in the grand canonical ensemble defines the density matrix of the system (or the lesser Green's function at equal times, in the formalism of chapter 4)

$$\rho_{ji}(t) = \langle c_i^\dagger(t) c_j(t) \rangle.$$

where the average  $\langle \dots \rangle$  is understood to be done with respect to  $\mathcal{H}_0$ . At time  $t = 0$  the electric field is suddenly switched on (see Fig. 5.1).

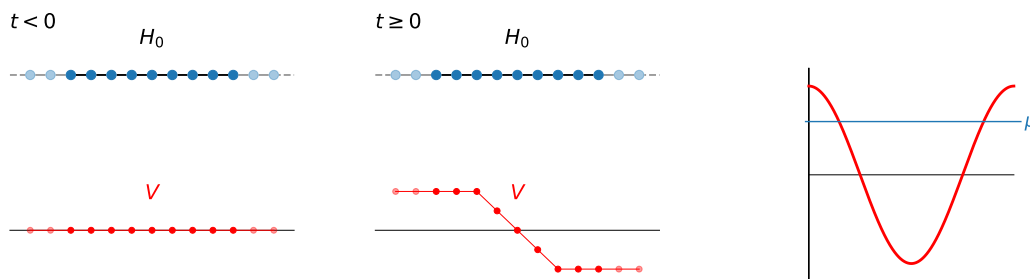


Figure 5.1: Partition-free setup.

It is included through a local electric potential term  $V_i$  in the Hamiltonian. The full Hamiltonian takes the form

$$\mathcal{H} = \mathcal{H}_0 + \sum_i V_i c_i^\dagger c_i.$$

The corresponding single-particle counterpart is  $H = H_0 + V$  and the time evolution

operator from  $t_0$  to  $t$  is done with the full Hamiltonian

$$U(t, t_0) = \exp\left(-\frac{i}{\hbar} H(t - t_0)\right)$$

which includes the perturbation, but the average is done with respect to the Hamiltonian at time  $t < 0$ , which does **not** include the perturbation. Therefore, it is useful to introduce two changes of variables. The first moves from the real-space basis  $\{|n\rangle\}$  to the eigenbasis of  $H$ , composed of states  $\{|\psi_m\rangle\}$  and the corresponding set of operators  $\{d_m\}$ :

$$c_j = \sum_m \langle j | \psi_m \rangle d_m$$

which takes care of the time evolution

$$c_j(t) = \sum_m \langle j | \psi_m \rangle d_m(t) = \sum_m \langle j | e^{-iHt/\hbar} | \psi_m \rangle d_m.$$

The other changes from the eigenbasis of  $H$  to that of  $H_0$ , composed of states  $\{|\phi_b\rangle\}$  and corresponding set of operators  $\{\gamma_b\}$

$$d_m = \sum_b \langle \psi_m | \phi_b \rangle \gamma_b$$

which takes care of the thermal average:

$$\langle \gamma_a^\dagger \gamma_b \rangle = \delta_{ab} f(\varepsilon_a^0) = \langle \phi_b | f(H_0) | \phi_a \rangle = \rho_{ab}^0$$

where  $\varepsilon_a^0$  is the eigenvalue corresponding to eigenstate  $|\phi_b\rangle$  of  $H_0$  and  $f$  is the Fermi function. This defines the initial density matrix  $\rho_0$ . With these ingredients, it's easy to show that the expectation value becomes

$$\langle c_i^\dagger(t) c_j(t) \rangle = \langle j | e^{-iHt/\hbar} \rho_0 e^{iHt/\hbar} | i \rangle = \langle j | \rho(t) | i \rangle.$$

As expected, when  $V = 0$ ,  $H = H_0$  and  $f(H_0)$  commutes with the time evolution operators, rendering the whole expression time-independent.  $\rho(t)$  can be interpreted as the density matrix in time  $t$  in the Schödinger Picture.

### 5.1.2 Partitioned

In the partitioned approach, we have to separate the unperturbed Hamiltonian into the left lead, the right lead and the sample (see Fig. 5.2):

$$\mathcal{H} = \mathcal{H}_L + \mathcal{H}_R + \mathcal{H}_S$$

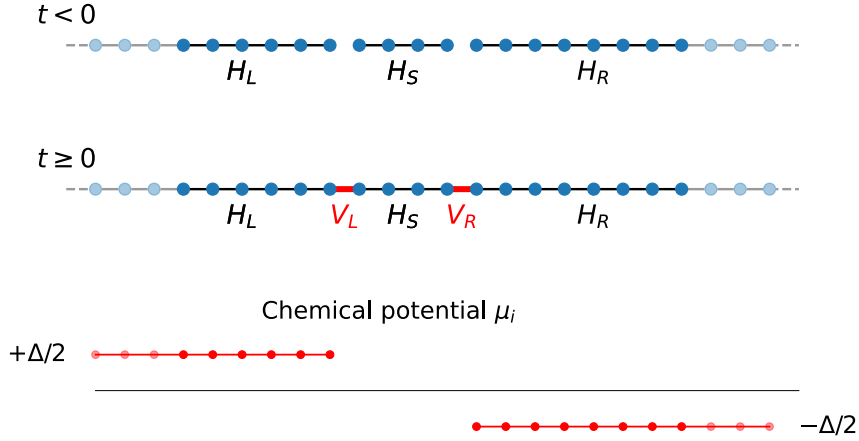


Figure 5.2: Partitioned setup. The chemical potential is not specified inside the sample because it is not needed. In effect, the sample can be considered to be deprived of particles initially.

where

$$\begin{aligned}\mathcal{H}_L &= \sum_{ij \in L} H_{ij}^L c_i^\dagger c_j \\ \mathcal{H}_R &= \sum_{ij \in R} H_{ij}^R c_i^\dagger c_j \\ \mathcal{H}_S &= \sum_{ij \in S} H_{ij}^S c_i^\dagger c_j\end{aligned}$$

are the corresponding Hamiltonians of each section. All these Hamiltonians commute with one another and before the perturbation is turned on, each can have a different chemical potential. This defines the density matrix as the direct sum of the density matrices of each subspace. No current can flow from one lead to the other because they are disconnected. The perturbation is simply the connection between each lead and the sample

$$\mathcal{V} = \sum_{i \in L, j \in S} V_{ij}^L c_i^\dagger c_j + \sum_{i \in S, j \in R} V_{ij}^R c_i^\dagger c_j.$$

$V_{ij}^L$  connects states  $i$  of the left lead to states  $S$  of the sample, and  $V_{ij}^R$  connects states  $i$  of the sample to states  $j$  of the right lead. The time evolution of the density matrix has the same formal expression as the partition-free case, just with different operators. This is the setup used by Caroli [28].

## 5.2 Nonlinear local current

Let us now focus only on the partition-free approach. The starting point of this discussion is the notion of a local current. We want to build up to the concept of current across a sample, so this is the smallest building block we can use towards that goal. In a tight-binding setup described by a general Hamiltonian  $H$

$$\mathcal{H} = \sum_{ij} H_{ij} c_i^\dagger c_j,$$

the local current is measured as the amount of charge that gets transferred from one state  $i$  to another adjacent state  $j$ . By adjacent in this context, we mean that  $i$  and  $j$  are geometrically close and that there is a nonzero Hamiltonian matrix element between them:  $H_{ij} \neq 0$ . The number of electrons in state  $i$  at time  $t$  is,

$$\langle \mathcal{N}_i \rangle = q \langle c_i^\dagger c_i \rangle$$

keeping in mind that  $i$  actually stands for a superindex which can include spin, sublattice and orbital degrees of freedom. Using the equation of motion for  $\mathcal{N}_i$ , we find the rate at which electron density changes in state  $i$ :

$$\frac{d}{dt} \mathcal{N}_i = \frac{i}{\hbar} [\mathcal{H}, \mathcal{N}_i] = -\frac{iq}{\hbar} \sum_j \left[ H_{ij} c_i^\dagger c_j - H_{ij}^* c_j^\dagger c_i \right] \quad (5.1)$$

Defining the current from site  $i$  to  $j$  as

$$\mathcal{I}_{ij} = \frac{iq}{\hbar} \left( H_{ij} c_i^\dagger c_j - H_{ij}^* c_j^\dagger c_i \right),$$

equation 5.1 is better understood as a continuity equation  $\dot{\mathcal{N}}_i = -\sum_j \mathcal{I}_{ij}$ . The sign has been chosen as such for the following reason. When  $\langle \mathcal{N}_i \rangle$  is increasing, charge is moving from  $j$  to  $i$ . Since  $\mathcal{I}_{ij}$  is defined as current from  $i$  to  $j$ , it has to be negative in this situation. The minus sign ensures that a negative  $\mathcal{I}_{ij}$  contributes positively to  $\langle \mathcal{N}_i \rangle$ . Let's define the single-particle local current operator from site  $i$  to  $j$  as

$$I_{i \rightarrow j} = \frac{iq}{\hbar} \left( H_{ij} |i\rangle \langle j| - H_{ij}^* |j\rangle \langle i| \right)$$

so that

$$\mathcal{I}_{ij} = \sum_{kl} (I_{i \rightarrow j})_{kl} c_k^\dagger c_l$$

defines a more natural operator which can be traced over in the end. The expectation value of this many-body operator as a function of time can be expressed in terms of the density matrix

$$\langle \mathcal{I}_{ij}(t) \rangle = \text{Tr} [I_{i \rightarrow j} \rho(t)] = \text{Tr} \left[ I_{i \rightarrow j} e^{-iHt/\hbar} f(H_0) e^{iHt/\hbar} \right]. \quad (5.2)$$

So far, this result is exact. The time evolution operators and the Fermi operator can be expanded in Chebyshev polynomials (eqs. 2.18 and 2.14) with the corresponding Hamiltonians  $H$  and  $H_0$  respectively, and the full nonlinear current across a bond is obtained. This is usually the starting point for the Kubo, Keldysh and Landauer formalisms. In the Kubo formalism, linear response is assumed.

For practical purposes, the whole trace does not need to be calculated, as the local current only has support on a very small region of the Hilbert space. In fact, only states  $|i\rangle$  and  $|j\rangle$  will contribute. Therefore, the current can be obtained as follows:

$$\langle \mathcal{I}_{ij}(t) \rangle = \langle i | I_{i \rightarrow j} | j \rangle \langle j | \rho(t) | i \rangle + \langle j | I_{i \rightarrow j} | i \rangle \langle i | \rho(t) | j \rangle.$$

Furthermore, noting that the second term is the complex conjugate of the first, we get

$$\langle \mathcal{I}_{ij}(t) \rangle = 2\text{Re} \langle i | I_{i \rightarrow j} | j \rangle \langle j | \rho(t) | i \rangle = 2\text{Re} \langle i | I_{i \rightarrow j} \rho(t) | i \rangle,$$

effectively reducing the process of evaluating the trace to a single computation. The numerical complexity of calculating this formula is  $\mathcal{O}(ZDN_P(N_F + N_T))$  where  $N_P$  is the number of points in time where the current is observed,  $N_F$  is the number of Chebyshev polynomials to expand the Fermi operator,  $N_T$  is the number of Chebyshev operators to expand the time evolution operator from two consecutive current time observation points,  $D$  is the size of the Hilbert space and  $Z$  is the coordination of the lattice.

### 5.3 Linear local current

Just like in chapter 4, the linear current can be obtained more easily in the Interaction Picture (IP), since the time evolution of the wave functions is given by the perturbation  $V$ . In the IP, the wavefunctions, operators and density matrix are

$$\begin{aligned} |\psi_I(t)\rangle &= e^{iH_0 t/\hbar} |\psi(t)\rangle \\ A_I(t) &= e^{iH_0 t/\hbar} A e^{-iH_0 t/\hbar} \\ \rho_I(t) &= \sum_{\psi} p_{\psi} |\psi_I(t)\rangle \langle \psi_I(t)|. \end{aligned}$$

The Schrödinger equation for the wavefunctions is

$$i\hbar \frac{\partial}{\partial t} |\psi_I(t)\rangle = V_I(t) |\psi_I(t)\rangle$$

and can be integrated to first order in  $V_I$

$$|\psi_I(t)\rangle = |\psi_I(0)\rangle + \frac{1}{i\hbar} \int_0^t dt' V_I(t') |\psi_I(t')\rangle.$$

Plugging this into the expression of the density matrix and keeping terms only up to first

order in  $V$ , we get

$$\rho_I(t) = \rho_0 + \frac{1}{i\hbar} \int_0^t dt' \left[ e^{iH_0 t'/\hbar} V \rho_0 - \rho_0 V e^{-iH_0 t'/\hbar} \right].$$

Finally, the expectation value of the local current operator, to first order in  $V$  is

$$\begin{aligned} \langle \mathcal{I}_{ij}^{\text{lin}}(t) \rangle &= \text{Tr} [\rho_0 I_{i \rightarrow j}] + \\ &+ \frac{1}{i\hbar} \int_0^t dt' \text{Tr} \left[ e^{iH_0 t'/\hbar} I_{i \rightarrow j} e^{iH_0(t'-t)/\hbar} V \rho_0 - \rho_0 V e^{-iH_0(t'-t)/\hbar} I_{i \rightarrow j} e^{-iH_0 t'/\hbar} \right]. \end{aligned}$$

This can be simplified further by realizing that without the perturbation there is no current, so the first term vanishes<sup>1</sup>. The two next terms are complex conjugates of each other, so

$$\langle \mathcal{I}_{ij}^{\text{lin}}(t) \rangle = \frac{2}{\hbar} \int_0^t dt' \text{ImTr} \left[ \rho_0 e^{iH_0 t'/\hbar} I_{i \rightarrow j} e^{iH_0(t'-t)/\hbar} V \right].$$

Finally, with a change of integration variables and rotating the trace we get the final form:

$$\langle \mathcal{I}_{ij}^{\text{lin}}(t) \rangle = \frac{2}{\hbar} \int_0^t d\tau \text{ImTr} \left[ I_{i \rightarrow j} e^{-iH_0 \tau/\hbar} V e^{iH_0 t/\hbar} \rho_0 \right]. \quad (5.3)$$

This linearized version of 5.2 can also be obtained directly from the Kubo formula. This formula has one big advantage in comparison to the previous one: the current operator is on the left-most side of the trace and the density matrix is on the right-most side. The first property means that only two terms of this trace will contribute,  $i$  and  $j$ , and the second property means that the Fermi operator only needs to be evaluated once for all times. The only downside is the need to perform an integral in time, but given the computational cost of the Fermi operator and the fact that several times have to be computed anyway, this is not a big problem.

With regards to numerical complexity, this formula is much simpler to compute. To calculate  $N_P$  time points with this method, one would require  $N_P^2/2$  evaluations of the integrand, each requiring one Chebyshev expansion for each time evolution operator, for a total scaling of  $N_P^2 N_T + N_F$ . However, there is redundancy here, because integrating over  $\tau$  requires calculating the same thing several times. This redundancy can be eliminated, bringing down the numerical complexity to  $\mathcal{O}(ZD(2N_P N_T + N_F))$ . Because  $N_F$  is no longer multiplied by  $N_P$ , the scaling is much more favorable than the nonlinear case.

## 5.4 Comparison with other formalisms

Equations 5.2 and 5.3 have a close resemblance to the starting point of the Kubo, Keldysh and Landauer formalisms. In fact, the Landauer formula can be obtained from the Keldysh formalism by using eq. 5.2 in the partitioned setup.

<sup>1</sup>For a time-dependent perturbation such as the electric field in the velocity gauge, this cannot be disregarded. A nonzero magnetic field also changes this picture.

### 5.4.1 Landauer formula

For further reference, it is useful to get a clear picture of all the objects involved in the Landauer formula. For a detailed technical derivation, see [124]. We begin with the leads disconnected from the sample, each lead in equilibrium with a particle reservoir at chemical potential  $\mu$  and no applied external electric field. The left (right) lead is characterized by a Hamiltonian  $\mathcal{H}_L$  ( $\mathcal{H}_R$ ) and both are characterized by a Fermi function as usual  $f(\varepsilon) = (1 + \exp(\beta(\varepsilon - \mu)))^{-1}$ . See Fig. 5.2 for a visual reference. Let's assume that the leads are noninteracting<sup>2</sup> and define  $H_L$  and  $H_R$  as the single-particle counterparts of  $\mathcal{H}_L$  and  $\mathcal{H}_R$ , respectively. The retarded surface Green's functions  $g_L^r$  and  $g_R^r$  are defined at this point as the submatrix of the retarded Green's matrix at the last slice before the sample. The disconnected sample (with Hamiltonian  $\mathcal{H}_S$ ) sits in the middle of both leads. For completeness, it can be assumed to be connected to a particle reservoir at chemical potential  $\mu$  too, but this is largely irrelevant. In here we are also going to assume the sample to be noninteracting, so we can define  $H_S$  as the single-particle counterpart of  $\mathcal{H}_S$ .

When an electric field  $\mathbf{E}$  is applied only between the leads, a potential energy drop  $\Delta V$  can be defined between them. At this point, they are not yet connected to the sample, but the effect of the electric field can be taken into account by raising the energy of the right lead and right reservoir by  $\Delta V/2$  and that of the left lead and reservoir by  $-\Delta V/2$ . This adds a constant term to each Hamiltonian but also shifts the Fermi function because the reservoirs were also changed. We can thus define the Fermi function of the left lead  $f_L(\varepsilon) = f(\varepsilon + \Delta V/2)$  and of the right lead  $f_R(\varepsilon) = f(\varepsilon - \Delta V/2)$ . The particle reservoir of the sample can be disregarded because the Keldysh relation [124] allows us to write the steady-state value of the sample's density matrix in terms of that of the leads'. Physically, this means that, while the transient regime depends on the specific details of the initial distribution of states of the sample, the steady state does not. It is completely determined by the leads' reservoirs. For this reason, we can simply ignore it.

Coming back to the full picture, these Fermi functions define the initial density matrix  $\rho_0$  which makes no mention to the sample and only has matrix elements within each of the leads separately:

$$\rho_0 = f\left(H_L + \frac{\Delta V}{2}\hat{\mathbf{1}}_L\right) + f\left(H_R - \frac{\Delta V}{2}\hat{\mathbf{1}}_R\right).$$

Here,  $\hat{\mathbf{1}}_L$  and  $\hat{\mathbf{1}}_R$  represent the identity operators restricted to the left and right leads, respectively.

The initial distribution of states is now completely described and the system is in thermal and chemical equilibrium with the respective reservoirs. Next, we turn on the perturbation  $\mathcal{V}$  by connecting the leads to the sample at  $t = 0$ . The connection to the left (right) lead is described by the perturbation  $\mathcal{V}_L$  ( $\mathcal{V}_R$ ) such that  $\mathcal{V} = \mathcal{V}_L + \mathcal{V}_R$ .

---

<sup>2</sup>This is a reasonable assumption, since the leads are assumed to be metallic.

This perturbation defines the leads' self-energies

$$\begin{aligned}\Sigma_L^r(\varepsilon) &= V_L g_L^r(\varepsilon) V_L^\dagger \\ \Sigma_R^r(\varepsilon) &= V_R g_R^r(\varepsilon) V_R^\dagger\end{aligned}$$

which define the level-width functions

$$\Gamma_{L,R}(\varepsilon) = i \left( \Sigma_{L,R}^r(\varepsilon) - \Sigma_{L,R}^{r\dagger}(\varepsilon) \right).$$

After a transient regime, the current across the sample will achieve a steady state given by the Landauer formula

$$I = \frac{e}{2\pi\hbar} \int_{-\infty}^{\infty} d\varepsilon (f_L(\varepsilon) - f_R(\varepsilon)) T(\varepsilon) \quad (5.4)$$

where  $T(\varepsilon)$  is interpreted as the transmission probability from one lead to the other and is given by

$$T(\varepsilon) = \text{Tr} [\Gamma_L(\varepsilon) G^r(\varepsilon) \Gamma_R(\varepsilon) G^a(\varepsilon)]$$

and  $G^r$  ( $G^a$ ) is the retarded (advanced) Green's function of the entire system. In this formulation, the potential drop is included inside the Hamiltonian. The linearized version of the Landauer formula at zero temperature does not depend on the particular shape of the electric potential drop inside the sample and is given by

$$I_{\text{lin}} = \frac{e\Delta V}{2\pi\hbar} T(\mu) \quad (5.5)$$

which defines the conductance by  $I_{\text{lin}} = \sigma\Delta V$ .

### 5.4.2 Bulk Kubo's formula

The Kubo formula for the conductivity is a bit different; the operator being estimated is not the local current but the total current operator, and the perturbation is an electric field inside the sample. Since no accumulation of charge is assumed, the current across each cross section should be the same, so this can be thought of as an average over cross sections. Done in this fashion, the Kubo formula is proven to yield the same result for the conductance as the Landauer formula [129]. This is not quite the same thing as usually found in numerical simulations of the Kubo formula for the **conductivity**. The sample is extended to be the whole system (no leads), which is then made periodic, and the Kubo formula is specified for a perturbation which consists of a uniform vector potential. This vector potential is responsible for the uniform electric field across the sample. It is clear that this bulk formulation cannot yield the same thing as the one with leads because in the perfectly clean limit, the physical picture is that of Bloch oscillations in the sample, not steady-state ballistic transport. Bloch oscillations are very sensitive to disorder, so

it is expected that the introduction of even the smallest amount of disorder break these oscillations. Furthermore, since this formula speaks of a conductivity, it is also expected that the system be in a diffusive regime.

## 5.5 Time-dependent current across a tight-binding chain

Before moving on, it is instructive to explore the time-dependent current in one of the simplest examples: the one-dimensional tight-binding chain (1D TB chain) [50]. Despite its simplicity, the 1D TB chain will allow us to see the quasi-stationary current developing and competing with the Bloch oscillations. The unperturbed Hamiltonian reads

$$\mathcal{H}_0 = t \sum_{i=0}^{N-1} [c_i^\dagger c_{i+1} + c_{i+1}^\dagger c_i]$$

where  $c_i^\dagger$  ( $c_i$ ) creates (annihilates) an electron in site  $i$ . The perturbation is

$$\mathcal{V} = \sum_{i=0}^{N-1} V_i c_i^\dagger c_i$$

such that

$$V_i = \begin{cases} \frac{\Delta V}{2} & \text{if } i \leq S \\ \frac{\Delta V}{2} + \frac{S-i}{R-S-1} \Delta V & \text{if } S < i < R \\ -\frac{\Delta V}{2} & \text{if } i \geq R. \end{cases}$$

$S$  is the left-most site belonging to the sample and  $R$  is the left-most site belonging to the right lead. This potential generates an electric field which is zero in the leads but uniform inside the sample and pointing left, so the electrons will move to the right (increasing  $i$ ). Now we just need to select a bond over which to calculate the nonlinear local current  $\langle \mathcal{I}_{ij}(t) \rangle$  (eq. 5.2) as a function of time. Since we expect a uniform current to develop across the sample, we can choose  $i$  to be a site in the middle of the sample and  $j$  to be the site to its right, that is  $j = i + 1$ . The results are summarized in Fig. 5.3.

In this simple example, without disorder, we see a general trend. At  $t = 0$ , the perturbation is turned on and a transient regime develops while the current ramps up. The larger the drop in potential, the faster the current ramps up, but it achieves a steady state in the same amount of time (Fig. 5.3 a)). The value of the current at the steady state is exactly the one obtained from the nonlinear Landauer formula from eq. 5.4 (black dashed lines), which is not surprising because they measure the same thing. As the potential drop is increased further, the agreement is still perfect, but a secondary plateau develops before the main one (panel b)). The value of the current at this intermediary plateau is given by the **linear** Landauer formula from eq. 5.5 (red dashed line).

For large drops in potential across the leads (larger than the bandwidth  $4t$ ), it is no longer possible to connect states from one lead to the other. Instead, the strong electric field localizes the eigenstates into Wannier-Stark states which are responsible for the Bloch

## 5.5 Time-dependent current across a tight-binding chain

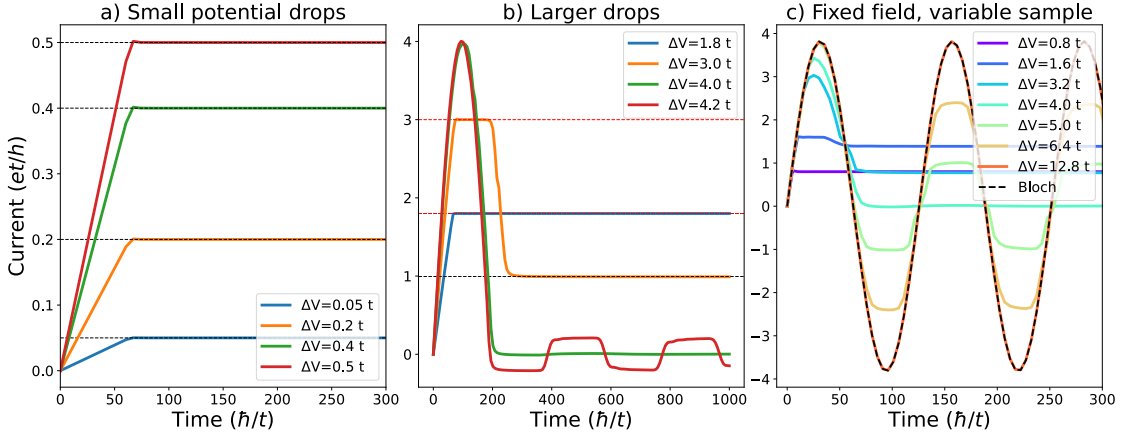


Figure 5.3: Current as a function of time for a 1D TB model with different values of the potential drop. The (red) black dashed lines represent the (linear) nonlinear Landauer current.

oscillations [44, 45] that start developing (Fig. 5.3 b). These partial Bloch oscillations develop into full Bloch oscillations once the drop is sufficiently large (Fig. 5.3 c)). Fixing the electric field and changing the sample size, we can see more clearly that reminiscing Bloch oscillations are the transient regime for the Landauer current. For all intents and purposes, the leads in these three examples are infinite, in the sense that the results do not change if the leads' size (4096) is further increased.

While the development of a steady-state current into Bloch oscillations is expected, one interesting aspect remains to be explained - the secondary plateau seen at  $\Delta V = 3t$ . In light of Fig. 5.3 b) and c), the secondary plateau develops as part of a partial Bloch oscillation, and its value corresponds exactly to the linearized Landauer value for the current. A clearer picture appears when we look at the charge density as a function of time at each point of the system (Fig. 5.4) for a chemical potential of  $\mu = 0.3t$ .

With Fig. 5.4 in mind, the electric field is uniform and applied only inside the sample, so the immediate effect in the charge density is to accumulate charge near the interface between the leads and the sample. This charge accumulation is propagated into the leads as time progresses and happens for every value of  $\Delta V$ .

To understand the next effect, it is useful to divide the charge inside the sample into several bits, each of which gets affected by the electric field. Under the semiclassical picture of Bloch oscillations, each of these bits tries to develop into a Bloch oscillation of amplitude  $A = 4t/eE$  [43]. Let's try to analyze what happens to the current qualitatively:

- If the electric field  $E$  is small, then the amplitude of oscillation is large, and once this portion of charge hits the right lead, it gets absorbed and is not allowed to oscillate.
- For stronger electric fields, when  $A < L_S/2$  (or  $\Delta V > 2t$ ), the pieces of charge inside the sample that are closest to the leads can perform a half-oscillation but get absorbed by the left lead when they come back. This portion of charge that is going into the left lead instead of the right lead may be the reason why a secondary plateau develops

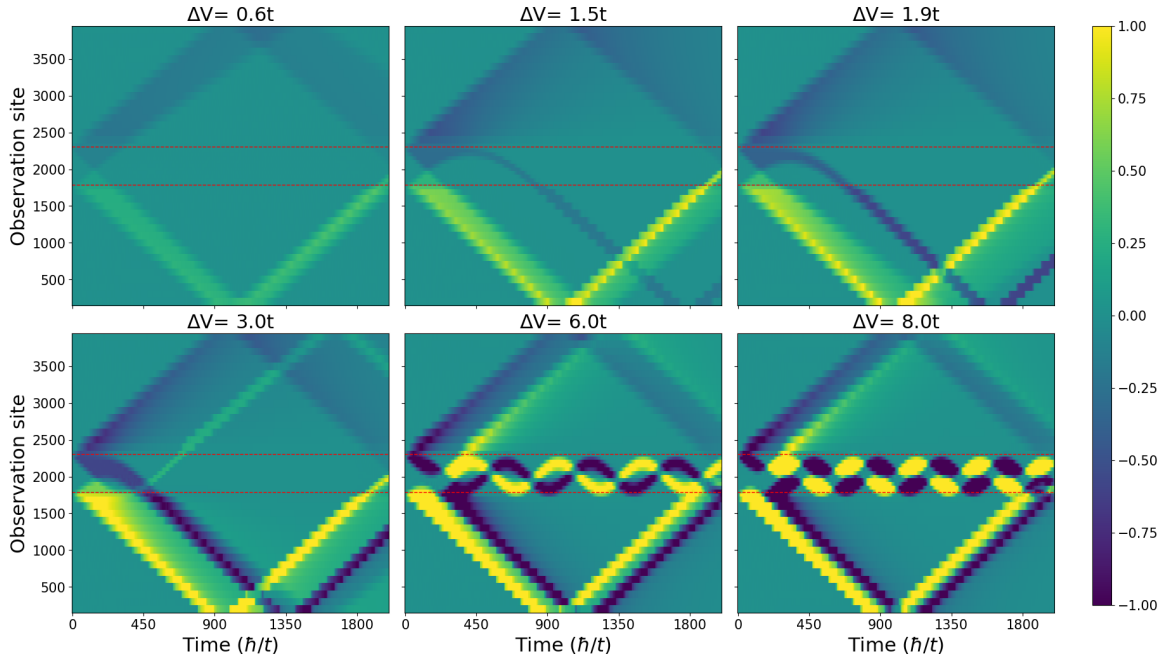


Figure 5.4: Charge across different parts of the system as a function of time, for several values of the potential drop across the leads. The region between the red dashed lines represents the sample. The chemical potential is  $\mu = 0.3t$ . The points within the two red lines have a higher resolution than the ones outside.

at the current given by the linear Landauer formula. Before it changes direction, it is contributing to the current going to the right. Since the linear Landauer formula is valid for very small values of  $\Delta V$ , a good “impedance matching” is expected between the sample and the leads, and all the charge going through the center of the sample will go through the leads. After this portion of charge inverts direction, it stops contributing to the linear Landauer current, and the nonlinear current will be the one to accurately describe it.

- For stronger fields still, the amplitude of oscillation becomes shorter, and the pieces of charge further away from the leads are allowed to start oscillating. When this amplitude of oscillation is equal to the length of the sample, then Bloch oscillations are allowed because the portion of charge in the middle of the sample can now complete a full oscillation. This happens when  $\Delta V = 4t$ . As the electric field becomes increasingly stronger, more and more portions are allowed to oscillate and the Bloch current develops into a perfect sinusoidal shape.

While this analysis is able to capture the main phenomena going on in Fig. 5.4, it is unable to accurately describe the energy scales at which they start to appear. For example, at intermediate electric fields, the half Bloch oscillation should start to appear only when  $\Delta V > 2t$ , but we see it already at  $\Delta V = 1.5t$ . This might be attributable to the dispersion of these charge packets, but further investigation would be required to justify it.

### 5.5.1 The role of the leads

In the previous section, we saw that meaningful currents can be obtained by using sufficiently large leads. By sufficiently large, it is meant that the results no longer change when the lead size is further increased. On the one hand, we want the leads to be as large as possible to achieve this. On the other hand, larger leads mean a larger Hilbert space which makes the numerical simulations more costly. If this method is to become a useful tool in the calculation of the conductance, the leads cannot be arbitrarily large. In this section, we want to clarify what happens when the leads are finite.

Figure 5.4 provides the first clue for the role of the lead size. The charge density wave propagates at the Fermi velocity  $v_F$  inside the leads and gets reflected at the boundaries of the leads. If we wait long enough, the current will invert. Therefore, we want to fix our time observation window such that the reflected current never reaches the sample. The maximum observation time  $\mathcal{T}_{\max}$  should then be smaller than the time that it takes for the charge wave to return, that is  $2L/v_F$ , where  $L$  is the lead size. More precisely, the reflected current should arrive at  $\mathcal{T}_1 = (2L + L_S/2)/v_F$ , taking into account the time that the most advanced portion of charge takes to reach the middle of the sample after reflecting, assuming that's the observation point. The inversion process stops once the reflected current has traversed the whole sample, at  $\mathcal{T}_2 = \mathcal{T}_1 + L_S/v_F$ . Fig. 5.5 shows precisely this behavior. The dashed lines represent  $\mathcal{T}_1$  and the dot-dashed lines  $\mathcal{T}_2$ .

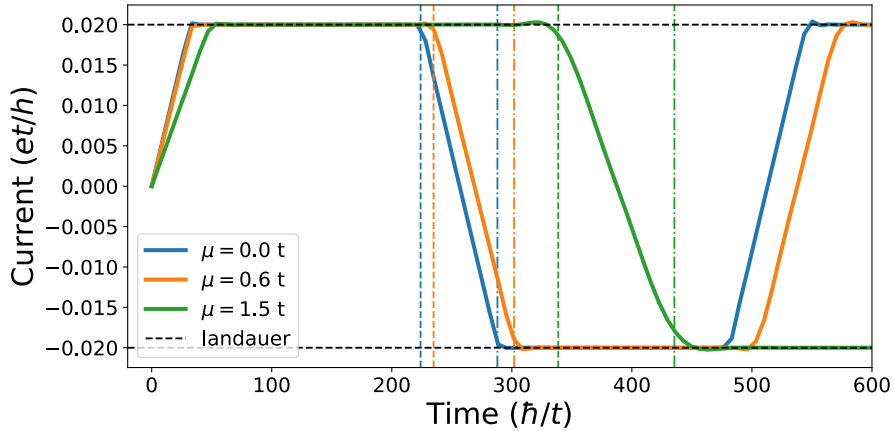


Figure 5.5: Current as a function of time for several Fermi energies, small leads and a sufficiently large time observation window to be able to see the reflected current arrive at the center of the sample.

There is another, small but nontrivial effect that happens due to the finite size of the leads. If we zoom closely into the current plateau, it is not entirely constant. It actually oscillates, with a frequency proportional to the potential drop (Fig. 5.5.1 a) and an amplitude inversely proportional to the lead size (Fig. 5.5.1 b), that is  $I(t) - I_{\text{plateau}} \approx \Delta V L^{-1} \sin(\Delta V t / \hbar)$ . This is a very fine effect that requires a much higher numerical resolution to see than the previous graphs shown. While the plateau can be adequately resolved with around  $2 \times 10^3$  Chebyshev polynomials in the expansion of the Fermi function, these

oscillations require at least  $5 \times 10^4$  polynomials to converge.

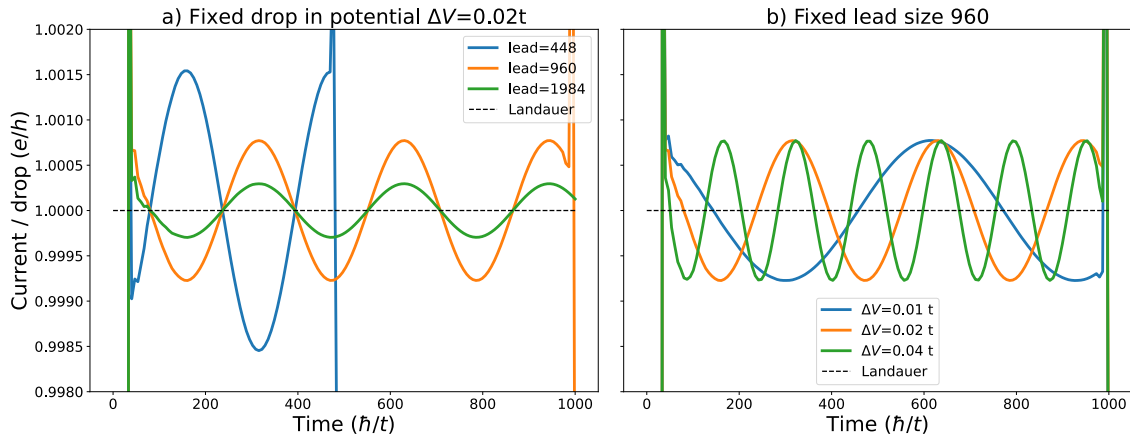


Figure 5.6: Close-up of the current at the plateau. On the left, the drop in potential is fixed to  $\Delta V = 0.02t$  and the lead size is varied. On the right, the lead size is fixed to 960 and the drop in potential is varied. In both cases, the current has been rescaled by  $\Delta V$ .

Despite their appearance, these oscillations should not be attributed to some sort of reminiscent Bloch oscillations. They are artificial in the sense that for sufficiently large leads, the oscillations are negligible. Instead, they are more likely to be related to the discreteness of the momentum basis describing the states of each lead. This is similar to the approximation of a square wave by its Fourier transform. In the limit of an infinite sum, the plateau is perfectly flat, but if only a finite amount of terms is kept in the sum, the oscillations are still visible.<sup>3</sup>

Interestingly, these oscillations only show up when the numerical resolution is sufficiently large and typically requires an order of magnitude better resolution to resolve than the plateau. Since they are physically artificial anyway, then one should use enough resolution to resolve the plateau completely, but not more than that, lest the nonphysical oscillations be resolved.

## 5.6 Generalization to cross sections

When the system is one-dimensional, the local current immediately provides the current across the system. The generalization to higher dimensions is straightforward when we think about the physical system being studied. We think of a sample connected to two leads, and current flowing from one lead to the other. The generalization to higher dimensions consists of a sum of the local currents across any cross section of the leads or the sample (see Fig. 5.7). Let  $J$  be this current and let  $\langle ij \rangle$  be the set of bonds which connects both sides of the cross section, such that  $i$  is on one side of the cross section and  $j$  is on

<sup>3</sup>This is not related to the Gibbs phenomenon because it is not at the discontinuity.

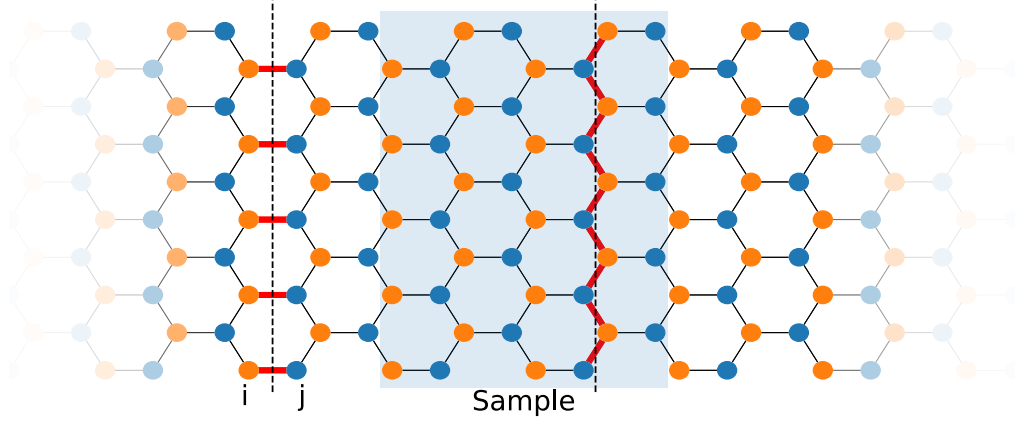


Figure 5.7: Two different cross sections across an armchair graphene nanoribbon. The first cross section only crosses horizontal bonds, but the second cross section crosses more generic bonds.  $i$  and  $j$  denote a site to the left and to the right of one of the cross sections, respectively.

the other. Consequently, the generalization is simply

$$J = \sum_{\langle ij \rangle} \langle \mathcal{I}_{ij}(t) \rangle = \sum_{\langle ij \rangle} \text{Tr} [I_{i \rightarrow j} \rho(t)]. \quad (5.6)$$

This generalization is still able to reproduce the Landauer plateau, even in more complex lattices. Figure 5.8 shows the current across a cross section of a graphene nanoribbon, with the contribution from each individual bond shown as well. Since the total current across the cross section is normalized by the drop in potential, it is perfectly quantized in units of the conductance quantum defined as  $\sigma_0 = e^2/h$ . The graphs on the right show the current across a cross section of the nanoribbon which crosses only horizontal bonds and agree perfectly with the linear Landauer formula as calculated with KWANT [92]. The current across each individual bond at these cross sections are shown in the graphs on the left.

### 5.6.1 Consideration on scaling

When thinking about practical applications for this method, it is important to see how it fares against other known ways to do the same thing. Our long-term goal with this method is to obtain a clear picture of a diffusive regime where one can meaningfully speak of a conductivity. The diffusive regime is reached when the mean free path is considerably smaller than the localization length. In two-dimensions, the localization length can be very large, so one might have to compute the conductance of very large samples, both in length  $L$  and in cross section  $C$ . The Landauer formula can be evaluated with help from the Recursive Green Function method (RGF) [35], which scales as  $LC^3$  because of the matrix inversions of matrices with dimensions  $C \times C$ . In contrast, our method scales as  $LC^2$ . One factor of  $LC$  comes from the size of the Hilbert space and is required for the computation of even just one local current, but the extra factor of  $C$  comes from the

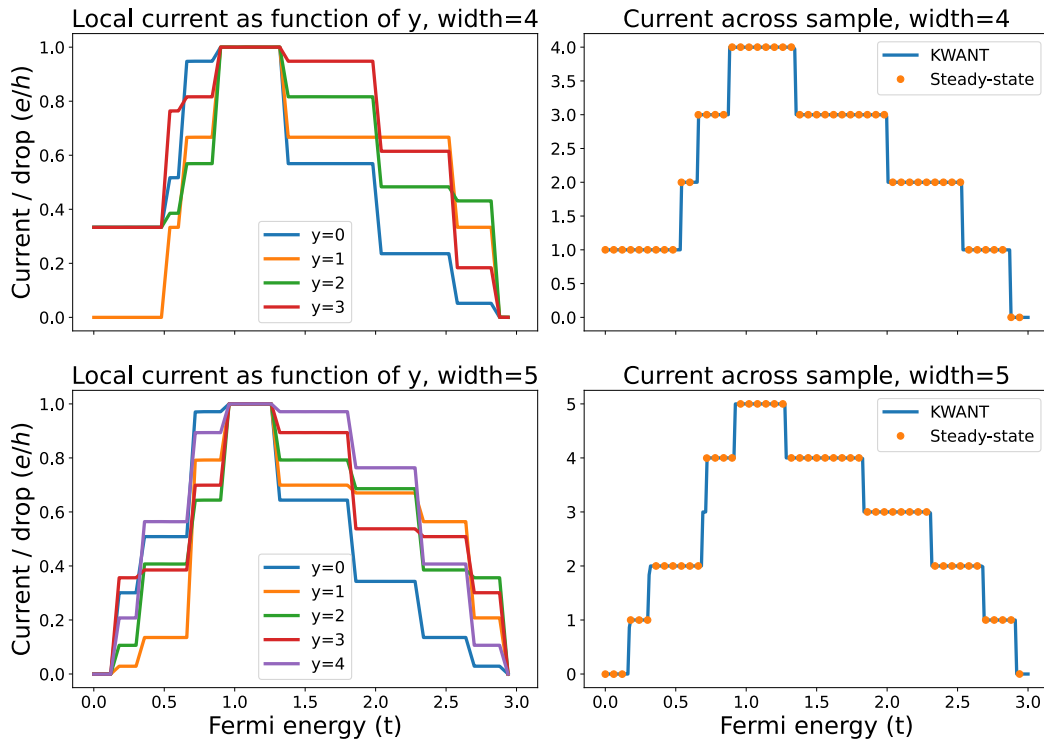


Figure 5.8: Current across an armchair graphene nanoribbon of width 4 (metallic, top) and width 5 (non-metallic, bottom). The cross-section over which the current is being calculated is shown in Fig. 5.7. The graphs on the left show the current across each individual bond, and the graphs on the right represent the total current.

sum across the cross section. Clearly, the scaling is advantageous in this situation, but the RGF method isn't the only way to compute the current across a sample. KWANT uses the nested dissection algorithm [130] which enables this calculation with the same scaling of  $LC^2$  thanks to a reorganization of the matrix elements. In this current formulation, the only advantage of our method in relation to this algorithm is the fact that this is easily parallelizable in the sum across the cross section, but we can still do better. This is the subject of the next sections.

## 5.7 Stochastic current

As mentioned in section 5.6.1, the main shortcoming of the sum of local currents across a cross section was its  $LC^2$  scaling. In this section, we will see how to bring this scaling down to  $LC$  with the help of random vectors. To see how, let's go back to the current across the cross section (eq. 5.6) and begin by writing out the trace explicitly

$$J = \sum_k \langle k | I_C \rho(t) | k \rangle$$

where  $I_C$  is defined as the sum of local current operators across the cross section:

$$I_C = \sum_{\langle ij \rangle} I_{i \rightarrow j}.$$

Like before, the sum over  $k$  simplifies to the sum over the set of states  $\Omega$  in the support of  $I_C$ . Furthermore, using the real part allows us to consider only the set of states  $\Omega_L$  that lie to just to the left of the cross section. Therefore, the current is evaluated with

$$J = 2\text{Re} \sum_{k \in \Omega_L} \langle k | I_C \rho(t) | k \rangle. \quad (5.7)$$

Up until now, we have not gained anything by doing this manipulation - it still requires computing each  $k \in \Omega_L$  individually. However, using random vectors, this can be made simpler, in a similar fashion to the STE. Let

$$|\xi_\Omega\rangle = \sum_{k \in \Omega_L} \xi_k |k\rangle \quad (5.8)$$

be a random vector defined in  $\Omega_L$  with random numbers  $\xi_k$  taken from a distribution such that  $\langle \xi_k^* \xi_{k'} \rangle = \delta_{kk'}$ , just as discussed in Chapter 2. Then, the current may be evaluated as simply the average over these random vectors

$$J = 2\text{Re} \overline{\langle \xi_\Omega | I_C \rho(t) | \xi_\Omega \rangle}. \quad (5.9)$$

One key difference from the results of Chapter 2 is that this random vector is only defined in a cross section, rather than the whole system.

### 5.7.1 Average over cross-sections

One of the main arguments of Chapter 2 was that larger system sizes gave rise to smaller variance in the estimator of the trace, so it is reasonable to think the same would apply here. All we would need to do is to average eq. 5.7 over cross sections. Then, the random vector 5.8 would be nonzero in several cross-sections, effectively increasing the number of random vectors. However, in this circumstance, averaging over cross sections is actually not advantageous. To see why, let's analyze one of the terms of the variance formula 2.20 applied to the operator  $A = I_C \rho$ , where the time dependency of  $\rho(t)$  has been omitted for brevity:

$$\text{Tr} \left( (I_C \rho)^2 \right) = \sum_{ij} \sum_{k\ell} I_{ik}^C \rho_{kj} I_{j\ell}^C \rho_{\ell i}. \quad (5.10)$$

Since  $I_C$  is a very sparse matrix, the sum over  $k$  and  $\ell$  is always limited to a very small number of terms, so this sum does not scale with the system size or the number of cross-sections being used. The sum over  $i$  and  $j$  is restricted to states on one side of the cross-section, so it does not scale with the number of cross-sections.

## 5 Stochastic conductance

Now suppose that  $I_C$  is averaged over several cross-sections. Define

$$I_{\text{av}} = \frac{1}{N_C} \sum_C I_C$$

as the average current over  $N_C$  cross-sections. Applying eq. 5.10 to  $I_{\text{av}}$ , the argument for the sum over  $k$  and  $\ell$  remains identical due to the sparseness of  $I_{\text{av}}$ . The sum over  $i$  and  $j$  is now no longer limited to a single cross-section, and scales as  $N_C^2$ . This exactly cancels the  $1/N_C^2$  coming from the definition of  $I_{\text{av}}$  and we are left with something very similar to eq. 5.10. Therefore, it is not advantageous to average over cross-sections and for the remainder of this chapter we shall not do so.

Nevertheless, it is interesting to see how this notion of averaging over cross-sections connects to the idea of the Kubo formula, as the average value of the velocity operator. Let's analyze the case of a one-band two-dimensional tight-binding square lattice in the shape of a nanoribbon along the  $x$  direction, with lattice constant  $a$ . The vector  $\mathbf{R} = an\hat{\mathbf{x}} + am\hat{\mathbf{y}}$  indexes any site in the lattice. Let  $\Omega_{\text{av}}$  be the set of sites in the support of  $I_{\text{av}}$ . Then, the current  $J$  can be expressed as an average of the local currents:

$$J = \frac{1}{N_c} \sum_n J_n = \text{Tr} \left[ \frac{1}{N_c} \sum_{\mathbf{R}, \mathbf{R}+\mathbf{x} \in \Omega_{\text{av}}} I_{\mathbf{R} \rightarrow \mathbf{R}+\mathbf{x}} \rho(t) \right]$$

where the sum runs over all the sites in  $\Omega_{\text{av}}$ . Let  $I_{\text{av}}$  be this average operator

$$I_{\text{av}} = \frac{1}{N_c} \sum_{\mathbf{R}, \mathbf{R}+\mathbf{x} \in \Omega_{\text{av}}} I_{\mathbf{R} \rightarrow \mathbf{R}+\mathbf{x}}.$$

It is interesting to unpack the definition of  $I_{\text{av}}$  to see its underlying structure. It can be expressed in terms of the vectors inside  $\Omega'$

$$I_{\text{av}} = \frac{1}{N_c} \frac{iq}{\hbar} \sum_{\mathbf{R}, \mathbf{R}+\mathbf{x} \in \Omega_{\text{av}}} (H_{\mathbf{R}, \mathbf{R}+\hat{\mathbf{x}}|\mathbf{R}\rangle \langle \mathbf{R}+\hat{\mathbf{x}}| - H_{\mathbf{R}+\hat{\mathbf{x}}, \mathbf{R}}^* |\mathbf{R}+\hat{\mathbf{x}}\rangle \langle \mathbf{R}|),$$

which is closely related to the velocity operator. To make this evident, define the projector  $P_{\Omega_{\text{av}}}$  into the sites  $\Omega_{\text{av}}$  as

$$P_{\Omega_{\text{av}}} = \sum_{\mathbf{R} \in \Omega_{\text{av}}} |\mathbf{R}\rangle \langle \mathbf{R}|.$$

Then,  $I_{\text{av}}$  can be expressed as

$$I_{\text{av}} = \frac{1}{N_c} \frac{q}{a} P_{\Omega_{\text{av}}} \sum_{\mathbf{R}} \left( \frac{ita}{\hbar} |\mathbf{R}\rangle \langle \mathbf{R}+\hat{\mathbf{x}}| - \frac{ita}{\hbar} |\mathbf{R}+\hat{\mathbf{x}}\rangle \langle \mathbf{R}| \right) P_{\Omega_{\text{av}}}.$$

The sum is unrestricted, allowing the introduction of the velocity operator along  $x$

$$I_{\text{av}} = \frac{1}{N_c} \frac{q}{a} P_S v_x P_S.$$

This provides an interpretation of  $J$  as an average of the projected velocity operator, similarly to the Kubo formula for the conductivity. Although this seems obvious, this should not be taken as a general statement. The identification of  $I_{\text{av}}$  as the average projected velocity operator was only possible because of the square structure of this specific lattice. Because of this, both the velocity operator and the local current always connect adjacent horizontal bonds with the same matrix element. The same does not happen for more complex lattices such as the honeycomb lattice, for which the velocity operator along  $x$  could connect adjacent sites with a factor of  $\cos(30^\circ)$  if they are not connected horizontally.

### 5.7.2 Choice of random vectors

So far, the only condition imposed upon the random vectors is that their components satisfy  $\overline{\xi_i^* \xi_j} = \delta_{ij}$ . Just like in section 2.6, the choice of random vectors can have significant consequences for the random fluctuations of the method, and so they must be carefully chosen. In this section we will look into the effect of the distribution, and whether or not complex random vectors should be used.

In equilibrium, we expect there to be no current flowing from one lead to the other, that is  $J(t=0) = 0$ , even in the presence of a magnetic field. Complex random vectors pose a problem here, because complex vectors carry current. On average, this contribution is zero, but it adds to the variance. This is confirmed by Fig. 5.9, where the current across a very small finite graphene armchair nanoribbon is calculated using random vectors. The dimensions in terms of unit cells are: width= 2, sample length= 4, lead size= 64.

Each curve in this Figure is the current calculated with a different random vector and each panel uses a different distribution. Since the curves are transparent, the shade of green gives us an idea of their distribution (for the detailed distribution of the uniform case, see Fig. 5.11). Notably, the curves in panel a) were calculated with complex random vectors with elements defined in the unit complex circle and have a standard deviation so large that they appear as flat lines.

The flatness of these curves also gives us an indication that for each random vector, the value of the current at every time is highly correlated. We can use this correlation to reduce the noise. By subtracting the value at  $t = 0$  (which we know has to be zero), we get panel b), where the standard deviation has been substantially reduced. We also know that the large variance is caused by the complex nature of the random vectors. Taking their real part, we get panel c). Of course, we can simply use uniformly distributed real random vectors, yielding panel d).

The differences between each method is quantified more clearly in Fig. 5.10. Panel a) is the result of averaging over the random vectors, compared against the same result calculated exactly. The last panel plots the standard deviation of each of the methods as a function of time. As expected, using random vectors yields the correct result on average (panel a)), but the standard deviation (panel b)) is not very different for each of them.

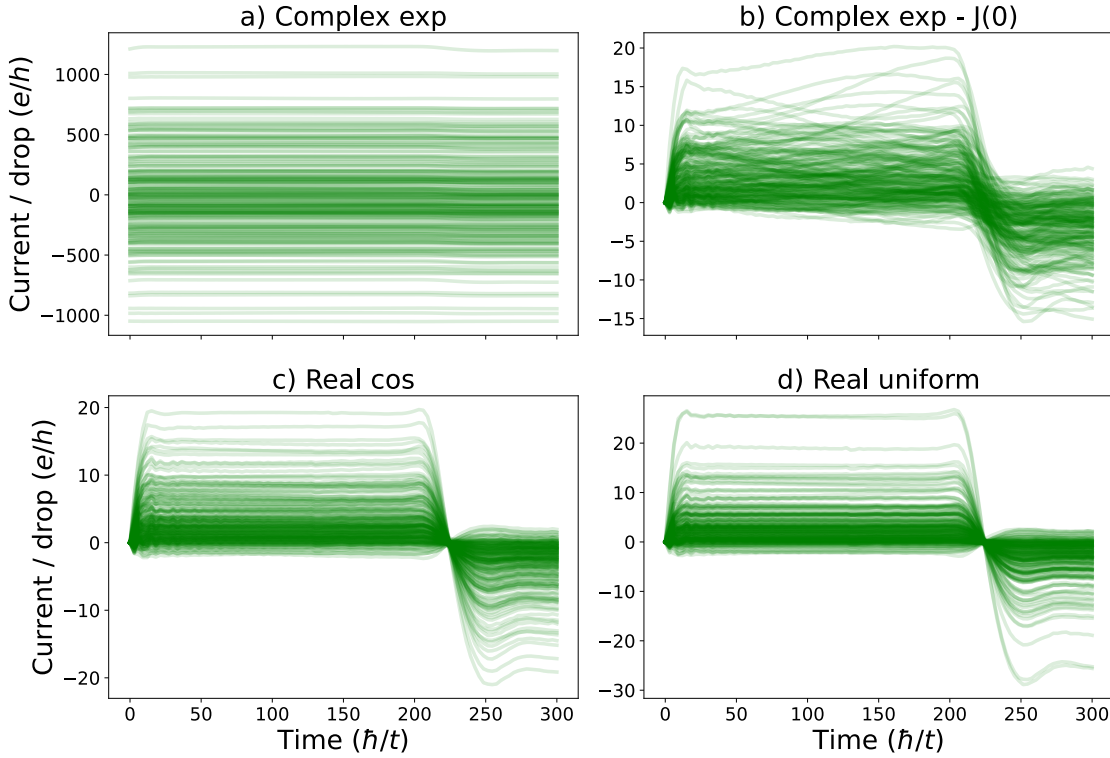


Figure 5.9: Current across a very small armchair graphene nanoribbon calculated using random vectors with different distributions.

Since there is no clear benefit in using either of the three distributions, for the next sections the uniform distribution is going to be used for simplicity.

### 5.7.3 Operator order

As previously discussed, one major shortcoming of calculating the nonlinear current in time is that the Fermi operator has to be evaluated once for every point in time where we want to observe the current. Using random vectors defined in the whole system, eq. 5.9 becomes a trace, so we can rotate the operators to something like

$$J = \overline{\langle \xi | e^{iHt/\hbar} I_C e^{-iHt/\hbar} f(H_0) | \xi \rangle}$$

with the understanding that  $|\xi\rangle$  is now defined in the whole Hilbert space rather than the subset  $\Omega$ . This has one major advantage: the Fermi operator only needs to be evaluated once for each random vector  $|\xi\rangle$ . However, we still need to compare the standard deviation of both methods.

To gain an intuition about this, let's analyze the variance at time  $t = 0$ , so that we can focus only on the simpler operator  $I_C f(H_0)$ . Since  $I_C$  only has nonzero elements inside of  $\Omega$ , it is clear that the contributions of  $|\xi\rangle$  to  $\langle \xi | I_C f(H_0) | \xi \rangle$  coming from  $\bar{\Omega}$ , the complement of  $\Omega$ , will necessarily have zero average. Concretely, let  $|\xi_\Omega\rangle$  be the projection

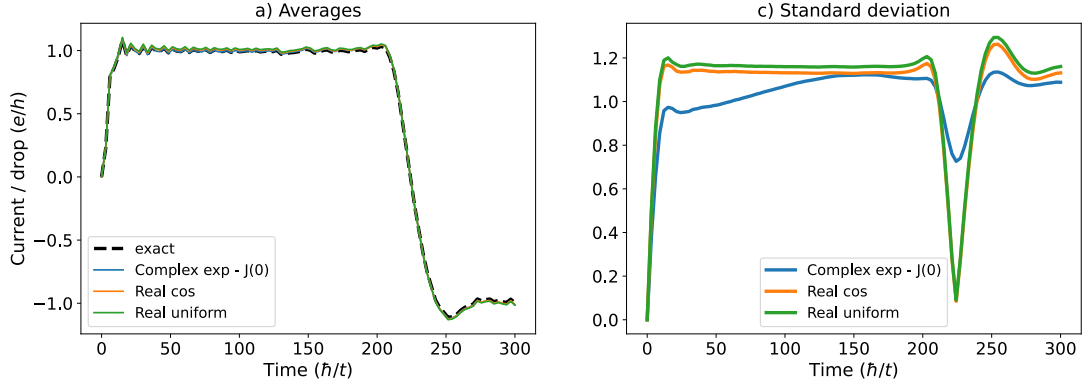


Figure 5.10: Statistical analysis of the current calculated with 2000 random vectors and different random vector distributions (blue - complex exponential minus initial current, orange - cosine distribution, green - uniform distribution). Panel a) shows the average current as a function of time for each distribution and panel b) shows the standard deviation of the stochastic current for each method.

of  $|\xi\rangle$  onto  $\Omega$  and  $|\xi_{\bar{\Omega}}\rangle$  the projection onto  $\bar{\Omega}$ , such that  $|\xi\rangle = |\xi_{\Omega}\rangle + |\xi_{\bar{\Omega}}\rangle$ . In symbols,

$$\langle \xi | I_C f(H_0) | \xi \rangle = \langle \xi_{\Omega} | I_C f(H_0) | \xi_{\Omega} \rangle$$

and

$$\langle \xi_{\bar{\Omega}} | I_C f(H_0) | \xi_{\bar{\Omega}} \rangle = 0.$$

Now, since the matrix elements between these two subspaces are nonzero:

$$\langle \xi_{\Omega} | I_C f(H_0) | \xi_{\bar{\Omega}} \rangle \neq 0$$

but its average is zero

$$\overline{\langle \xi_{\Omega} | I_C f(H_0) | \xi_{\bar{\Omega}} \rangle} = 0,$$

this means that region  $\bar{\Omega}$  does not contribute to the current, but adds to the variance. In general, region  $\bar{\Omega}$  is much larger than  $\Omega$ , so a lot of variance will be coming from this region, bringing the usefulness of this particular approach into question.

Thus, we expect the variance of this approach to be much larger, at least for small times, and a trade-off occurs between variance and the number of times that  $f(H_0)$  is required to be evaluated. Figure 5.11 shows the histograms resulting from both approaches after the current plateaus, at  $T = 80\hbar/t$  in Fig. 5.10. Clearly, the standard deviation of the stochastic current evaluated with the rotated operators (right) is much higher than the non-rotated counterpart (left). The distribution is also different. The former approximates an exponential distribution for larger values of the current, while the latter has a gaussian profile. The factor of 30 relating both standard deviations indicates that  $30^2$  more random vectors would be required to achieve the same error bar. Therefore, the rotated version of the stochastic current only becomes more efficient than its alternative when the number

of observation points is approximately of this order.

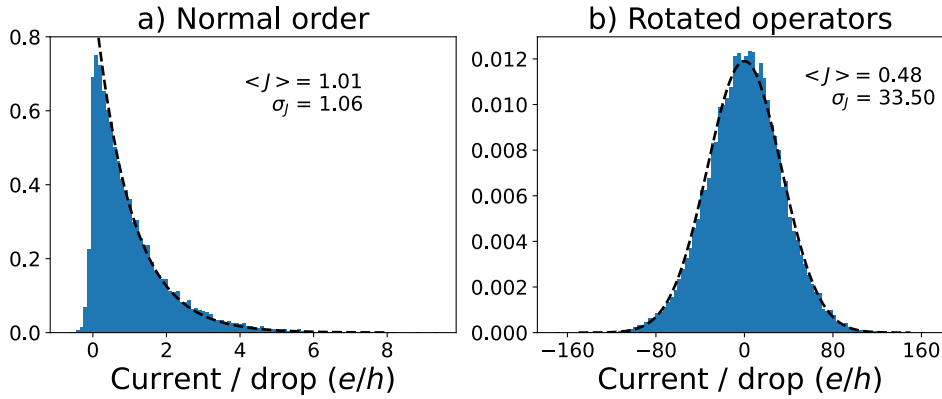


Figure 5.11: Histogram of the stochastic current normalized by the potential drop  $\Delta V$  with and without the rotated trace.

## 5.8 Stochastic vs exact

To prove the usefulness of this method, we have to go to larger lattices and see how the variance of the stochastic current changes with the size of the cross-section. Ideally, for sufficiently large cross-sections, only one random vector would be required to have a sufficiently small error bar. Figure 5.12 shows the average current as a function of time across a sample in a 2D TB lattice, as well as the standard deviation of this stochastic variable (blue shaded area). As the cross-section width  $W$  increases, the relative error of the current decreases. When  $W = 1024$ , the standard deviation is already very small compared to the value of the current at the plateau.

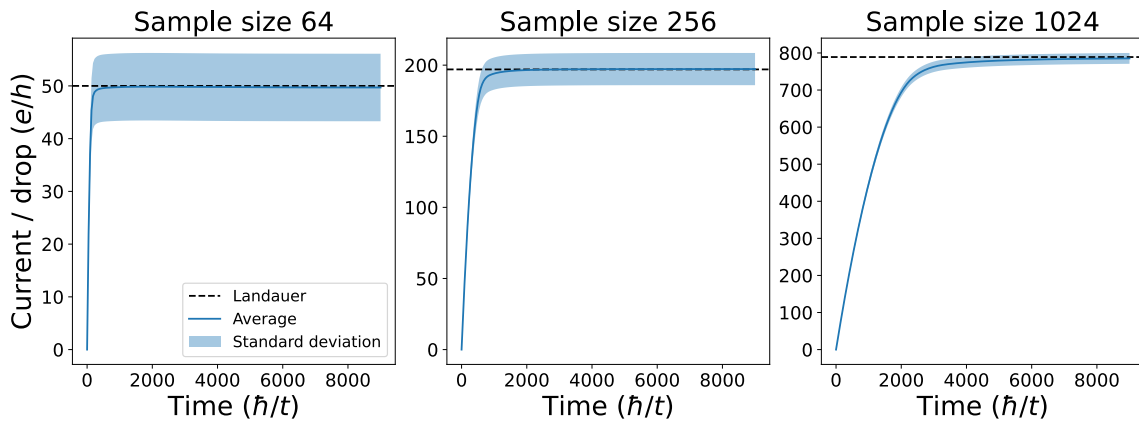


Figure 5.12: Current across a sample estimated through random vectors for different cross-section widths  $W$ . Each sample is a square of dimensions  $W \times W$ . The 2D TB lattice has length  $L_x = 16384$  (which includes both leads and sample length).

This method requires the exact same computational effort to compute the local current across a bond as to compute the stochastic current for one random vector, so it will be

advantageous for larger cross-sections. In order to quantify this, let us suppose that the statistical error is reasonable when the relative error is below 1%. Let us also suppose that for a fixed cross-section width  $W$ , the standard deviation of the method is  $\sigma_W$  and the current is  $J_W$ . Assuming the central limit theorem is valid, an average over  $N_R$  random vectors would yield a standard deviation of  $\sigma_W/\sqrt{N_R}$  for this average value. Then, the number of random vectors required to get the desired accuracy can be estimated as

$$\sqrt{N_R} = 100 \frac{\sigma_W}{J_W}.$$

Next, suppose that  $\sqrt{W}\sigma_W$  is relatively constant and approximately equal to a value  $\tilde{\sigma}$ , which is reasonable if the current does not change considerably across the cross-section. It is also reasonable to assume that the current across a sample is roughly proportional to the cross section, such that  $J_W \approx W\tilde{J}$ . Then, for sufficiently large  $W$ , we have the following estimate for  $N_R$ :

$$N_R = \frac{1}{W} \left( \frac{100\tilde{\sigma}}{\tilde{J}} \right)^2.$$

In contrast, we have to perform  $W$  calculations to get the current across the sample as a sum of local currents across the cross-section. Therefore, the stochastic evaluation of the current becomes the most efficient method when  $N_R < W$ , that is, when

$$W > \frac{100\tilde{\sigma}}{\tilde{J}}.$$

Coming back to Fig. 5.12, we can estimate  $\tilde{\sigma} \approx 0.7$  and  $\tilde{J} \approx 0.8$ , indicating that for cross-sections of the order of  $W \approx 100$ , it's more efficient to use random vectors than to sum over the local currents.

## 5.9 Further optimizations and limitations

There are two main sources of inefficiency for the stochastic evaluation of the current. The first is the need to evaluate the Fermi function for every point in time where the current is being observed. We saw that rotating the order of the operators could help in principle, but the added increase in variance made it unappealing. One way around this is to use the linearized version of the stochastic current, which does not have this problem. But if we are actually interested in the nonlinear current, a more careful choice of observation points can be useful. If we have an estimate for how long the current takes to stabilize, we can use a coarser grid of times during that period, and a finer one after that, to ensure stabilization. Alternatively, we can simply read off its value at one single time after the stabilization, thus requiring only one observation.

The second source of inefficiency is the need for very long leads. If there are resonances inside the sample, some states can bounce around long enough inside the sample for the reflected current wave to reach it before they have escaped into the leads. One way to

prevent this is to slow down this wave through the use of smooth boundary conditions inside the leads [131]: the farther away from the sample, the smaller the hoppings in the leads. The intuition behind this is the following: if we look back at the Landauer formula 5.4, we realize that all of the contribution to the current comes from states in an energy window of size  $\Delta V$  around the Fermi energy  $\varepsilon_F$ . If we wanted twice the resolution inside this energy window, we would have to double the size of the leads, which would also increase the resolution in the remainder of the spectrum. This wasted resolution can be put to use by changing the spectrum of the leads to lie within this energy window. This increases the number of states around the Fermi surface considerably.

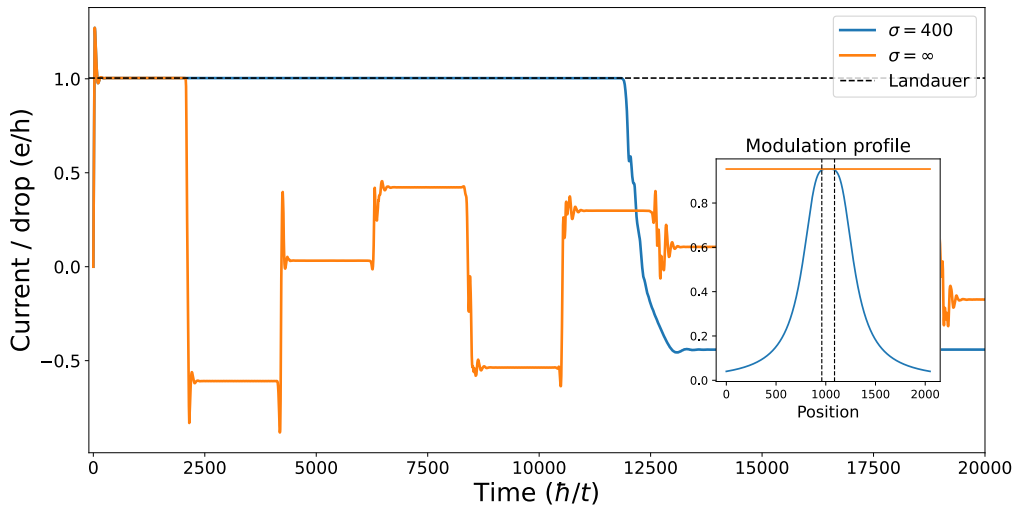


Figure 5.13: The effect of modulated hoppings in the stationary current plateau (left) and modulation profile (inset). The region between the vertical dashed lines in the inset represents the sample.

To see this in action, we can apply a modulation profile to the hoppings of the whole system and shift the energies to place the Fermi energy at zero. We applied the following hopping profile (see inset of Fig. 5.9):

$$t(n) = \frac{t - \Delta V/2}{\sqrt{1 + \left(\frac{2n - L_S}{2\sigma}\right)^4}} + \frac{\Delta V}{2}$$

to the 1D TB chain of lattice parameter  $a$ . Here,  $n$  is the position along the nanoribbon length,  $L_S$  is the length of the sample and  $\sigma$  is an adjustable parameter to tune how quickly the hopping changes. In this model, this has shown to bring considerable improvements to the plateau's longevity (see Fig. 5.9). The introduction of a hopping modulation through a Cauchy-like curve increases the reflection time by a factor of around 4, while still providing the same stationary current inside the sample.

## 5.10 Further applications

The unitary evolution of the stochastic current in time with finite leads appears here as a promising alternative to the more standard infinite leads approach and is a truly complexity  $\mathcal{O}(N)$  method. Its linear scaling means that one is now able to study very wide samples connected to leads in a fully parallelized fashion. While this chapter was largely exploratory, this technique promises a new avenue to study localization phenomena at weaker disorders.



# 6 Spectral methods in superconductors with dilute impurities

Disordered superconductors are an intrinsically difficult system to study. On the one hand, one has to include interactions, which greatly increases the computational complexity of the problem. On the other hand, the absence of translation invariance means that the momentum basis cannot be used to simplify the problem. While a full treatment of interactions is currently out of practical reach for these kinds of problems, a mean-field approximation to interactions is a useful way to simplify the problem while still keeping the most important features. In the case of superconductivity, Cooper pairs are responsible for the superconducting state. Being a bound state of two electrons, a mean-field theory has to include terms which create two electrons explicitly.

Several mechanisms have been proposed as mediators for these Cooper pairs, from phonons to plasmons [79, 83], but the overall effect is the same: an effective attractive electron-electron interaction. In this Chapter, we will not concern ourselves with the particular mechanism behind the superconducting effect. Our starting point will be the existence of this interaction, which will then be treated as a mean-field theory subject to a self-consistency condition. The purpose of this chapter is to develop a new way to treat the self-consistency equation in superconductors with dilute impurities that greatly reduces the computational cost of this procedure. Its effectiveness is shown for plasmon-mediated superconducting graphene [132].

## 6.1 Interacting Hamiltonian

The starting point of our discussion is an effective Hamiltonian which treats the superconducting effect simply as an electron-electron interaction (see [133] for a similar derivation). Let's start with generality and let the indices  $ijkl$  run over the whole single-particle Hilbert space. Each of them runs from 1 to  $2N$ , the 2 being there for convenience because of spin. The general many-body interacting Hamiltonian can be written as

$$\mathcal{H} = \sum_{ij} t_{ij} c_i^\dagger c_j + \frac{1}{2} \sum_{ijkl} V_{ijkl} c_i^\dagger c_j^\dagger c_k c_l.$$

In virtue of being a many-body operator,  $V$  has the following properties

$$V_{ijkl} = -V_{jikl} = -V_{ijlk} = V_{lkji}^* = V_{klji}^*.$$

## 6 Spectral methods in superconductors with dilute impurities

Treating interacting Hamiltonians directly is very complicated, so we want to approximate this Hamiltonian by an effective non-interacting Hamiltonian  $\mathcal{H}_{\text{eff}}$  which nevertheless is able to capture some key properties of the interacting one. As we will see, the price to pay for this process is that we will be left with a complicated self-consistent equation to solve.

To simplify the analysis, and because we are only going to study superconductivity at zero-temperature, we want to obtain the best possible non-interacting approximation  $|\Phi_0\rangle$  to the many-body ground state, described as

$$|\Phi_0\rangle = \sum_{n < N} d_n^\dagger |0\rangle$$

for a set of states  $d_n^\dagger$  to be determined. Let  $\langle \dots \rangle = \langle \Phi_0 | \dots | \Phi_0 \rangle$  denote the expectation value with respect to this ground state. To get the best approximation to the ground state, we want to find the set of states  $d_n^\dagger$  which minimize the expectation value of the interacting Hamiltonian:

$$\langle \mathcal{H} \rangle = \langle \Phi_0 | \mathcal{H} | \Phi_0 \rangle = \sum_{ij} t_{ij} \langle c_i^\dagger c_j \rangle + \frac{1}{2} \sum_{ijkl} V_{ijkl} \langle c_i^\dagger c_j^\dagger c_k c_l \rangle$$

and this can be done with resort to the Hartree-Fock approximation. Since the average is done with respect to a non-interacting Hamiltonian, Wick's theorem applies

$$\langle c_i^\dagger c_j^\dagger c_k c_l \rangle = \langle c_i^\dagger c_j^\dagger \rangle \langle c_k c_l \rangle - \langle c_i^\dagger c_k \rangle \langle c_j^\dagger c_l \rangle + \langle c_i^\dagger c_l \rangle \langle c_j^\dagger c_k \rangle$$

and the expectation value factorizes into

$$\langle \mathcal{H} \rangle = \sum_{ij} t_{ij} \langle c_i^\dagger c_j \rangle + \frac{1}{2} \sum_{ijkl} V_{ijkl} \left[ \langle c_i^\dagger c_j^\dagger \rangle \langle c_k c_l \rangle - \langle c_i^\dagger c_k \rangle \langle c_j^\dagger c_l \rangle + \langle c_i^\dagger c_l \rangle \langle c_j^\dagger c_k \rangle \right].$$

We want to minimize this expectation value with respect to small variations in the basis, so after some simplification using the properties of  $V$ , we get

$$\begin{aligned} \delta \langle \mathcal{H} \rangle &= \sum_{ij} t_{ij} \delta \langle c_i^\dagger c_j \rangle + \frac{1}{2} \sum_{ijkl} \left[ V_{ijkl} \langle c_k c_l \rangle \delta \langle c_i^\dagger c_j^\dagger \rangle + V_{ijkl}^* \langle c_k^\dagger c_l^\dagger \rangle \delta \langle c_i c_j \rangle \right] \\ &\quad + 2 \sum_{ijkl} V_{ijkl} \langle c_j^\dagger c_k \rangle \delta \langle c_i^\dagger c_l \rangle \end{aligned}$$

For notational convenience, let

$$\Delta_{ij} = \sum_{kl} V_{ijkl} \langle c_k c_l \rangle \tag{6.1}$$

$$U_{ij} = 2 \sum_{lk} V_{iljk} \langle c_l^\dagger c_k \rangle \tag{6.2}$$

which casts the previous expression into

$$\delta \langle \mathcal{H} \rangle = \sum_{ij} (t_{ij} + U_{ij}) \delta \langle c_i^\dagger c_j \rangle + \frac{1}{2} \sum_{ij} \Delta_{ij} \delta \langle c_i^\dagger c_j^\dagger \rangle + \frac{1}{2} \sum_{ij} \Delta_{ij}^* \delta \langle c_j c_i \rangle.$$

Now consider the following effective Hamiltonian:

$$\mathcal{H}_{\text{eff}} = \sum_{ij} \tilde{t}_{ij} c_i^\dagger c_j + \sum_{ij} \left[ \tilde{\Delta}_{ij} c_i^\dagger c_j^\dagger + \tilde{\Delta}_{ij}^* c_j c_i \right],$$

which is in fact the most general form of a quadratic Hamiltonian. The fact that it is quadratic means that a single-particle counterpart can be obtained, and its spectrum calculated with the help of the Bogoliubov transformation explained in the next section. For now, we can assume that its spectrum and eigenvectors are known. If a ground state  $|\Phi_0\rangle$  is constructed with these states, then it is obvious that any variation to it will have a larger expectation value on  $\mathcal{H}_{\text{eff}}$ . Taking  $\tilde{t}_{ij} = t_{ij} + U_{ij}$  and  $\tilde{\Delta}_{ij} = \frac{1}{2} \Delta_{ij}$ , we see that  $\delta \langle \mathcal{H}_{\text{eff}} \rangle = \delta \langle \mathcal{H} \rangle$  and thus choosing a ground state composed of the first (lowest energy) states of  $\mathcal{H}_{\text{eff}}$  ensures  $\langle \mathcal{H} \rangle$  is minimized. This sets a self-consistent equation, because  $\mathcal{H}_{\text{eff}}$  depends on  $U$  and  $\Delta$ , which themselves depend on  $\mathcal{H}_{\text{eff}}$  through the expectation values. The  $U_{ij}$  potential is usually disregarded, because it is obtained via a sum over the Fermi sea, rather than the Fermi surface like  $\Delta$ , thus its effect on superconducting excitations is minimal. Therefore, we have found the basis of states which provide the best approximation to the ground state of  $\mathcal{H}$ , and these define the effective Hamiltonian  $\mathcal{H}_{\text{eff}}$  which will be used in the remainder of the Chapter.

### 6.1.1 The Bogoliubov-de Gennes Hamiltonian

To proceed, we will represent the effective Hamiltonian in a different way, by putting the creation and annihilation operators under a single operator. Define  $T = t + U$  for notational simplicity. Then, the effective Hamiltonian can be put in the following form

$$\mathcal{H}_{\text{eff}} = \frac{1}{2} \sum_i T_{ii} + \frac{1}{2} \sum_{ij} T_{ij} c_i^\dagger c_j + \frac{1}{2} \sum_{ij} (-T_{ji}) c_i c_j^\dagger + \frac{1}{2} \sum_{ij} \Delta_{ij} c_i^\dagger c_j^\dagger + \frac{1}{2} \sum_{ij} \Delta_{ij}^* c_j c_i.$$

The matrix form becomes more obvious when considering the particle and hole subspaces individually. Let

$$\begin{pmatrix} c \\ c^\dagger \end{pmatrix} = \begin{pmatrix} c_1 & c_2 & \cdots & c_N & c_1^\dagger & c_2^\dagger & \cdots & c_N^\dagger \end{pmatrix}^T$$

represent the creation and annihilation in a compact way. Then, the Hamiltonian can be written as

$$\mathcal{H}_{\text{eff}} = \varepsilon_0 + \frac{1}{2} \begin{pmatrix} c^\dagger & c \end{pmatrix} \begin{bmatrix} \mathbf{H} & \Delta \\ \Delta^\dagger & -\mathbf{H}^* \end{bmatrix} \begin{pmatrix} c \\ c^\dagger \end{pmatrix},$$

## 6 Spectral methods in superconductors with dilute impurities

where  $\varepsilon_0 = \frac{1}{2} \sum_i T_{ii}$ . Define

$$\Omega = \begin{bmatrix} \mathbf{H} & \Delta \\ \Delta^\dagger & -\mathbf{H}^* \end{bmatrix}$$

as the single-particle Bogoliubov-de Gennes (BdG) Hamiltonian. The fermionic nature of the creation and annihilation operators dictates that  $\Delta^T = -\Delta$ . While the original single-particle Hamiltonian matrix was a  $2N \times 2N$  matrix, this one is  $4N \times 4N$  because the basis has been doubled. This means that the eigenvectors cannot be considered as independent and that there must be a symmetry in this matrix. Let  $s_y$  be the  $y$  Pauli matrix defined in the particle-hole space, that is:

$$s_y = i \begin{bmatrix} \mathbf{0}_{2N \times 2N} & -\mathbf{1}_{2N \times 2N} \\ \mathbf{1}_{2N \times 2N} & \mathbf{0}_{2N \times 2N} \end{bmatrix}$$

That symmetry is

$$s_y \Omega s_y = -\Omega^*$$

or, defining the conjugation operator as  $CAC^{-1} = A^*$  such that  $C^{-1} = C$  and  $T = s_y C$ ,

$$T \Omega T = -\Omega.$$

This means that if one is able to find an eigenvector  $\psi$  with eigenvalue  $E$ , then  $T\psi$  is also an eigenvector, but with eigenvalue  $-E$ . Let us then search for the  $2N$ -dimensional vectors  $u_n$  and  $v_n$  such that

$$\begin{bmatrix} \mathbf{H} & \Delta \\ \Delta^\dagger & -\mathbf{H}^* \end{bmatrix} \begin{pmatrix} u_n \\ v_n \end{pmatrix} = E_n \begin{pmatrix} u_n \\ v_n \end{pmatrix}.$$

In elements:

$$\begin{aligned} \sum_j H_{ij} u_{jn} + \sum_j \Delta_{ij} v_{jn} &= u_{in} E_n \\ \sum_j (\Delta^\dagger)_{ij} u_{jn} + \sum_j (-H^*)_{ij} v_{jn} &= v_{in} E_n. \end{aligned}$$

This suggests the definition of the matrices  $\mathbf{u}$ ,  $\mathbf{v}$  and the diagonal matrix  $\mathbf{E}$  such that

$$\begin{aligned} \mathbf{H}\mathbf{u} + \Delta\mathbf{v} &= \mathbf{u}\mathbf{E} \\ \Delta^\dagger\mathbf{u} - \mathbf{H}^*\mathbf{v} &= \mathbf{v}\mathbf{E} \end{aligned}$$

Since this combination composes an eigenvector of energy  $E_n$ , then

$$T \begin{pmatrix} u_n \\ v_n \end{pmatrix} = s_y C \begin{pmatrix} u_n \\ v_n \end{pmatrix} = i \begin{bmatrix} \mathbf{0}_{N \times N} & -\mathbf{1}_{N \times N} \\ \mathbf{1}_{N \times N} & \mathbf{0}_{N \times N} \end{bmatrix} \begin{pmatrix} u_n^* \\ v_n^* \end{pmatrix} = i \begin{pmatrix} -v_n^* \\ u_n^* \end{pmatrix}$$

has eigenvalue  $-E_n$ . Now this set of vectors can be organized into a matrix to compose the matrix of change of basis  $P_{in} = \langle i|n\rangle$

$$P = \begin{bmatrix} \mathbf{u} & -\mathbf{v}^* \\ \mathbf{v} & \mathbf{u}^* \end{bmatrix}.$$

The condition  $P^\dagger P = 1$  imposes some restrictions on the matrices  $\mathbf{u}$  and  $\mathbf{v}$ :

$$\begin{aligned} \mathbf{u}^\dagger \mathbf{u} + \mathbf{v}^\dagger \mathbf{v} &= \mathbf{1}_{N \times N} \\ \mathbf{v}^T \mathbf{u} &= \mathbf{u}^T \mathbf{v} \end{aligned}$$

or in terms of the eigenvectors  $i$  and  $j$

$$\begin{aligned} \sum_k (u_{ki}^* u_{kj} + v_{ki}^* v_{kj}) &= \delta_{ij} \\ \sum_k (v_{ki} u_{kj} - u_{ki} v_{kj}) &= 0 \end{aligned}$$

its action on the BdG Hamiltonian is

$$P \begin{bmatrix} \mathbf{H} & \mathbf{\Delta} \\ \mathbf{\Delta}^\dagger & -\mathbf{H}^* \end{bmatrix} P^\dagger = \begin{bmatrix} \mathbf{E} & \mathbf{0} \\ \mathbf{0} & -\mathbf{E} \end{bmatrix}$$

This is the Bogoliubov transformation that can be used to diagonalize the BdG Hamiltonian, but it is usually cast in a different way in nonmagnetic materials. This will be shown in the next section, but first we need to include spin explicitly in our computations. At this point it is useful to introduce the bra-ket notation for these objects. Let  $|e, i\rangle$  denote the usual (electron) state  $i$  and  $|h, i\rangle$  the hole state  $i$ . The previous objects have the representation

$$\begin{aligned} \langle e, i | \Omega | e, j \rangle &= H_{ij} \\ \langle e, i | \Omega | h, j \rangle &= \Delta_{ij} \\ \langle h, i | \Omega | e, j \rangle &= \Delta_{ji}^* \\ \langle h, i | \Omega | h, j \rangle &= -H_{ij}^* \end{aligned}$$

which will become useful later on.

### 6.1.2 Spin, symmetry and types of superconductors

Spin plays the central role in superconductivity, so it is useful to write it out explicitly in the Hamiltonian. The matrices  $\mathbf{H}$  and  $\mathbf{\Delta}$  get further split into their spin components. From now on, let's consider spin separately, so the indices  $i$  now run from 1 to  $N$  to

## 6 Spectral methods in superconductors with dilute impurities

represent all the non-spin degrees of freedom. The Hamiltonian takes the general form

$$\mathcal{H} = \varepsilon_0 + \frac{1}{2} \begin{pmatrix} c_{\uparrow}^{\dagger} & c_{\downarrow}^{\dagger} & c_{\uparrow} & c_{\downarrow} \end{pmatrix} \begin{bmatrix} \mathbf{H}_{\uparrow\uparrow} & \mathbf{H}_{\uparrow\downarrow} & \Delta_{\uparrow\uparrow} & \Delta_{\uparrow\downarrow} \\ \mathbf{H}_{\downarrow\uparrow} & \mathbf{H}_{\downarrow\downarrow} & \Delta_{\downarrow\uparrow} & \Delta_{\downarrow\downarrow} \\ \Delta_{\uparrow\uparrow}^{\dagger} & \Delta_{\uparrow\downarrow}^{\dagger} & -\mathbf{H}_{\uparrow\uparrow}^* & -\mathbf{H}_{\uparrow\downarrow}^* \\ \Delta_{\downarrow\uparrow}^{\dagger} & \Delta_{\downarrow\downarrow}^{\dagger} & -\mathbf{H}_{\downarrow\uparrow}^* & -\mathbf{H}_{\downarrow\downarrow}^* \end{bmatrix} \begin{pmatrix} c_{\uparrow} \\ c_{\downarrow} \\ c_{\uparrow}^{\dagger} \\ c_{\downarrow}^{\dagger} \end{pmatrix}.$$

Hermiticity imposes  $\mathbf{H}_{\downarrow\uparrow} = \mathbf{H}_{\uparrow\downarrow}^{\dagger}$  and the fermionic nature of the pairing terms imposes the following conditions on the blocks:

$$\Delta^T = \begin{bmatrix} \Delta_{\uparrow\uparrow} & \Delta_{\uparrow\downarrow} \\ \Delta_{\downarrow\uparrow} & \Delta_{\downarrow\downarrow} \end{bmatrix}^T = - \begin{bmatrix} \Delta_{\uparrow\uparrow} & \Delta_{\uparrow\downarrow} \\ \Delta_{\downarrow\uparrow} & \Delta_{\downarrow\downarrow} \end{bmatrix} = -\Delta.$$

More explicitly,  $\Delta_{\uparrow\uparrow}^T = -\Delta_{\uparrow\uparrow}$ ,  $\Delta_{\downarrow\downarrow}^T = -\Delta_{\downarrow\downarrow}$  and  $\Delta_{\downarrow\uparrow}^T = -\Delta_{\uparrow\downarrow}$ . The structure of this matrix determines the symmetry of the superconducting state [134–136]. The matrix  $\Delta$  can be written in an alternative way using the vector of matrices  $\vec{\mathbf{d}} = (\mathbf{d}_x, \mathbf{d}_y, \mathbf{d}_z)$  [135]

$$\Delta = \begin{bmatrix} -\mathbf{d}_x + i\mathbf{d}_y & \mathbf{d}_z + \Delta_s \\ \mathbf{d}_z - \Delta_s & \mathbf{d}_x + i\mathbf{d}_y \end{bmatrix}$$

where

$$\begin{aligned} \Delta_s &= \frac{1}{2} (\Delta_{\uparrow\downarrow} - \Delta_{\downarrow\uparrow}) \\ \mathbf{d}_x &= \frac{1}{2} (\Delta_{\downarrow\downarrow} - \Delta_{\uparrow\uparrow}) \\ \mathbf{d}_y &= \frac{1}{2i} (\Delta_{\downarrow\downarrow} + \Delta_{\uparrow\uparrow}) \\ \mathbf{d}_z &= \frac{1}{2} (\Delta_{\uparrow\downarrow} + \Delta_{\downarrow\uparrow}). \end{aligned}$$

When the superconducting state is a singlet,  $\vec{\mathbf{d}} = 0$  and when it is a triplet,  $\Delta_s = 0$ . For a 1-band translational invariant square lattice with nearest neighbor hoppings and pairings, s-wave superconductivity would have the order parameter in  $k$ -space  $\Delta_k = \Delta_0$ , which is isotropic and has the same symmetry as  $s$ -orbitals. p-wave superconductivity may be characterized by an order parameter like  $\Delta_k = \Delta_0 (\sin(k_x) - i \sin(k_y))$  which at low momenta is  $\Delta_k \sim k_x - ik_y$ , which is proportional to the  $(\ell, m) = (1, -1)$  spherical harmonic, or in terms of atomic orbitals,  $p_x - ip_y$ . As a last example, one could also have for d-wave superconductivity,  $\Delta_k = \Delta_0 (\cos(k_x) - \cos(k_y)) \sim k_x^2 - k_y^2$  which has the same symmetry as the  $d_{x^2-y^2}$  orbitals. The kind of pairing that appears depends on the interaction mechanism. Phonon-mediated e-e attraction favors s-wave superconductivity, but the mechanism behind the other (unconventional) superconducting states is still a point of debate. Several theories have been put forward, such as resonating Valence Bond Theory (RVB), which states that electrons bound in valence bonds can act as mobile Cooper pairs, and others which replace the bosonic phonon modes by plasmons and spin fluctuations.

d-wave superconductivity is typically favored when the electron interaction is repulsive at short range but attractive at longer distances, thus benefiting from the lobules of the  $d$  orbitals being farther away from each other [136].

These symmetry classifications don't make a lot of sense in the lattice because the angular momentum is not a good quantum number, but they still correspond to the nomenclature at small momenta. The nomenclature is nevertheless useful to distinguish them because these symmetries have an effect in the response to disorder. Because of its robustness to disorder, s-wave superconductivity was the first to be discovered and was the main actor of the BCS theory. Shortly after the microscopic mechanism had been discovered, Anderson proved that this new condensed state was robust to impurities so long as they were non-magnetic. The possibility of a p-wave type superconducting state has been proposed shortly after Anderson's theorem [137, 138] and it was found to be very sensitive even to nonmagnetic impurities and so very clean samples would be required to see this state.

### 6.1.3 Nonmagnetic materials

So far, this approach has been general, but now we want to use this information to study the specific kinds of Hamiltonian that interest us for this Chapter. These are the ones whose noninteracting term is spin independent and whose interacting term only connects different spins. In the BdG form, this is

$$\mathcal{H} = \varepsilon_0 + \frac{1}{2} \begin{pmatrix} c_{\uparrow}^{\dagger} & c_{\downarrow}^{\dagger} & c_{\uparrow} & c_{\downarrow} \end{pmatrix} \begin{bmatrix} \mathbf{H} & \mathbf{0} & \mathbf{0} & \Delta \\ \mathbf{0} & \mathbf{H} & -\Delta^T & \mathbf{0} \\ \mathbf{0} & -\Delta^* & -\mathbf{H}^* & \mathbf{0} \\ \Delta^{\dagger} & \mathbf{0} & \mathbf{0} & -\mathbf{H}^* \end{bmatrix} \begin{pmatrix} c_{\uparrow} \\ c_{\downarrow} \\ c_{\downarrow}^{\dagger} \\ c_{\uparrow}^{\dagger} \end{pmatrix}.$$

This Hamiltonian is block diagonal, which is made clear by swapping the second and fourth lines and columns

$$\mathcal{H} = \varepsilon_0 + \frac{1}{2} \begin{pmatrix} c_{\uparrow}^{\dagger} & c_{\downarrow} & c_{\uparrow} & c_{\downarrow}^{\dagger} \end{pmatrix} \begin{bmatrix} \mathbf{H} & \Delta & \mathbf{0} & \mathbf{0} \\ \Delta^{\dagger} & -\mathbf{H}^* & \mathbf{0} & \mathbf{0} \\ \mathbf{0} & \mathbf{0} & -\mathbf{H}^* & -\Delta^* \\ \mathbf{0} & \mathbf{0} & -\Delta^T & \mathbf{H} \end{bmatrix} \begin{pmatrix} c_{\uparrow} \\ c_{\downarrow}^{\dagger} \\ c_{\downarrow} \\ c_{\uparrow}^{\dagger} \end{pmatrix}.$$

Remarkably, the upper-left block is exactly of the form presented before and the lower-right block is its negative complex conjugate. Since the lower block is related to the upper block, it is useful to consider only the first one, so let's define the  $2N \times 2N$  matrix  $\Xi$  to be the upper-left block:

$$\Xi = \begin{bmatrix} \mathbf{H} & \Delta \\ \Delta^{\dagger} & -\mathbf{H}^* \end{bmatrix}$$

## 6 Spectral methods in superconductors with dilute impurities

and the operator vectors

$$\psi = \begin{pmatrix} c_{\uparrow} \\ c_{\downarrow} \end{pmatrix} \quad \text{and} \quad \psi^* = \begin{pmatrix} c_{\uparrow}^{\dagger} \\ c_{\downarrow} \end{pmatrix}$$

which is just  $\psi$  under the operation of the conjugation operation. Then the Hamiltonian can also be expressed in the form

$$\mathcal{H} = \varepsilon_0 + \frac{1}{2} \psi^{\dagger} \Xi \psi - \frac{1}{2} \left( \psi^{\dagger} \Xi \psi \right)^*.$$

Defining the excitation operators through the aforementioned matrix of change of basis,

$$\psi = P \begin{pmatrix} \gamma_{\uparrow} \\ \gamma_{\downarrow} \end{pmatrix} \quad \text{and} \quad \psi^* = P^* \begin{pmatrix} \gamma_{\uparrow}^{\dagger} \\ \gamma_{\downarrow} \end{pmatrix}$$

defines the Bogoliubov transformation which diagonalizes this Hamiltonian

$$\mathcal{H} = \varepsilon_0 + \frac{1}{2} \begin{pmatrix} \gamma_{\uparrow}^{\dagger} & \gamma_{\downarrow} & \gamma_{\uparrow} & \gamma_{\downarrow}^{\dagger} \end{pmatrix} \begin{bmatrix} \mathbf{E} & \mathbf{0} & \mathbf{0} & \mathbf{0} \\ \mathbf{0} & -\mathbf{E} & \mathbf{0} & \mathbf{0} \\ \mathbf{0} & \mathbf{0} & -\mathbf{E} & \mathbf{0} \\ \mathbf{0} & \mathbf{0} & \mathbf{0} & \mathbf{E} \end{bmatrix} \begin{pmatrix} \gamma_{\uparrow} \\ \gamma_{\downarrow}^{\dagger} \\ \gamma_{\uparrow}^{\dagger} \\ \gamma_{\downarrow} \end{pmatrix}.$$

Finally, writing this explicitly yields

$$\mathcal{H} = \frac{1}{2} \sum_i H_{ii} - \frac{1}{2} \sum_{i\sigma} E_i + \sum_{i\sigma} E_i \gamma_{i\sigma}^{\dagger} \gamma_{i\sigma},$$

where  $H$  is the single-particle counterpart of  $\mathcal{H}$ . The expectation values in the eigenbasis are easily found to be

$$\begin{aligned} \langle \gamma_{i\sigma}^{\dagger} \gamma_{i\sigma} \rangle &= f(E_i) \\ \langle \gamma_{i\sigma} \gamma_{i\sigma}^{\dagger} \rangle &= f(-E_i) \end{aligned}$$

and can be used to find all other correlators

$$\langle c_i^{\dagger} c_j \rangle = \langle j | f(H) | i \rangle \quad (6.3)$$

and the whole computation comes down to the evaluation of several matrix elements of  $f(H)$ . In terms of the  $\mathbf{u}$  and  $\mathbf{v}$  matrices, this is more commonly written as

$$\begin{aligned} \langle c_{i\uparrow} c_{j\uparrow} \rangle &= \langle c_{i\downarrow} c_{j\downarrow} \rangle = 0 \\ \langle c_{i\uparrow} c_{j\downarrow} \rangle &= \sum_n u_{ni} v_{nj}^* [1 - f(E_n)] - \sum_n u_{nj} v_{ni}^* f(E_n) \\ \langle c_{i\uparrow}^{\dagger} c_{j\downarrow} \rangle &= 0 \\ \langle c_{i\uparrow}^{\dagger} c_{j\uparrow} \rangle &= \langle c_{i\downarrow}^{\dagger} c_{j\downarrow} \rangle = \sum_n u_{ni}^* u_{nj} f(E_n) + \sum_n v_{ni} v_{nj}^* [1 - f(E_n)] \end{aligned}$$

The last thing we need to do is to express the Fermi operator in terms of something easier

to calculate, which can be done in the same way as with the optical conductivity. For example, expressing it in terms of the Dirac delta operator or, similarly, the retarded Green's function

$$\langle j | f(H) | i \rangle = \int_{-\infty}^{\infty} d\varepsilon f(\varepsilon) \langle j | \delta(\varepsilon - H) | i \rangle = -\frac{1}{\pi} \text{Im} \int_{-\infty}^{\infty} d\varepsilon f(\varepsilon) \langle j | G^R(\varepsilon) | i \rangle, \quad (6.4)$$

it's now possible to treat it in exactly the way described in 2.16, by expanding it in a series of Chebyshev polynomials. The only difference is that no random vectors are required. This is the basis for the Chebyshev-Bogoliubov-de Gennes formalism (CBdG) [88–91]. Within the mean-field approximation, this is numerically exact for inhomogeneous systems and can be used to study rather large systems, of the order of  $10^4$  atoms.

#### 6.1.4 Consideration on numerical efficiency

The main limiting factor here is nevertheless the same: the order parameter  $\Delta$  and the Hartree-Fock potential  $U$  need to be evaluated at every point in space (or pair of points if the interaction connects different sites), and so one individual simulation is required for each. And since this is a self-consistent equation, it has to be repeated to convergence, adding on top of the numerical inefficiency.

## 6.2 Dealing with inhomogeneities

As explained in the introduction, several methods exist in order to deal with inhomogeneities. It is clear that inhomogeneity is a severe limiting factor in the efficiency of the numerical methods and can arise in several situations. Boundary effects and impurities are among the most interesting ones in superconductors. Under certain circumstances, evaluating eq. 6.3 at every point in space is not necessary. Fluctuations in the order parameter can be neglected if the coherence length is much higher than the lattice spacing [86, 139]. In these cases of relative homogeneity away from impurities and boundaries, it is redundant to evaluate eq. 6.3 at every point. One possible way to reduce numerical complexity is to compute these equations in a regular mesh, and then interpolate  $\Delta$  and  $U$  from there, while refining the mesh closer to sources of inhomogeneity.

Another closely related possibility is to take these to be uniform away from the inhomogeneities, and then to allow them to vary when close to impurities. This requires complete computation around the impurity, but only requires one computation away from the impurity. This reduces the numerical complexity considerably, to something which scales with the concentration of impurities, but we can go further. If we look at the order parameter around individual impurities, we do not expect much variation from one impurity to the next. This is the inspiration for the next step. We impose that the order parameter modulation around each impurity is an average of the modulations around every impurity. And now that we're talking about averages, we can again use random vectors. This reduces

## 6 Spectral methods in superconductors with dilute impurities

the numerical complexity tremendously. Instead of calculating the order parameter around every impurity, now the numerical cost is the same as doing it just for one impurity.

To better understand the validity of this procedure, it is necessary to get a better grasp of the exact spatial variation of the order parameters around impurities. Friedel oscillations are considerable in 1D, where they span several hundreds of unit cells [140]. While both the s-wave and p-wave superconducting order parameters get modified in 1D, only the s-wave order parameter oscillates. In 2D, both oscillate, but they only span a couple of unit cells. This is the green light for our method: the smaller the region around which the order parameter varies, the more efficient the method becomes, so it is expected to fare well in 2D.

To understand the method in its generality, it's useful to begin with an illustrative example in 1 dimension. Consider the simple 1D tight-binding chain with a Hubbard interaction

$$\mathcal{H} = \sum_{ij} t_{ij} \left( c_{i\uparrow}^\dagger c_{j\uparrow} + c_{i\downarrow}^\dagger c_{j\downarrow} \right) + V \sum_i c_{i\uparrow}^\dagger c_{i\downarrow}^\dagger c_{i\downarrow} c_{i\uparrow}.$$

Without impurities, the hopping matrix  $t_{ij}$  is  $t$  if  $i$  and  $j$  are nearest neighbors, and zero otherwise. In the presence of impurities,  $t_{ii}$  is allowed to be nonzero when  $i$  is an impurity site. For the sake of simplicity, we consider only nonmagnetic impurities, so  $t_{ii}$  does not depend on spin. Let  $I$  be the set of sites with impurities, such that  $t_{ii} = \varepsilon_0$  when  $i \in I$ . Plugging this interaction operator in eqs. 6.1 and 6.2, the mean-field matrices are

$$\begin{aligned} \Delta_{i\uparrow j\downarrow} &= V \langle c_{i\downarrow} c_{i\uparrow} \rangle \delta_{ij} = \Delta_i \delta_{ij} \\ U_{i\uparrow j\uparrow} &= 2V_{\uparrow\downarrow\uparrow} \langle c_{i\downarrow}^\dagger c_{i\downarrow} \rangle = U_{i\uparrow} \delta_{ij} \\ U_{i\downarrow j\downarrow} &= 2V_{\downarrow\uparrow\downarrow} \langle c_{i\uparrow}^\dagger c_{i\uparrow} \rangle = U_{i\downarrow} \delta_{ij}. \end{aligned}$$

For the reasons stated above, the term  $U$  is ignored. The effective Hamiltonian becomes

$$\mathcal{H}_{\text{eff}} = \sum_{ij} t_{ij} \left( c_{i\uparrow}^\dagger c_{j\uparrow} + c_{i\downarrow}^\dagger c_{j\downarrow} \right) + \sum_i \left[ \Delta_i c_{i\uparrow}^\dagger c_{i\downarrow}^\dagger + \Delta_i^* c_{i\downarrow} c_{i\uparrow} \right],$$

which after the Bogoliubov transformation leads to

$$\begin{pmatrix} u_{ni} \\ v_{ni} \end{pmatrix} E_n = \sum_j \begin{pmatrix} t_{ij} - \mu \delta_{ij} & \Delta_j \delta_{ij} \\ \Delta_j^* \delta_{ij} & - (t_{ij}^* - \mu \delta_{ij}) \end{pmatrix} \begin{pmatrix} u_{nj} \\ v_{nj} \end{pmatrix}. \quad (6.5)$$

The self-consistent equations that describe  $\Delta_i$  are

$$\Delta_i = V \langle e, i | 1 - 2f(H) | h, i \rangle. \quad (6.6)$$

After solving the self-consistent equations, the order parameter is expected to have some

variation around the impurities. In 1D, this variation can have very long tails before reaching the homogeneous value, of the order of hundreds of nanometers [140], but this behavior is highly suppressed in higher dimensions. In what follows, we will assume that the impurities are sufficiently far apart that the  $\Delta_i$  attain their homogeneous value between each impurity. In 1D, this represents an extremely dilute scenario because of the long tails, but in 2D this is not the case. It is also reasonable to expect that  $\Delta_i$  around an impurity doesn't change appreciably from one impurity to the next (refer to Fig. 6.1). Let  $R_a$  be the site where the  $a$ -th impurity is located. Then, mathematically, for  $i$  around any impurity site  $R_a \approx i$ , this is expressed as

$$\Delta_i \approx g(i - R_a)$$

for some function  $g$ . This is only valid in the vicinity of the impurity, where  $\Delta_i$  varies

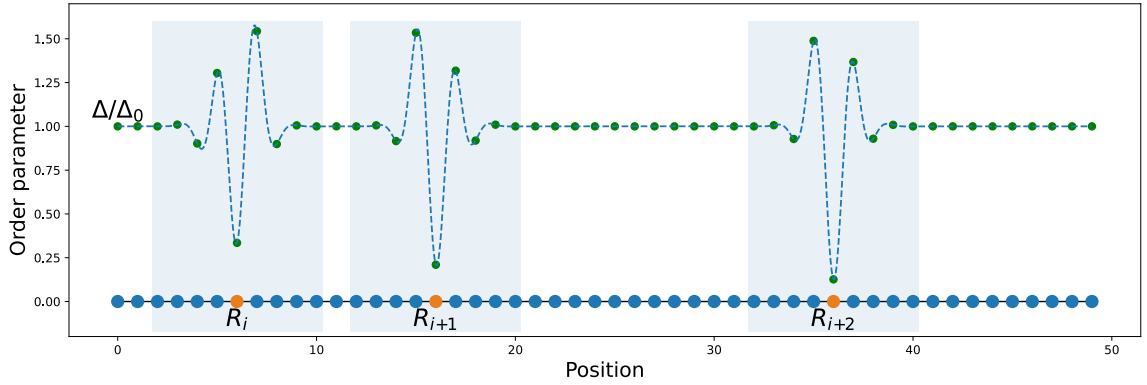


Figure 6.1: Representation of the order parameter around several impurities.

appreciably. Let  $z$  be a cutoff distance where this relation is expected to hold, imposing  $|R_a - i| < z$ . When  $|R_a - i| > z$ ,  $\Delta_i$  should return to a homogeneous value  $\Delta^*$  yet to be determined as well (not necessarily the same as the case without impurities)

$$\Delta_i \approx \Delta^*.$$

The next question is obvious: how to determine both  $\Delta^*$  and the function  $g$ ? This is the next step of the approximation: we choose  $g(i)$  to be the average of  $\Delta_i$  around every single one of the  $N_a$  impurities, that is:

$$g(i) = \frac{1}{N_a} \sum_{\{R_a\}} \Delta_{i+R_a},$$

while making sure that  $|i| < z$ . The advantage of this becomes clear when  $g$  is expressed as a sum of matrix elements

$$g(i) = V \frac{1}{N_a} \sum_{\{R_a\}} \langle e, i + R_a | 1 - 2f(H) | h, i + R_a \rangle.$$

## 6 Spectral methods in superconductors with dilute impurities

Next, to avoid calculating each matrix element individually, we can employ a similar trick to KPM. Let  $|\xi_i, h\rangle$  and  $|\xi_i, e\rangle$  be random vectors defined in the hole and electron sectors, respectively, with random entries only on sites  $R_a + i$ :

$$\begin{aligned} |\xi_i, h\rangle &= \frac{1}{\sqrt{N_a}} \sum_{\{R_a\}} \xi_{R_a} |h, i + R_a\rangle \\ |\xi_i, e\rangle &= \frac{1}{\sqrt{N_a}} \sum_{\{R_a\}} \xi_{R_a} |e, i + R_a\rangle. \end{aligned}$$

The random numbers  $\xi_i$  have zero average and satisfy  $\overline{\xi_i^* \xi_j} = \delta_{ij}$ , where the average is taken with respect to a sample of random vectors. This casts the previous expression into

$$g(i) = V \overline{\langle \xi_i, e | 1 - 2f(H) | \xi_i, h \rangle}.$$

Finally, to avoid calculating the Fermi function, this is written as

$$g(i) = V \int_{-\infty}^{\infty} d\varepsilon [1 - 2f(\varepsilon)] \overline{\langle \xi_i, e | \delta(\varepsilon - H) | \xi_i, h \rangle} \quad (6.7)$$

which closely resembles the expression for the KPM calculation of the density of states. A similar procedure is followed for  $\Delta^*$ . Its value is the average of  $\Delta_i$  away from the impurities. Let  $B$  be the set of sites  $i$  such that  $|R_a - i| > z$  for every  $R_a$ . Then,  $\Delta^*$  is calculated with

$$\Delta^* = V \int_{-\infty}^{\infty} d\varepsilon [1 - 2f(\varepsilon)] \overline{\langle \xi_B, e | \delta(\varepsilon - H) | \xi_B, h \rangle} \quad (6.8)$$

where

$$\begin{aligned} |\xi_B, h\rangle &= \frac{1}{\sqrt{N_a}} \sum_{j \in B} \xi_j |h, j\rangle \\ |\xi_B, e\rangle &= \frac{1}{\sqrt{N_a}} \sum_{j \in B} \xi_j |e, j\rangle. \end{aligned}$$

Now that both  $g$  and  $\Delta^*$  have been determined, we can finally determine the parameters that go inside the Hamiltonian for the next self-consistent step. Instead of 6.5 where the exact order parameter  $\Delta_i$  is used, we define the averaged order parameter

$$\overline{\Delta}_i = \begin{cases} g(i - R_a) & \text{if } |i - R_a| < z \\ \Delta^* & \text{otherwise} \end{cases}$$

to get

$$H_{ij} = \begin{pmatrix} t_{ij} - \mu\delta_{ij} & \overline{\Delta}_i\delta_{ij} \\ \overline{\Delta}_i^*\delta_{ij} & -\left(t_{ij}^* - \mu\delta_{ij}\right) \end{pmatrix}. \quad (6.9)$$

It's worth to emphasize that  $\overline{\Delta}_i$  still retains spatial variation around the impurities, but

it's now the same around every impurity, by construction. The parameter  $z$  controls how much variation is allowed. A smaller  $z$  means that  $\bar{\Delta}_i$  is only allowed to vary in a very small region around each impurity, while a larger  $z$  allows a wider region for  $\bar{\Delta}_i$  to vary. Consequently, the larger the  $z$ , the more values of  $g$  need to be calculated, and the higher the computational cost.

### 6.2.1 Considerations on the choice of $z$

There are three competing length scales here: 1) the length  $\ell_0$  around the impurity such that order parameter varies considerably, 2) the length  $z$  used in this method and 3) the mean distance between impurities, which depends on the concentration  $n$ ,  $d_n$ . Ideally, we want to be in a situation where  $\ell_0 \ll d_n$  so that we can safely set  $z$  such that  $\ell_0 < z < d_n$ , without risk of overlapping regions. In 1D,  $\ell_0$  is of the order of several hundreds of nanometers, which imposes a very dilute limit of less than  $n = 0.2\%$  impurity concentration. In 2D, the scales are typically very different, and we can expect  $\ell_0$  of the order of a few nanometers, imposing a concentration smaller than around  $n = 4\%$ . In 3D, assuming the value of  $\ell_0$  is similar to 2D, then  $n = 0.8\%$ . Thus, this method should be more useful in two dimensions than in one or three.

Even if the condition  $\ell_0 < z < d_n$  is met, it is still possible that two impurities lie close to each other, since this is only a condition on the average distance between impurities. The probability of this happening is  $\approx z^2 n^2$  and so for smaller concentrations and values of  $z$ , it is unlikely to happen. One way to avoid this explicitly is to choose a distribution of impurities such that this never happens. For simplicity, this is the approach followed in section 6.3, but we can still briefly discuss what could be done were this not the case.

When two impurities are close together, nothing needs to be done to eqs. 6.7 and 6.8. The function  $g$  and the parameter  $\Delta^*$  can be calculated in exactly the same way. However, now the claim that  $\Delta_i \approx g(i - R_a)$  when  $|i - R_a| < z$  no longer holds. By evaluating eqs. 6.7 and 6.8 in this way, a small fraction of the summands contributing to  $g$  will contain information about the double impurities. For sufficiently small concentrations, this fraction should be small and no noticeable change should happen. If the concentration is higher, it should start becoming relevant, and will impose a change on every order parameter through  $\bar{\Delta}_i$ , even in places without double impurities. A better alternative would be to treat these situations individually. In the vicinity of double impurities, the order parameter would be calculated directly with eq. 6.6, that is,  $\bar{\Delta}_i = \Delta_i$ , instead of through the means of function  $g$ . While this would incur in a performance penalty, the number of such cases should be small enough for this not to be an issue.

### 6.2.2 Higher dimensions and further generalization

In the previous section, we focused on the 1D tight-binding lattice for illustrative purposes, but everything that has been discussed can easily be extended to higher dimensions and more complicated lattices. The generalization to higher dimensions is the simplest: the

## 6 Spectral methods in superconductors with dilute impurities

indices  $i, j$  as well as the impurity sites  $R_a$  get promoted to vectors, and the length  $z$  becomes a radius.

More complicated lattices and interactions originate more complicated pairing terms, which can connect several unit cells. The reasoning remains the same, though. The pairing term is calculated with eq. 6.3 and it is expected to be approximately the same around every impurity. This can be encapsulated in a straightforward generalization of function  $g$

$$\Delta_{\mathbf{R}\alpha, \mathbf{R}'\beta} \approx g_{\alpha\beta} (\mathbf{R} - \mathbf{R}_a, \mathbf{R}' - \mathbf{R}_a). \quad (6.10)$$

For notational simplicity, both the spin and the other (orbital) degrees of freedom are encapsulated in the superindices  $\alpha$  and  $\beta$ , while the unit cell position is in  $i$  and  $j$ . It is also expected to attain a homogeneous value away from the impurities,

$$\Delta_{\mathbf{R}\alpha, \mathbf{R}'\beta} \approx \Delta_{\alpha\beta}^* (\mathbf{R} - \mathbf{R}').$$

These are more complicated than before because in addition to the previous complexity, now they also have to be evaluated for all  $\alpha, \beta$  and  $\mathbf{R} - \mathbf{R}'$ . One last point that deserves to be mentioned is the subtle change to the random vectors required. For example, a term in eq. 6.10 such as

$$\frac{1}{N_a} \sum_{\{\mathbf{R}_a\}} \langle e\alpha, \mathbf{R} + \mathbf{R}_a | f(H) | h\beta, \mathbf{R}' + \mathbf{R}_a \rangle$$

can be evaluated with the following random vectors:

$$\begin{aligned} |\xi_{\mathbf{R}'}, h\beta\rangle &= \frac{1}{\sqrt{N_a}} \sum_{\{\mathbf{R}_a\}} \xi_{\mathbf{R}_a} |h\beta, \mathbf{R}' + \mathbf{R}_a\rangle \\ |\xi_{\mathbf{R}}, e\alpha\rangle &= \frac{1}{\sqrt{N_a}} \sum_{\{\mathbf{R}_a\}} \xi_{\mathbf{R}_a} |e\alpha, \mathbf{R} + \mathbf{R}_a\rangle \end{aligned}$$

to yield the simple expression

$$\overline{\langle \xi_{\mathbf{R}}, e\alpha | f(H) | \xi_{\mathbf{R}'}, h\beta \rangle}$$

which is going to be useful for later.

### 6.3 Superconducting graphene

The method described so far can be used to study the effect of impurity scattering in superconducting doped graphene. For concreteness, we focus on monolayer graphene, whose leading superconducting instabilities as a function of doping include chiral p-wave pairing states. This kind of superconductivity has caused great excitement because it provides a platform to realize Majorana zero modes that are insensitive to local perturbations and thus can be used to construct topological qubits [141]. It is therefore important to un-

derstand how disorder can affect each kind of superconductivity. Conventional s-wave superconductivity is in general robust to nonmagnetic impurities due to Anderson's theorem [142], but it can be detrimental to unconventional superconducting states when the impurities violate the pairing symmetry. However, there are exceptions to this. In d-wave cuprates, disorder is known to enhance the critical temperature through the appearance of superconducting islands around the impurities [143]. It might be the case that something similar could happen with graphene and p-wave superconductivity.

p-wave superconductivity is normally associated with spin triplets, which forces the angular momentum component of the superconducting wavefunction to be odd in virtue of the total antisymmetry of its fermion wavefunction. However, the same spatial behavior can be achieved with spin singlets if the wavefunction has an extra degree of freedom, such as a sublattice degree of freedom. Such is the case of graphene, which therefore is able to support a p-wave type pairing [132]. In [132], the authors show that in a competition between s-wave and p-wave, the p-wave state is favorable if the on-site electron-electron interactions are repulsive

This model of superconductivity is described by the normal graphene Hamiltonian

$$H_0 = -\mu \sum_i \left( a_{is}^\dagger a_{is} + b_{is}^\dagger b_{is} \right) - t \sum_{\langle ij \rangle_s} a_{is}^\dagger b_{js} - t \sum_{\langle ij \rangle_s} b_{is}^\dagger a_{js}$$

to which a Hubbard interaction  $H_I$  is added, both on-site and nearest-neighbor

$$H_I = \frac{g_0}{2} \sum_{is} \left[ a_{is}^\dagger a_{is} a_{i\bar{s}}^\dagger a_{i\bar{s}} + b_{is}^\dagger b_{is} b_{i\bar{s}}^\dagger b_{i\bar{s}} \right] + g_1 \sum_{\langle ij \rangle_{ss'}} a_{is}^\dagger a_{is} b_{js'}^\dagger b_{js'}$$

Using the prescription of the previous section, this interaction term is decoupled into the pairing Hamiltonian

$$H_P = E_0 + g_0 \sum_i \left( \Delta_{i,a}^0 a_{i\uparrow}^\dagger a_{i\downarrow}^\dagger + \Delta_{i,b}^0 b_{i\uparrow}^\dagger b_{i\downarrow}^\dagger \right) + \text{HC} + g_1 \sum_{\langle i,j \rangle} \Delta_{1,ij} \left( a_{i\uparrow}^\dagger b_{j\downarrow}^\dagger - a_{i\downarrow}^\dagger b_{j\uparrow}^\dagger \right) + \text{HC}$$

or, in the form of the last section,

$$\psi^\dagger \Xi \psi = \frac{1}{2} \begin{pmatrix} a_\uparrow^\dagger & b_\uparrow^\dagger & a_\downarrow & b_\downarrow \end{pmatrix} \begin{bmatrix} -\mu & t & \Delta_{0,A} & \Delta_1 \\ t^\dagger & -\mu & \Delta_1 & \Delta_{0,B} \\ \Delta_{0,A}^\dagger & \Delta_1^\dagger & \mu & -t^* \\ \Delta_1^\dagger & \Delta_{0,B}^\dagger & -t^T & \mu \end{bmatrix} \begin{pmatrix} a_\uparrow \\ b_\uparrow \\ a_\downarrow^\dagger \\ b_\downarrow^\dagger \end{pmatrix}$$

with the other block being trivially related to this one. The superconducting order parameters being given by

$$\begin{aligned} \Delta_{i,a}^0 &= \langle a_{i\downarrow} a_{i\uparrow} \rangle \\ \Delta_{i,b}^0 &= \langle b_{i\downarrow} b_{i\uparrow} \rangle \\ \Delta_{ij}^1 &= \langle a_{i\downarrow} b_{j\uparrow} - a_{i\uparrow} b_{j\downarrow} \rangle \end{aligned}$$

## 6 Spectral methods in superconductors with dilute impurities

and the condensation energy by  $E_0 = -g_0\Delta_0^2 - 3g_1\Delta_1^2$ . The form of  $\Delta_1$  is specifically chosen as to only keep the p-wave structure.

Before adding the impurities, let's briefly discuss what happens in the homogeneous case. The Hamiltonian  $\Xi$  restricted to the first block in momentum space is

$$\psi^\dagger \Xi \psi = \frac{1}{2} \sum_{\mathbf{k}} \begin{pmatrix} a_{\mathbf{k}\uparrow}^\dagger & b_{\mathbf{k}\uparrow}^\dagger & a_{-\mathbf{k}\downarrow} & b_{-\mathbf{k}\downarrow} \end{pmatrix} \begin{bmatrix} -\mu & t\gamma_{\mathbf{k}} & \Delta_0 & \Delta_1\gamma_{\mathbf{k}} \\ t\gamma_{\mathbf{k}} & -\mu & \Delta_1\gamma_{\mathbf{k}}^* & \Delta_0 \\ \Delta_{0,A}^\dagger & \Delta_1\gamma_{\mathbf{k}} & \mu & -t\gamma_{\mathbf{k}} \\ \Delta_1\gamma_{\mathbf{k}}^* & \Delta_{0,B}^\dagger & -t\gamma_{\mathbf{k}}^* & \mu \end{bmatrix} \begin{pmatrix} a_{\mathbf{k}\uparrow} \\ b_{\mathbf{k}\uparrow} \\ a_{-\mathbf{k}\downarrow}^\dagger \\ b_{-\mathbf{k}\downarrow}^\dagger \end{pmatrix}$$

where  $\gamma_{\mathbf{k}} = e^{i\mathbf{k}\cdot\delta_1} + e^{i\mathbf{k}\cdot\delta_2} + e^{i\mathbf{k}\cdot\delta_3}$  is the usual graphene structure factor which close to the Dirac point takes the form  $\gamma_{\mathbf{k}} \approx k_x + ik_y$ . The important factor to notice here is that the p-wave superconducting  $\Delta_1\gamma_{\mathbf{k}}$  is proportional to  $\gamma_{\mathbf{k}}$  and therefore has the expected p-wave structure symmetry as discussed earlier. In this case, this is made possible because of the existence of two sublattices. The order parameters become determined by the equations

$$\begin{aligned} \Delta_0 &= - \sum_{\mathbf{k},s} (g_0\Delta_0 + s|\gamma_{\mathbf{k}}|g_1\Delta_1) \frac{\tanh(\beta\omega_{\mathbf{k}s})}{2\omega_{\mathbf{k}s}} \\ \Delta_1 &= - \sum_{\mathbf{k},s} |\gamma_{\mathbf{k}}| (g_1\Delta_1|\gamma_{\mathbf{k}}| + sg_0\Delta_0) \frac{\tanh(\beta\omega_{\mathbf{k}s})}{6\omega_{\mathbf{k}s}}. \end{aligned}$$

This system displays different superconducting phases depending on the chemical potential and the values of the coupling constants  $g_0$  and  $g_1$  (see [132]). At half-filling, there are several regions of distinct symmetry. Away from half filling, every region is of mixed symmetry but p-wave dominates when the onsite interaction is more repulsive, and s-wave dominates when the nearest neighbor interaction is more repulsive. The important point here is that for the right values of the coupling constants, p-wave can be the dominant pairing symmetry.

To this model, we added a non-magnetic impurity term (see Fig. 6.2):

$$H_I = \Delta t \sum_{\langle ij \rangle: i \in \{\mathbf{R}_A\}} a_{i_s}^\dagger b_{j_s} + \Delta t \sum_{\langle ij \rangle: j \in \{\mathbf{R}_B\}} a_{i_s}^\dagger b_{j_s} + \text{HC}$$

where the  $\mathbf{R}_A$  ( $\mathbf{R}_B$ ) correspond to a set of impurity sites located in sublattice A (B) and  $\Delta t$  represents the change in the hopping from the impurity site to its nearest neighbors, such that the new hopping becomes  $t' = \Delta t + t$  when this term is added to the clean Hamiltonian. This is a special kind of impurity, which does not change the local energy at the impurity sites but weakens the bonds around the impurity sites. Locally, this has the same  $C_3$  symmetry as the graphene lattice and the p-wave interaction term.

In what follows, we used  $z = 3a_0$ , where  $a_0$  is the graphene carbon-carbon distance,  $\Delta t = -0.3t$  and the concentration of impurities was chosen as 5%. Since we already know

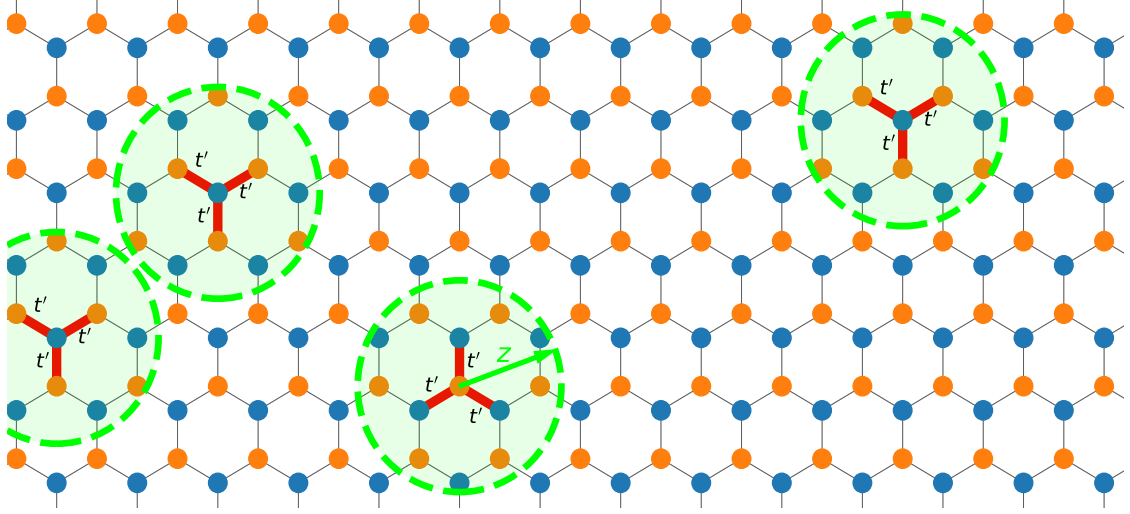


Figure 6.2: Graphene lattice with symmetric bond impurities. The red lines represent the bonds that have been modified from  $t$  to  $t'$ . The green circles have radius  $z$  and correspond to the area where the order parameters are allowed to vary.

the main superconducting phases in each region of the phase diagram, the interesting quantity to analyze is the change to the order parameters for each value of the pair  $g_0, g_1$ . Furthermore, we want to analyze what happens to the superconductor as a whole and not just around the impurities, so we want to look at the order parameters away from the impurities, that is  $\Delta_0^*$  and  $\Delta_1^*$ . This is what is represented in Fig. 6.3 a) through the use of a two-dimensional color scale. The redder (greener) the regions, the more positive change to  $\Delta_0^*$  ( $\Delta_1^*$ ) and the yellow region represents a positive change to both.

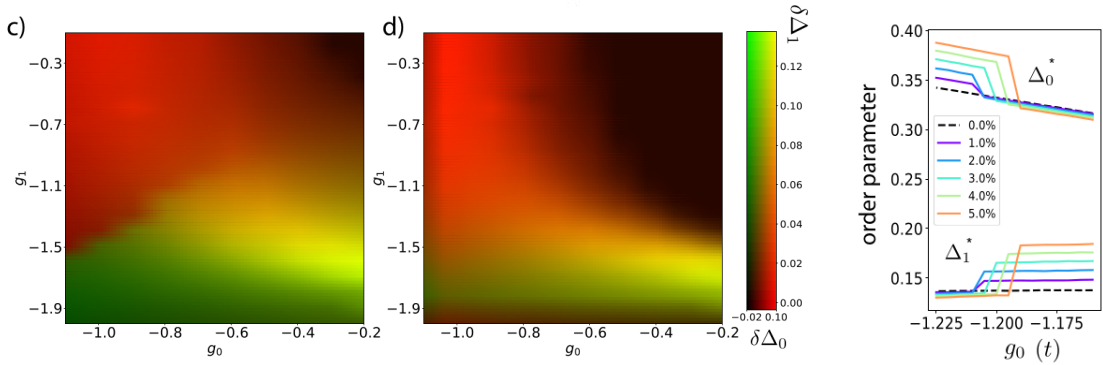


Figure 6.3: Change to the bulk superconducting order parameters  $\Delta_0^*$  and  $\Delta_1^*$ .

These impurities tend to weaken the bonds, making both the superconducting couplings larger in comparison. Therefore, it is not surprising that the net effect of this kind of impurities is to increase the order parameters. To make this statement more concrete, let's imagine that the impurities cover the whole lattice, effectively changing  $t$  to  $t'$ . Then, we can imagine that the energy scales get modified accordingly, supposing  $\varepsilon \rightarrow \varepsilon[1 + \alpha t/t']$  for some  $\alpha$  dependent on the concentration. Using  $\alpha = 1.15$ , we get panel b), indicating that

some of the qualitative features of panel a) can be attributed to this renormalization of the clean case. This renormalization fails to explain the increase of the order parameters for smaller (in absolute value) of the coupling constants. This feature could have its origin in the appearance of superconducting islands around the impurities, but this has not been checked.

The most striking property of panel a) is the discontinuity of colors, which can be made quantitative by plotting the order parameters across it (panel c)). The discontinuity seems to be present at arbitrarily small concentrations, but it disappears in the absence of impurities. Interestingly,  $\Delta_0^*$  is close to its clean value for less attractive onsite interactions (more positive  $g_0$ ), and  $\Delta_1^*$  is close to its clean value for more attractive onsite interactions (more negative  $g_0$ ), which seems to indicate that for most of the diagram, impurities seem to favor only one superconducting phase. In the region where both phases are favored, this behavior can be explained by a simple renormalization of the energy scales.

Wrapping up, the main message of this section is that it is possible to selectively increase p-wave superconductivity in the phase diagram of superconducting graphene due to the effect of impurities. One important issue that should be addressed in more realistic realizations of this model is the simplicity of the interacting potential.  $H_I$  may suffer considerable changes around impurities, and this could change the qualitative picture of this analysis.

## 7 Conclusion

Spectral methods have existed for almost 30 years now [95, 97, 99], but the ever-growing numerical capabilities of modern computers have brought them to the spotlight as some of the most efficient ways to simulate large-scale lattices. In this thesis, I presented several new ways to use spectral methods in different contexts.

The exact calculation of the disordered self-energy operator opens up a new way to look at numerical diagrammatics. On a fundamental level, the self energy is connected to the four-point vertex functions of linear response theory through exact symmetry relations known as Ward identities [144–146], and thus the knowledge of all its matrix elements is essential to obtain physically sensible transport equations. Because our approach provides a systematic way to accurately evaluate the disorder self energy of arbitrarily complex model Hamiltonians, regardless of the type and strength of disorder, it could provide new insights into the array of rich interfacial magnetic phenomena beyond the reach of diagrammatic calculations.

In the field of nonlinear optics, we applied the Keldysh nonequilibrium Green’s function formalism to develop a basis-independent perturbation expansion to higher orders in the electric field. These expressions are in a form directly applicable to spectral methods, thus enabling the study of the nonlinear response of disordered systems or systems under a magnetic field. The numerical application of these formulas requires a triple Chebyshev expansion, which is the main limiting factor in practical terms. For systems with translation invariance, a  $\mathbf{k}$ -space integration is very quick and is preferred over our method. If the systems do not have this property, spectral methods become the most efficient way to calculate the second-order conductivity with disorder. At this point, the viability and validity of a perturbative approach comes back into question, and it might be more numerically efficient to perform the full Hamiltonian time evolution with a Chebyshev expansion of the time-ordered time-evolution operator [98].

In this same line, time-resolved numerics are becoming increasingly popular in several fields. While their most interesting application is certainly the transient regime, they can also be used as an efficient tool to compute steady-state properties. We developed an order  $\mathcal{O}(N)$  algorithm to compute the Landauer current through a unitary time-evolution, casting this problem into the realm of spectral methods.

In the field of superconductivity, unconventional superconductors continue to be one of the biggest puzzles in modern Condensed Matter Physics, and inhomogeneous superconductors provide a fertile ground in which to test new ways to explore their properties. Alongside the development of powerful new methods to treat disorder, the numerical tool-

## 7 Conclusion

box available to physicists also continues to enlarge, as software becomes more powerful and more available to the general public. Spectral methods are now firmly part of any such toolbox and hopefully this chapter proved that even in the superconducting context, they are a very flexible set of tools that can be used to provide large gains in numerical performance. In [88, 91], it is already possible to study superconducting tight-binding lattices of the order of  $10^5$  atoms with the help of GPU processing to speed up the sparse matrix products. Here we reach  $10^6$  atoms with CPU processing in a highly parallelized environment. At this point, this method is tailored to dilute impurities, making explicit use of the fact that the order parameters don't vary in an arbitrary fashion. The underlying point here is that it may not be required to find the order parameters everywhere. Sometimes, it's enough to do it at just a smaller number of points. Moving forward, it would be interesting to see how this method could be adapted close to boundaries or how it could be used with an adaptive mesh of points to avoid the need to calculate the order parameter everywhere. For completeness, it should also be compared against other standard approximation schemes like the T-matrix or CPA within superconductivity.

All of these advancements were made possible thanks to the modern computational power we enjoy, and the KITE open-source initiative [3] has been instrumental as a *de facto* numerical laboratory to test these methods.

# Bibliography

- <sup>1</sup>S. Meneses, J. Penedones, S. Rychkov, J. M. Viana Parente Lopes, and P. Yvernay, “A structural test for the conformal invariance of the critical 3d ising model”, *Journal of High Energy Physics* **2019**, 115 (2019).
- <sup>2</sup>S. M. João and J. M. V. P. Lopes, “Basis-independent spectral methods for non-linear optical response in arbitrary tight-binding models”, *Journal of Physics: Condensed Matter* **32**, 125901 (2019).
- <sup>3</sup>S. M. João, M. Anđelković, L. Covaci, T. G. Rappoport, J. M. V. P. Lopes, and A. Ferreira, “KITE: high-performance accurate modelling of electronic structure and response functions of large molecules, disordered crystals and heterostructures”, *Royal Society Open Science* **7**, 191809 (2020).
- <sup>4</sup>S. Meneses João, J. P. Santos Pires, and J. M. Viana Parente Lopes, “A new microscopic look into pressure fields and local buoyancy”, *American Journal of Physics* **90**, 179–186 (2022).
- <sup>5</sup>S. M. João, J. M. V. P. Lopes, and A. Ferreira, “High-resolution real-space evaluation of the self-energy operator of disordered lattices: gade singularity, spin-orbit effects and p-wave superconductivity”, *arXiv:2110.00574 [cond-mat]* (2021).
- <sup>6</sup>J. P. S. Pires, S. M. João, A. Ferreira, B. Amorim, and J. M. V. P. Lopes, “Nodal vacancy bound states and resonances in t-symmetric weyl semimetals: spectral and bulk transport properties”, (2022).
- <sup>7</sup>J. P. Santos Pires, S. M. João, B. Amorim, A Ferreira, and J. M. Viana Parente Lopes, “Anomalous charge transport in t -symmetric weyl semimetals with point defects”, (2022).
- <sup>8</sup>M. F. C. M. Quintela, J. C. C. Guerra, and S. M. João, “Electronic properties of twisted bilayer graphene in the presence of a magnetic field”, *EPJ Web of Conferences* **233**, Publisher: EDP Sciences, 03004 (2020).
- <sup>9</sup>S. M. João and J. M. V. P. Lopes, “Non-linear optical response in disordered 2d materials”, *EPJ Web of Conferences* **233**, Publisher: EDP Sciences, 03002 (2020).
- <sup>10</sup>P. W. Anderson, “Absence of diffusion in certain random lattices”, *Phys. Rev.* **109**, 1492–1505 (1958).
- <sup>11</sup>W. Kohn and J. M. Luttinger, “Quantum theory of electrical transport phenomena”, *Physical Review* **108**, Publisher: American Physical Society, 590–611 (1957).

## Bibliography

- <sup>12</sup>S. F. Edwards, “A new method for the evaluation of electric conductivity in metals”, *The Philosophical Magazine: A Journal of Theoretical Experimental and Applied Physics* **3**, 1020–1031 (1958).
- <sup>13</sup>J. Rammer, “Quantum transport theory of electrons in solids: a single-particle approach”, *Reviews of Modern Physics* **63**, 781–817 (1991).
- <sup>14</sup>R. Gade, “Anderson localization for sublattice models”, *Nuclear Physics B* **398**, 499–515 (1993).
- <sup>15</sup>R. Gade and F. Wegner, “The  $n = 0$  replica limit of  $u(n)$  and  $u(n)SO(n)$  models”, *Nuclear Physics B* **360**, 213–218 (1991).
- <sup>16</sup>V. Häfner, J. Schindler, N. Weik, T. Mayer, S. Balakrishnan, R. Narayanan, S. Bera, and F. Evers, “Density of states in graphene with vacancies: midgap power law and frozen multifractality”, *Physical Review Letters* **113**, 186802 (2014).
- <sup>17</sup>H. Nakano, “A method of calculation of electrical conductivity”, *Progress of Theoretical Physics* **15**, 77–79 (1956).
- <sup>18</sup>R. Kubo, “A general expression for the conductivity tensor”, *Canadian Journal of Physics* **34**, 1274–1277 (1956).
- <sup>19</sup>R. Kubo, “Statistical-mechanical theory of irreversible processes. i. general theory and simple applications to magnetic and conduction problems”, *Journal of the Physical Society of Japan* **12**, 570–586 (1957).
- <sup>20</sup>D. A. Greenwood, “The boltzmann equation in the theory of electrical conduction in metals”, *Proceedings of the Physical Society* **71**, 585–596 (1958).
- <sup>21</sup>R. Kubo, S. J. Miyake, and N. Hashitsume, “Quantum theory of galvanomagnetic effect at extremely strong magnetic fields”, in *Solid state physics*, Vol. 17, edited by F. Seitz and D. Turnbull (Academic Press, Jan. 1, 1965), pp. 269–364.
- <sup>22</sup>A. Bastin, C. Lewiner, O. Betbeder-matibet, and P. Nozieres, “Quantum oscillations of the hall effect of a fermion gas with random impurity scattering”, *Journal of Physics and Chemistry of Solids* **32**, 1811–1824 (1971).
- <sup>23</sup>P. Středa and L. Smrčka, “Galvanomagnetic effects in alloys in quantizing magnetic fields”, *physica status solidi (b)* **70**, 537–548 (1975).
- <sup>24</sup>L. Smrcka and P. Streda, “Transport coefficients in strong magnetic fields”, *Journal of Physics C: Solid State Physics* **10**, 2153–2161 (1977).
- <sup>25</sup>V. Bonbien and A. Manchon, “Symmetrized decomposition of the kubo-bastin formula”, *Physical Review B* **102**, 085113 (2020).
- <sup>26</sup>R. Landauer, “Spatial variation of currents and fields due to localized scatterers in metallic conduction”, *IBM Journal of Research and Development* **1**, 223–231 (1957).
- <sup>27</sup>M. Büttiker, “Four-terminal phase-coherent conductance”, *Physical Review Letters* **57**, 1761–1764 (1986).

- <sup>28</sup>C. Caroli, R. Combescot, P. Nozieres, and D. Saint-James, “Direct calculation of the tunneling current”, *Journal of Physics C: Solid State Physics* **4**, 916–929 (1971).
- <sup>29</sup>J. Nicol, S. Shapiro, and P. H. Smith, “Direct measurement of the superconducting energy gap”, *Physical Review Letters* **5**, 461–464 (1960).
- <sup>30</sup>I. Giaever, “Electron tunneling between two superconductors”, *Physical Review Letters* **5**, 464–466 (1960).
- <sup>31</sup>J. Bardeen, “Tunnelling from a many-particle point of view”, *Physical Review Letters* **6**, 57–59 (1961).
- <sup>32</sup>L. V. Keldysh, “Diagram technique for nonequilibrium processes”, *Zh. Eksp. Teor. Fiz.* **47**, 1018 (1964).
- <sup>33</sup>M. P. L. Sancho, J. M. L. Sancho, J. M. L. Sancho, and J. Rubio, “Highly convergent schemes for the calculation of bulk and surface green functions”, *Journal of Physics F: Metal Physics* **15**, 851–858 (1985).
- <sup>34</sup>A. MacKinnon and B. Kramer, “One-parameter scaling of localization length and conductance in disordered systems”, *Physical Review Letters* **47**, 1546–1549 (1981).
- <sup>35</sup>C. H. Lewenkopf and E. R. Mucciolo, “The recursive green’s function method for graphene”, *Journal of Computational Electronics* **12**, 203–231 (2013).
- <sup>36</sup>S. Nonoyama and A. Oguri, “Direct calculation of the nonequilibrium current by a recursive method”, *Physical Review B* **57**, 8797–8800 (1998).
- <sup>37</sup>A. Cresti, R. Farchioni, G. Grosso, and G. P. Parravicini, “Keldysh-green function formalism for current profiles in mesoscopic systems”, *Physical Review B* **68**, 075306 (2003).
- <sup>38</sup>B. K. Nikolić, L. P. Zârbo, and S. Souma, “Imaging mesoscopic spin hall flow: spatial distribution of local spin currents and spin densities in and out of multiterminal spin-orbit coupled semiconductor nanostructures”, *Physical Review B* **73**, 075303 (2006).
- <sup>39</sup>L. P. Zârbo and B. K. Nikolić, “Spatial distribution of local currents of massless dirac fermions in quantum transport through graphene nanoribbons”, *Europhysics Letters (EPL)* **80**, 47001 (2007).
- <sup>40</sup>A.-P. Jauho, N. S. Wingreen, and Y. Meir, “Time-dependent transport in interacting and noninteracting resonant-tunneling systems”, *Physical Review B* **50**, 5528–5544 (1994).
- <sup>41</sup>A. Croy and U. Saalman, “Propagation scheme for nonequilibrium dynamics of electron transport in nanoscale devices”, *Physical Review B* **80**, 245311 (2009).
- <sup>42</sup>B. S. Popescu and A. Croy, “Efficient auxiliary-mode approach for time-dependent nanoelectronics”, *New Journal of Physics* **18**, 093044 (2016).
- <sup>43</sup>B. S. Popescu and A. Croy, “Emergence of bloch oscillations in one-dimensional systems”, *Physical Review B* **95**, 235433 (2017).
- <sup>44</sup>F. Bloch, “Über die Quantenmechanik der Elektronen in Kristallgittern”, *Zeitschrift für Physik* **52**, 555–600 (1929).

## Bibliography

- <sup>45</sup>C. Zener and R. H. Fowler, “A theory of the electrical breakdown of solid dielectrics”, *Proceedings of the Royal Society of London. Series A, Containing Papers of a Mathematical and Physical Character* **145**, Publisher: Royal Society, 523–529 (1934).
- <sup>46</sup>K. A. Al-Hassanieh, A. E. Feiguin, J. A. Riera, C. A. Büsser, and E. Dagotto, “Adaptive time-dependent density-matrix renormalization-group technique for calculating the conductance of strongly correlated nanostructures”, *Physical Review B* **73**, Publisher: American Physical Society, 195304 (2006).
- <sup>47</sup>J. Eckel, F. Heidrich-Meisner, S. G. Jakobs, M. Thorwart, M. Pletyukhov, and R. Egger, “Comparative study of theoretical methods for non-equilibrium quantum transport”, *New Journal of Physics* **12**, 043042 (2010).
- <sup>48</sup>S. R. White and A. E. Feiguin, “Real-time evolution using the density matrix renormalization group”, *Physical Review Letters* **93**, Publisher: American Physical Society, 076401 (2004).
- <sup>49</sup>A. J. Daley, C. Kollath, U. Schollwöck, and G. Vidal, “Time-dependent density-matrix renormalization-group using adaptive effective hilbert spaces”, *Journal of Statistical Mechanics: Theory and Experiment* **2004**, Publisher: IOP Publishing, P04005 (2004).
- <sup>50</sup>J. P. Santos Pires, B. Amorim, and J. M. Viana Parente Lopes, “Landauer transport as a quasisteady state on finite chains under unitary quantum dynamics”, *Physical Review B* **101**, 104203 (2020).
- <sup>51</sup>P. A. Franken, A. E. Hill, C. W. Peters, and G. Weinreich, “Generation of optical harmonics”, *Phys. Rev. Lett.* **7**, 118–119 (1961).
- <sup>52</sup>M Bass, P. Franken, J. Ward, and G Weinreich, “Optical rectification”, *Physical Review Letters* **9**, 446 (1962).
- <sup>53</sup>G. New and J. Ward, “Optical third-harmonic generation in gases”, *Physical Review Letters* **19**, 556 (1967).
- <sup>54</sup>D. E. Aspnes, “Energy-band theory of the second-order nonlinear optical susceptibility of crystals of zinc-blende symmetry”, *Physical Review B* **6**, 4648–4659 (1972).
- <sup>55</sup>J. E. Sipe and E. Ghahramani, “Nonlinear optical response of semiconductors in the independent-particle approximation”, *Phys. Rev. B* **48**, 11705–11722 (1993).
- <sup>56</sup>E. Ghahramani, D. J. Moss, and J. E. Sipe, “Full-band-structure calculation of first-, second-, and third-harmonic optical response coefficients of ZnSe, ZnTe, and CdTe”, *Physical Review B* **43**, 9700–9710 (1991).
- <sup>57</sup>F. Bonaccorso, Z. Sun, T. Hasan, and A. Ferrari, *Graphene photonics and optoelectronics*, Vol. 4 (June 2010).
- <sup>58</sup>M. Glazov and S. Ganichev, “High frequency electric field induced nonlinear effects in graphene”, *Physics Reports* **535**, 101–138 (2014).

- <sup>59</sup>S. A. Mikhailov and K Ziegler, “Nonlinear electromagnetic response of graphene: frequency multiplication and the self-consistent-field effects”, *Journal of Physics: Condensed Matter* **20**, 384204 (2008).
- <sup>60</sup>J. Cheng, N. Vermeulen, and J. Sipe, “Third order optical nonlinearity of graphene”, *New Journal of Physics* **16**, 053014 (2014).
- <sup>61</sup>S. A. Mikhailov, “Non-linear electromagnetic response of graphene”, *EPL (Europhysics Letters)* **79**, 27002 (2007).
- <sup>62</sup>J. Cheng, N. Vermeulen, and J. Sipe, “Numerical study of the optical nonlinearity of doped and gapped graphene: from weak to strong field excitation”, *Physical Review B* **92**, 235307 (2015).
- <sup>63</sup>D. J. Passos, G. B. Ventura, J. M. V. P. Lopes, J. M. B. L. d. Santos, and N. M. R. Peres, “Nonlinear optical responses of crystalline systems: results from a velocity gauge analysis”, *Physical Review B* **97**, 10.1103/PhysRevB.97.235446 (2018).
- <sup>64</sup>G. B. Ventura, D. J. Passos, J. M. B. Lopes dos Santos, J. M. Viana Parente Lopes, and N. M. R. Peres, “Gauge covariances and nonlinear optical responses”, *Phys. Rev. B* **96**, 035431 (2017).
- <sup>65</sup>F. J. Wegner, “Electrons in disordered systems. scaling near the mobility edge”, *Zeitschrift für Physik B Condensed Matter* **25**, 327–337 (1976).
- <sup>66</sup>B. Shapiro, “Self-consistent calculation of the frequency-dependent conductivity near the anderson transition”, *Physical Review B* **25**, 4266–4269 (1982).
- <sup>67</sup>P. Lambrianides and H. B. Shore, “Numerical-scaling experiments in anderson localization”, *Physical Review B* **50**, 7268–7271 (1994).
- <sup>68</sup>H. Shima and T. Nakayama, “Critical behavior of ac conductivity near the anderson transition”, *Physical Review B* **60**, 14066–14071 (1999).
- <sup>69</sup>A. Weisse, “Chebyshev expansion approach to the AC conductivity of the anderson model”, *The European Physical Journal B - Condensed Matter and Complex Systems* **40**, 125–128 (2004).
- <sup>70</sup>G. Schubert, G. Wellein, A. Weisse, A. Alvermann, and H. Fehske, “Optical absorption and activated transport in polaronic systems”, *Physical Review B* **72**, 104304 (2005).
- <sup>71</sup>L. He, J. Sun, C. Yang, and Y. Song, “A numerical study of the effect of disorder on optical conductivity in inhomogeneous superconductors”, *Journal of Modern Physics* **4**, 14–16 (2013).
- <sup>72</sup>J. Sun, L. He, Y. Zhao, and Y. Song, “Disorder driven superconductor-insulator transition in inhomogenous d-wave superconductor”, *Science China Physics, Mechanics & Astronomy* **59**, 617401 (2015).
- <sup>73</sup>R. Oiwa and H. Kusunose, “Systematic analysis method for nonlinear response tensors”, *Journal of the Physical Society of Japan* **91**, 014701 (2022).

## Bibliography

- <sup>74</sup>D. van Delft and P. Kes, “The discovery of superconductivity”, *Physics Today* **63**, 38–43 (2010).
- <sup>75</sup>J. Bardeen, L. N. Cooper, and J. R. Schrieffer, “Microscopic theory of superconductivity”, *Physical Review* **106**, 162–164 (1957).
- <sup>76</sup>E. Maxwell, “Isotope effect in the superconductivity of mercury”, *Physical Review* **78**, 477–477 (1950).
- <sup>77</sup>E. Maxwell, “Superconductivity of  $\text{sn}^{124}$ ”, *Physical Review* **79**, 173–173 (1950).
- <sup>78</sup>C. A. Reynolds, B. Serin, W. H. Wright, and L. B. Nesbitt, “Superconductivity of isotopes of mercury”, *Physical Review* **78**, 487–487 (1950).
- <sup>79</sup>H. Fröhlich, “Theory of the superconducting state. i. the ground state at the absolute zero of temperature”, *Physical Review* **79**, Publisher: American Physical Society, 845–856 (1950).
- <sup>80</sup>W. L. McMillan, “Transition temperature of strong-coupled superconductors”, *Physical Review* **167**, 331–344 (1968).
- <sup>81</sup>J. G. Bednorz and K. A. Müller, “Possible high $T_c$  superconductivity in the ba-la-cu-o system”, *Zeitschrift für Physik B Condensed Matter* **64**, 189–193 (1986).
- <sup>82</sup>Y. Cao, V. Fatemi, S. Fang, K. Watanabe, T. Taniguchi, E. Kaxiras, and P. Jarillo-Herrero, “Unconventional superconductivity in magic-angle graphene superlattices”, *Nature* **556**, 43–50 (2018).
- <sup>83</sup>H. Fröhlich, “Superconductivity in metals with incomplete inner shells”, *Journal of Physics C: Solid State Physics* **1**, Publisher: IOP Publishing, 544–548 (1968).
- <sup>84</sup>P. W. Anderson, “The resonating valence bond state in  $\text{la}_2\text{cuo}_4$  and superconductivity”, *Science* **235**, Publisher: American Association for the Advancement of Science, 1196–1198 (1987).
- <sup>85</sup>S. H. Pan, E. W. Hudson, K. M. Lang, H. Eisaki, S. Uchida, and J. C. Davis, “Imaging the effects of individual zinc impurity atoms on superconductivity in  $\text{bi}_2\text{sr}_2\text{cacu}_2\text{o}_8+\delta$ ”, *Nature* **403**, 746–750 (2000).
- <sup>86</sup>R. Moradian, J. F. Annett, B. L. Györfy, and G. Litak, “Superconducting alloys with weak and strong scattering: anderson’s theorem and a superconductor-insulator transition”, *Physical Review B* **63**, 024501 (2000).
- <sup>87</sup>R. Moradian, B. L. Györfy, and J. F. Annett, “Impurity bound states in disordered d-wave superconductors”, *Physical Review Letters* **89**, 287002 (2002).
- <sup>88</sup>L. Covaci, F. M. Peeters, and M. Berciu, “Efficient numerical approach to inhomogeneous superconductivity: the chebyshev-bogoliubov–de gennes method”, *Physical Review Letters* **105**, 167006 (2010).
- <sup>89</sup>L. Covaci and F. M. Peeters, “Superconducting proximity effect in graphene under inhomogeneous strain”, *Physical Review B* **84**, 241401 (2011).

- <sup>90</sup>W. A. Muñoz, L. Covaci, and F. M. Peeters, “Tight-binding study of bilayer graphene josephson junctions”, *Physical Review B* **86**, 184505 (2012).
- <sup>91</sup>W. A. Muñoz, L. Covaci, and F. M. Peeters, “Disordered graphene josephson junctions”, *Physical Review B* **91**, 054506 (2015).
- <sup>92</sup>C. W. Groth, M. Wimmer, A. R. Akhmerov, and X. Waintal, “Kwant: a software package for quantum transport”, *New Journal of Physics* **16**, 063065 (2014).
- <sup>93</sup>B. Gaury, J. Weston, M. Santin, M. Houzet, C. Groth, and X. Waintal, “Numerical simulations of time-resolved quantum electronics”, *Physics Reports, Numerical simulations of time-resolved quantum electronics* **534**, 1–37 (2014).
- <sup>94</sup>A. Ferreira and E. R. Mucciolo, “Critical delocalization of chiral zero energy modes in graphene”, *Physical Review Letters* **115**, 106601 (2015).
- <sup>95</sup>A. Weisse, G. Wellein, A. Alvermann, and H. Fehske, “The kernel polynomial method”, *Reviews of modern physics* **78**, 275 (2006).
- <sup>96</sup>F. Triozon and S. Roche, “Efficient linear scaling method for computing the landauer-büttiker conductance”, *The European Physical Journal B - Condensed Matter and Complex Systems* **46**, 427–431 (2005).
- <sup>97</sup>H. Tal-Ezer and R. Kosloff, “An accurate and efficient scheme for propagating the time dependent schrödinger equation”, *The Journal of chemical physics* **81**, 3967–3971 (1984).
- <sup>98</sup>M. Ndong, H. Tal-Ezer, R. Kosloff, and C. P. Koch, “A chebychev propagator with iterative time ordering for explicitly time-dependent hamiltonians”, *The Journal of Chemical Physics* **132**, 064105 (2010).
- <sup>99</sup>R. Silver, “Densities of states of mega-dimensional hamiltonian matrices”, *Int. J. Mod. Phys. C* **5**, 935 (1994).
- <sup>100</sup>Z. Fan, J. H. Garcia, A. W. Cummings, J. E. Barrios-Vargas, M. Panhans, A. Harju, F. Ortman, and S. Roche, “Linear scaling quantum transport methodologies”, *Physics Reports* **903**, 1–69 (2021).
- <sup>101</sup>J. P. S. Pires, B. Amorim, A. Ferreira, I. Adagideli, E. R. Mucciolo, and J. M. V. P. Lopes, “Breakdown of universality in three-dimensional dirac semimetals with random impurities”, *Physical Review Research* **3**, 013183 (2021).
- <sup>102</sup>L. M. Canonico, J. H. García, T. G. Rappoport, A. Ferreira, and R. B. Muniz, “Shubnikov-de haas oscillations in the anomalous hall conductivity of chern insulators”, *Physical Review B* **98**, 085409 (2018).
- <sup>103</sup>L. Fejér, “Untersuchungen über fouriersche reihen”, *Mathematische Annalen* **58**, 51–69 (1903).
- <sup>104</sup>T. Iitaka and T. Ebisuzaki, “Random phase vector for calculating the trace of a large matrix”, *Physical Review E* **69**, 057701 (2004).

## Bibliography

- <sup>105</sup>W. Gautschi, “Construction of gauss-christoffel quadrature formulas”, *Mathematics of Computation* **22**, 251–270 (1968).
- <sup>106</sup>R. Sack and A. Donovan, “An algorithm for gaussian quadrature given modified moments”, *Numerische Mathematik* **18**, 465–478 (1971).
- <sup>107</sup>J Skilling, *Maximum entropy and bayesian methods*, 1st ed., Fundamental Theories of Physics (Springer Dordrecht, 1988).
- <sup>108</sup>H. Boschker, T. Harada, T. Asaba, R. Ashoori, A. Boris, H. Hilgenkamp, C. Hughes, M. Holtz, L. Li, D. Muller, H. Nair, P. Reith, X. Renshaw Wang, D. Schlom, A. Soukiasian, and J. Mannhart, “Ferromagnetism and conductivity in atomically thin SrRuO<sub>3</sub>”, *Physical Review X* **9**, 011027 (2019).
- <sup>109</sup>J. J. Randall and R. Ward, “The preparation of some ternary oxides of the platinum metals<sup>1,2</sup>”, *Journal of the American Chemical Society* **81**, 2629–2631 (1959).
- <sup>110</sup>G. Koster, L. Klein, W. Siemons, G. Rijnders, J. S. Dodge, C.-B. Eom, D. H. A. Blank, and M. R. Beasley, “Structure, physical properties, and applications of SrRuO<sub>3</sub> thin films”, *Reviews of Modern Physics* **84**, 253–298 (2012).
- <sup>111</sup>P. García-Fernández, M. Verissimo-Alves, D. I. Bilc, P. Ghosez, and J. Junquera, “First-principles modeling of the thermoelectric properties of SrTiO<sub>3</sub>/SrRuO<sub>3</sub> superlattices”, *Physical Review B* **86**, 085305 (2012).
- <sup>112</sup>M. Verissimo-Alves, P. García-Fernández, D. I. Bilc, P. Ghosez, and J. Junquera, “Highly confined spin-polarized two-dimensional electron gas in SrTiO<sub>3</sub>/SrRuO<sub>3</sub> superlattices”, *Physical Review Letters* **108**, 107003 (2012).
- <sup>113</sup>D. J. Groenendijk, C. Autieri, T. C. van Thiel, W. Brzezicki, J. R. Hortensius, D. Afanasiev, N. Gauquelin, P. Barone, K. H. W. van den Bos, S. van Aert, J. Verbeeck, A. Filippetti, S. Picozzi, M. Cuoco, and A. D. Caviglia, “Berry phase engineering at oxide interfaces”, *Physical Review Research* **2**, 023404 (2020).
- <sup>114</sup>B. Sohn, E. Lee, W. Kyung, M. Kim, H. Ryu, J. S. Oh, D. Kim, J. K. Jung, B. Kim, M. Han, T. W. Noh, B.-J. Yang, and C. Kim, “Sign-tunable anomalous hall effect induced by symmetry-protected nodal structures in ferromagnetic perovskite oxide thin films”, [arXiv:1912.04757 \[cond-mat\]](https://arxiv.org/abs/1912.04757) (2019).
- <sup>115</sup>Z. Fang, N. Nagaosa, K. S. Takahashi, A. Asamitsu, R. Mathieu, T. Ogasawara, H. Yamada, M. Kawasaki, Y. Tokura, and K. Terakura, “The anomalous hall effect and magnetic monopoles in momentum space”, *Science* **302**, 92–95 (2003).
- <sup>116</sup>K. S. Novoselov, A. K. Geim, S. V. Morozov, D. Jiang, Y. Zhang, S. V. Dubonos, I. V. Grigorieva, and A. A. Firsov, “Electric field effect in atomically thin carbon films”, *Science* **306**, 666–669 (2004).
- <sup>117</sup>K. S. Novoselov, A. K. Geim, S. V. Morozov, D. Jiang, M. I. Katsnelson, I. V. Grigorieva, S. V. Dubonos, and A. A. Firsov, “Two-dimensional gas of massless dirac fermions in graphene”, *Nature* **438**, 197 (2005).

- <sup>118</sup>A. C. Neto, F Guinea, N. M. Peres, K. S. Novoselov, and A. K. Geim, “The electronic properties of graphene”, *Reviews of modern physics* **81**, 109 (2009).
- <sup>119</sup>D. A. Abanin, A. V. Shytov, and L. S. Levitov, “Peierls-type instability and tunable band gap in functionalized graphene”, *Physical Review Letters* **105**, 086802 (2010).
- <sup>120</sup>T. O. Wehling, S. Yuan, A. I. Lichtenstein, A. K. Geim, and M. I. Katsnelson, “Resonant scattering by realistic impurities in graphene”, *Physical Review Letters* **105**, 056802 (2010).
- <sup>121</sup>N. M. R. Peres, F. Guinea, and A. H. Castro Neto, “Electronic properties of disordered two-dimensional carbon”, *Physical Review B* **73**, 125411 (2006).
- <sup>122</sup>P. Ostrovsky, I. Protopopov, E. König, I. Gornyi, A. Mirlin, and M. Skvortsov, “Density of states in a two-dimensional chiral metal with vacancies”, *Physical Review Letters* **113**, 186803 (2014).
- <sup>123</sup>P. M. Ostrovsky, I. V. Gornyi, and A. D. Mirlin, “Electron transport in disordered graphene”, *Physical Review B* **74**, 235443 (2006).
- <sup>124</sup>R. A. Jishi, *Feynman diagram techniques in condensed matter physics* (Cambridge University Press, 2013).
- <sup>125</sup>J. T. Devreese and V. E. van Doren, *Linear and nonlinear electron transport in solids*, 1st ed., Vol. 17, Nato Science Series B (Springer New York, NY, 1976).
- <sup>126</sup>R. Peierls, “Zur theorie des diamagnetismus von leitungselektronen”, *Zeitschrift für Physik* **80**, 763–791 (1933).
- <sup>127</sup>D. E. Parker, T. Morimoto, J. Orenstein, and J. E. Moore, “Diagrammatic approach to nonlinear optical response with application to weyl semimetals”, *Phys. Rev. B* **99**, 045121 (2019).
- <sup>128</sup>F Hipolito, T. G. Pedersen, and V. M. Pereira, “Nonlinear photocurrents in two-dimensional systems based on graphene and boron nitride”, *Physical Review B* **94**, 045434 (2016).
- <sup>129</sup>H. U. Baranger and A. D. Stone, “Electrical linear-response theory in an arbitrary magnetic field: a new fermi-surface formation”, *Physical Review B* **40**, 8169–8193 (1989).
- <sup>130</sup>A. George, “Nested dissection of a regular finite element mesh”, *SIAM Journal on Numerical Analysis* **10**, 345–363 (1973).
- <sup>131</sup>L. Mao, T. Deng, and P. Zhang, “Boundary condition independence of non-hermitian hamiltonian dynamics”, *Physical Review B* **104**, Publisher: American Physical Society, 125435 (2021).
- <sup>132</sup>B. Uchoa and A. H. Castro Neto, “Superconducting states of pure and doped graphene”, *Physical Review Letters* **98**, 10.1103/PhysRevLett.98.146801 (2007).
- <sup>133</sup>L. Ballentine, *Quantum mechanics: a modern development: 2nd edition* (Jan. 2014), 1–722.

## Bibliography

- <sup>134</sup>K. Maki, “Introduction to d-wave superconductivity”, *AIP Conference Proceedings* **438**, 83–128 (1998).
- <sup>135</sup>C. Kallin and J. Berlinsky, “Chiral superconductors”, *Reports on Progress in Physics* **79**, 054502 (2016).
- <sup>136</sup>J. F. Annett, “Unconventional superconductivity”, *Contemporary Physics* **36**, 423–437 (1995).
- <sup>137</sup>P. W. Anderson and P. Morel, “Generalized bardeen-cooper-schrieffer states and the proposed low-temperature phase of liquid he3”, *Physical Review* **123**, 1911–1934 (1961).
- <sup>138</sup>R. Balian and N. R. Werthamer, “Superconductivity with pairs in a relative p wave”, *Physical Review* **131**, 1553–1564 (1963).
- <sup>139</sup>M. Ausloos and A. A. Varlamov, eds., *Fluctuation phenomena in high temperature superconductors* (Springer Netherlands, Dordrecht, 1997).
- <sup>140</sup>L. Lauke, M. S. Scheurer, A. Poenicke, and J. Schmalian, “Friedel oscillations and majorana zero modes in inhomogeneous superconductors”, *Physical Review B* **98**, 134502 (2018).
- <sup>141</sup>D. A. Ivanov, “Non-abelian statistics of half-quantum vortices in p-wave superconductors”, *Physical Review Letters* **86**, 268–271 (2001).
- <sup>142</sup>P. W. Anderson, “Theory of dirty superconductors”, *Journal of Physics and Chemistry of Solids* **11**, 26–30 (1959).
- <sup>143</sup>M. Leroux, V. Mishra, J. P. C. Ruff, H. Claus, M. P. Smylie, C. Opagiste, P. Rodière, A. Kayani, G. D. Gu, J. M. Tranquada, W.-K. Kwok, Z. Islam, and U. Welp, “Disorder raises the critical temperature of a cuprate superconductor”, *Proceedings of the National Academy of Sciences* **116**, 10691–10697 (2019).
- <sup>144</sup>B. Velický, A. Kalvová, and V. Špička, “Ward identity for nonequilibrium fermi systems”, *Physical Review B* **77**, 041201 (2008).
- <sup>145</sup>M. Milletari, M. Offidani, A. Ferreira, and R. Raimondi, “Covariant conservation laws and the spin hall effect in dirac-rashba systems”, *Physical Review Letters* **119**, 246801 (2017).
- <sup>146</sup>V. Janiš, “Parquet approach to nonlocal vertex functions and electrical conductivity of disordered electrons”, *Physical Review B* **64**, 115115 (2001).
- <sup>147</sup>B. L. Altshuler, D. Khmel’nitzkii, A. I. Larkin, and P. A. Lee, “Magnetoresistance and hall effect in a disordered two-dimensional electron gas”, *Physical Review B* **22**, 5142–5153 (1980).

# 8 Appendix

## 8.1 Self averaging property

The self-averaging behavior of the disorder self-energy yields highly converged results in a computationally efficient manner and so it must be justified. While a rigorous general proof is beyond the scope of this thesis, we show below that under some rather general assumptions, the matrix elements  $G_{\alpha\beta}(\mathbf{k}, z) = \langle \alpha, \mathbf{k} | G(z) | \beta, \mathbf{k} \rangle$  (and hence the quasiparticle self-energy) satisfy the self-averaging lemma

$$\frac{\overline{[\text{Im } G_{\alpha\beta}(\mathbf{k}, z)]^2} - \overline{\text{Im } G_{\alpha\beta}(\mathbf{k}, z)}^2}{\overline{\text{Im } G_{\alpha\beta}(\mathbf{k}, z)}^2} \propto \frac{1}{D}$$

where  $\langle \dots \rangle$  indicates disorder (configurational) averaging and  $D$  is the Hilbert space dimension of the lattice model that scales with the volume (a similar expression holds for the real part of the matrix elements). To simplify the discussion, we specialize to single-orbital models and thus omit the orbital index  $\alpha, \beta$  hereafter. Let  $\xi_{\mathbf{k}} = \text{Im} \langle \mathbf{k} | G(z) | \mathbf{k} \rangle$  denote the imaginary part of the matrix element that will be used to determine the self-energy. The dependency on  $z$  is left implicit. It is implied that  $G(z) = (z - H)^{-1}$  with  $H = H_0 + V$  and  $z = \varepsilon + i\eta$ , for a small  $\eta$ .  $H$  is the full Hamiltonian, which includes the clean (translation-invariant) Hamiltonian  $H_0$  and the disorder operator  $V$ . The clean Green's function is defined as  $g(z) = (z - H_0)^{-1}$ .

Specifically, we want to show that  $\xi_{\mathbf{k}}$  displays self-averaging behavior, that is  $\text{var } \xi_{\mathbf{k}} \equiv \overline{\xi_{\mathbf{k}}^2} - \overline{\xi_{\mathbf{k}}}^2 \propto D^{-1}$ . The argument is identical for the real part of  $\langle \mathbf{k} | G(z) | \mathbf{k} \rangle$ . We consider two common classes of problems for lattice models defined on arbitrary number of spatial dimensions: (i) systems characterized by perturbative (weak) disorder effects; and (ii) systems possessing exponentially localized single-particle states in their spectrum. Finally, we provide a numerical evidence to our claim.

### 8.1.1 Weak disorder

If the diagrammatic expansion of the Green's function is convergent, then we can use an expansion in powers of  $V$ , the disorder potential:

$$\xi_{\mathbf{k}} = \sum_{n=0}^{\infty} \text{Im} \langle \mathbf{k} | g(Vg)^n | \mathbf{k} \rangle$$

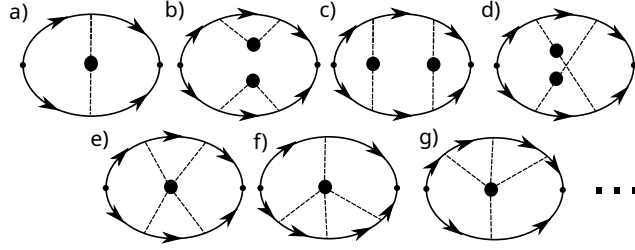


Figure 8.1: Feynman diagrams that contribute to the variance of  $\text{Im } G_{\mathbf{k}}$  up to second order in  $\hat{V}_{\text{dis}}$ .

to evaluate the disorder average  $\overline{\xi_{\mathbf{k}}\xi_{\mathbf{k}}}$ , keeping in mind that the term  $\overline{\xi_{\mathbf{k}}\xi_{\mathbf{k}}}$  will remove all the terms in the diagrammatic expansion which do not connect both Green's functions. Defining  $g_{\mathbf{k}} = \langle \mathbf{k} | g(z) | \mathbf{k} \rangle$  for convenience (with the dependency on  $z$  left implicit again) and using  $\langle \mathbf{R} | \mathbf{k} \rangle = D^{-1/2} e^{i\mathbf{R}\cdot\mathbf{k}}$  to express the disorder potential in real space, we obtain

$$\begin{aligned} \xi_{\mathbf{k}} &= \text{Im}g_{\mathbf{k}} + \text{Im}g_{\mathbf{k}} \left( \sum_{\mathbf{R}} \frac{1}{D} V_{\mathbf{R}} \right) g_{\mathbf{k}} + \\ &+ \text{Im}g_{\mathbf{k}} \sum_{\mathbf{q}} \sum_{\mathbf{R}\mathbf{R}'} \frac{1}{D^2} e^{i(\mathbf{R}-\mathbf{R}')\cdot(\mathbf{q}-\mathbf{k})} V_{\mathbf{R}} g_{\mathbf{q}} V_{\mathbf{R}'} g_{\mathbf{k}} + \dots \end{aligned}$$

We get a factor of  $1/D$  from every disorder insertion  $V_{\mathbf{R}}$  and also a factor of  $D$  due to the sum over  $\mathbf{R}$ . We assume that  $V_{\mathbf{R}}$  is an uncorrelated disorder potential with Gaussian statistics, i.e.  $\overline{V_{\mathbf{R}}} = 0$ ,  $\overline{V_{\mathbf{R}}V_{\mathbf{R}'}} \propto \delta_{\mathbf{R}\mathbf{R}'}$ ,  $\overline{V_{\mathbf{R}}V_{\mathbf{R}'}V_{\mathbf{R}''}} = 0$ , etc. As explained below this assumption is not essential, but it substantially simplifies the analysis. The configurational average introduces correlations between the disorder insertions as Kronecker deltas  $\delta_{\mathbf{R}\mathbf{R}'}$  between different positions. Each  $\delta_{\mathbf{R}\mathbf{R}'}$  effectively contributes with an additional factor of  $1/D$ . Lastly, each loop in the diagrams (representing integrations over internal momenta) contributes with another factor of  $D$ .

Figure 8.1 shows the diagrams that contribute to the variance up to fourth order in  $V$ . Counting all the powers of  $D$ , one can check that each term is associated with a factor of  $1/D$  except for diagram (b). Instead, this diagram is proportional to  $(D-1)/D$ , but the constant term gets cancelled precisely by  $\overline{\xi_{\mathbf{k}}\xi_{\mathbf{k}}}$  and what is left is again proportional to  $1/D$ . At higher orders in  $V$ , similar arguments can be made. If the upper branch of the diagrams is not connected to the lower branch, then it will get almost completely cancelled by  $\overline{\xi_{\mathbf{k}}\xi_{\mathbf{k}}}$ , leaving only the  $1/D$  contribution. If both branches are connected, the number of loops is not large enough to destroy the  $1/D$  dependency.

While we have only strictly presented our argument for uncorrelated disorder, we argue that a generalization to correlated disorder should also be possible provided the correlation

length is finite. In such a scenario, averaging over disorder would introduce asymptotically decreasing functions of the distance between  $\mathbf{R}$  and  $\mathbf{R}'$  in lieu of Kronecker deltas. In any case, a sum over the position (which would contribute with a factor of  $D$  as noted in the previous paragraph) now contributes with a factor of order unity, effectively having the same effect as the Kronecker delta for the purposes of self averaging.

### 8.1.2 Localized states

Next, we analyze an important class of problems where diagrammatic methods break down [147]: strongly disordered systems with localized states in their spectrum. We assume that the value of  $\varepsilon$  is such that all the states in an energy window  $\eta$  around  $\varepsilon$  are localized, with a maximum localization length of  $\zeta$ . We begin by expressing  $\xi_{\mathbf{k}}$  in terms of the eigenstates with energies  $\{\varepsilon_\alpha\}$  resolved in space

$$\xi_{\mathbf{k}} = \frac{1}{D} \text{Im} \sum_{\mathbf{R}\mathbf{R}'\alpha} e^{i\mathbf{k}\cdot(\mathbf{R}' - \mathbf{R})} \frac{\langle \mathbf{R} | \alpha \rangle \langle \alpha | \mathbf{R}' \rangle}{z - \varepsilon_\alpha} = \frac{1}{D} \text{Im} \sum_{\mathbf{R}} g_{\mathbf{R},\mathbf{k}}$$

where  $g_{\mathbf{R},\mathbf{k}}$  represents the contribution to  $\xi_{\mathbf{k}}$  from the sites around  $\mathbf{R}$ . By assumption, these states are localized, so, for each  $\mathbf{R}$ , only localized states with localization center within a distance  $2\zeta$  around  $\mathbf{R}$  contribute. Let  $S$  be this region. This means that  $g_{\mathbf{R},\mathbf{k}}$  and  $g_{\mathbf{R}',\mathbf{k}}$  have appreciable correlation only if  $|\mathbf{R} - \mathbf{R}'| < 2\zeta$ . It is important to note that  $g_{\mathbf{R},\mathbf{k}}$  is independent of the system size, since the percentage of localized states is assumed to be an intensive property. This is a key assumption in the proof and fundamentally relies on the existence of a mobility edge. Note that  $g_{\mathbf{R},\mathbf{k}}$  is a random variable with a finite maximum absolute value because only a finite number  $N_e$  of elements contribute to both the sum over  $\mathbf{R}'$  and the sum over  $\alpha$ . Using the triangle inequality,

$$\begin{aligned} |g_{\mathbf{R},\mathbf{k}}| &\leq \sum_{\mathbf{R}'\alpha} \frac{|\langle \mathbf{R} | \alpha \rangle| |\langle \alpha | \mathbf{R}' \rangle|}{(\varepsilon - \varepsilon_\alpha)^2 + \eta^2} \\ &\leq \eta^{-2} \sum_{\mathbf{R}'\alpha} |\langle \mathbf{R} | \alpha \rangle| |\langle \alpha | \mathbf{R}' \rangle|. \end{aligned}$$

For both sums,  $N_e$  is the number of degrees of freedom inside a  $d$ -dimensional sphere of radius  $2\zeta$ . Therefore, the sum  $D^{-1} \sum_{\mathbf{R}} g_{\mathbf{R},\mathbf{k}}$  can be seen as a sum of bounded random variables which are only correlated within a distance  $|\mathbf{r}| < 2\zeta$  of one another. Thus  $\xi_{\mathbf{k}}$  follows the central limit theorem and so  $\text{var } \xi_{\mathbf{k}} \sim D^{-1/2}$ , hence proving the self-averaging property. We note the only assumptions made in this derivation were the locality of the localized wave functions and that only localized wave functions have relevant spectral weight in  $\langle \mathbf{k} | G(z) | \mathbf{k} \rangle$ .